Modelling Polymer Electrolyte Membrane Fuel Cells for Dynamic Reliability Assessment

by

Andrey Vasilyev

DOCTORAL THESIS

Submitted in partial fulfilment of the
requirements for the award of

Doctor of Philosophy

of Loughborough University

February 2019

Modelling PEM Fuel Cells for Dynamic Reliability Assessment

Abstract

Tackling climate change is arguably the biggest challenge humanity faces in the 21st century. Rising average global temperatures threaten to destabilize the fragile ecosystem of the Earth and bring unprecedented changes to human lives if nothing is done to prevent it. This phenomenon is caused by the anthropogenic greenhouse effect due to the increasing atmospheric concentrations of carbon dioxide (CO_2). One way to avert the disaster is to drastically reduce the consumption of fossil fuels in all spheres of human activities, including transportation. To do this, research and development of electric vehicles (EVs) to make them more efficient, reliable and accessible is essential.

There are different types of EVs that exist, but the focus of this research project is on the Fuel Cell Electric Vehicles (FCEVs). FCEVs use a device called a Polymer Electrolyte Membrane Fuel Cell (PEMFC) to generate the power on-board the vehicle by an electrochemical process that combines hydrogen and oxygen gases. The primary product of such a reaction is useful electricity and the by-products are water vapour and heat. Consequently, fuel cells offer a zero-emissions solution for the transportation industry.

Unfortunately, current generation of PEMFCs faces a number of issues that prevent them from large-scale market adoption. These issues include high costs, absence of hydrogen fuelling infrastructure and reliability concerns. This research project is focused on the modelling methods for PEMFCs that would allow to make improved reliability predictions depending on chosen hardware configurations, operational conditions and modes. During this project a novel model for dynamic reliability analysis of a PEM fuel cell system is developed using Modelica language. The model takes into account multi-state dynamics and ageing of system components. This is achieved through the combination of physical and stochastic sub-models with shared variables. The physical model created using bond graph approach consist of deterministic calculations of the system state described by variables such as temperature, pressure, mass flow rates and voltage output. Additionally, component degradation models are also taken into account.

The non-deterministic sub-model, on the other hand, is implemented with stochastic Petri nets which represent different events that can occur at random times during the fuel cell lifetime. The hybrid nature of the resulting model makes it possible to gather statistical information of the most probable lifetime scenarios of the system with given starting operational parameters. The analysis of this information reveals the pattern for long-term reliability predictions of the system, thereby providing decision support to improve the overall lifetime performance of the PEMFCs.

Keywords: PEM Fuel Cells, Dynamic Reliability, Bond Graphs, Petri Nets

Publications

Journal papers:

- Vasilyev, A., Andrews, J., Jackson, L. M., Dunnett, S. J., & Davies, B. (2017). Component-based modelling of PEM fuel cells with bond graphs. International Journal of Hydrogen Energy, 42(49), 29406–29421.

- *In preparation:* Vasilyev, A., Andrews, J., Jackson, L. M., Dunnett, S. J., & Davies, B. (2019). Dynamic Reliability Assessment of PEM Fuel Cell Systems.

Peer reviewed conference papers:

- Vasilyev, A., Andrews, J., Jackson, L., & Dunnett, S. (2017). Reliability modelling of PEM fuel cells with hybrid Petri nets. In Safety and Reliability – Theory and Applications (pp. 415–415). CRC Press.

- Vasilyev, A., Dunnett, S. J., & Jackson, L. M. (2015). Model-Based Fault Detection and Isolation of PEM fuel cells using Bond Graphs. In Safety and Reliability of Complex Engineered Systems - Proceedings of the 25th European Safety and Reliability Conference, ESREL 2015.

- Vasilyev, A., Jackson, L., & Dunnett, S. (2015). Fault Detection and Isolation of Polymer Electrolyte Membrane Fuel Cells Using Bond Graphs. In 5th European PEFC and H2 Forum 2015.

- Vasilyev, A., Jackson, L., & Dunnett, S. (2015). Model-based Fault Detection and Isolation of Polymer Electrolyte Membrane Fuel Cells Using Bond Graph Approach. In Advances in Risk and Reliability Technology Symposium 2015.

Acknowledgements

I would like to express my gratitude to my supervisors Professor Lisa Jackson and Dr Sarah Dunnett for allowing me to undertake this research, their guidance, support and patience. I am also thankful to Professor John Andrews for providing me with the means to expand my research interests and further improve my skills.

A big thanks, of course, goes to my PhD colleague Ben Davies for his friendship and support. His diligence with the fuel cell test rig contributed tremendously to validation of my modelling efforts.

I am also thankful to my family and friends anywhere in the world for their love and support.

Contents

Figures

Tables

Abbreviations

BEV Battery Electric Vehicle

BG Bond Graph

BoP Balance of Plant

BPP Bipolar Plate

CDF Cumulative Distribution Function

CL Catalyst Layer

CPN Coloured Petri Net

CV Control Volume

DPRA Dynamic Probabilistic Risk Assessment

EASA Electrochemically Active Surface Area

EIS Electrochemical Impedance Spectroscopy

ET Event Tree

EV Electric Vehicle

FC Fuel Cell

FCEV Fuel Cell Electric Vehicle

FCS Fuel Cell System

FMEA Failure Modes and Effect Analysis

FMECA Failure Modes, Effects and Criticality Analysis

FT Fault Tree

FTA Fault Tree Analysis

FSPN Fluid Stochastic Petri Net

GDL Gas Diffusion Layer

GHG Greenhouse Gases

GSPN Generalised Stochastic Petri Net

HAZOP HAZard and OPerability

HEV Hybrid Electric Vehicle

ICE Internal Combustion Engine

MAE Mean Absolute Error

MC Monte Carlo

MEA Membrane Electrode Assembly

MRE Mean Relative Error

MSL Modelica Standard Library

OCV Open Circuit Voltage

ODE Ordinary Differential Equation

ORR Oxygen Reduction Reaction

PDF Probability Density Function

PDMP Piecewise Deterministic Markov Process

PEM Polymer Electrolyte Membrane

PEMFC Polymer Electrolyte Membrane Fuel Cell

PN Petri Net

PRA Probabilistic Risk Assessment

PRNG Pseudo-Random Number Generator

RAMS Reliability, Availability, Maintainability and Safety

RH Relative Humidity

SOFC Solid Oxide Fuel Cell

SPN Stochastic Petri Net

VHDL Very High Speed Integrated Circuit Hardware Description Language

Background and Motivation

Contents

1.1   Introduction

Climate change is arguably the biggest challenge humanity faces in the 21st century. The continuously increasing global average temperatures promise to bring changes to the environment on a massive scale. So in order to mitigate the effects of climate change, the 2015 Paris Agreement signed by the leaders of 174 countries set out to limit the rise of global temperature to $1.5\,°\mathrm{C}$ [1]. Achieving this goal is a tremendous challenge because the last three decades were the warmest on record and latest average global temperature is already $0.9\,°\mathrm{C}$ above pre-industrial levels and only expected to increase [2]. This trend in global temperatures since 1880 is illustrated in Figure 1.1.

This temperature increase is attributed to the anthropogenic *'greenhouse effect'* primarily caused by the growing global atmospheric concentrations of Greenhouse Gases (GHG) such as carbon dioxide (CO_2), methane (CH_4), nitrous oxide (N_2O) and others. The measurements of historic GHG concentrations were gathered from several ice core studies as
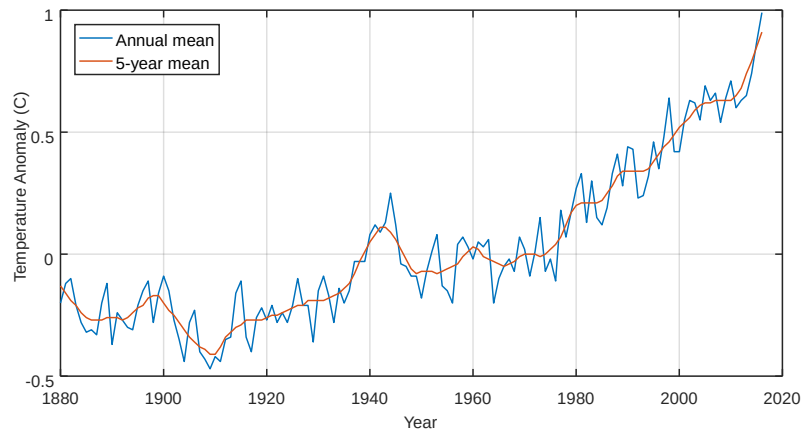
Figure 1.1: Global temperatures change since 1880 [2].
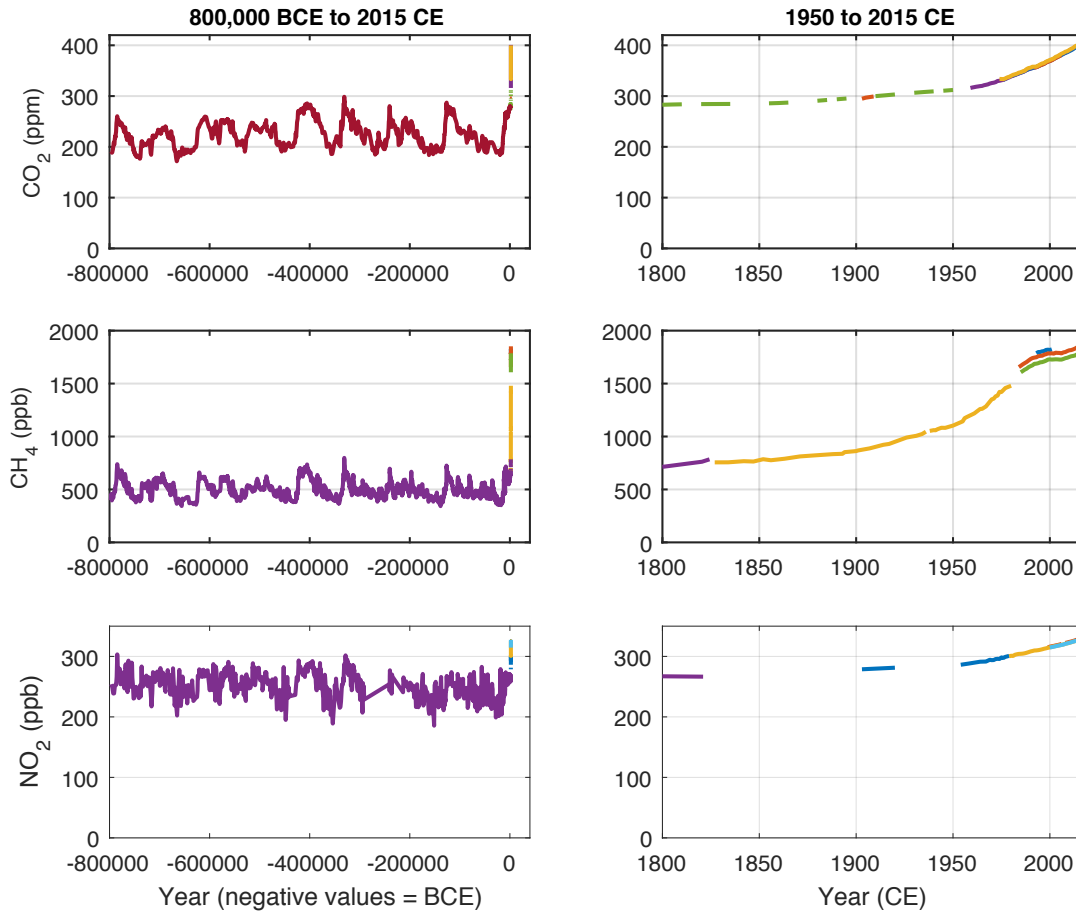
Figure 1.2: Global atmospheric concentrations of CO_2, CH_4 and N_2O over time.

well as modern atmospheric measurements and show an unprecedented increase in GHG concentrations in the last 200 years [3].

The graphs depicting these changes are shown in Figure 1.2 left-hand side of which depicts the concentrations of GHG from 800,000 years Before Common Era (BCE) through to 2015 Common Era (CE). The graphs in the right column of Figure 1.2 provide a more detailed depiction of trends since 1800. It can be seen that up-to 1800 the concentration of CO_2 fluctuated between 171 parts per million (ppm) and 298 ppm, while rising from 282.9 ppm to 400.8 since 1800, a 41 % increase in concentration. Similar trends observed for CH_4 and NO_2: 154 % and 23 % increases since the beginning of the 19th century respectively.

Such rapid growth of GHG in the last 200 years is due to burning of fossil fuels and other human activity [4]. If continued at the current rate of GHG emissions, the global average temperature will continue to grow. Luckily, policy makers around the world recognize the problem and continue to introduce new legislation in order to tackle the problem of climate change. According to a recent study, the total number of policies concerned with climate change now exceeds 1200 – 20 times more than in 1997 [5]. This shows a positive tendency,
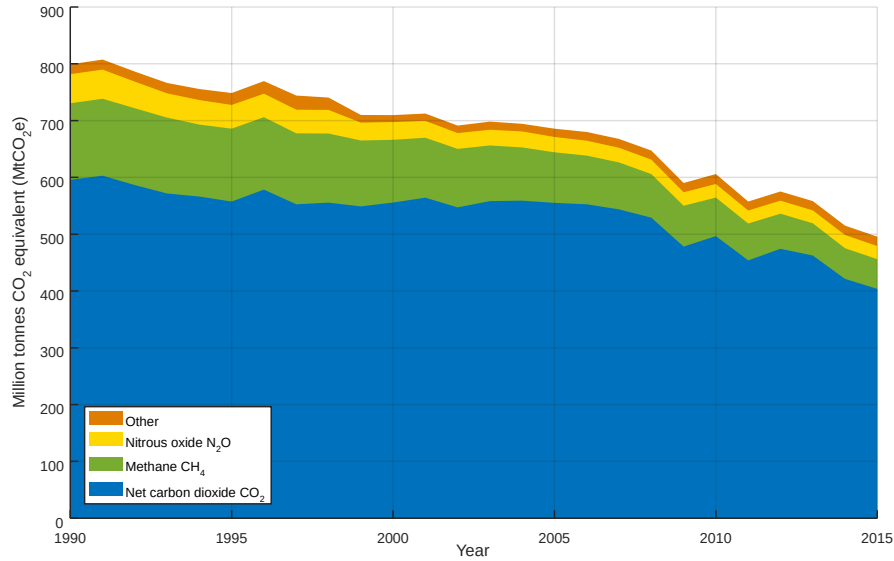
Figure 1.3: Total UK greenhouse gas emissions 1990-2015.

but more needs to be done in order to ensure the impact of anthropogenic greenhouse effect is contained.

In the UK the Climate Change Act adopted in 2008 established the legal requirements for the reduction of greenhouse gases by 80 % of the 1990 baseline. Recently published data shows the progress toward the target so far [6]. Figure 1.3 depicts changes of the amount of CO_2, CH_4, N_2O and other emissions (as expressed in million tonnes carbon dioxide equivalent) throughout the years from 1990 to 2015. As can be seen from Figure 1.3 the total emissions decreased by 38 % from 799 to 495.7 $MtCO_2e$.

Further insight into the UK's emissions data can be gained by analysing the contributions of each economic sector to the total numbers. Figure 1.4 shows the changes of emissions subdivided by seven types of human activity [6].

From this diagram it can be seen that the energy supply sector is the biggest source of GHG emissions with transportation being second and business in third position. However, accelerating development of renewable sources of energy and curtailment of coal consumption in power plants resulted in a significant emissions reduction of 133.8 $MtCO_2e$. This is, therefore, the most significant contributor to the total reduction of GHG emissions in the UK. Other sectors of the economy also underwent technological development resulting in cuts to the emissions.

Table 1.1 summarises the absolute and percentile changes of each sector from 1990 to 2015, which shows that with a mere 1.9 $MtCO_2e$ (1.56 %) decrease in emissions, transportation is lagging far behind other sectors in terms of de-carbonisation rates [6]. Such poor performance of the transport sector is explained by the continuing rise of conventional (Internal Combustion Engine (ICE)) car ownership. Latest statistics on the numbers of registered cars in the UK is summarised in Figure 1.5 [7]. It shows the variation in numbers of different cars in the UK by types of propulsion from 1994 to 2016. From this diagram it
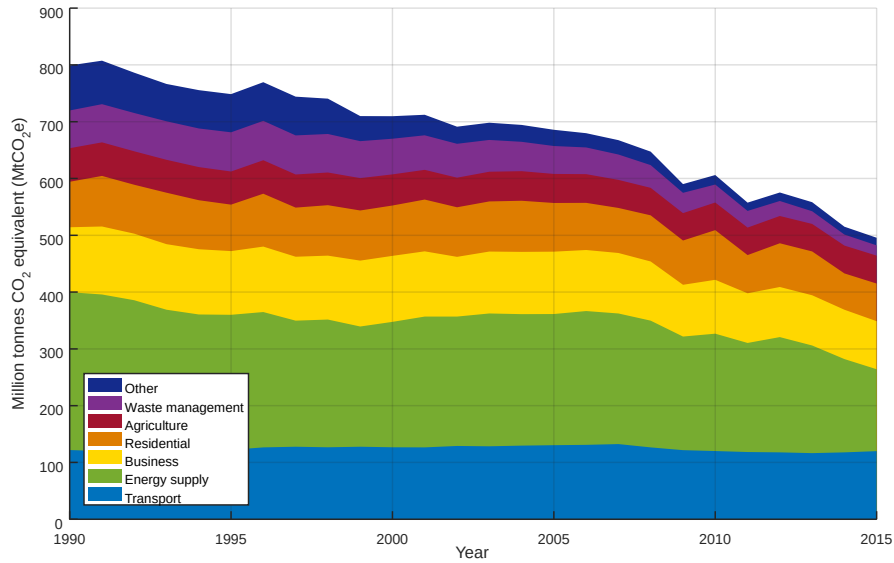
Figure 1.4: Total UK greenhouse gas emissions by source 1990-2015.

Table 1.1: Changes in total UK GHG emissions 1990-2015

Type of activity	1990, MtCO$_2$e	2015, MtCO$_2$e	Change, MtCO$_2$e	Change, %
Energy supply	277.9	144.1	-133.8	-48.15
Transport	121.9	120	-1.9	-1.56
Business	114.4	84.6	-29.8	-26.05
Residential	80.1	66.3	-13.8	-17.23
Other	79.2	13.4	-65.8	-83.08
Waste management	66.6	18.2	-48.4	-72.67
Agriculture	58.9	49.1	-9.8	-16.64
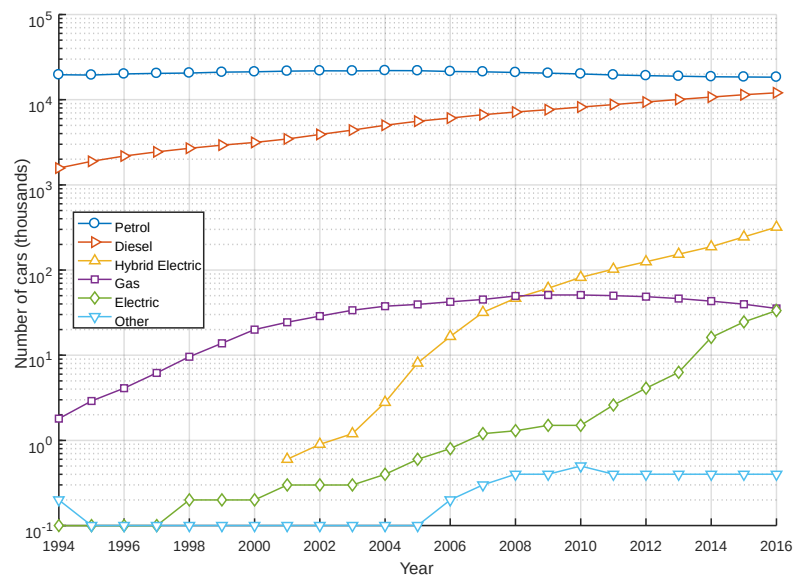
Figure 1.5: The number of cars registered in Great Britain by the propulsion type 1994-2016.

can be seen that the numbers of ICE cars (powered by diesel and petrol) continuously grew during this period and remain the dominant force in the automotive market. Such growth of the numbers of ICE cars inevitably results in the increase of fossil fuel consumption and only imposition of stricter CO_2 regulations and improvements of fuel efficiency was able to balance out and maintain the amounts of transportation emissions at approximately the same level as 1990 figures.

Clearly, the transportation sector is in need of new solutions to rapidly de-carbonize it. One such solution is the development of alternative types of propulsion, less reliant on fossil fuels. Electric Vehicles (EVs) can be powered by renewable sources of energy such as wind or solar thus eliminating the dependency on fossils. Several types of EVs exist: Hybrid Electric Vehicle (HEV), Battery Electric Vehicle (BEV) and Fuel Cell Electric Vehicle (FCEV). HEVs fuse a traditional ICE with an electric propulsion system, thus achieving significant increase in fuel efficiency. BEVs carry a battery on board and use purely electric propulsion to achieve better performance and a complete elimination of CO_2 emissions. FCEVs also use fully electric propulsion, but instead of storing the energy in batteries, they generate the electric power on-board using a device called a Fuel Cell (FC). Multiple types of FCs exist including Solid Oxide, Phosphoric Acid, Alkaline, Molten Carbonate and Polymer Electrolyte Membrane (PEM) fuel cells. FCs generate electrical energy from fuel through an electrochemical reaction taking place at two separate electrodes. The catalysts for such a reaction are often composed of noble metals such as platinum (Pt). This process is described in more detail in the following section.

Among all the diversity of FC types, Polymer Electrolyte Membrane Fuel Cells (PEMFCs) are the most suitable for use in automotive applications due to their fast start-up time and low operating temperatures. Therefore, from this point onwards, in the rest of this dissertation the use of term fuel cell refers specifically to PEM fuel cells.

Figure 1.5 shows that the UK's market of vehicles with such alternative technologies is still in its infancy [7]. This graph shows that the numbers of HEVs soared in the last decade thanks to the popularization of vehicles such as Toyota's Prius and others, while BEVs only recently appeared on the market [7]. Despite the fact that FCEVs offer a number of advantages over all other types of cars, the market for fuel cell powered cars is virtually non-existent. Compared to conventional cars and HEVs, FCEVs do not emit any harmful emissions and operate with minimum noise. Compared to BEVs they offer a significantly increased range and much faster refuelling times. Nevertheless, as of the end of 2016, there were a total of 27 FCEVs registered in the UK [7]. This is because a number of issues related to the technology and infrastructure are needed to be overcome in order to increase the rates of adoption of this technology.

The Fuel Cells Technologies Office within the US Department of Energy compiled a list of key performance indicators of fuel cell technology in automotive applications, some of which are presented in Table 1.2 [8]. The table shows that the cost per kW generated by an automotive fuel cell system in 2015 is still relatively high compared to the targets. One of

Table 1.2: Performance targets for automotive PEMFC systems

Characteristic	Units	2015 Status	2020 Targets	Ultimate Targets
Cost	$/kW$_e$(net)	53	40	30
Peak energy efficiency	%	60	65	70
Volumetric power density	W/L	640	650	850
Gravimetric power density	W/kg	659	650	650
Lifetime durability	hours	3900	5000	8000
Start-up/shut-down durability	cycles	–	5000	5000

the main reasons for high FC costs is the necessity to use platinum as the catalyst in order to ensure the best performance. However, the platinum loading of catalysts was drastically reduced in the past decade, reducing the overall costs of PEMFCs by about 80 % since 2006 (from \$275/kW to \$55/kW in 2013) [9]. Further reductions in costs can be achieved with the development of new types of materials that would provide equal performance without the need for platinum. Alternatively, the costs can be reduced through mass manufacturing and economy of scale.

Next, energy efficiency needs further improvement by means of optimising the components of the system. Volumetric power density (ratio between the total power output to the volume of the FC unit) is close to its 2020 goal, but needs significant improvement for the future. On the other hand, gravimetric power density (ratio between the total power output to the mass of the FC unit) already exceeded its ultimate target.

Fuel cell reliability is also a big concern especially in automotive applications. According to BS:4778, *reliability is the ability of an item to perform a required function, under given environmental and operational conditions and for a stated period of time* [10]. Unfortunately, as can be seen from Table 1.2, current generation of automotive PEMFCs do not meet their reliability targets as they only last for approximately 3900 out of the required 5000 hours under the assumption of average projected lifetime to 10 % voltage degradation. The main reason for the poor reliability performance is the fact that automotive PEMFCs operate under very dynamic operational and ambient conditions. Driving an FCEV subjects the PEMFC system to frequently altering loads, start-stop events, idling and periods of high power demand [11]. Such rapid changes in the operational conditions may negatively affect the internal state of the PEMFC system, thereby exacerbating the various degradation mechanisms. Additionally, impurities present in the reactants and variations in temperature and humidity of the ambient air can negatively contribute to the state of health of the system. In contrast, stationary PEMFC systems can last up to 30 000 h due to the fact that their operating conditions are much more static in comparison [11]. This is because stationary PEMFC are usually used to generate power for buildings, and as

a result their loads are more predictable and slow-changing with significantly less start-stop events making it easier to maintain optimal operating conditions and thus extend the system lifetime for much longer.

Both automotive and stationary PEMFC systems require a host of auxiliary components and sub-systems to support their operation and as with any engineering system, any of these components can fail and disrupt the normal operating regime of the fuel cell. Consequently, in order to prevent and minimise such disruptions an appropriate maintenance strategy is required. On the other hand, in order to mitigate the negative effects of dynamic operating conditions a suitable control strategy is also essential. Implementation of such strategies will lead to a prolonged system lifetime, reduced maintenance costs and ultimately resulting in the reduction of FCEV price, increased safety and customer satisfaction as well as growth of societal acceptance of the technology.

Among other factors hindering the dissemination of FCEVs in the UK are the lack of fuelling stations, technical and societal barriers to hydrogen production, delivery and storage. Nevertheless, UK's EV market is only beginning its life and with sufficient technological development, FCEVs could overcome the hurdles and find their area of application [12].

This dissertation is focused on the underlying causes of unsatisfactory reliability performance of modern automotive PEMFC systems and methods of reliability analysis and prediction. The main factors affecting reliability of PEMFCs considered in this research work are various degradation mechanisms within PEM fuel cells, alterations of the operational load and failures of auxiliary components in the overall system. In order to understand and analyse this problem, knowledge of the operating principles of fuel cells and system architecture is essential.

1.2 PEM Fuel Cell Fundamentals

A fuel cell is a power generation device that converts energy stored within chemical bonds of the fuel directly into useful electrical power. The first fuel cell was invented by Welsh physicist and lawyer William Grove in 1838. He knew that passing electrical current through water (H_2O) separates it into constituent hydrogen (H_2) and oxygen (O_2). This process is called water electrolysis and Grove realised that the reverse reaction must be possible. So in his early experiments, he placed strips of platinum (Pt) connected by a wire into bottles containing H_2 and O_2 gases. He then submerged the bottles into a solution of sulphuric acid (H_2SO_4) and detected the electrical current passing through the wires [13].

What Grove observed was the occurrence of two electrochemical half-reactions that take place at the two electrodes (the platinum strips) which are separated by an electrolyte (H_2SO_4). At one electrode (called the *anode*), the atoms of chemical species (referred to as '*reductant*') are stripped from its valence electron (e^-) in a half-reaction called *oxidation*

as described by Equation 1.1:

$$Reductant \longrightarrow Product + e^- \qquad (1.1)$$
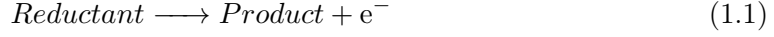
where *reductant* is any chemical species that can release an electron and *product* is the positively charged ion created in the oxidation process.

The electrolyte separating the electrodes is a substance that does not conduct electrons but conducts ions instead. Such electrolyte placed between the electrodes forces the electrons released during oxidation to flow from the anode to the other electrode (called the *cathode*) through an external circuit thereby generating useful electrical current.

The cathode electrode, on the other hand, facilitates the *reduction* half-reaction by combining the '*oxidant*' species with the electrons acquired from the anode according to Equation 1.2:

$$Oxidant + e^- \longrightarrow Product \qquad (1.2)$$

where *oxidant* is a chemical species ready to receive an electron and *product* is the resulting chemical species.

The combined oxidation and reduction half-reactions are commonly referred to as the '*redox*' reaction. Since Grove's invention, other variations of redox reactions were discovered and new materials developed that led to the invention of PEM and other types of FCs.

PEMFCs were created by General Electric engineers in 1960 [14]. The novelty of the invention was due to the solid polymeric electrolyte (called PEM) in contrast to previously used liquid electrolytes. This opened new avenues of fuel cell design and initiated the growth of the PEM fuel cell industry and research. The electrolyte in PEMFCs is a protonic conductor, so the two half reactions are described by Equations 1.3 and 1.4:

$$2\,H_2 \longrightarrow 4\,H^+ + 4\,e^- \qquad (1.3)$$

$$O_2 + 4\,H^+ + 4\,e^- \longrightarrow 2\,H_2O \qquad (1.4)$$

The overall redox reaction is therefore described by Equation 1.5

$$2\,H_2 + O_2 \longrightarrow 2\,H_2O \qquad (1.5)$$

The basic operating principles of PEMFCs is very similar to Grove's original invention and illustrated by Figure 1.6. The anode electrode is supplied with hydrogen gas and the oxidation reaction generates the protons and electrons. The protons travel through the membrane, while electrons move via the external circuit and recombine with O_2 molecules in the reduction reaction. As a result, the only by-products of the PEMFC operation is water and heat. The oxygen provided to the cathode side can be either pure ($100\,\%$ O_2) or as air ($21\,\%$ O_2 and $79\,\%$ N_2).
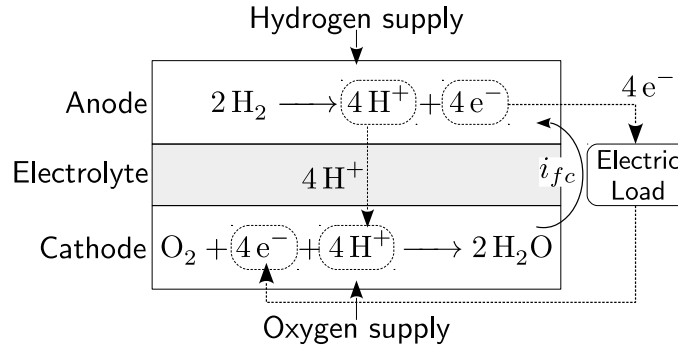
Figure 1.6: Operating principles of PEM fuel cells

PEM fuel cells offer a number of appealing advantages for multiple power generation applications. Firstly, PEM fuel cells operate at low temperatures of 40 °C to 90 °C meaning they can start-up very fast. Secondly, they demonstrate excellent gravimetric power density characteristics and increased fuel efficiency compared to conventional combustion-based generators. Additionally, the ability to refuel an FCEV within several minutes is another highly attractive feature for automotive applications. PEMFCs-based drivetrains were successfully implemented in many light duty vehicles, passenger vehicles and buses. Such powertrains include hybrids, range extenders and fully PEMFC-powered vehicles.

However, the versatility of PEMFCs comes with several drawbacks, some of which were discussed in the previous section. One of the most important of which is the need for careful water and temperature management of the device. This is because the ionic conductivity properties of the membrane strongly depend on the amount of water present within it. When there is no water present and the membrane is dry it's conductivity drops to zero, thus impairing the redox reaction and halting power generation. This means operation temperature must be maintained below 100 °C in order to minimize water evaporation and prevent overheating. On the contrary, when there is too much water present within the cell, it blocks the transport of H_2 and O_2 gases to the electrodes also impairing the electro-chemical reaction. Therefore, automotive PEMFCs must include an array of components that regulate the level of membrane hydration to ensure optimal performance.

The need to operate at low temperatures in turn limits the choice of available electrode materials suitable for the redox reaction. This means that Pt-based electrodes are currently the only types suitable for this task.

1.3 PEM Fuel Cell Components and Structure

A typical PEMFC is a layered assembly consisting of five main components: one Membrane Electrode Assembly (MEA), two Bipolar Plates (BPPs) and two gaskets. The arrangement of these components is illustrated by a diagram in Figure 1.7 in which the MEA is sandwiched between the gaskets and BPPs. The MEA is the heart of a PEM fuel cell and this is where the electricity is generated. It is in itself a 5-layer structure less than
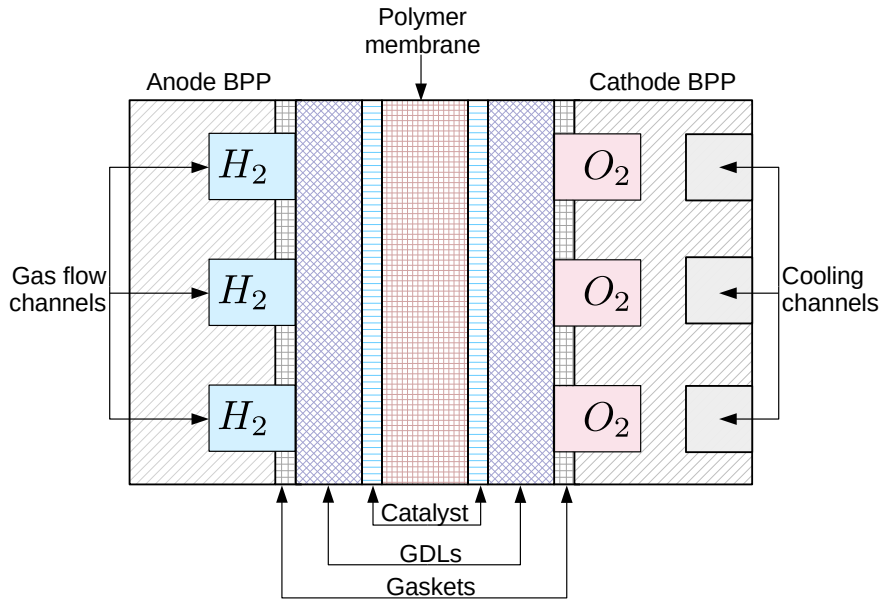
Figure 1.7: PEM fuel cell structure.

1 mm thick. It is comprised of flexible polymeric membrane with catalyst and gas diffusion layers to either side of it. The BPPs have gas flow and cooling channels embedded in them to supply the flow of reactants and coolant fluid to the fuel cell. The gaskets ensure the structure is sealed and eliminate potential gas leaks.

1.3.1 Polymer Electrolyte Membrane

PEM (also known as proton exchange membrane) is an electrolyte approximately 50 µm to 254 µm thick, the main purpose of which is to conduct H^+ ions from the anode to the cathode, while repelling electrons [15]. It is manufactured from polytetrafluoroethylene (PTFE, or Teflon) by adding sulfonic acid ($SO_3^-H^+$) groups to its structure. The sulfonic acid charge sites provide the means for ion transport, while the PTFE base ensures mechanical strength and acts as a barrier that prevents hydrogen and oxygen from uncontrollably mixing and reacting. The most commonly adopted type of membrane is Nafion$^{\mathrm{TM}}$developed by Dupont, which has very high protonic conductivity. However, Nafion's conductivity strongly depends on the amount of water present in it's pores.

When the level of humidification is too low, the membrane is said to be dry and it's conductivity is drastically reduced. Such conditions occur when the increased temperature of the fuel cell leads to increased rates of water evaporation. In contrast, when the temperature is too low or the level of external humidification is too high, it leads to formation of water droplets within the cell. These water droplets cause gas transport issues by limiting the amount of gases capable of reaching the reaction sites.

It is, therefore, very important to carefully maintain the water balance in the PEM fuel cell in order to ensure maximum performance.

Although, flooding and drying-out of the membrane can cause significant reductions in performance, their effects are largely reversible as the excess water can be purged from the cell, while additional water can be injected in order to stop drying out. Nevertheless several ageing phenomena that cause permanent damage to the membrane are discussed next.

As the water content in Nafion changes during fuel cell operation, the membrane can swell up to 22 % of it's dry volume [16]. In dynamic conditions, the temperature and humidification levels can change multiple times, causing the membrane to expand and contract accordingly. The resulting mechanical stresses may lead to local deformations or even fracture. This is especially dangerous as it leads to the breach of the membrane and thus direct mixing of hydrogen with oxygen. The resulting exothermal reaction creates local membrane dry-out, which imposes greater thermal stresses leading to the growth of existing fractures and appearance of new ones. Ultimately this process leads to complete breakdown of the membrane [17].

If the PEMFC is operated in environments where the temperatures can drop below $0\,°C$, it can lead to the formation of ice crystals within the membrane when the system is not in operation. Consequent melting of the ice when the fuel cell is started up causes additional mechanical stress on the membrane leading to gradual breakdown.

Furthermore, under certain unfavourable operating conditions (low relative humidity, high temperatures and high electrical loads), the redox reaction (Equation 1.5) may lead to formation of highly oxidative chemical species such as hydrogen peroxide (H_2O_2), hydroxyl (HO), and hydroperoxyl (HO_2). These highly reactive species (called *'radicals'*) attack the membrane and lead to polymer decay. This process slowly eats away the membrane material, reducing its thickness, and increasing the rate of fuel crossover. If the membrane becomes very thin, electrons can pass directly through it, thus short-circuiting the fuel cell. As a result, the output voltage of the fuel cell falls drastically, as it fails to provide electrical current through an external load. Therefore, humidification cycles and extreme operating conditions must be avoided or minimized in order to increase membrane longevity.

1.3.2 Catalyst Layer

The catalyst layers facilitate the oxidation and reduction reactions (Equations 1.3 and 1.4) which occur most effectively at $40\,°C$ to $90\,°C$ in PEMFCs. Operation in these temperatures is possible due to utilisation of noble metals, such as platinum (Pt) and Pt-based alloys as the catalytic agent. Maximising the amount of available reaction sites is important for increased reaction rate. Therefore, catalyst nano-particles of approximately the same size are uniformly deposited onto a supporting layer of carbon called the '*catalyst support*' layer. As a result, the total surface area of the catalyst is very large.

Smaller Pt nano-particles have increased surface energy compared to larger ones. This causes them to naturally agglomerate into larger ones in order to minimize the surface energy. As the particles grow in size, their collective surface area decreases, thus reducing

the overall Electrochemically Active Surface Area (EASA). This process, called '*Ostwald ripening*' is one of the leading causes for catalyst deterioration.

The corrosion of the carbon support layer also negatively affects catalyst longevity as it weakens the bonds between platinum and carbon. As a consequence, Pt particles can detach from the underlying support layer. The released particles can simply redeposit on another spot within the Catalyst Layer (CL) or subside on other parts of the fuel cell. Some amount can even be washed away from the system altogether [18].

Low operating temperatures of PEM fuel cells cause the Pt-based catalysts to be susceptible to poisoning by unwanted chemical species in both the hydrogen and oxygen supply. Poisoning is a process which results in drastically limited catalyst reaction kinetics and significantly reduced fuel cell performance [18, 19]. Increased concentrations of impurities can cause permanent damage not only to the catalyst, but to other components of the MEA. However, when the concentrations are low enough, it may be possible to reverse the poisoning by flushing the system with clean air [15, 20]. In any case, both reactants must undergo rigorous filtration before they are used in PEMFCs.

Operating conditions also have significant impact on catalyst health. Increased temperature and relative humidity accelerate Pt particle agglomeration. Load cycling in automotive fuel cells is another serious threat due to greatly increased rates of corrosion of the carbon support leading to increased Pt migration [18].

1.3.3 Gas Diffusion Layer

The Gas Diffusion Layer (GDL) is the layer between the CL and the BPPs that facilitates the transfer of reactant gases and liquid water toward and away from the CLs. In order to enable such mass transport capability, the GDL is manufactured out of a porous, hydrophobic and at the same time hydrophilic material. Additionally, GDLs assist with electron transfer from the CLs to the bipolar plates, so the GDL material must also be electrically conductive. Carbon paper or cloth are the best materials that perform all of the above functions [16].

The porous structure of the GDL can undergo electrochemical degradation and mechanical stresses. Carbon corrosion and erosion due to fuel cell activity weakens the material composition and leads to loss of hydrophobic agent, which affects its mass transport properties. In addition, during fuel cell stack (the combination of multiple cells in series to increase the total voltage output) assembly, over-clamping can occur. This causes increased mechanical strain on the MEA in general and GDL in particular, reducing its porosity and leading to the decrease of the mass transport properties [18].

1.3.4 Bipolar plates

BPPs perform multiple functions within the fuel cell stack. The first major function of bipolar plates is mass transport. The gases are redistributed to the reaction sites of the CL via flow channels (called '*flow field*') engraved on one side of the plates. The

(a) Parallel   (b) Serpentine   (c) Interdigitated
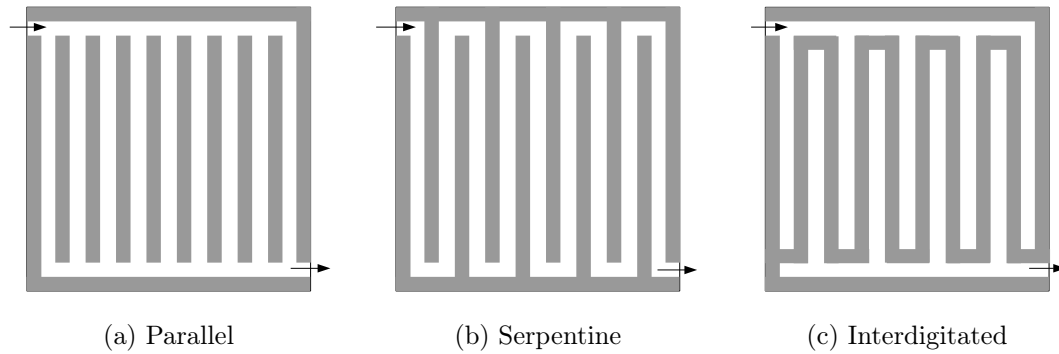
Figure 1.8: Various channel topologies.

design of these channels aims to allow the gases to be redistributed to the reaction sites as uniformly as possible with minimal pressure losses while allowing the condensed water to be removed easily. Various flow fields have been designed and tested over the years, such as parallel, serpentine and interdigitated topologies depicted in Figure 1.8 [21, 22]. The choice of a particular topology depends on multiple parameters such as the field of application, operating conditions and others. Apart from gas transport, bipolar plates can also facilitate thermal management of the fuel cell. Certain BPP designs incorporate cooling channels engraved on the other side of the plate which enable the flow of a coolant to remove the excess heat generated as a result of the fuel cell operation. Furthermore, BPPs must be electrically conductive in order to transfer the electric current from the MEAs to the current collectors of the external load. In order to perform all of the above functions, BPPs are usually manufactured from graphite (or graphite composites) or stainless steel. Each of these options have their own advantages and disadvantages and the choice of one over the other usually depends on the application area.

Since the environment inside the fuel cells is highly oxidative, steel plates quickly corrode and oxide film develops on their surface. This film increases the electrical resistance between the MEA and the plate, which impedes the electron transfer, thus reducing the power output of the fuel cell. Therefore, steel bipolar plates must be coated with an additional layer of anti-corrosion material [23]. Nevertheless, steel plates are the preferred choice for automotive applications because they are highly resistant to mechanical stress and are potentially much cheaper to produce in large quantities.

Graphite plates, on the other hand, are highly corrosion-resistive but suffer from being naturally brittle and prone to cracks and fractures. Such mechanical deformations not only compromise system integrity, but also increase the internal contact resistance [24]. Therefore, graphite plates are often used for research and development purposes because the mechanical stresses are minimal.

1.3.5 Gaskets

Gaskets seal the system and prevent any hydrogen, oxygen, or water leaks. They are usually made from silicon. As with other materials, gaskets are susceptible to degradation. One of the obvious consequences of gasket deterioration is the occurrence of leaks, but it may also lead to non-uniform clamping pressure distribution on the BPPs and MEA. Additionally, the deteriorating silicone releases ions that migrate through to the MEA and cause catalyst poisoning [24].

1.4 PEM Fuel Cell System

So far in this chapter only the basic constituent elements of PEMFCs were discussed, but in order for a fuel cell system to operate an array of supporting equipment is required. The purpose of such equipment is to regulate the amount of fuel delivered to the fuel cell, control its temperature and manage the accumulated liquid water in order to make sure of optimal power output. The combination of the fuel cell and all the additional devices creates a Fuel Cell System (FCS).

Configuration and sizing of the auxiliary components varies based on the intended purpose of the design, but it typically includes the following sub-systems: fuel/air processing and supply, thermal and water management, power distribution and control sub-systems [16, 15, 25]. A schematic representation of a generalised automotive FCS and its interaction with the environment and fuel storage, power conditioning and vehicle control sub-systems is depicted in Figure 1.9.

The arrows in Figure 1.9 indicate all the interactions between the sub-systems. Dashed lines represent the distribution of power from the fuel cell stack to all the other sub-systems, while solid lines correspond to exchanges of matter and energy between the components or the environment.

The diagram in Figure 1.9 illustrates that the sub-systems within the FCS are highly interdependent, which means that occurrence of failures in one sub-system can lead to unwanted consequences in another. This is especially important for the fuel cell stack.

1.4.1 Fuel Cell Stack Sub-system

A single PEMFC can generate only up-to 1 V with typical operational voltages being in the range 0.6 V to 0.7 V. However, automotive applications require electricity at hundreds of volts or even higher. In order to deliver such amount of potential, individual fuel cells are connected in series to form a so-called fuel cell stack. Voltages of cells in such arrangement add up, thus removing the 1 V cap on the output. A typical stack is illustrated in Figure 1.10 which shows a stack of N cells between two end plates and held together with clamping bolts. The end plates are often included in the stack assembly to provide additional rigidity to the structure. Since fuel cells are connected in series, the output voltage and as a consequence the reliability of stacks depends on the state of health of
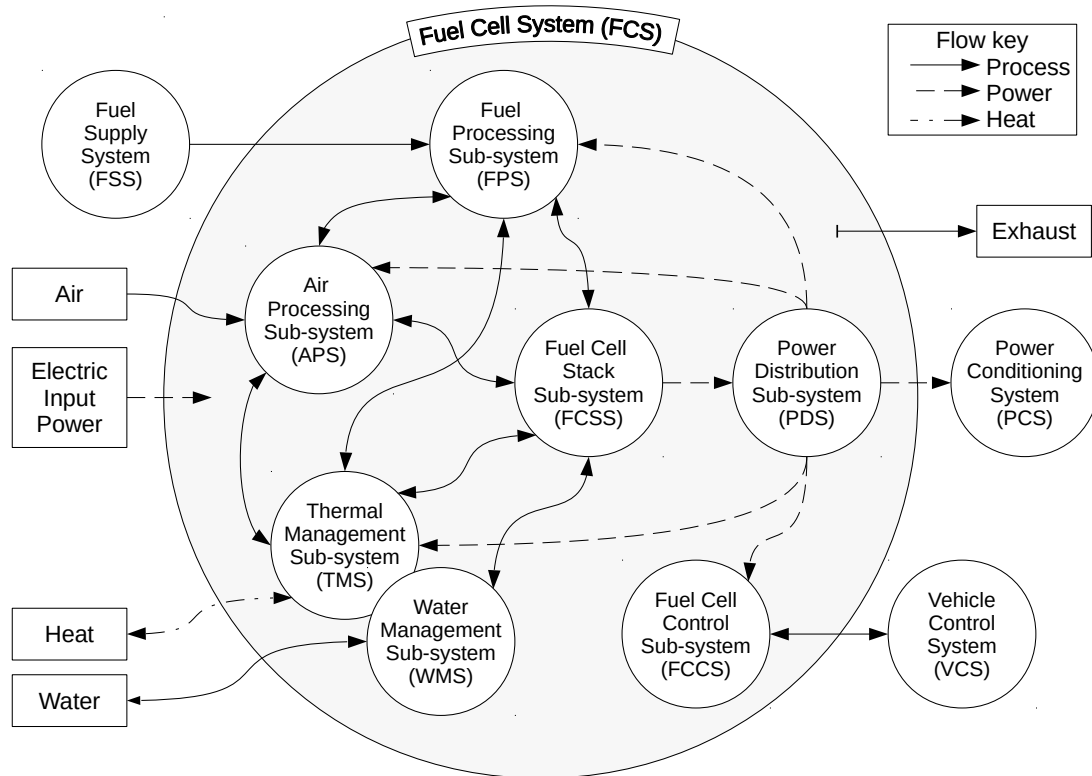
Figure 1.9: General automotive fuel cell system structure (adapted from [25]).
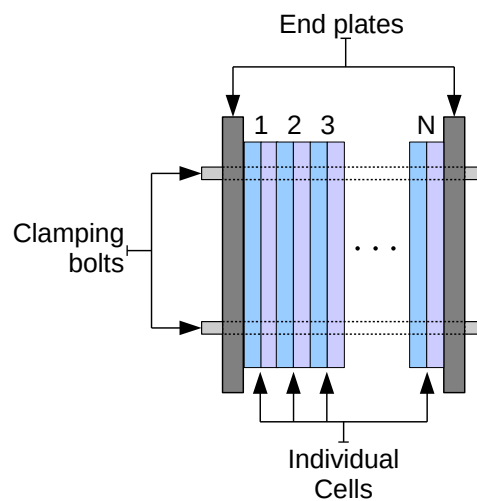
Figure 1.10: PEM fuel cell stack structure.

each cell within it. Unfortunately, individual cells do not degrade at the same rate due to non-homogeneities in fuel supply, uneven temperature and pressure gradients. Thus, special care must be taken when designing, assembling and operating fuel cell stacks.

1.4.2   Fuel Supply Sub-system

The fuel supply system is the collection of components that ensure the delivery of the fuel to the stack. It consists of piping, mass flow controllers and pressure regulators. There are two main strategies to supplying hydrogen to the stack: dead-end and flow-through modes. In dead-end configuration, the outlet of the anode side of the stack is fitted with a control valve which is normally closed. This is a simple and cheap design, but due to the accumulation of unwanted chemical species in the anode volume, it must be purged by periodically opening the control valve. In flow-through design, on the other hand, whatever amount of H_2 not used up in the reaction is redirected back to the inlet line by a pump.

1.4.3   Fuel Processing Sub-system

Fuel processing is a set of components that ensure the fuel is suitable to enter the fuel cell stack. Such processing may include filtration, humidification, heating and pressure regulation. Often the H_2 must be humidified to 100% Relative Humidity (RH) in order to ensure sufficient amount of water within the membrane. Humidification can be achieved by several means such as direct steam injection or passing the gas through a dedicated humidifier vessel.

1.4.4   Air Processing Sub-system

The air processing sub-system ensures the FC stack receives sufficient amounts of oxidant for the electrochemical reaction. This sub-system may include components that perform filtration, compression, humidification and flow rate control. In low pressure FCS designs, a simple fan may be sufficient, but in high pressure systems the supplied air may need to be compressed by a an additional compressor.

1.4.5   Thermal Management Sub-system

The electrochemical process taking place within FCs generates excess heat, which must be dissipated in order to maintain optimal operating temperature of the stack assembly. This can be achieved with either active or passive cooling. Passive cooling relies on dissipating the heat to the environment via natural convection and it is better suited for smaller fuel cell designs. Active cooling introduces a flow of liquid coolant through the dedicated channels inside BPPs which removes the heat via forced convection. This method is most often used in larger stacks.

1.4.6   Water Management Sub-system

The water management sub-system is a set of components that ensure the water is suitable to be used within the fuel cell stack. Such components may include water demineralizing/deionizing equipment and water recuperation for use within humidification components.

1.5 Chapter Summary and Proposed Research Objectives

The discussion in this chapter revealed the fact that the transportation sector in the UK is lagging behind other industries in terms of CO_2-reduction targets – 1.56 % reduction between 1990 and 2015 compared to, for example, 48.15 % reduction in the energy supply industry over the same period. Therefore, in order to ensure the reduction of CO_2 emission from the transport sector, an alternative powertrain technology must be adopted. PEMFCs technology is widely considered to be among the most promising avenues to wide-scale transport electrification. However, current generation of FCEVs struggle to obtain any significant market share due to a number of barriers such as the absence of refuelling stations, price and reliability. In this chapter, the brief summary of the main factors affecting the longevity of the PEMFC components showed that the reliability of automotive FCS depends on a range of factors such as operating and environmental conditions and quality of assembly.

The aim of this thesis is to investigate and develop an effective modelling technique that provides the means to predict the future reliability performance of automotive PEMFC systems. In order to achieve this aim the following objectives are defined:

1. Gain understanding of FC operational principles, structure, durability issues.

2. Conduct a review of existing literature related to reliability assessment and modelling of PEMFCs.

3. Design and implement a model of PEMFCs capable of evaluating system performance under various conditions over extended periods of time.

4. Conduct experimental validation and verification of the developed model.

5. Demonstrate the application of the proposed approach to reliability assessment.

1.6 Thesis Outline

The rest of this thesis is structured in the following way:

Chapter 2 – Literature Review.
This chapter is subdivided into two main parts which provide a comprehensive evaluation and critique of existing publications on the topic of reliability analysis and modelling of PEMFCs. The first part is focused on comparing the classical (static) and advanced (dynamic) reliability assessment techniques. The second part of this chapter is devoted to the discussion of the various approaches to physics-based modelling of PEMFC and some of the most noteworthy of the published models are analysed. The objective of this chapter is to assess and identify the potential gaps in knowledge in this field, thus setting the direction for the research activities described in the following chapters.

Chapter 3 – Bond Graph Model of PEM Fuel Cell.
The primary focus of this chapter is to describe the process of designing, implementing and validating a physics-based model of a PEMFC. First, a brief introduction into the chosen modelling technique called bond graphs is provided. Then a set of modelling assumptions is outlined and the hierarchical structure of the model is proposed. The procedure for independently modelling each of the fuel cell components is described based on the proposed model architecture by considering the physical interactions across thermal, fluidic and electro-chemical domains. The model implementation and simulation within Modelica modelling environment is also discussed. Finally, the discussion of model validation is provided.

Chapter 4 – Reliability Modelling of PEM Fuel Cells.
This chapter is dedicated to extending the original model developed in Chapter 3 with capabilities to evaluate the fuel cell component degradation and the effects of supporting equipment failures. This chapter introduces Petri net methodology for component failure modelling. Simulation results of several failure scenarios are demonstrated and discussed.

Chapter 5 – Reliability Analysis.
This chapter covers some practical aspects of performing simulation-based reliability analysis using Monte Carlo sampling method. The evaluation of the reliability performance of the same system under different operational conditions is demonstrated.

Chapter 6 – Conclusions and Future Work.
The final chapter summarises the key contributions and highlights the potential avenues for the future work in this area of study.

Literature Review

Contents

2.1 Introduction

Global research activities into the field of fuel cells have generated a large amount of publications. Many textbooks, scientific articles and other publications provide a rich source of knowledge in all areas of fuel cell development - from materials engineering to economic aspects of fuel cell adoption in society. Therefore, it is necessary to review the publications and determine any aspects of fuel cell research that are in need of further investigation.

In this chapter a selection of the most relevant publications to the topic of this research are reviewed and evaluated. First, the classical reliability modelling methods are outlined and existing papers that apply such techniques are analysed. The findings of this review reveal that an emerging field of dynamic reliability is a highly attractive direction of research. Such a dynamic approach to reliability modelling involves incorporation of the physical laws describing the behaviour of the system into the overall reliability model. Therefore, in order to create a model for dynamic reliability analysis of Polymer Electrolyte Membrane (PEM) fuel cells, thorough understanding of various techniques for modelling physical behaviour is also needed.

The review of literature dedicated to analytical modelling of fuel cells revealed that the primary focus of such modelling activities is control and design applications. There is a distinct lack of models dedicated specifically to reliability assessment of fuel cell systems.

2.2 Fuel Cell Reliability Analysis

Reliability analysis of any engineering system is a process that requires detailed understanding of all components, their respective functions and the overall goal that the system needs to achieve. Several techniques that help the analyst to perform such analysis exist,

Table 2.1: Example of an FMEA template

Component Name	Component Function	Failure Cause	Failure Mode	Failure Effect	Failure Detection Method	Mitigating Provisions
. . .	. . .	. . .	. . .	. . .	. . .	. . .

such as Failure Modes and Effect Analysis (FMEA) and HAZard and OPerability (HA-ZOP). Further investigations into Probabilistic Risk Assessment (PRA) can be performed with deductive methods like Fault Trees (FTs) or Event Trees (ETs). Mathematical modelling techniques such as Petri Nets (PNs) can also be applied when reliability of the system depends on sequences and inter-dependencies of various events.

2.2.1   Failure Mode and Effect Analysis

FMEA is a method for systematic analysis of engineering systems with the purpose of identifying the potential failure modes, causes and effects of all functional components of the system [26].
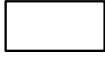
FMEA is an iterative process and should be performed at all stages of system development and it often comes as a first step in reliability analysis. It begins with decomposing the system into its basic constituent modules and components, classified by their function and/or location within the system. Next, starting from the lowest hierarchical level, the potential failure modes and the consequences of their occurrence are listed. Additionally, methods for detection, prevention and other comments may also be added. The results of FMEA are often presented by filling in a table such as Table 2.1, although additional columns can be added as needed.

An extension of FMEA called Failure Modes, Effects and Criticality Analysis (FMECA) includes a metric for assessing the criticality of a failure mode. This extension, therefore enables the measures for failure prevention to be prioritized.

The flexibility of the FMEA approach makes it useful for analysis at all tiers of system hierarchy. Because of this, several FMEAs of Polymer Electrolyte Membrane Fuel Cells (PEMFCs) systems have been performed at both high- and low-levels of components interactions.

One high-level FMEA was a part of a report by the US Department of Transportation on the safety of compressed hydrogen electrical vehicles [27]. The main objective of the report was to assess the likelihood, criticality and potential consequences of hydrogen leaks occurring in the vehicle. For the purposes of FMEA, authors classified the fuel cell components into three functional sub-systems – compressed hydrogen fuel storage, hydrogen flow control and the fuel cell stack. Failures within the hydrogen storage and delivery systems were found to be of low or medium likelihood, whilst bearing high risk due to release of hydrogen into the surroundings. The failures associated with the fuel cell

Table 2.2: Typical elements of a fault tree

Name	Symbol	Description
Top/intermediate event		Total system failure or an unwanted event
Basic event		Failure of a component
OR gate		Output event occurs when at least one input event occurs
AND gate		Output event occurs when all input events occur

stack sub-system are more likely to occur and bear a high degree of criticality and risk. Within the fuel cell itself, authors identified the mechanical failure of the membrane to be the most critical failure mode. Overall, the report is a good starting point for reliability analysis even though it doesn't provide very much technical detail.

Other authors developed FMEAs with the focus on fuel cell components and materials. A book by Wang et al. provides detailed findings on the investigations of the causes and consequences of fuel cell materials degradation [18]. The book classifies the sources of degradation to be associated with internal and external causes. Internal causes are related to material deterioration such as catalyst poisoning, Pt-particle agglomeration, loss of hydrophobic properties of the Gas Diffusion Layer (GDL), etc. Other sources of degradation are attributed to external changes of operating conditions such as overheating, over-pressurisation and others.

One major limitation of the FMEA approach is the fact that during the analysis only one independent failure mode is considered at a time. When, however, a system is complex and failure modes interact with one another, additional techniques such as FTs are necessary.

2.2.2 Fault Tree Analysis

Fault Tree Analysis (FTA) is a top-down deductive approach for reliability modelling of systems. The approach consists of graphically decomposing the occurrence of an undesirable event by a collection of logical steps into sets of intermediate and basic events. The relationships between the events are expressed via logical AND and OR operations. Some of the conventionally used symbols in FTA are listed in Table 2.2 [28].

In order to illustrate how the symbols are used a simple example of a fault tree is shown in Figure 2.1. Traditional solution of a FT involves derivation of so-called *minimal cut sets*. Minimal cut sets are all necessary and sufficient combinations of basic events, occurrence of which cause the top event. In this diagram, the occurrence of both basic events B2 and
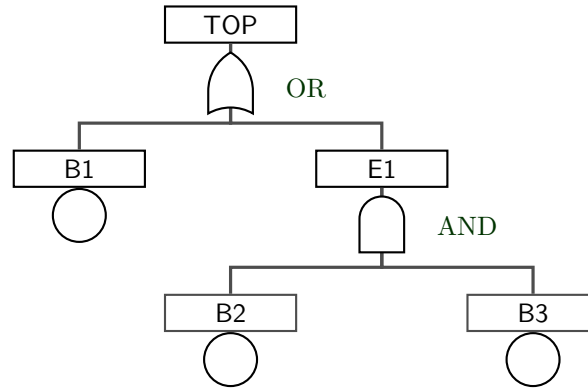
Figure 2.1: An example of a basic fault tree.

B3 leads to intermediate event E1. Using boolean algebra this relationship is expressed as:

$$E1 = B2 \times B3 \tag{2.1}$$

The occurrence of either basic event B1 or intermediate event E1 leads to the top event TOP. Similarly, this can be expressed as:

$$TOP = B1 + E1 \tag{2.2}$$

Combining Equations 2.1 and 2.2 the expression for the top event probability can be expressed in terms of basic events:

$$TOP = B1 + B2 \times B3 \tag{2.3}$$

Therefore, the TOP event will occur when either $B1$ or $B2 \times B3$ take place, resulting in two cut sets: $B1$ and $B2 \times B3$. The derivation of FT minimal cut sets may reveal critical components and system structural vulnerabilities to failures. Furthermore, if the probabilities of occurrence of all the basic events is known, the top event probability can be estimated using boolean algebra operations or probability laws.

The FT approach to reliability assessment of PEMFCs is widely used among researchers in the field. A review paper by Yousfi Steiner et al. [29] shows how fault trees can be applied to various fuel cell failure modes. The authors present two fault trees designed to represent flooding or drying of the membrane within PEMFC stacks. The basic events in these fault trees correspond to changes of state variables such as temperature, relative humidity and stack current load. The authors also illustrate the application of FTA to understanding the failures encountered in Solid Oxide Fuel Cell (SOFC) systems. The authors then derive a so-called Fault Signature Matrix (FSM). Such a matrix is a way of mathematically formulating the link between the faults and fault symptoms, which is useful in fault diagnostics procedures. Overall, the authors proposed a generalised fault detection

and identification scheme, however, no demonstrations of fault diagnosis or numerical evaluations of fault probabilities were provided in this publication.

A paper by Placca and Kouta [30] describes fault trees for the degradation of the three main components of a fuel cell – the membrane, catalyst layer and the GDL. The authors define the top event as 'Degradation of the cell' with three major intermediate events: 'Membrane degradation', 'Catalyst layer degradation' and 'Gas diffusion layer degradation'. These intermediate events are further broken down into more than 40 basic events such as 'Drop of ionic conductivity', 'Contamination' and 'Long term operation'. The authors also compile a list of failure rates for each basic event in the fault tree in order to estimate the probability of occurrence of the top event quantitatively. The authors estimated that after 100 h of fuel cell operation under cycling conditions, the probability of membrane mechanical degradation is the highest among other failure modes. They also concluded that the two most critical basic events in the fault tree are drop of ionic conductivity and Membrane Electrode Assembly (MEA) breakdown. This finding agrees with the results of previously discussed FMEA analysis [27]. One major drawback of this publication is the fact that 100 hours of Fuel Cell (FC) lifetime is negligible when the aim is make sure the fuel cells operate for at least 5000 hours.

In a publication by Collong and Kouta [31] the authors applied FTA to the safety issues of automotive PEMFCs. They created FTs for 'Tank rupture' and 'Explosion of hydrogen release'. The probability of the basic events is expressed in terms of component failure rates. Such failure rate data for PEMFC systems is sparse, so the authors used data obtained from the offshore reliability data base (OREDA). As a result of the analysis, the authors were able to estimate the probability a safety-critical events and define the targets for component reliability. The authors suggest coupling a physics-based model in order to adjust the reliability predictions according to the operational conditions.

Brik et al. in [32] also construct a fault tree for the top event 'fuel cell system degradation' with intermediate events 'auxiliary elements degradation' and 'fuel cell degradation'. Basic events for the auxiliary components included failures of pumps, filters and sensors. Some of the basic events for the fuel cells were 'formation of hydrogen peroxide', 'overheating' and 'flooding'. The authors determined minimal cut sets, but emphasize that it is impossible to quantitatively evaluate the top event probability because of the lack of data for all the basic events. Instead, the authors propose to include the variations of key state variables such as temperature and mass flow rates and pressures of reactant gases. The resulting fault tree has several inhibiting logic gates, the output of which depends on whether the state variables exceed a defined threshold or not. Consequently, the authors were able to couple a physics-based dynamic model of the process to a corresponding system fault tree. Although this approach expands the traditional view of FTs for PEMFC system analysis, it still operates within the boundaries of boolean logic imposed by the FT methodology. Therefore, it fails to capture the gradual nature of many degradation mechanisms occurring within the fuel cell components.

Publication by Rama et al. [33] developed an FMEA focussed on the five main causes of performance degradation in PEMFCs: activation, ohmic and mass transport losses as well as efficiency deterioration and catastrophic failure. The authors identified 22 potential faults and 47 plausible causes and constructed the corresponding FTs to describe the failure interactions. Based on the analysis performed, the authors suggested a number of improvements to the fuel cell design. For example, the formation of liquid water and its subsequent uptake by the membrane was determined as one of the critical processes that needed to be avoided. Therefore, the authors suggested, it is beneficial to operate the fuel cell at temperatures above $100\,°C$.

Another fault tree analysis carried out by Whiteley et al. [34] shows that the Boolean logic of fault trees is not an ideal method for estimating the probability of fuel cell failure due to complex dependencies of failure modes under differing operating conditions. The authors highlighted that a different FT needs to be constructed for all possible operating conditions, what is not realistic and hence an alternative method which can deal with such dependencies is preferred.

To sum up, FT analysis is a remarkable tool for identifying weaknesses in the system design and estimating the likelihood of occurrence of undesired events. However it is not suitable in situations where quantifying the scale of the degradation is important and the rates of failure depend on changing operating conditions. Because of this, an alternative method capable of taking such aspects into account should be employed for PEMFC reliability analysis.

2.2.3   Petri Nets

A modelling technique called PN is also applicable for reliability analysis and it provides the tools for representation of dependencies [35]. Petri nets are capable of representing discrete states of the system and transitions between these states. The method provides the means for modelling cause and effect sequences of events making it useful for simulating fault propagation within systems. In general Petri nets are a bipartite graph with two types of nodes: *places* and *transitions*. Places represent various states of the system or component, while transitions correspond to various events that alter the state of the system. The current state of the system is determined by the location of *tokens* within the PN places. Graphically places are depicted as circles, transitions as rectangles and tokens are shown as dots inside places. An example of a basic PN consisting of four places corresponding to different states of health of a system (healthy, degraded, damaged and failed) is depicted in Figure 2.2. Transitions T_1, T_2 and T_3 in Figure 2.2 represent the time intervals corresponding to ageing of the system. The time intervals can be known in advance (deterministic) or unknown (stochastic). This example shows that PNs can be applied to model multiple stages of degradation, unlike FTs where the failures are considered as binary occurrences. More detailed Petri nets for reliability modelling of engineering systems can be created with the knowledge of component failure behaviour.
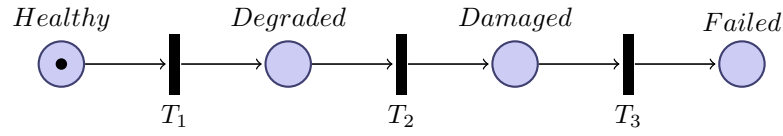
Figure 2.2: Petri net of a generic degradation process.

Several researchers have applied PNs to the reliability modelling of PEMFCs. For instance, Wieland et al. [36] created a simple Petri net for automotive stack degradation and maintenance. The model described four states of the system: stack is operational, stack is out of order, state of spontaneous events and state of repair. The authors compiled the degradation rates for various spontaneous events and performed multiple simulations with a pre-defined drive cycle. The drive cycle included city and highway driving, high temperature, idle and dry operation as well as driving in smog and starting from sub-zero temperatures. As a result of simulations performed, the authors deduced that the most significant contributors to the total fuel cell degradation are: natural ageing (50 %) and starting from sub-zero temperatures (26.5 %). However, multiple assumptions and simplifications were adopted in this model. For example, the failure modes of individual components of the system are ignored and the degradation simply manifests itself through the reduction of voltage. Additionally, the failure rates were assumed constant throughout the fuel cell lifetime.

Degradation modelling by means of Petri nets was carried out by Whiteley et al. [37]. The authors designed 21 Petri net sub-modules corresponding to various phenomena leading to fuel cell degradation based upon previously conducted FMEA and FTA. In this paper, the authors focused on the Petri net module describing the conditions for hydrogen peroxide (H_2O_2) formation and its debilitating effect on fuel cell performance. The negative side-effects of load cycling are also discussed and represented with a separate PN module. The authors use degradation rates gathered from the literature to run model simulations and yield results that correlate with experimentally obtained degradation patterns. The authors conclude, however, that the addition of a fuel cell performance model would improve the simulation results by calculating the evolution of key variables alongside the degradation.

Reviewing the existing literature devoted to reliability assessment of PEMFCs in this section revealed that classical Reliability, Availability, Maintainability and Safety (RAMS) methods such as FMEA, FTA and PNs alone are insufficient to provide accurate reliability estimates when the operating conditions undergo dynamic changes during a FC lifetime. Therefore, an advanced modelling approach capable of representing the dependency of component failure rates on dynamically changing operating states is needed. The concept of dynamic reliability offers an approach to bypass the assumption of constant failure rates.

2.3 Dynamic Reliability Analysis

Dynamic Probabilistic Risk Assessment (DPRA) (also called dynamic reliability) is a field of study originating from nuclear engineering. The approach aims to expand the classical RAMS techniques by taking into account the multi-state operational and failure mechanisms of the studied system and its changing environmental and operational conditions. In principle, such a dynamic approach offers more realistic reliability estimations, but it has not found widespread adoption within industry and remains largely in the domain of academic research due to the complexity of implementation and lack of generalised software tools [38, 39]. The complexity of implementation arises from the fact that DPRA methods aim to capture the inter-dependence and interaction of both deterministic (continuous) and stochastic (discrete) dynamics of the system in order to obtain more accurate reliability estimates.

Davis [40] established a formal mathematical definition of systems where such inter-dependencies exist via a class of processes called Piecewise Deterministic Markov Process (PDMP). Bouissou et. al. [41] provide a summary of the definition as follows. PDMP is a process, the state of which at any point in time t is characterised by two vectors $\mathbf{x}(t)$ and $\mathbf{m}(t)$. Vector $\mathbf{x}(t)$ contains a set of continuous variables (usually governed by Ordinary Differential Equations (ODEs)) corresponding to physical descriptors such as pressure, flow rate, temperature and others, while $\mathbf{m}(t)$ specifies the system in terms of discrete states such as 'open/closed' or 'on/off'. The coupling between the two vectors can occur when the time-evolution of $\mathbf{x}(t)$ leads to the occurrence of boundary conditions within the system and thus causes a change of state $\mathbf{m}(t)$ (e.g. overpressure of a tank causes rupture). Additionally, the state transitions in $\mathbf{m}(t)$ may affect the dynamics of $\mathbf{x}(t)$ (e.g. failure of a cooling fan causes system overheating). Therefore, mathematically, PDMPs are expressed as sets of stochastic differential equations, analytical solutions to which are often computationally demanding or even unattainable [38, 39, 42]. In order to bypass this limitation and resolve the dynamic reliability problems, the state-of-the-art approaches rely on performing so-called Monte Carlo (MC) simulations. MC simulation involves recursively evaluating the system dynamic behaviour with selected input parameters being sampled from a random distribution. The collection of such numerical results can provide statistical insight into the system reliability metrics.

There are several methods for implementing the system models suitable for DPRA, each with their own advantages and disadvantages, several of which are discussed below. It is worth emphasising the fact that the field of DPRA is relatively new, so the published literature on the topic is only conceptual in nature as the methods were not demonstrated to be valid in real industrial applications.

Codetta-Raiteri and Bobbio [43, 44] show the application of two different types of PNs in the dynamic reliability analysis of a heated tank problem. Specifically, the authors compare the performance of Generalised Stochastic Petri Nets (GSPNs) and an extended class of PNs, the authors call Fluid Stochastic Petri Nets (FSPNs). GSPN contain both

ordinary timed and stochastic transitions, while FSPN further extend the capabilities of GSPN by introducing '*fluid*' places and arcs. The adjective 'fluid' is used by the authors to highlight the fact that unlike conventional Petri nets (including GSPNs) where the state of the system is described by a discrete number of tokens, FSPNs are designed to handle continuous numbers of tokens. Thus the evolution of FSPN state is determined by the flow of 'fluid' between the places. This concept is used by the authors to incorporate continuous variables such as temperature and fluid level within the tank into the PN formalism. Although, GSPNs are not designed to handle continuous variables, the authors adapt them to model the same system by discretizing the fluid level and representing it with regular tokens. After performing MC simulations, the authors compared the outputs of both approaches to a benchmark result from the literature and concluded that both methods provide satisfactory results. However, it is certain that FSPNs allow for greater modelling flexibility, while GSPNs would not be able to handle more complex systems where multiple continuous variables are involved. One drawback of FSPNs is the fact that the ODEs governing the continuous-time evolution of the system must be coded directly into the PN structure. This, means that the model code has to be written for a specific modelling purpose and cannot be reused in different scenarios.

Fecarotti et al. [45] introduced ideas of DPRA to evaluating the reliability characteristics of PEMFC systems. The authors developed a PN model of the full Fuel Cell System (FCS) containing the fuel cell stack and all the main auxiliary components within cooling, humidification and gas supply sub-systems. The authors also included the continuous variables within their extended PN model, but in contrast to FSPNs a different approach was chosen. The traditional tokens were converted into objects capable of storing values of continuous variables. Such modified tokens are called '*coloured*' and the resulting Petri net is a Coloured Petri Net (CPN). Furthermore, transitions were also augmented with functionality to alter the variables stored within the coloured tokens. The authors assigned the values of gas flow rates to the tokens, which allowed them to obtain results based on realistic measurements. The model consists of four PN modules (one for each auxiliary sub-system), outputs of which are fed into the stack PN module which computes the FC voltage. The model also includes modelling of maintenance procedures such as scheduled inspection and repair. This aspect of the model represents a degree of performance recovery that occurs after the system was repaired. Performing the model simulations several thousand times provided statistical estimations of the expected lifetime of the system under predefined operating conditions and maintenance schedule. The developed CPN model does not take into account the change of degradation state of the stack due to the changes of operating conditions, resulting in a more static view of system reliability, so a more detailed stack representation is desirable. Additionally, this modelling approach, suffers from the same limitation as FSPN and the code cannot be easily adapted and extended to include some of the more nuanced fuel cell dynamics or even model some other engineering system altogether.

Manno et al. [46] recognised the fact that when adapting FSPNs and CPNs for DPRA both deterministic and stochastic aspects of the process are fused together and cannot be separated. The authors, thus, suggested to 'separate the concerns' and implement the two aspects of system behaviour independently from each other. The non-deterministic side is represented by a Stochastic Activity Network (SAN), which is another extension of stochastic PNs. SANs include additional building blocks which allow modelling of large complex systems in a concise way. The method was applied to modelling an air conditioning system in a data centre in the Matlab/Simulink environment. The deterministic part of the model contained temperature of air within the room as the only state-variable, while the stochastic model was designed under the assumption that the components age only when they are switched on. Thus, the failure rates of the components are state-dependent. A specialised simulation algorithm was proposed and the results demonstrated the change of the failure rate depending on the ambient temperature.

An alternative way to represent the system for dynamic reliability is through the use of so-called 'smart' components [39]. The main principle of this approach is to explicitly code both nominal and faulty physical behaviours of individual components within the system. Consequently, system models composed of such fault-augmented components, are inherently suitable for reliability estimations via simulations. One example of using this approach was demonstrated by Schallert [47] who developed a set of fault-augmented models of basic electrical components using an object-oriented modelling language called Modelica. These component models were then used to create a system model of an aeroplane electric network. As a next step, the author devised a procedure to automatically detect the minimal path sets (complement to the minimal cut sets) through simulation and model structure analysis. This knowledge allowed the calculation of the probability of occurrence of an undesirable event (such as loss of power supply to an engine) as well as estimate component importance metrics. The approach, therefore, incorporates the capabilities of a classical RAMS technique such as FTs into a physics-based simulation model.

To summarise this section, the following conclusions can be drawn. Dynamic reliability is an active area of research with a large potential to expand the classical RAMS techniques for analysis of complex engineering systems exhibiting hybrid dynamics. Although various modelling paradigms (PDMP, PNs, SANs and 'smart' components) are capable of representing such systems, the primary method for evaluating the reliability is through simulation. Furthermore, DPRA studies published in the literature tend to analyse systems, whose continuous dynamics are fully described within one or two physical domains, whereas such an analysis of multi-domain systems is largely unexplored. The application of DPRA concepts to reliability assessment of PEMFCs is highly attractive, especially in automotive applications because the degradation rates of the stack depend on the different modes of operation and discrete events such as start/stop cycles. However, to the best of the authors knowledge, only one study in this area was published by Fecarotti et al. [45] as discussed above. The proposed approach can be used for DPRA, but it suffers from

modelling limitations due to the fact that the physical properties of the system have to be interpreted in a modelling paradigm, originally not designed for this use. Therefore, an alternative, more flexible modelling approach for dynamic reliability analysis of PEMFCs is needed. The following section is focused on the various techniques for modelling the physical behaviour of PEMFCs.

2.4 PEM Fuel Cell Modelling

Fuel cell modelling has received a significant amount of attention since the early 90's when the advancements in fuel cell technology made them more accessible and appealing for the wider public. Modelling fuel cell behaviour provides multiple benefits for design and control purposes. Models provide indispensable means to test and adjust various aspects of fuel cell design even before assembling prototypes. Tweaking geometric parameters, material properties and operating conditions within a model allows engineers to predict the performance of the final product. Additionally, a class of models dedicated specifically for tuning the control algorithms (called control-oriented models) are also very important. Such models capture only the most essential aspects of fuel cell behaviour for the purposes of regulating the auxiliary components for provision of optimal operating conditions.

Modelling is such an integral part of fuel cell research and development that it created a separate field of study that generated thousands of publications over the years. Several review papers such as [48, 49, 50, 51] attempt to summarise the sheer diversity of publications according to various criteria which can loosely be grouped into primary and secondary. Primary characteristics relate to the underlying analytical relations of the model and include the following criteria:

- **Modelling approach** dictates how the model equations were derived. Theoretical (also called mechanistic) models rely on known fundamental physical laws to describe the process with great detail and complexity. Empirical models, on the other hand, are derived from experimental evidence and are used when there is lack of knowledge about the process. Finally, semi-empirical models combine the two approaches.

- **Transient behaviour** of the model describes how it responds to the changes of input signals. Static models are specifically derived around a set operating point. This is useful when it is needed to calculate the performance of the final product during the design stage. Dynamic models, on the other hand, contain sets of ODEs that represent how state variables such as temperature and pressure change dynamically over time.

- **Model dimensionality** describes how model parameters and variables are distributed in space. 0D models are designed with a simplifying assumption that all the phenomena occur in a single point in space without any spacial distribution. 1D models assume the distribution of variables along one axis. In fuel cell models,

this axis is usually normal to the surface of the MEA. By extension, 2D and 3D models, are concerned with the distribution of the model variables across multiple dimensions.

- **Model boundary** defines the geometric scale of modelled phenomena. It can range from nano-scale models that capture the interaction of atoms and molecules within fuel cell materials to system-wide events that govern the stack performance.

- **Complexity** of the model signifies what physical phenomena are implemented in the model. In fuel cells such phenomena include, but are not limited to, electrochemical, thermodynamic and fluid dynamics. Depending on modelling goals, models can be focused on a particular physical aspect or include all of the above phenomena.

Secondary model characteristics specify the model implementation technique within a computational engine. These include the following criteria:

- **Model causality** defines how model equations are represented within the software environment. Causal models operate by computing the model output from the defined input by calculating intermediate steps in a strictly sequential fashion. The Matlab/Simulink environment and other programming languages are representative of such an approach. A-causal models, on the contrary, assemble all the equations into a single system of equations and execute them all at the same time [52]. Such an approach is adopted by the Simscape environment and modelling languages such as Modelica and Very High Speed Integrated Circuit Hardware Description Language (VHDL).

- **Graphical representation** of a model provides the visual depiction of the modelled process. This can be in the form of causal block diagrams, bond graphs or other methods.

- **Source code** of the model can either be proprietary or open-source.

- **Flexibility** of a model determines how easy it is to modify and extend the model parameters and capabilities.

- **Simulation speed and accuracy** is how fast a model can provide the results and how well do they represent the real-life system.

Each fuel cell model can be classified according to various primary and secondary criteria. In this review some of the key publications in fuel cell modelling are first discussed with respect to primary and then secondary model characteristics.

2.4.1   Models According to Primary Characteristics

The internal processes occurring within PEMFCs are complex and describing them requires in-depth knowledge of the fundamental principles of electrochemistry and physics. Models

that use first principles to describe the process are called mechanistic or theoretical. Such an approach was employed by Franco et al. [53] to develop a multi-scale model of the MEA. The model relies on the principles of thermodynamics and electrodynamics to represent various phenomena such as double layer capacitance and gas diffusion through the MEA. The authors compared the simulation outputs to experimental results and illustrated how specific physical quantities (e.g. Pt/Nafion mass ratios) influence the performance. The model provides a number of advantages for studying internal processes within the fuel cell, however it does not include the processes occurring in components other than the MEA.

Development of mechanistic models is very demanding and time consuming so in order to simplify the modelling process, some aspects of fuel cell behaviour are described with empirically obtained equations. Such models sacrifice accuracy and complexity for simplicity, flexibility and generality. As a consequence, a large amount of published models are created using a semi-empirical approach.

A paper by Springer et al. [54] was one of the earliest and currently one of the most cited publications in this area to date. In the paper, the authors created an isothermal, 1D and steady state model based on semi-empirical evidence. The authors propose an empirical relationship for the Nafion membrane water content dependent on the vapour activity and consequently derive an expression to describe the dependency of membrane ionic resistance on water content. A description of electro-osmotic drag and water back diffusion are also described in this paper. The equations presented in this paper are still widely used today and form the basis of many other models.

The model presented by Amphlett et al. [55, 56] is also 1D, isothermal and steady state and was designed to describe the performance of a single Ballard Mark IV fuel cell by employing semi-empirical methods. A number of simplifying assumptions adopted by the authors allowed them to create parametric expressions for the voltage losses and ionic resistance of the membrane. Additionally, an expression for the cathode activation voltage losses η_{act} were derived as shown by Equation 2.4:

$$\eta_{act} = \xi_1 + \xi_2 T + \xi_3 T \ln(c_{O_2}^*) + \xi_4 T \ln(i) \tag{2.4}$$

where T is temperature, $c_{O_2}^*$ is the effective concentration of O_2 and i is current density. The values of derived parameters ξ_{1-4} were obtained empirically for the specific conditions and hardware, which means that they must be re-evaluated before being used in modelling different fuel cell configurations. Such parameter identification can be costly, thus making the model less practical.

A paper by Rowe and Li [57] presents a semi-empirical, 1D, non-isothermal model of a single PEMFCs which was developed to study the effects of changing design and operating conditions on the fuel cell performance. The model describes the variable levels of membrane hydration, phase transitions of water and uneven temperature distribution within the fuel cell. The results of simulations showed that lower operating temperatures resulted in an increased temperature difference between the layers of the fuel cell compared

to higher operating temperatures. This result highlights the need for temperature regulation by incorporation of cooling channels. Additionally, the effects of fuel cell operation on the reformed fuel, which contained some amount of CO_2 in the anode inlet stream were investigated. The simulations showed that the performance is reduced throughout the whole operating range due to the decreased H_2 partial pressure as well as reduced water diffusion coefficient causing the decreased membrane humidification. The model can be used for optimizing the operating temperatures, pressures and Relative Humidity (RH) of PEMFCs for a given application and configuration. However, the model lacks the fluid and temperature dynamics within gas flow channels and bipolar plates, which should be included if modelling a PEMFC stack.

Del Real et al. [58] developed a dynamic, 1D model of a multi-cell stack using a semi-empirical approach. The model was designed to study the influence of auxiliary components on the PEMFC performance. The model features fluid and thermal dynamics within fuel cell components and computes the voltage output based on several experimental parameters. The behaviour of the auxiliary equipment was modelled using a black box approach, as transfer functions. The authors adjusted the model parameters to correspond to an air-cooled Ballard 1.2 kW stack and performed four experiments to validate the model. Firstly, a start-up sequence was simulated during which no load was applied, the air pump and cooling fan switch on and the anode inlet valve opens. The anode purge valve also stays open to ventilate the anode channels. Secondly, a constant current load was applied and anode flooding was observed. Simulating the purging of the anode volume resulted in voltage recovery as observed experimentally. During two other experiments, variable loads were applied to study cell transient behaviour. It was noted that during dynamic conditions, it is harder to observe the voltage recovery due to purging.

Park and Choe [59] designed a distributed 1D model of a PEMFC stack considering water phase transition effects and thermal dynamics. The authors first compared the simulation results to the data obtained from a 2-cell stack and then extended the model to a 20-cell stack. The simulations showed uneven temperature distributions throughout the stack with 4 cells near the edges of the stack having significantly lower temperatures compared to cells in the middle as shown in Figure 2.3. In order to mitigate the temperature difference and facilitate optimal start-up, the authors compared several start-up sequences. As a result, the authors suggest desirable values for the load current, coolant flow rates and temperature that minimise temperature difference and reduce the start-up time. In addition to that, the authors suggest reducing the coolant flow rates in end-cells in order to further reduce temperature variation among the cells. Additionally, the simulated performance under the assumption of single phase was compared to the performance under a two-phase assumption. As expected, the two-phase assumption yields lower voltage output compared to the single-phase model due to reduced partial pressure of oxygen in the cathode catalyst layer. However, the model does not consider the pressure losses within gas flow and coolant channels, which is an important effect influencing performance in fuel cell
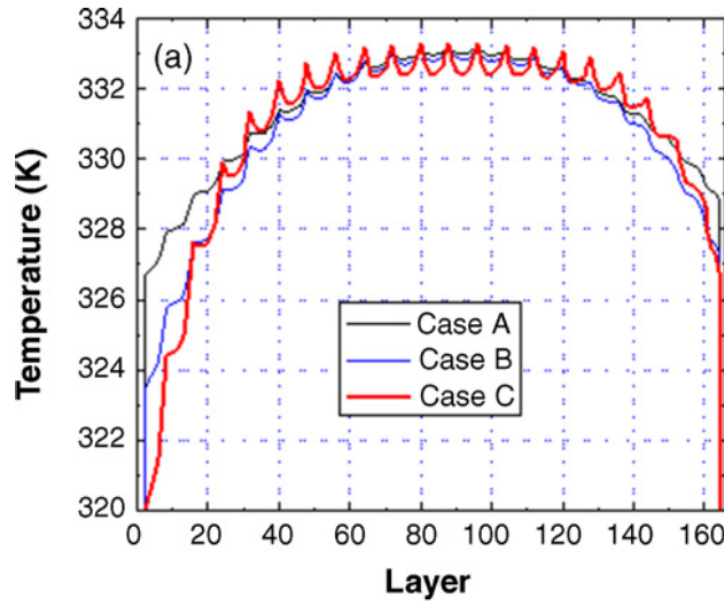
Figure 2.3: Simulated temperature distribution in a 20-cell stack [59].

stacks as it introduces additional imbalances to performances of individual cells. Moreover the stack model was not validated experimentally.

Control-oriented models tend to incorporate only the most important dynamic phenomena and often disregard spacial distribution of variables within the fuel cell (i.e. 0D models). One such control-oriented model for automotive applications was developed by Pukrushpan et al. [60]. The paper is specifically focused on transient effects such as flow and inertia dynamics of the air compressor, the anode and cathode manifold filling dynamics and the membrane water content. The model however does not consider temperature variations during fuel cell operation, which is a very important factor in automotive applications, where increased current load can cause overheating of the stack. Additionally, the model was not validated with experimental data.

Another control-oriented model of an evaporatively cooled PEMFC stack in aircraft applications was created by Schultze and Horn [61]. Due to the nature of the thermal management subsystem, the model includes the behaviour of components such as heat exchangers, cyclone separators and water droplet catchpot. The model is 0D and based on several empirically obtained parameters. Constant temperature distributions throughout the stack is also assumed. The simulation results were validated against experimental data, however the scope of the model is limited to the specific hardware configuration.

The models discussed up to now are 0D or 1D with varying degrees of complexity with regards to modelled phenomena. Such models are usually used for control and component sizing purposes. Models of higher dimensionality (2D and 3D) are much more computationally intensive because they calculate the parameter distributions in 2D and 3D space.
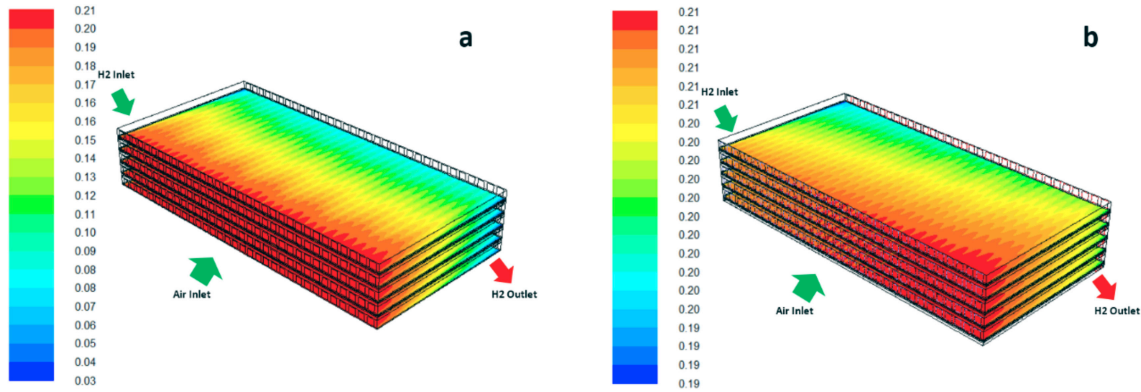
Figure 2.4: 3D CFD visualisation of oxygen concentration distribution in a stack with straight air flow channels at $0.6\,\text{V}$ (left) and $0.8\,\text{V}$ (right) [62].

A 3D model by Macedo-Valencia et al. [62] was developed using Computational Fluid Dynamics (CFD). The model represents a 5-cell stack with 2-fold parallel serpentine channel topology on the anode side and straight channels on the cathode side. The results of model simulations provided a detailed insight into the distribution of reactant concentrations, current density and temperature throughout the stack. Figure 2.4 illustrates the variation of O_2 concentration at different cell voltages. It can be seen that at higher cell potentials oxygen is distributed more uniformly along the channels. Furthermore, the simulation results confirm that the temperature distribution is also more uniform at higher cell potentials as previously mentioned in [57]. The simulation results were validated against a traditional current-voltage characteristic which doesn't provide any information regarding spacial distribution of variables. Additionally, the authors highlight that each simulation took around $24\,\text{h}$ to complete. Therefore models of this complexity are not suitable for performing fast calculations necessary in control applications and should be used primarily for design purposes.

To sum up, the complexity and the level of detail of any particular model depends on the modelling objective. If the aim is to study temperature variation within a stack of a given size, there is no real need in modelling inter-molecular forces within the MEAs. In general, the majority of research papers on PEMFC modelling published so far are focused on the higher level phenomena. This means that the low scale effects are often omitted, resulting in semi-empirical approximations of the underlying processes.

2.4.2   Models According to Secondary Characteristics

There are two different ways of translating the model equations into a computational engine. The first one is called '*causal*' modelling and it requires the equations to be rearranged in a strict sequence of input-output assignments and then either typed as lines of code in a programming language such as Matlab or implemented as block diagrams using tools such as Simulink. The second method is called '*a-causal*' (or '*declarative*') and it allows declaring the model equations without manipulating them first. Such an approach
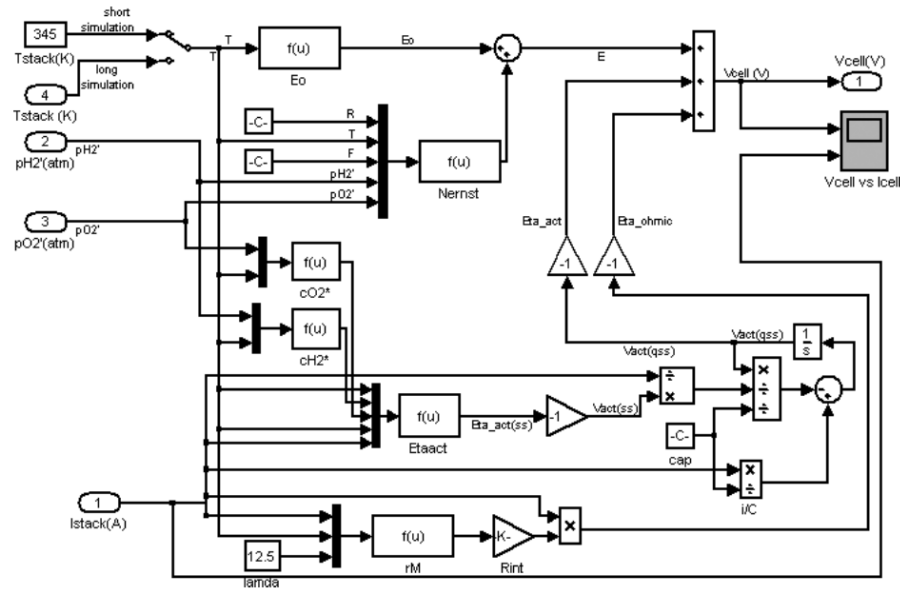
Figure 2.5: Simulink model of a PEMFC stack [63].

was made possible by specialised software tools such as Modelica, VHDL and Simscape which use symbolic interpretation of equations to automatically determine the inputs and outputs.

The causal modelling approach is very popular for developing control-oriented fuel cell models, many of which were implemented in Simulink. For example, Khan and Iqbal [63] created a lumped parameter, 1D, isothermal model for a FC stack considering gas flow and temperature dynamics. The model assumes constant water content within the membrane so the change in membrane ionic conductivity is only a function of temperature and current. Figure 2.5 depicts the part of the model that calculates the cell potential as a function of temperature, partial pressures of H_2 and O_2 and current. From the block diagram in Figure 2.5 it can be seen that each block performs a specific mathematical operation or function. Therefore, such a representation defines the algorithm for solution of the model equations. One drawback of such an approach is in the fact that if an additional phenomenon needs to be modelled at a later stage, the structure of the existing model would undergo significant modifications and adjustments [52].

The a-causal approach resolves this problem by approaching the model definition in a structural way by breaking down the modelled systems into individual physical components. Several fuel cell models were developed using a-causal modelling techniques. For example, the model by Blunier and Miraoui [64] was developed using VHDL with Analog and Mixed Signal (AMS) extension. This modelling language allows the model to be structured in such a way that it repeats the physical composition of a fuel cell, i.e. the model contains blocks for the gas channels, GDLs, Catalyst Layers (CLs) and the membrane. The model was designed under the assumption of a uniform temperature distribution throughout the layers and ignores the pressure losses within the channels, but despite of this the
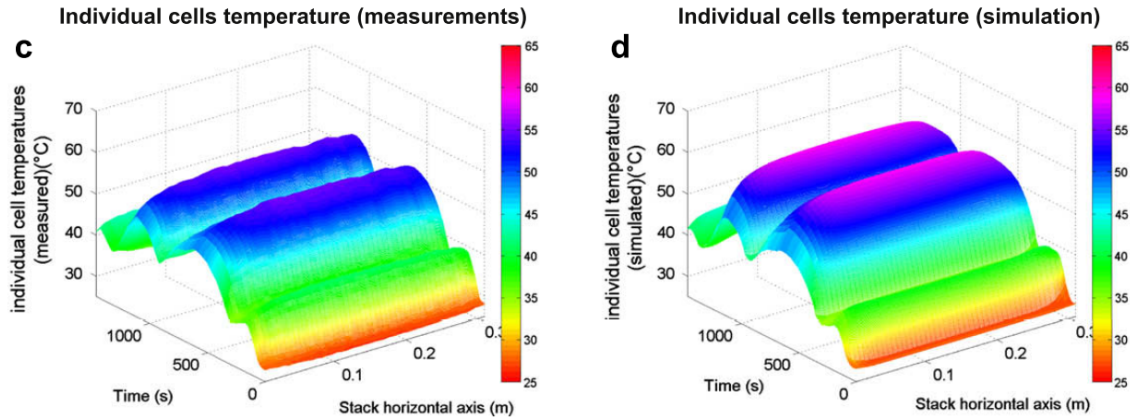
Figure 2.6: Experimental and simulated 1D temperature distribution within a stack [65].
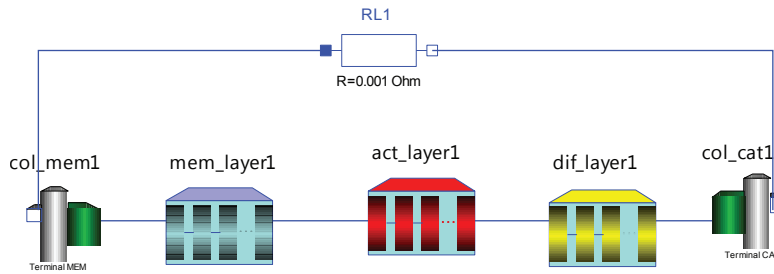
Figure 2.7: 3-layer fuel cell model in FuelCellLib Modelica library [66].

simulated and experimental results were shown to be in good agreement. This publication provides a good overview of how an a-causal approach can be used for modelling PEMFCs.

The model by Gao et al. [65] also uses the VHDL-AMS language and extends the model created in [64] by incorporating a 1D temperature distribution throughout their 47-cell stack. The model also features pressure losses and detailed cooling dynamics. The comparison of simulated and experimental temperature variations are shown in Figure 2.6. It can be seen that the cells located closer to the edges of the stack are cooler which agrees with results obtained by Park and Choe [59].

Several PEMFC models were implemented using another a-causal modelling language called Modelica. Rubio et al. [66] developed an open-source Modelica library called Fuel-CellLib for modelling 1D, two-phase fuel cell models. The model architecture also follows the physical topology of a fuel cell and consists of three main blocks corresponding to the layers of a PEMFC. This is illustrated by Figure 2.7, which depicts a basic model consisting of three blocks corresponding to the membrane (mem_layer1), catalyst (act_layer1) and gas diffusion (dif_layer1) layers. The two current collectors (col_mem1 and col_cat1) are connected to an external electrical load represented by an electrical resistor RL1. The structure of the model has the potential to be expanded by including layers representing neighbouring cells in a stack, but the model was designed under the assumption of constant temperature and the fluidic phenomena are also ignored.
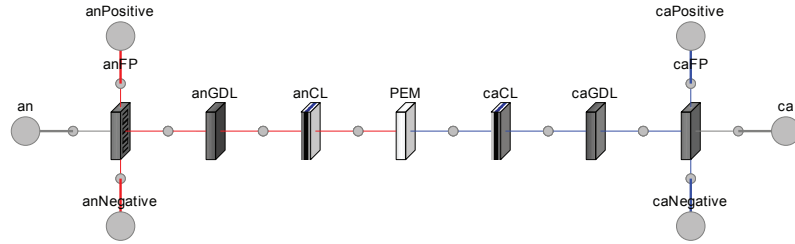
Figure 2.8: 7-layer PEM fuel cell model in FCSys Modelica library [67].

Another open-source Modelica library for fuel cell modelling called FCSys was developed by Davies et al. [67]. The architecture of the model is designed to be highly modular. The implementation makes it easy to not only alter the fuel cell structural composition, but it is also possible to include or remove additional gas species from the calculations by toggling them on or off. The modular nature of the model is illustrated by Figure 2.8 which shows a 7-layer structure of the fuel cell model in FCSys. Similar to previously discussed a-causal models, each block in this diagram corresponds to the fuel cell layers. The blocks labelled anFP and caFP represent the respective anode and cathode Bipolar Plates (BPPs). Circular objects labelled an(ca)Positive and an(ca)Negative correspond to the respective anode and cathode channel inlets and outlets. Due to the modular nature of the model, it is possible to gain insight into the distribution of temperatures and gas concentrations throughout the layers of the fuel cell, as demonstrated by simulation results presented in [68]. This model is among the most flexible and comprehensive PEMFC models, which is also freely available to download and use by anyone.

As shown in Figures 2.5, 2.7 and 2.8 fuel cell models can have different graphical representation within the software. However, as discussed before, block diagrams contain only algorithmic information of the model equations, and iconic diagrams in Modelica only reveal the structural composition of the system. Another graphical modelling technique that incorporates both structural and phenomenological characteristics of the modelled process is called Bond Graph (BG) modelling. Several fuel cell models implemented with BGs are discussed below.

2.4.3 Bond Graph Fuel Cell Models

Bond graphs are a modelling technique for representation of multiple physical phenomena in a unified graphical notation. Generally speaking bond graphs are a-causal and can be used to create hierarchical models of systems [69, 70, 71]. The method is popular within the fuel cell modelling community due to it's versatility with regards to the application area. Bond graphic models were used in fuel cell system simulation [72, 73, 74, 75, 76, 77], controller optimization [78, 79, 80, 81], fault diagnostics [82] and hardware design [83].

Saisset et al. developed a dynamic model of PEMFC with the aim of studying fuel cell interactions with the DC/AC converters [72]. The voltage dynamics at the anode and cathode electrodes was represented by two dissociated double-layer capacitors. Figure 2.9
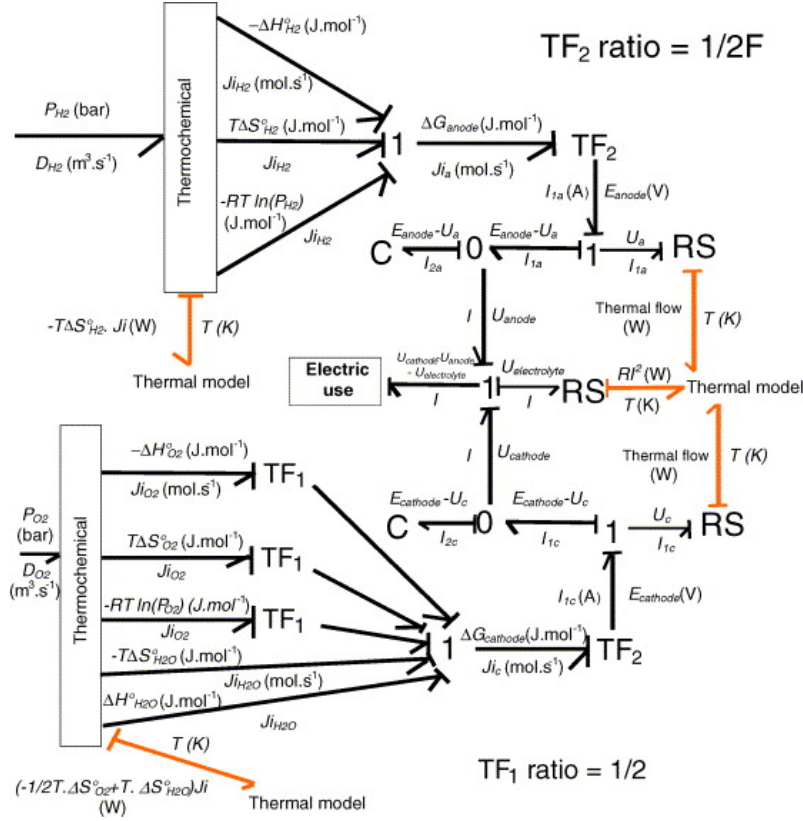
Figure 2.9: A bond graph model of a PEM fuel cell with dissociated electrodes [72].

depicts the electro-chemical part of the model. In this diagram the so-called transformer elements (depicted as **TF**) represent the conversion of chemical energy of gases into electrical power. The three elements labelled **RS** correspond to heat generation due to voltage losses during fuel cell operation. The two capacitors (**C**) represent the double-layer capacitance of electrodes. The model also takes into account thermal dynamics that include heat conduction through the layers of the cell. Heat transfer to the environment through convection and radiation was also considered, although the coefficients were assumed constant. Additionally, the model does not include hydraulic losses in the gas channels and the hydration changes of the membrane. The analysis is also limited to non-humidified fuel and oxidant. The model performance was only compared to a current-voltage characteristic, so it is not clear how well the model performs in the thermal domain.

Mzoughi et al. adopted the model from [72] and extended it through the addition of diffusion dynamics at the cathode GDL and the CL [73]. Furthermore, the authors included a more detailed representation of the cooling process by setting the convection coefficients dependent on the coolant flow rate. Similar to [72], only the current-voltage performance of the model was evaluated. The difference with experimental results was explained by omission of changing membrane water content and pressure losses within channels.

In another paper by Mzoughi et al. the authors focused on the control-oriented aspects of fuel cells [78]. The authors employed a similar approach to [73] but simplified the thermal

domain dynamics by neglecting heat transfer between individual layers of the cell. The model also assumes no pressure losses within channels and constant membrane hydration. The solenoid valve that controls hydrogen flow rate and the air compressor were modelled as transfer functions. The authors used an iterative approach to tune the coefficients of the controllers and demonstrated the improvement of simulated voltage output when compared to an open-loop configuration.

Peraza et al. designed a simple 0D, static, control oriented model of a single PEMFC [74]. The model uses block diagrams to compute the reversible potential of the fuel cell at constant temperature and pressure. The electrical part of the model is modelled using the bond graph method and considers activation, ohmic and concentration losses within the fuel cell. The coefficients for polarization curve simulation were obtained using curve fitting with an average relative error of $1.18\,\%$. The resulting model is simple, yet accurate and effective at demonstrating how structural information can be embedded within bond graph models.

Rabih et al. published a bond graph model of the hydraulic part for the gas supply into the PEMFC stack [75]. The model is composed of a sequence of resistive R- and C-elements. The model assumes laminar flow of pure H_2 and O_2 at constant temperature. The pressure losses are determined as a function of gas viscosity and channel geometry. This model was connected to electro-chemical and thermal models from [72] in order to study the effects of current, temperature and channel dimensions. The authors presented the results of simulations which show that pressure losses are significantly higher at the cathode side of the fuel cell and they linearly increase with increasing current. Additionally, the pressure difference non-linearly decreases with increases in pipe diameter.

McCain and Stefanopoulou created a distributed model of a GDL consisting of 3 identical sections [76]. Liquid water condensation, evaporation and transport are implemented within the model and its effect on the lumped current density during flooding is considered. The model was experimentally validated using a 24-cell PEMFC stack. The authors emphasise that even though the model is not too complex it still contains 25 states, which is too high for control applications. This is why the authors employ a special model order reduction algorithm in order to eliminate model components that do not bear significant effect on model performance. As a result, the authors reduced the number of states to 19.

Hung et al. developed a control oriented bond graph model of a single PEMFC [79]. The bond graph is separated into parts: thermofluid and electrochemical. The flows of binary gas mixtures are controlled by inlet and outlet valves, and chemical potentials of species are calculated within special chemical reactor blocks. The gas diffusion through the GDLs and pressure losses within channels are neglected. Thermal dynamics are simplified to include only convective heat transfer between the gases and the body of the cell. Additionally, heat generation due to electrochemical conversion and voltage losses is also ignored. The model was linearised around a set operating point and transformed into state-space form. The authors did not present any experimental validation results.

Yang et al. developed a bond graph model of a PEMFC suitable not only for simulation but also for fault diagnostics [82]. The diagnosis procedure relies on the structural and causal information from the bond graph to detect and identify a set of faults such as flooding or drying of the membrane, loss of catalytic activity and failures related to H_2 supply. The temperature of the FC was assumed constant, as thermal domain modelling was not included. Unfortunately, neither the model nor the diagnosis procedure were verified experimentally in this paper.

Bruun in her PhD thesis developed a 1D distributed model of a tubular SOFC for use in marine power plants [77]. The author first created a lumped parameter section of the cell, which was later used to create a model consisting of six identical sections. Each section incorporates thermal, fluid dynamics and electorochemical phenomena. The model also features auxiliary components such as ejectors, fuel reformers, valves, afterburners and heat exchangers. The author presented the results of simulating several model configurations to compare the performance of a lumped and distributed models, however, no experimental validation was presented.

Vijay et al. developed a control-oriented, 0D, bond graph model of a SOFC [80, 81]. The model includes the representation of binary gas mixtures, thermal dynamics and gas entropy variation due to changes in molar compositions. The control strategy was designed to ensure 80 % to 90 % fuel utilization and air stoichiometry of more than 8. A secondary control objective to maintain the cell temperature at acceptable levels was also included. The model was validated with data from the literature and after performing simulations the authors concluded that the defined control objective was found to be conflicting and needs to be adjusted. The same team of researchers continued their research into an optimal control strategy of SOFC and published another paper suggesting an algorithm to determine the optimal operating conditions for a given current load [81]. The authors also included a model of afterburner and heat exchangers. One drawback of the modelling approach employed in [80] and [81] is the fact that the model was developed such that chemical potentials of gas species were used not only for characterising electro-chemical reactions, but also for describing the flow rates within the fuel cell. Although this yields a unified power representation, the approach is counter-intuitive.

Robin et al. presented a 2D model of a PEMFC based on the bond graph methodology to study the heterogeneous processes occurring on the surface of the cell layers [83]. The authors created a 2D grid of the MEA with each block representing a control volume. These control volumes were linked by various transfer mechanisms such as diffusion, conduction and convection. Simulation results were compared against a six-cell stack with an integrated printed circuit board containing an array of sensors for measuring the magnetic field. As a result, the authors were able to obtain the current density and temperature distribution maps of the MEAs. The authors were interested in analysing the effects of operating conditions on the occurrence of heterogeneities. For example, it was possible to detect local hotspots arising where the flow of liquid coolant was slowing down due
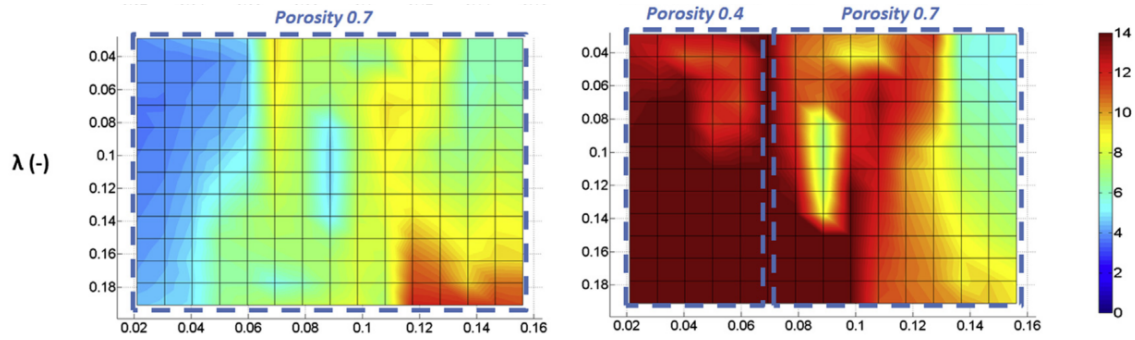
Figure 2.10: Simulated 2D distribution of membrane water content under uniform GDL porosity of 0.7 (left) and non-uniform GDL porosity of 0.4 and 0.7 (right) [83].

to the channel geometry. Additionally, the effects of changing GDL porosity on fuel cell performance was investigated. The graph on the left hand side of Figure 2.10 depicts the distribution of membrane water content when the GDL has constant porosity of 0.7. The graph on the right hand side of Figure 2.10 shows the effects on reducing the pore size of the GDL to 0.4. It can be seen that the reduced porosity increased membrane humidification due to better water retention properties. The resulting model can be used for fine tuning the channel geometries and material properties of the fuel cell for optimised performance.

Section 2.4 was devoted to analysing the literature on PEMFC modelling. It is clear that there is a large variety of modelling methods and approaches, mostly focusing on control and design aspects of PEMFCs. Several modelling characteristics were identified and segmented into two groups: primary and secondary. Primary model characteristics deal with the general level of detail and what model equations are included and how they fit together. Secondary characteristics determine how the model is implemented in a computational engine.

Among the various modelling methods, the bond graph approach stands out due a number of advantages. Firstly, the uniform graphical notation across multiple physical domains makes bond graphs very attractive for modelling multi-physical systems such as fuel cells. Such uniformity in representation incorporates an additional layer of knowledge into the model by including not only algorithmical and mathematical information about the model, but also structural, causal and physical information about the modelled system itself. This provides the modeller with deeper insight into the system under investigation and helps with understanding how the different physical phenomena interact with each other, what is especially valuable when analysing the cause and effect relationships during reliability investigations. Secondly, the bond graphs method is a flexible object-oriented modelling technique that allows the creation of custom component models. One direct application of this property is that bond graphic models can be modified directly or coupled with other object-oriented techniques such as Petri nets to emulate component failure dynamics in both continuous and discrete time.

Because of these unique capabilities and advantages of bond graphs over other modelling methods, they were chosen for conducting physics-based modelling in this dissertation. The following chapter introduces the core concepts of the approach and describes the architecture and the process of developing a bond graph model of PEMFC.

2.5   PEM Fuel Cell Degradation Modelling

Modelling the degradation mechanisms in PEMFCs is very difficult because many phenomena are coupled and thus it is often impossible to observe the change of a specific quantity explicitly. Nevertheless over the years, a number of researchers proposed various degradation laws either derived from first principles or from empirical observations. The primary focus of such research is into modelling the degradation of catalyst and membranes.

Fowler et al. [84] extended a previously published empirical model by Mann et al. [85] by incorporating additional parameters that represent fuel cell ageing under steady state conditions. The authors experimentally observed the increase of the internal resistance of a single fuel cell and devised a linear empirical law for membrane conductivity loss. Additionally, the loss of catalytic activity was also taken into account by modifying term ξ_2 in Equation 2.4:

$$\xi_2 = k_{DR} \times \frac{age}{T} + k_{cell}^0 + 0.000197 \ln A + 4.3 \times 10^{-5} \ln c_{\text{H}_2}^* \tag{2.5}$$

where k_{DR} is the empirical degradation rate, k_{cell}^0 is the parameter describing the initial catalytic activity, T is temperature, A is the active area and $c_{\text{H}_2}^*$ is the effective concentration of hydrogen at the reaction sites. The value of the ageing rate parameter k_{DR} was found to be approximately $-0.055 \, \mu\text{V K h}^{-1}$ based on the experimentally observed voltage decay. Although, this result allows some preliminary predictions into the lifetime of the fuel cell to be performed, the value of k_{DR} will be vary depending on the catalyst type and operational conditions, so it must be re-evaluated for each different hardware configuration.

Joiun et al. [86] proposed a set of equations describing time-dependent degradation of key parameters influencing the power output of a fuel cell such as leak current density, catalyst surface area, change of GDL morphology and others. For example, the increase of leak current density $i_{loss}(t)$ is expressed exponentially as follows:

$$i_{loss}(t) = i_{loss,0} \times \exp[\beta_{loss} \times t], \tag{2.6}$$

where $i_{loss,0}$ is the initial value of the leak current density and β_{loss} is the degradation coefficient. The equations were created by reviewing experimental observations found in the literature. Although the degradation equations are not always justified physically, the estimated parameters and the overall model was validated with experimental data nonetheless. The model was then used for predicting the remaining useful life of the fuel cell. The same authors continued to validate the approach with three additional

experimental data sets (stationary, automotive and dynamic) [87]. Obvious drawback of such an approach is that it neglects the influence of changing operating conditions on the degradation coefficients.

Reimer et al. [88] used a similar approach to degradation modelling as in [86], but attempt to incorporate the contribution of voltage and heat on degradation. According to the authors, the Equation 2.6 can be augmented with a sigmoidal membership function $F(E)$ that takes values in $(0, 1)$ and acts as a switch that turns the degradation on or off depending on the value of cell potential E. The resulting degradation equation is:

$$X(t) = X(0) \exp[\beta \times t \times F(E)], \tag{2.7}$$

where $X(t)$ is a degrading quantity as a function of time t, β is a degradation parameter. However, Equation 2.7 is only valid for a constant values of E and cannot be applied in situations when the voltage is changing dynamically.

Zhang et al. [89] propose the evaluation of PEMFC voltage degradation via calculation of so-called load profile characteristic value φ. This metric was designed to accommodate the influence of current load and voltage during various operating regimes of an automotive PEMFC. These operating regimes were constant-speed cruising, speeding up or slowing down, idling and rapid acceleration. The authors derived the following expression for the voltage degradation rate at a given current density value:

$$\dot{U}(\varphi) = -\frac{dU_{cell}}{dt}|_i = \delta_a(\varphi) + i\delta_R(\varphi) \tag{2.8}$$

where $\dot{U}(\varphi)$ is the average voltage degradation rate, i is the current density. Two empirical functions $\delta_a(\varphi)$ and $\delta_R(\varphi)$ describe the rate of activation over-voltage and inner resistance increase respectively. The authors used the data available in the literature to obtain the necessary coefficients at $0.5\,\mathrm{A/cm^2}$. The resulting model provides a convenient method for calculation of the voltage decay rate based on the current load profile, however, the equation coefficients need to be re-evaluated for a specific fuel cell configuration and at all current density values in order to be accurate.

The models of degradation phenomena designed from a mechanistic point of view usually focus on a single degradation mechanism within specific fuel cell components. Catalyst and membrane deterioration mechanisms have received the most attention in the literature due to their increased criticality and importance to fuel cell performance. While, modelling the degradation of the GDLs has not been extensively covered in the literature to date.

Zhang and Pisu [90] focused on the issue of catalyst active area degradation. They approached the problem by viewing the catalyst as a collection of spherical Pt nano-particles with varying radii. Next they segregated these particles into 2 groups and evaluated how the respective radii will change as a function of Pt-dissolution rate. The total geometric area of the catalyst A_{geo} was determined as the total sum of surface areas of these particles.

The general form of the resulting equation is shown by Equation 2.9:

$$\frac{dA_{geo}}{dt} = \varepsilon g_1(\Delta\phi_c)g_2(A_{geo}),\tag{2.9}$$

where ε is a scaling parameter, $g_1()$ is a non-linear function of the phase potential at the cathode catalyst $\Delta\phi_c$ and $g_2()$ is a non-linear function of A_{geo}. The structure of Equation 2.9 can be separated into two parts: the state of catalyst health evaluated by $g_2(A_{geo})$ and the magnitude of the imposed stress due to the applied current load ($g_1()$). Although no direct comparison with the experimental measurements was demonstrated by the authors, the model, nevertheless, demonstrates the same decrease of the degradation rate as experimentally observed by other authors.

In addition to high level 1D and 2D phenomena occurring at the cell scale, the model by Robin et al. [83] previously discussed in Section 2.4.3 also includes low level nano- and micro-scale interactions within fuel cell layers. Such multi-scale modelling provided the possibility to incorporate various degradation mechanisms such as catalyst dissolution into the model [91]. The authors established the rate of catalyst area degradation as a function of Pt particles radii as follows:

$$S_{\mathrm{Pt}_C} = N \times 4\pi r^2 \tag{2.10}$$

$$dr = -v_{diss}\frac{m_{\mathrm{Pt}}}{\rho_{\mathrm{Pt}}} \tag{2.11}$$

where S_{Pt_C} is the cathode Pt specific surface, N is the number of Pt particles, r is their average radius, m_{Pt} and ρ_{Pt} are the Pt mass and density, v_{diss} is the reaction rate of Pt chemical dissolution. Other degradation mechanisms such as start/stop cycles, carbon corrosion, membrane mechanical degradation and others are not included in the model. The authors validated the capability of the model to describe the catalyst degradation against experimental data obtained from a 30-cell stack under static and dynamic current load profiles [92]. The simulation results were found to be in good agreement with both data sets.

Chandesris et al. [93] performed experimental evaluation of membrane degradation rates by measuring the concentration of fluoride ions in the exhaust water flows. As a result, the authors proposed a semi-empirical method for calculating fluoride release rate and subsequent membrane thinning as a function of voltage, humidity and gas pressure. The authors highlight that the membrane degradation rate is significantly higher at increased cell potentials.

Although, some of the previously discussed models in Section 2.4 incorporate liquid water formation, none of them consider the effects of water freezing within the fuel cells. Zhou et al. [94] created a model to investigate how ice formation affects the PEMFC stack performance and suggested variable heating and load control strategy to be used when the fuel cell starts up in sub-zero temperatures. Such start-up strategy takes into account the fact that there is higher ice volume fraction forming within a cell located near the edges

of the stack. Therefore, an optimal start-up procedure would involve providing heating to selected cells inside the stack, while applying current load to still active cells in the middle of the stack. The active cells would eventually produce enough heat to melt the frozen cells at the edges of the stack. This model does not include damage of the MEA associated with ice formation.

In summary, two main approaches to degradation modelling of PEMFCs exist: empirical and mechanistic. The advantage of the empirical method is that it provides the means to incorporate multiple degradation phenomena in a model in a generalised fashion. The downside is that such an approach is often hard to justify from the physics-of-failure point of view. On the other hand, a mechanistic method provides physical justification for the modelled process, but model equations usually contain many physical parameters that may be difficult to obtain.

2.6 Chapter Summary and Proposed Modelling Approach

Several studies into the reliability assessment of PEMFCs using classical methods such as FTs and PNs conclude that these methods are useful for analysing the performance when the operating conditions are constant and known in advance. However, such methods assume fixed degradation rates for the fuel cell components, thus failing to capture the effect of unpredictably changing operating conditions on the degradation rate. As a result, the predictions calculated using classical methods overestimate the system reliability metrics. More accurate estimations can be obtained when utilising advanced modelling techniques from the field of dynamic reliability.

The core idea of dynamic reliability is to extend the classical PRA evaluations of system failure rates by taking into account the changes in system dynamics due to component degradation, failures, repairs and other events. Published models in this area rely on some method of system state representation such as SPN and physical process modelling with ODEs. Despite offering a path to more accurate and realistic reliability predictions, the publications on dynamic reliability tend to focus on a handful of benchmark case-studies where the physical dynamics are limited to one or two domains.

One of the first attempts to apply the ideas of dynamic reliability to PEMFCs was a paper published by Fecarotti et al. [45]. However, it also suffers from limited physical process modelling and the assumption of constant load. In order to bypass these limitations, a more detailed and complex fuel cell model is required. Consequently, a detailed review of existing FC modelling methodologies was provided in this chapter. Among the different techniques, bond graphs stand out as the most versatile method for capturing all the dynamics occurring within the fuel cell in multiple physical domains.

All in all, the analysis in this chapter makes it clear that both fields of DPRA and fuel cell reliability assessment are in need of further research into advanced modelling, implementation and evaluation methods.

The rest of this thesis is dedicated to advance the knowledge and understanding of PEMFC modelling and reliability assessment through development, validation and evaluation of enhanced models.

Bond Graph Model of PEM Fuel Cell

Contents

3.1   Introduction

The Bond Graph (BG) methodology is a graphical modelling technique for representing engineering systems as sets of connected elements regardless of the physical domain to which they belong. BGs, therefore, provide a single modelling language for multiple engineering systems from different physical domains. Originally developed by Professor Henry Paynter in 1960s [95] to represent mechatronic systems, the bond graph approach evolved into a separate field of study. The method has been applied in multiple areas from modelling nuclear reactors [96], hydro-electric devices [97] and solar cells [98] to socio-economic processes [99, 100] and biomechanical structures [101]. A comprehensive description of the BG approach can be found in multiple textbooks [70, 71, 102], but a short review is provided in this chapter, in Section 3.2.

The sections thereafter are devoted to the application of the BG formalism to modelling Polymer Electrolyte Membrane Fuel Cells (PEMFCs). A set of modelling assumptions and objectives is established in Section 3.3. Next, a component-based model of a Polymer Electrolyte Membrane (PEM) fuel cell is developed in Sections 3.4 and 3.5. The procedure of model initialization and simulation is outlined in Section 3.6. Experimental set-up and parameter identification is described in Section 3.7. The results and discussion of model validation is presented in Section 3.8. Section 3.9 draws conclusions on this chapter.

3.2   Bond Graph Method

A bond graph is a mathematical structure consisting of '*bond graph elements*' as vertices of the graph, which are connected by directed edges called '*power bonds*' (or simply '*bonds*').

Table 3.1: Physical analogies for power variables

Domain	Effort $e(t)$	SI unit	Flow $f(t)$	SI unit
Electrical	Voltage U	V	Current I	A
Mechanical	Force F	N	Velocity u	m/s
Pneumatic	Pressure P	N/m^2	Volume flow $\dot{v}$	m^3/s
Chemical	Chemical potential μ	J/mol	Molar flow $\dot{n}$	mol/s
Thermal	Temperature T	K	Entropy flow $\dot{S}$	J/K s

The bonds represent the bi-directional transfer of physical energy between engineering components or systems.

Many types of bonds exist, but the first type considered in this review is the *'true'* bond, which has two variables called *'effort'* and *'flow'* associated with it. Such a bond between two arbitrary energy objects **A** and **B** is illustrated in Figure 3.1:

$$\mathbf{A} \xrightarrow[\text{\textit{flow}}]{\text{\textit{effort}}} \mathbf{B}$$

Figure 3.1: Power bond between two energy objects.

The effort and flow variables represent different quantities depending on the physical domain of the model. These quantities are selected such that their product yields power:

$$e(t) \times f(t) = Power(t) \tag{3.1}$$

where $e(t)$ and $f(t)$ are instantaneous effort and flow and $Power(t)$ is the instantaneous power as measured in watts (W). For this reason the efforts and flows are called *'power variables'* [70, 71]. Several pairs of power variables that satisfy the requirement of Equation 3.1 in various physical domains are listed in Table 3.1. Similar pairs can be listed for other physical domains as required.

3.2.1   Bond Graph Elements

The bonds always connect one bond-graphic element to another through connectors called *'ports'*. Such ports are abstractions for a physical point of connection between the two engineering components. Only one bond can be connected to an individual port. Some bond graphic-elements have one port, while others have two or more ports.

The bond graph elements themselves represent different energy manipulation mechanisms. For example, resistive elements (denoted with symbol **R**) determine the rate of energy dissipation or energy transfer between components. In such elements, the power variables are related by a linear or non-linear function. In the electrical domain this is a basic resistor, which signifies the following current-voltage dependency:

$$U(t) = R \times I(t) \tag{3.2}$$

where R is the value of electrical resistance, $U(t)$ and $I(t)$ are voltage and current respectively.

A second type of bond-graphic elements are energy storage components such as capacitor (**C**) and inertia (**I**) which accumulate and release energy without dissipation. Capacitive elements, constitute the dependency between the effort and the time integral of the flow. So, continuing with the electrical domain analogy, bond graphic **C**-element is an idealized capacitor described by the following equation:

$$U(t) = \frac{1}{C} \int I(t) dt \tag{3.3}$$

where C is the capacitance of the element in farads (F). In other physical domains, the capacitive bond-graphic element may correspond to a spring or a hydraulic accumulator. Inertia elements, on the other hand establish the relationship between the flow and the time integral of effort. In physical terms, this element represents an electrical inductor or mass in mechanical domains.

The other types of BG-elements are sources of effort (**Se**) and flow (**Sf**). These elements are called '*active*' elements because they provide input of corresponding power variables to the system. For example, the **Se**-element in an electrical BG represents a battery providing voltage into a circuit.

Detectors of effort (**De**) and flow (**Df**) are passive elements because they do not participate in energy exchange, but rather act as sensors and measure the corresponding power variables. To emphasise this distinction, detectors are connected with a so-called '*signal*' bond instead of the regular bond. Signal bonds carry only one power-variable at a time and are drawn as a full arrow ($\longrightarrow$) instead of a half-arrow.

The bond-graphic elements can be controlled and their parameters adjusted by an external signal bond. Such elements are called '*modulated*' and denoted by a prefix '**m**', e.g. **mSe**. All of the one-port BG elements and corresponding constitutive equations are listed in Table 3.2.

Two basic two-port elements exist, both of which act as energy transducers converting power from one physical domain to another. The first two-port element is called a '*transformer*' (**TF**) and it can be used to model pumps in hydraulics or gear boxes in mechanical systems. The second type of two-port is a '*gyrator*' (**GY**), which can be used to model electric motors. Their corresponding equations are listed in Table 3.3, where m is the transformer or gyrator coefficient.

Multiple power bonds can meet at one of two junction types: **0**- and **1**-type, which enforce the laws of energy conservation within the system. All the bonds entering or leaving a **0**-junction carry the same efforts, while the sum of the respective flows always add up to 0. The opposite is true for **1**-junctions: the sum of efforts adds up to 0, while all the flows are equal. In the electrical domain, **0**- and **1**-junctions correspond to Kirchhoff's current and voltage laws accordingly. In other words, **1**-junctions correspond to a series connection

Table 3.2: Bond Graph One-Port Elements

Type	Symbol	Equations
Resistance	$\longrightarrow$ **R**	$e(t) = R \times f(t)$
Capacitance	$\longrightarrow$ **C**	$e(t) = \frac{1}{C} \int f(t) dt$
Inertia	$\longrightarrow$ **I**	$f(t) = \frac{1}{I} \int e(t) dt$
Source of effort	**Se** $\xrightarrow{e}$	$e(t)$ is known, $f(t)$ is arbitrary
Source of flow	**Sf** $\xrightarrow{f}$	$f(t)$ is known, $e(t)$ is arbitrary
Detector of effort	$\xrightarrow{e}$ **De**	$e = e(t),\ f = 0$
Detector of flow	$\xrightarrow{f}$ **Df**	$f = f(t),\ e = 0$

Table 3.3: Bond Graph Two-Port Elements

Type	Symbol	Equations
Transformer	$\xrightarrow[f_1]{e_1}$ **TF** $\underset{m}{\xrightarrow[f_2]{e_2}}$	$e_1 = me_2,\ f_2 = mf_1$
Gyrator	$\xrightarrow[f_1]{e_1}$ **GY** $\underset{m}{\xrightarrow[f_2]{e_2}}$	$e_1 = mf_2,\ e_2 = mf_1$

Table 3.4: Bond Graph Junctions

Type	Symbol	Equations
1-junction	$\xrightarrow[f_1]{e_1}$ **1** $\xrightarrow[f_N]{e_N}$	$f_1 = f_2 = \ldots = f_N,\ \sum e_N = 0$
0-junction	$\xrightarrow[f_1]{e_1}$ **0** $\xrightarrow[f_N]{e_N}$	$e_1 = e_2 = \ldots = e_N,\ \sum f_N = 0$

of electrical components, while **0**-junctions are for parallel connections. Table 3.4 shows
the graphical implementation and governing equations of BG junctions.

3.2.2   Bond Graph Extensions

The BGs discussed previously are well suited for modelling a wide range of engineering
systems in electrical, mechanical and other domains. However, using classical BGs defined
by Equation 3.1 and power variables listed in Table 3.1 can be limiting and inconvenient

Table 3.5: Pseudo-power variables

Domain	Effort	Flow
Pneumatic	Pressure P (N/m^2)	Mass flow rate $\dot{m}$ (kg/s)
Thermal conduction	Temperature T (K)	Heat flow rate $\dot{Q}$ (J/s)
Thermal convection	Temperature T (K)	Enthalpy flow rate $\dot{H}$ (J/s)

when describing certain phenomena such as heat transfer and compressible fluid flows. In order to overcome these limitations several modifications and extensions to the classical definitions of BGs have been proposed. A summary of two such extensions called pseudo-bonds and multi-bonds is provided below.

3.2.2.1 Pseudo-bonds

Conventionally, linear heat conduction problems are described in terms of temperature difference (T) and heat flow rate ($\dot{Q}$) [103]. But the product of these two quantities does not equal power, as heat flow rate itself is measured in units of power. Similarly, thermal convection is described in terms of temperature and enthalpy flow rates ($\dot{H}$). Another example is the hydraulic systems where the fluid is compressible (i.e. has variable density). In this case, the mass flow rate ($\dot{m}$) is more suitable for the description of the processes as it doesn't depend on density, while volumetric flow rate ($\dot{v}$) does. In this case, again the product of mass flow rate and pressure is not power.

So in order to account for such situations, Karnopp [71] proposed the notion of '*pseudo-power variables*'. Pseudo-variables are those which do not obey Equation 3.1, i.e. $e_p(t) \times f_p(t) \neq Power(t)$, where $e_p(t)$ and $f_p(t)$ are pseudo-effort and flow accordingly. Some commonly used pseudo power-variables are listed in Table 3.5, but other pairs can be added as appropriate for a particular model.

Another application of pseudo-bonds is modelling thermo-fluid phenomena, such as liquid cooling. In such systems the movement of matter is coupled with the transfer of heat. To describe this process two power variables is not enough, as four variables are required: temperature, pressure, mass flow rate and enthalpy flow rate. The two energy domains are coupled according to the following equation:

$$\dot{H} = \dot{m}c_p T \tag{3.4}$$

where $\dot{H}$ is enthalpy flow rate and c_p is the specific heat capacity of the fluid. Graphically, the representation of thermo-fluidic power exchange between two components is depicted in Figure 3.2. In this diagram, two coupled pseudo-bonds carrying four pseudo-power variables connect energy objects A and B. The dashed line signifies the two bonds are coupled together.
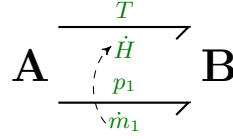
Figure 3.2: Coupled pseudo bonds between energy components A and B.
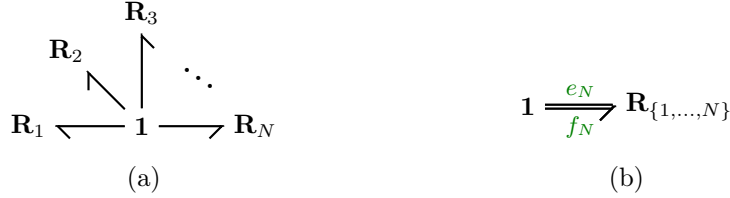
Figure 3.3: Multi-bond equivalent representation of multiple **R**-elements in series.
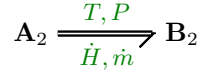
Figure 3.4: Multi-bond with dimension 2 can represent the coupled pseudo-bonds.

3.2.2.2   Multi-bonds

The second extension of the classical bond graphs are '*multi-bonds*' (also called '*vector-bonds*'). Such bonds are designed to simplify the graphical depiction of multiple instances of regular bonds in the same or related domains. To illustrate the concept, Figure 3.3a depicts a BG representation of N **R**-elements connected in series via **1**-junction. Alternatively, Figure 3.3b provides an equivalent representaion by combining the N regular bonds into a single multi-bond with dimension N, while fusing the N **R**-elements into a single multi-port resistor of the same dimension.

Such vector-bonds can easily be adapted to model pseudo-bonds, where two coupled bonds are enclosed in a single two-dimensional multi-bond, as shown in Figure 3.4.

3.3   Modelling Approach

The fundamental structure of a PEM fuel cell depicted in Figure 1.7 is taken as the basis for the model architecture which is shown in Figure 3.5. This diagram shows three blocks of the model that correspond to physical components of the fuel cell: anode and cathode bipolar plates and the Membrane Electrode Assembly (MEA). Cooling channels are implemented as a separate block in order to account for the fact that not all bipolar plates have cooling channels embedded in them. The bonds connecting the blocks illustrate the power flows between components. Inlet and outlet blocks correspond to mass flow controllers or valves and provide flow of matter in or out of the cell. This is shown by multi-bonds labelled with P, T as efforts and $\dot{m}, \dot{H}$ as flows. The source of electric current, denoted as **Sf**, represents the load demanded from the fuel cell. Once the load is applied, energy stored
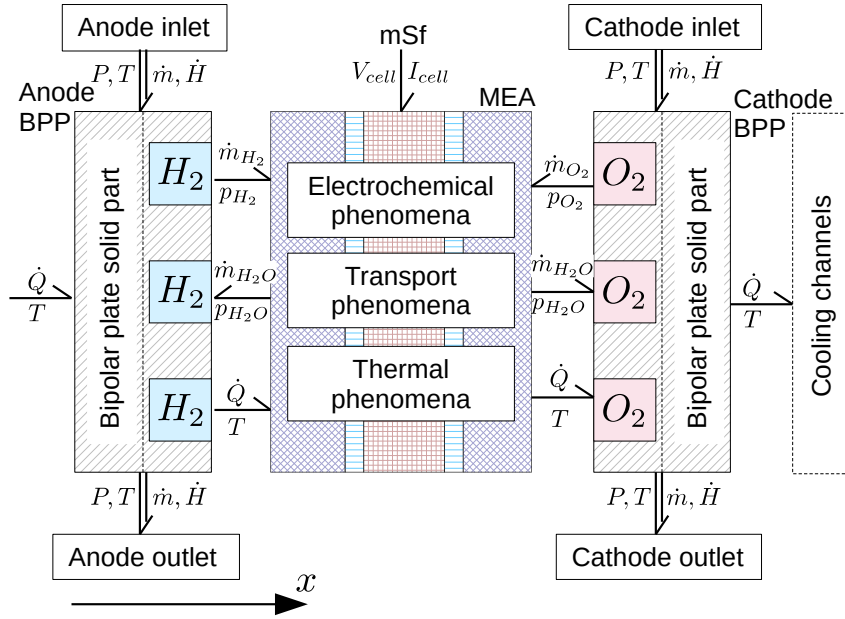
Figure 3.5: Word bond graph of a fuel cell.

within the bipolar plate components is converted into electricity and heat flows within the MEA block. Heat transfer by conduction, convection, and radiation between components and the environment are shown by bonds with T as effort and $\dot{Q}$ as flow. Since the model includes heat transfer between the cell layers, it is necessary to choose the positive direction of heat flow. Therefore the axis is set to be normal to the surface of the MEA adjoining the bipolar plates and positive in the direction from the anode side of the cell to the cathode side as depicted in Figure 3.5.

Any mathematical model is only an abstraction of the real system created for analytical purposes. It is impractical and often unnecessary to recreate every aspect of physical behaviour within a mathematical framework. So it is important to determine a set of modelling assumptions that simplify the model enough to provide an optimal trade-off between accuracy and complexity. Since the primary goal of the modelling effort in this chapter is to create a model that calculates the system performance based on the environmental and operating conditions, the following assumptions are established:

A.1 Gases obey the ideal gas law due to the fact that the gases are at low pressures and temperatures compared to their critical values.

A.2 Thermal properties of materials are constant during simulations. This is acceptable due to the fact that thermal properties of materials do not change significantly in the range of operating temperatures.

A.3 Reactant gases are humidified. This means the anode feed consists of a two-component mixture of pure hydrogen and water vapour, while the cathode feed is a mixture of oxygen, nitrogen, and water vapour.

A.4 The pressure within the catalyst layer and the Gas Diffusion Layer (GDL) is the same. This acceptable because the thicknesses of the GDLs and Catalyst Layers (CLs) are small resulting in an insignificant pressure loss.

A.5 The diffusion of gases through the membrane is neglected due to the very low permeability values of Nafion.

A.6 Only the gaseous phase of gases is considered.

3.4   Model Components

The following sections describe the modelling procedure for each physical component of the PEM fuel cell. Firstly, the valve component implemented as a bond graphic element that computes the mass flow rates of gases in and out of the fuel cell, is described in Section 3.4.1. Next, the pneumatic and thermal phenomena within the bipolar plates are analysed and implemented in Section 3.4.2. The description of diffusive mass transfer and electro-chemical reactions occurring within the MEA is provided in Section 3.4.3. The voltage loss mechanisms are described in Section 3.4.4.

3.4.1   Inlet/outlet Valves

In order for a fuel cell to perform its function, it requires a steady supply of reactant gases. Therefore, the modelling procedure begins with the analysis of components and processes that enable delivery of the necessary gases. With reference to the diagram of Figure 3.5, this section elaborates upon the 'Anode inlet/outlet' and 'Cathode inlet/outlet' blocks.

The total mass flow rate ($\dot{m}$) into and out of the fuel cell volume depends on the pressure difference and is described by Equation 3.5 [71].

$$\dot{m} = u_d(t) \ A \ sign(\Delta P) \ \sqrt{2\rho_{mix}|\Delta P|} \tag{3.5}$$

where u_d is the valve discharge signal used to control the flow rate, A is the orifice area, ρ_{mix} is the density of the gas mixture and ΔP is the pressure difference between the upstream and downstream volumes.

The gases entering and leaving the fuel cell are mixtures containing a certain amount of water vapour. This amount can be quantified by the partial pressure of water vapour $p_{\mathrm{H_2O}}$ which is a function of Relative Humidity (RH) denoted with a symbol ϕ and saturation pressure of water vapour at a given temperature $P_{sat}(T)$ [103]:

$$p_{\mathrm{H_2O}} = \phi P_{sat}(T) \tag{3.6}$$

Molar and mass fractions are used to describe the gas compositions of gas mixtures. For the case of the anode gas stream, the molar fractions of water vapour $x_{\mathrm{H_2O}}$, and hydrogen

gas x_{H_2} are:

$$x_{H_2O} = \frac{p_{H_2O}}{P_{an}} = \frac{\phi P_{sat}(T)}{p_{H_2O} + p_{H_2}} \tag{3.7}$$

$$x_{H_2} = \frac{p_{H_2}}{P_{an}} = \frac{p_{H_2}}{p_{H_2O} + p_{H_2}} \tag{3.8}$$

where P_{an} is the total gas pressure in the anode volume and p_{H_2} is the partial pressure of hydrogen. Since, air is often used as the source of oxygen, for the reaction at the cathode CL, the gas mixture is assumed to consist of two gases – oxygen (O_2) and nitrogen (N_2). The molar fractions of these gases in dry air are assumed to be $x_{O_2}^{dry} = 0.21$ and $x_{N_2}^{dry} = 0.79$ [16]. When the air is humidified, however, molar fractions are calculated as follows:

$$x_{H_2O} = \frac{p_{H_2O}}{P_{ca}} = \frac{\phi P_{sat}(T)}{p_{H_2O} + p_{O_2} + p_{N_2}} \tag{3.9}$$

$$x_{O_2} = \frac{p_{O_2}}{P_{ca}} = 0.21(1 - x_{H_2O}) \tag{3.10}$$

$$x_{N_2} = \frac{p_{N_2}}{P_{ca}} = 0.79(1 - x_{H_2O}) \tag{3.11}$$

where P_{ca} is the total pressure in the cathode volume, p_{O_2} and p_{N_2} are partial pressures of oxygen and nitrogen gases.

The mass flows of individual components in the gas mixture ($\dot{m}_i$) are determined by the mass fraction w_i:

$$\dot{m}_i = w_i \, \dot{m} \tag{3.12}$$

where w_i depends on the molar composition of the gas and molar masses of the individual chemical species M_i:

$$w_i = \frac{x_i M_i}{\sum_i^N x_i M_i} \tag{3.13}$$

where N is the number of species in the mixture. The corresponding enthalpy flow rate is calculated according to Equation 3.14:

$$\dot{H} = \dot{m} \, c_{p,mix} \, T \tag{3.14}$$

where $c_{p,mix} = \sum_i x_i \, c_{p,i}$ is the specific heat capacity of the mixture at constant pressure.

Equation 3.5 is a non-linear function which does not have any variable integration, so there is no energy stored during this process. Therefore, Equations 3.5 to 3.14 are constitutive laws for a multi-port thermo-hydraulic resistive element **mRth**$_{N+1}$ with dimension $N+1$ as illustrated in Figure 3.6:

This element has N ports dedicated to the transfer of matter. Each of these ports carries the information regarding the mass flow rates and partial pressures of N chemical components in the gas mixture. An additional thermal port is also included in order to calculate the total transfer of thermal energy (described by T and $\dot{H}$) through the valve.

$$u_d$$
$$\downarrow$$

$$\xRightarrow{\substack{T, p_{u,\{N\}} \\ \dot{H}, \dot{m}_{\{N\}}}} \mathbf{mRth}_{N+1} \xRightarrow{\substack{T, p_{d,\{N\}} \\ \dot{H}, \dot{m}_{\{N\}}}}$$
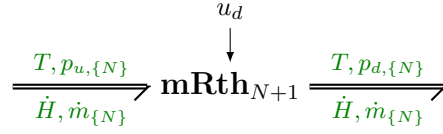
Figure 3.6: Pneumatic resistor with two multi-ports representing an inlet/outlet valve.
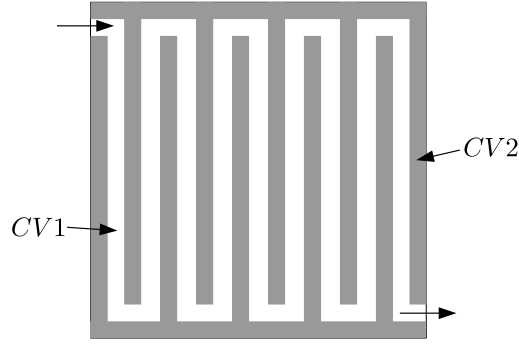
Figure 3.7: Control volumes within a bipolar plate.

The element $\mathbf{mRth}_{N+1}$ is modulated by an external signal to alter the coefficient of valve discharge u_d in Equation 3.5, thus controlling the overall mass flow rate.

3.4.2 Bipolar Plates

In this model, each plate is approximated by two Control Volumes (CVs), each of which corresponds to the specific physical domain:

CV1 Gas flow channels (pneumatic domain)

CV2 Solid material of the plate (thermal domain)

The distinction between the two control volumes is illustrated by Figure 3.7 where the grey area corresponds to CV2 and the white area is the CV1. Firstly, the phenomena occurring in CV1 are discussed followed by the discussion of CV2.

3.4.2.1 Pneumatic Domain

Optimal mass transport within the gas flow channels is important to provide the fuel cell with a steady supply of reactants at sufficient concentrations. When the gases enter the fuel cell they begin to fill the volume of the channels and simultaneously, diffuse through the GDL towards the CL, where they are consumed in the redox reaction. Some amount of reactants, however is flushed out of the cell into the environment or the next cell in the stack. This distribution of mass flows must be conserved and can be described by the

(a) Water vapour balance   (b) Hydrogen balance   (c) Nitrogen balance
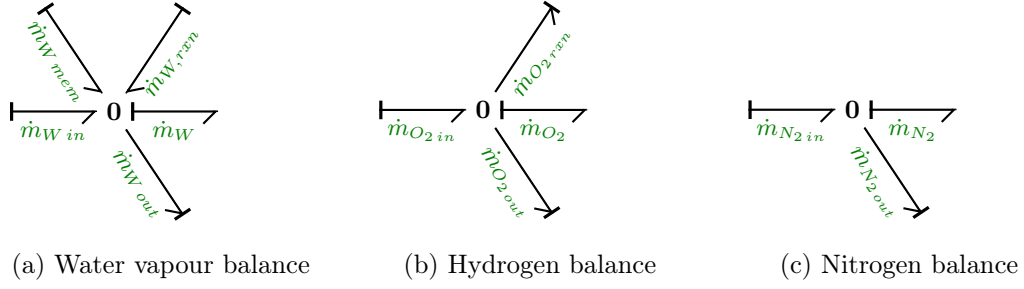
Figure 3.8: Graphical representation of mass balances in cathode channels

following equations for the cathode volume:

$$\frac{dm_{c,\mathrm{H_2O}}}{dt} = \dot{m}_{c,\mathrm{H_2O},in} - \dot{m}_{c,\mathrm{H_2O},out} \pm \dot{m}_{c,\mathrm{H_2O},MEA} \tag{3.15}$$

$$\frac{dm_{\mathrm{O_2}}}{dt} = \dot{m}_{\mathrm{O_2},in} - \dot{m}_{\mathrm{O_2},out} - \dot{m}_{\mathrm{O_2},MEA} \tag{3.16}$$

$$\frac{dm_{\mathrm{N_2}}}{dt} = \dot{m}_{\mathrm{N_2},in} - \dot{m}_{\mathrm{N_2},out} \tag{3.17}$$

where $\dot{m}_{\mathrm{H_2O}}$, $\dot{m}_{\mathrm{O_2}}$ and $\dot{m}_{\mathrm{N_2}}$ are mass flow rates of water vapour, oxygen and nitrogen respectively. Subscripts in and out are assigned to quantities entering and leaving the control volume. Subscript MEA corresponds to the amounts of gases diffused to and from the MEA. Equations 3.15 to 3.17 are implemented in graphical form by a set of zero-junctions, as shown in Figure 3.8. Bonds pointing towards the **0**-junctions have positive sign and provide inflow of matter, while bonds directed away from the junctions represent the outflows.

Similar arrangements can be written for the anode chamber volume, where hydrogen and water are taken into account:

$$\frac{dm_{a,\mathrm{H_2O}}}{dt} = \dot{m}_{a,\mathrm{H_2O},in} - \dot{m}_{a,\mathrm{H_2O},out} + \dot{m}_{a,\mathrm{H_2O},MEA} \tag{3.18}$$

$$\frac{dm_{\mathrm{H_2}}}{dt} = \dot{m}_{\mathrm{H_2},in} - \dot{m}_{\mathrm{H_2},out} - \dot{m}_{\mathrm{H_2},MEA} \tag{3.19}$$

Equations 3.18 and 3.19 can be graphically represented as **0**-junctions in a similar fashion as those in Figure 3.8.

Pressure losses within the channels arise due to friction with the channel walls. Because of this the mass flow rate in all parallel channels can be approximated as follows:

$$\dot{m} = \frac{D_h^2 \ A_{ch} \ N_{ch} \ \rho_{mix}}{2 \ fRe \ L_{ch} \ \mu_{mix}} \ \Delta P \tag{3.20}$$

where A_{ch} is the cross-sectional area of the channels, N_{ch} is the number of parallel channels and D_h is the hydraulic diameter. The length of the channels L_{ch} can be calculated using

$$\xrightarrow[\dot{H}_1, \dot{m}_{1,\{N\}}]{T, p_{1,\{N\}}} \mathbf{Rth}_{N+1} \xrightarrow[\dot{H}_2, \dot{m}_{2,\{N\}}]{T, p_{2,\{N\}}}$$
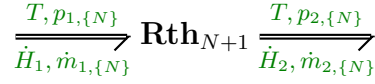
Figure 3.9: Pressure losses in the channels are modelled by another resistive element
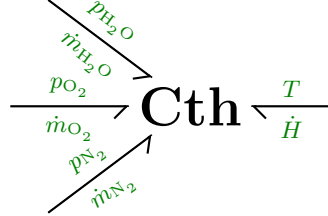
Figure 3.10: Multi-port thermo-hydraulic capacitive element for mixture of three gases.

Equation 3.21 [104]:

$$L_{ch} = \frac{A_{cell}}{N_{ch}(w_{ch} + l_{ch})} \tag{3.21}$$

where w_{ch} is channel width and l_{ch} is the distance between channels. The hydraulic diameter for rectangular channels is:

$$D_h = \frac{4\,w_{ch}\,d_{ch}}{2(d_{ch} + w_{ch})} \tag{3.22}$$

where d_{ch} is the channel depth. The product of frictional losses f with the Reynolds number Re for rectangular channels is governed by Equation 3.23 [16].

$$fRe = 24(1 - 1.3553\alpha_{ch} + 1.9467\alpha_{ch}^2 - 1.7012\alpha_{ch}^3 + 0.9564\alpha_{ch}^4 - 0.2537\alpha_{ch}^5) \tag{3.23}$$

where $\alpha_{ch} = w_{ch}/d_{ch}$. The dynamic viscosity μ_{mix} is calculated using Sutherland's formula [16].

Pressure losses are modelled by another resistive element depicted in Figure 3.9, but uses equations Equations 3.20 to 3.23 to compute the pressure difference and mass flow rate through the channels.

The total fluidic and thermal dynamics within CV1 are governed by a multi-port capacitive element proposed by [71]. Such an element is a thermo-hydraulic accumulator with constant volume which, similarly to the **Rth**, has $N + 1$ ports – N ports for each gas in the mixture and an additional port to accommodate heat transfer. Figure 3.10 shows how such an element labelled as **Cth** is used to represent the cathode channel volume. The three bonds on the left-hand side correspond to the transfer of hydraulic energy associated with the three gases in the mixture (H_2O, O_2 and N_2), while the bond on the right-hand side signifies the thermal energy transfer to the neighbouring control volume.

This element computes partial and total pressures in the volume according to the ideal gas law of Equation Equation 3.24.

$$PV = \frac{m}{M}RT = \frac{m_{H_2O} + m_{O_2} + m_{N_2}}{M_{mix}}RT \tag{3.24}$$

Thermal energy within the volume depends on the temperature, total mass and heat capacity of gases as well as heat transfer to CV2. This process is defined by Equation 3.25.

$$H = c_v mT = c_v(m_{H_2O} + m_{O_2} + m_{N_2})T \tag{3.25}$$

where c_v is the specific heat capacity of the gas mixture at constant volume calculated by:

$$c_v = x_{H_2O}c_{v_{H_2O}} + x_{O_2}c_{v_{O_2}} + x_{N_2}c_{v_{N_2}} \tag{3.26}$$

where x_i are molar fractions of mixture components. Because **Cth** receives the values of mass flows, it is necessary to integrate these values to obtain instantaneous masses of species in order to compute molar fractions according to Equation 3.27

$$x_i = \frac{\frac{m_i}{m \cdot M_i}}{\Sigma_i \frac{m_i}{m \cdot M_i}} \tag{3.27}$$

where m is the total mass of the mixture and M_i is the molar mass of the chemical species.

3.4.2.2 Thermal Domain

Temperature dynamics involves heat radiation to the environment, conduction through the materials, and convection by gases and liquids within the cell. Thermal energy carried by the gases within CV1 participates in the overall energy balance of CV2 as shown by Equation 3.28.

$$\frac{dE_{th}}{dt} = \dot{H}_{in} - \dot{H}_{out} + \dot{Q}_{ch} \tag{3.28}$$

where, E_{th} is the total thermal energy of the volume, $\dot{H}_{in}$ and $\dot{H}_{out}$ are total enthalpies of gases flowing in and out of the volume. Quantity $\dot{Q}_{ch}$ describes the convective heat transfer between the solid part of the plate and the volume of gas flow channels.

The thermal balance of the CV2 is governed by conductive heat transfer to the neighbouring layers ($\dot{Q}_{left}$ and $\dot{Q}_{right}$), convective heat transfer to and from the cooling and gas flow channels ($\dot{Q}_{cool}$, $\dot{Q}_{ch}$) and energy exchange with the environment ($\dot{Q}_{amb}$):

$$mc_p\frac{dT}{dt} = \dot{Q}_{left} + \dot{Q}_{right} + \dot{Q}_{cool} + \dot{Q}_{ch} + \dot{Q}_{amb} \tag{3.29}$$

The convective heat transfer between channels and the solid part of the plate is calculated according to Newton's cooling law:

$$\dot{Q}_{conv} = h_{forced}A_{surf}(T_{bulk} - T_{surf}) \tag{3.30}$$

where A_{surf} is the area of solid material in contact with the gas. T_{bulk} and T_{surf} are temperatures in the middle of the channel and at the surface of the material, the coefficient of forced convection h_{forced} is calculated as:

$$h_{forced} = \frac{Nu \ \kappa_{gas}}{D_h} \tag{3.31}$$

where κ_{gas} is the thermal conductivity of the gas, Nu is the Nusselt number which depends on the properties of the fluid characterised by the Prandtl number $Pr = c_p \ \mu_{mix}/\kappa_{gas}$ [65]:

$$Nu = 3.657 + \frac{0.0677 \left(Re \ Pr \ \frac{D_h}{L_{ch}} \right)^{1.33}}{1 + 0.1 \ Pr \ \left(Re \ \frac{D_h}{L_{ch}} \right)^{0.3}} \tag{3.32}$$

The heat flow between the surfaces of two solid materials can be expressed by Fouriers' law [103]:

$$\dot{Q}_{cond} = \kappa A_{surf} \frac{\Delta T}{\delta} \tag{3.33}$$

where κ is the material thermal conductivity, A_{surf} is the contact area, ΔT is the temperature difference between the two layers, and δ is the material thickness.

The amount of heat lost due to thermal radiation is described by the following relation:

$$\dot{Q}_{rad} = \sigma \varepsilon A_{surf}(T_{surf}^4 - T_{amb}^4) \tag{3.34}$$

where σ is the Boltzmann constant, ε is the emissivity of the surface, T_{surf} is the temperatures of the surface of the layer and T_{amb} is the ambient temperature.

The heat capacity of materials dictates how fast a component can heat up or cool down. The dynamics of these processes is described by the following equation:

$$\dot{Q} = m \ c_p \ \frac{dT}{dt} \tag{3.35}$$

where m is the mass of the component, c_p is the specific heat capacity of the layer and $\dot{Q}$ is the heat flow through the layer. Equations 3.30, 3.33 and 3.34 can be represented by **R**-elements connected to **1**-junctions, which compute the temperature difference. Equation 3.35 corresponds to the capacitive **C**-element discussed in Section 3.2.1. Figure 3.11 depicts this analogy.

Figure 3.11a shows a generic piece of material of thickness δ with temperature T_2 located between two other layers with temperatures T_1 and T_3 respectively. The sign of the heat flow is calculated according to the direction of axis z. Figure 3.11b illustrates a BG representation of thermal conduction through Layer 2. The amount of heat transferred between layers 1 and 2 ($\dot{Q}_1$) is computed by **R**$_1$-element, while **R**$_2$ calculates the heat transfer ($\dot{Q}_2$) between layers 2 and 3. The values of **R**$_1$ and **R**$_2$ are set to $\kappa A/\delta$ according to Equation 3.33. The temperature of layer 2 is determined by a thermal **C**-element with
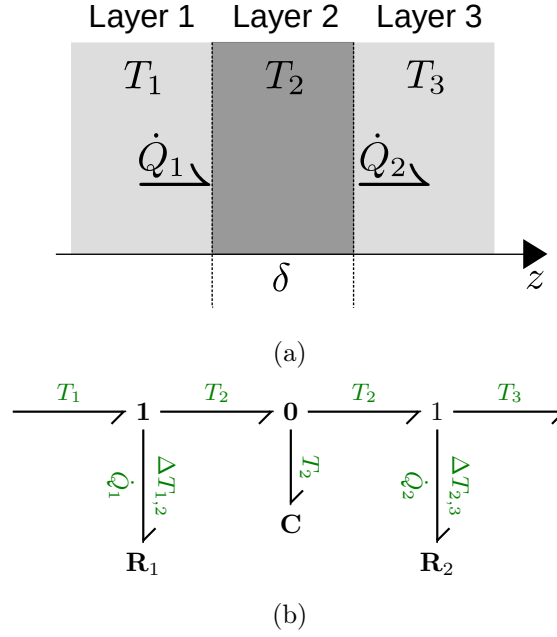
Figure 3.11: Heat transfer through generic solid walls a) diagram b) pseudo-bond graph representation.

its capacitance set to mc_p in line with Equation 3.35. Therefore, fuel cell layers can be represented by such arrangements of bond graphic elements in the thermal domain.

3.4.3 Membrane Electrode Assembly

The combination of the GDLs, the CLs and the PEM is modelled as a single block named MEA. Within this block, sub-graphs representing the diffusion and electrochemical conversion of gases, as well as heat conduction are implemented.

3.4.3.1 Gas Diffusion Layers

As the reactants are being consumed in the electrochemical reaction, the concentration of gases across the GDLs changes. The mass flow of reactants through the GDLs arises due to the difference of concentrations and can be derived from Fick's law of diffusion as shown in Equation 3.36.

$$\dot{m}_i = -D_{ij} \frac{p_i(\delta_{GDL}) - p_i(0)}{RT\delta_{GDL}} A_{GDL} M_i \tag{3.36}$$

where D_{ij} is the binary diffusion coefficient of species i in gas j, $p_i(x)$ is the molar concentration of species i across the layer, and δ_{GDL} is the thickness of the GDL.

The diffusion coefficient depends on the temperature and pressure of the mixture and it's values can be found in the literature or it can be computed using Equation 3.37 [16].

$$D_{ij} = \frac{a}{P} \left(\frac{T}{\sqrt{T_{ci}T_{cj}}} \right)^b (p_{ci}p_{cj})^{1/3} (T_{ci}T_{cj})^{5/12} \times \left(\frac{1}{M_i} + \frac{1}{M_j} \right)^{1/2} \tag{3.37}$$

where $p_{ci,cj}$ are the critical pressures, $M_{i,j}$ are molar masses and $T_{ci,cj}$ are the critical temperatures of the gases in the mixture. Constants a and b depend on the kind of gases involved.

The calculated value of D_{ij} needs to be adjusted for the case when the process occurs within a medium. GDLs are often made out of carbon fibre paper, and, therefore consist of random fibrous media. Nam and Kaviany [105] suggest a percolation type correlation for the calculation of an effective diffusion coefficient that takes into account the amount of liquid water present inside the layer:

$$D^*_{ij} = D_{ij} \times \varepsilon \left(\frac{\varepsilon - 0.11}{1 - 0.11} \right)^{0.785} \times (1 - s)^{1.5} \tag{3.38}$$

where ε is the porosity of the layer and s is the liquid water saturation of the volume and calculated as $s = V_l/V_p$, where V_l is the volume occupied by liquid water and V_p is the volume of the pores.

The limiting current density at each GDL is calculated by:

$$i_{L,i} = \frac{zF}{RT} \frac{D^*_{ij}}{\delta_{GDL}} p_i(0) \tag{3.39}$$

where z is the number of electrons participating in the reaction, F is the Faraday constant.

Equations 3.36 to 3.39 are constitutive equations for a bond-graphic restrictive element **Rd** (illustrated by Figure 3.12) that calculates the diffusion mass flow of gases through the GDL due to the pressure difference.

$$\xRightarrow[\dot{m}_{\{N\}}]{p_{1,\{N\}}} \mathbf{Rd}_N \xRightarrow[\dot{m}_{\{N\}}]{p_{2,\{N\}}}$$

Figure 3.12: Diffusion resistance element

In this model, the heat exchange between the gases within the pores of the GDL and the solid material of the GDL is neglected, as it cannot be simply described by Equation 3.30 (due to difficulty in estimating the convection coefficient and the total surface area of the pores). Instead, the heat transfer through the GDL is assumed to be purely conductive. This is why the multi-port element **Rd** in Figure 3.12 does not carry any thermal information about the flows of matter into the GDL volume. Therefore, this element has only N ports.

3.4.3.2   Catalyst Layer

The amount of reactant gas consumed in each reaction is determined by the current (I) applied to the cell and is expressed in molar flow rate ($\dot{n}$). It is needed, therefore, to transform the power variables used in the pneumatic domain ($\dot{m}$ and p) into chemical ones ($\dot{n}$ and μ).

Table 3.6: Reference enthalpy and entropy of gases

Gas	h^0, J/mol	s^0, J/mol K
H_2	0	130.59
O_2	0	205.14
H_2O	$-28\,583 \times 10^3$	70.05
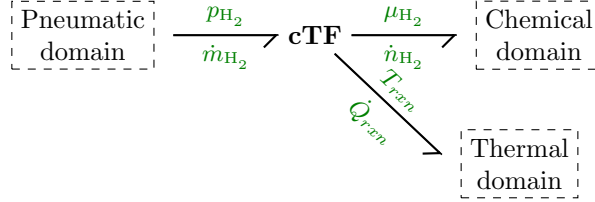
Figure 3.13: Chemical transformation element

The molar flow rate is related to mass flow rate as $\dot{n}_i = \dot{m}_i/M_i$, where M_i is the molar weight of the gas. In order to calculate the chemical potential of the species, the changes in the enthalpy Δh and entropy Δs of the reactions are needed. These thermodynamic variables are calculated with the following equations:

$$\Delta h_i = h_i^0 + M_i c_{pi}(T - T_{ref}) \tag{3.40}$$

$$\Delta s_i = s_i^0 + M_i c_{pi} \log\left(\frac{T}{T_{ref}}\right) \tag{3.41}$$

where h_i^0 and s_i^0 are the enthalpy and entropy values of individual species at reference state conditions ($T_{ref} = 298\,\text{K}$, $P_{ref} = 101\,325\,\text{Pa}$). These values are summarised in Table 3.6 [103]. The chemical potential is then calculated as:

$$\mu_i = \Delta h_i - T\Delta s_i + R_u T \log\left(\frac{p_i}{P_{ref}}\right) \tag{3.42}$$

The heat of the reaction is:

$$\dot{Q}_{rxn} = -\Delta s T \dot{n} \tag{3.43}$$

In order to perform this transformation, an additional element called 'chemical transformer' (denoted with symbol **cTF**) is introduced to convert pneumatic variables into chemical ones. Graphically, such a chemical transformer for the reaction at the anode catalyst layer is illustrated by Figure 3.13. The diagram shows that the proposed **cTF**-element has three ports – one for each physical domain involved in the transformation (pneumatic, chemical and thermal). The incoming bond carries partial pressure and mass flow rate of hydrogen. This information is translated into the corresponding hydrogen chemical potential and molar flow rates using Equation 3.42 and carried by the outgoing bond on the right-hand side of **cTF**. The amount of thermal energy released during the conversion is calculated with Equation 3.43 and represented by the thermal bond connecting the chemical transformer to thermal domain of the model.

The bond graph representation of chemical reactions is related to the concepts of reaction affinities ($\mathcal{A}$) and reaction rates (ξ), which are defined as follows [70, 106]:

$$\mathcal{A} = \sum_i \pm \nu_i \mu_i \tag{3.44}$$

$$\dot{n}_i = \pm \, \nu_i \xi \tag{3.45}$$

where μ_i are the chemical potentials of species and ν are reaction stoichiometric coefficients. The '+' sign is set for forward affinity $\mathcal{A}_f$ corresponding to reactants and the '-' sign is set for reverse affinity $\mathcal{A}_r$ of reaction products. The sum of reaction affinities is the change of Gibbs free energy, which is equal to the amount of energy released in the chemical process. This relation can be written in the form of the Gibbs-Duhem Equation:

$$\Delta G = \nu_{H_2}\mu_{H_2} + \nu_{O_2}\mu_{O_2} - \nu_{H_2O}\mu_{H_2O} \tag{3.46}$$

where ΔG - Free Gibbs energy, $\dot{n}_i$ - molar flow rates, ν_i - stoichiometric coefficients, μ_i - chemical potentials of species. The reaction rate, ξ, is governed by the electrical current drawn from the cell according to Faraday's law:

$$I = 2F\xi \tag{3.47}$$

where F is the Faraday's constant. The reversible potential of the cell, E^0, is expressed as:

$$E^0 = -\frac{\Delta G}{2F} \tag{3.48}$$

The effect of partial pressure change on the reversible cell potential is found according to the Nernst equation:

$$E_{Nernst} = -\frac{\Delta G}{2F} - \frac{R_u T}{2F} \ln \left(\frac{p_{H_2O}}{p_{H_2} \cdot \sqrt{p_{O_2}}} \right) \tag{3.49}$$

Graphically, the Nernst equation is implemented in bond graph form as illustrated by Figure 3.14.
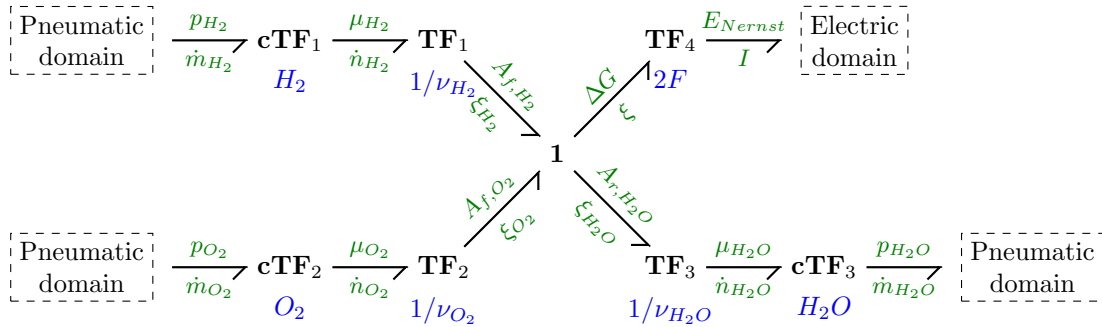
Figure 3.14: Chemical transformation sub-graph

The chemical transformers $\mathbf{cTF}_{1,2,3}$ perform transformations as described by Equations 3.40 to 3.43 for hydrogen, oxygen and water vapour (thermal bonds are not shown for clarity). Three bond-graphic transformers $\mathbf{TF}_{1,2,3}$ and the $\mathbf{1}$-junction recreate the Gibbs-Duhem equation (Equation 3.46). And finally, transformer $\mathbf{TF}_4$ with coefficient of transformation of $2F$ translates the chemical quantities into electrical ones, thus implementing Equations 3.47 and 3.49.

3.4.3.3 Polymer Electrolyte Membrane

Nafion's ionic conductivity properties are strongly dependent on it's level of humidification. Since water is generated at the cathode electrode, the membrane is humidified non-uniformly along it's thickness. The amount of water in the membrane is thus a function of thickness $(\lambda(z))$. The level of humidification at each side of the membrane can be estimated using the empirical equation [16]:

$$\lambda_k = \begin{cases} 0.0043 + 17.81 a_{\mathrm{H_2O},k} - 39.85 a_{\mathrm{H_2O},k}^2 + 36 a_{\mathrm{H_2O},k}^3, & 0 < a_{\mathrm{H_2O},k} \leq 1 \\ 14 + 1.4(a_{\mathrm{H_2O},k} - 1), & 1 < a_{\mathrm{H_2O},k} \leq 3 \end{cases} \tag{3.50}$$

where $k \in \{an, ca\}$ - subscripts denoting anode or cathode volumes respectively and $a_{H_2O,k}$ is water activity equal to the ratio of water vapour pressure and saturation pressure $P_{sat}(T)$ at the given temperature:

$$a_{H_2O,k} = \frac{p_{H_2O,k}}{P_{sat}(T)} \tag{3.51}$$

The mean water content in the membrane is therefore:

$$\lambda = (\lambda_{an} + \lambda_{ca})/2 \tag{3.52}$$

There is also a mass flow of water occurring through the membrane and which is governed by two phenomena: electro-osmotic drag and back diffusion. The former is caused by water molecules dragged by hydrogen ions as they travel through the membrane and the latter is caused by the difference of the partial pressure of water vapour at each side of the membrane.

The mass flow of water due to electro-osmotic drag is calculated according to [16]:

$$\dot{m}_{H_2O,drag} = \frac{n_d}{11} \; \lambda(z) \; \frac{I}{2F} \; M_{H_2O} \tag{3.53}$$

where n_d is the coefficient of electro-osmotic drag which depends on the water content as follows [59]:

$$n_d = 0.0029\lambda^2 + 0.05\lambda - 3.4 \times 10^{-19} \tag{3.54}$$

The back diffusion of water from the cathode to the anode depends on the difference of the water content and physical properties of the membrane [16]:

$$\dot{m}_{H_2O,bd} = -\frac{\rho_{mem}}{M_{mem}} D_w M_{H_2O} A_{mem} \frac{d\lambda(z)}{dz} \tag{3.55}$$

where ρ_{mem} is the density of the dry membrane, M_m is the equivalent weight of the polymer, A_{mem} is the surface area of the membrane, δ_{mem} is the membrane thickness and the effective diffusivity coefficient D_w is calculated using:

$$D_w = D_\lambda \exp\left[2416\left(\frac{1}{303} - \frac{1}{T}\right)\right] \tag{3.56}$$

where diffusivity of water is calculated by:

$$D_\lambda = (2.563 - 0.33\lambda + 0.0264\lambda^2 - 0.000671\lambda^3) \times 10^{-6} \tag{3.57}$$

The net mass flow of water through the membrane is the sum of $\dot{m}_{H_2O,drag}$ and $\dot{m}_{H_2O,bd}$.

$$\dot{m}_{H_2O,net} = \dot{m}_{H_2O,drag} + \dot{m}_{H_2O,bd} \tag{3.58}$$

Substituting Equations 3.53 and 3.55 into Equation 3.58 yields:

$$\dot{m}_{H_2O,net} = 2\frac{n_d}{22}\,\lambda(z)\,\frac{I}{2F}\,M_{H_2O} - \frac{\rho_{mem}}{M_{mem}} D_w M_{H_2O} A_{mem} \frac{d\lambda(z)}{dz} \tag{3.59}$$

It can be seen that $\dot{m}_{H_2O,net}$ depends on the water content within the membrane and the current load. Two cases are considered - when $I = 0$ and $I \neq 0$. In order to solve this differential equation two additional variables are introduced:

$$X_1 = \frac{n_d I M_{H_2O}}{22F} \tag{3.60}$$

and

$$X_2 = D_w\,M_{H_2O}\,A_{mem}\frac{\rho_{mem}}{M_{mem}} \tag{3.61}$$

Therefore Equation 3.59 can be rewritten in the following form:

$$\frac{d\lambda(z)}{dz} = \begin{cases} -\frac{1}{X_2}\dot{m}_{H_2O,net} & I = 0 \\ \frac{X_1}{X_2}\lambda(z) - \frac{1}{X_2}\dot{m}_{H_2O,net}, & I \neq 0 \end{cases} \tag{3.62}$$

Integrating this equation along the thickness of the membrane from $\lambda(0)$ to $\lambda(\delta_{mem})$ the mass flow rate of water can be obtained as calculated by Equation 3.63.

$$\dot{m}_{H_2O,net} = \begin{cases} X_2\frac{\lambda_{an}-\lambda_{ca}}{\delta_{mem}}, & I = 0 \\ X_1\dfrac{\lambda_{an}\,\exp\left[\frac{X_1}{X_2}\delta_{mem}\right]-\lambda_{ca}}{\exp\left[\frac{X_1}{X_2}\delta_{mem}\right]-1}, & I \neq 0 \end{cases} \tag{3.63}$$

As was previously discussed, the ionic resistance R_{ion} of Nafion membranes is highly dependent on λ. It can be calculated by computing the following integral:

$$R_{ion} = A_{mem} \int_0^{\delta_{mem}} \frac{dz}{\sigma(T, \lambda(z))} \tag{3.64}$$

where $\sigma(T, \lambda(z))$ is the ionic conductivity of Nafion which is a function of temperature and membrane water content [16]:

$$\sigma(T, \lambda(z)) = (0.005193\lambda(z) - 0.00326) \exp\left[1268\left(\frac{1}{303} - \frac{1}{T}\right)\right] \tag{3.65}$$

Calculations of Equations 3.50 to 3.64 are performed by a special $\mathbf{Rd}_{mem}$-block (see Figure 3.15) that receives partial pressures of water from the anode and the cathode sides, temperature of the membrane, and electrical current. It then computes the R_{ion} as a function of water content and the total mass flow of water through the membrane.
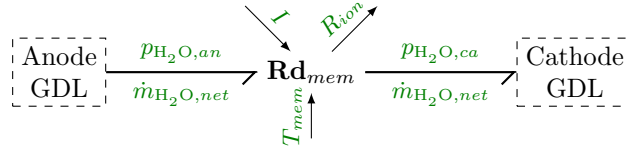
Figure 3.15: A bond graph element for calculation of water content through the membrane

3.4.4   Voltage Output

The reversible potential of a fuel cell from Equation 3.49 is reduced by various voltage loss effects. In electro-chemistry such losses are often referred to as overvoltages. There are three main types of voltage loss mechanisms in PEM fuel cells: activation, ohmic, and concentration loss. The voltage produced by a fuel cell is expressed with the following equation:

$$U_{fc} = E_{Nernst} - -\eta_{act} - \eta_{ohm} - \eta_{conc}, \tag{3.66}$$

where η_{act} η_{ohm} and $\eta_{conc,c}$ are the activation, ohmic and concentration overvoltages respectively.

3.4.4.1   Activation Losses

The reactions occurring at the catalyst layers require a certain amount of energy to be spent in order to start and maintain the electrochemical process. This energy is called the *activation barrier* and the voltage loss as a result of this process is called *activation loss*. It is well known that these losses are several orders of magnitude lower at anode than cathode electrode [16, 15]. Therefore, only the activation losses at the cathode are considered in

this model. This phenomenon can be described by Equation 3.67:

$$\eta_{act} = \frac{RT}{\alpha F} \ln \left(\frac{i + i_{loss}}{i_0} \right),$$ (3.67)

where α is an experimental parameter called the transfer coefficient, i_0 is the exchange current density and parameter i_{loss} describes the amount of current density loss due to the direct electron transfer through the membrane bypassing the external load.

3.4.4.2 Ohmic Losses

Ohmic losses arise as a result of inefficiencies of charge transfer within the fuel cell. The ion transfer through the membrane is hindered by the level of humidification, while electron transfer is impeded by natural resistances of fuel cell materials. Therefore the overall ohmic losses occur due to the combination of ohmic and ionic effects:

$$\eta_{ohm} = I(R_{ion} + R_{ohm})$$ (3.68)

3.4.4.3 Concentration Losses

The concentration overpotential η_{con} occurs at higher current densities when the reactants are consumed faster than they are supplied. Under such conditions, the concentration of fuel or oxidant at the catalyst layer tends to 0 leading to drastically reduced voltage output. The effects of O_2 partial pressure at the cathode side is the primary factor for concentration losses which are expressed as follows:

$$\eta_{con} = \frac{RT}{z\alpha F} \ln \frac{i_{L,i}}{i_{L,i} - i}$$ (3.69)

where $i_{L,i}$ is calculated using Equation 3.39.

Each of the overvoltages η_{act}, η_{ohm} and η_{con} are represented by a two-port non-linear thermo-electrical resistor denoted as **RS** (here 'S' stands for source). In contrast to ideal one-port **R** resistive elements, where no thermal energy is dissipated, **RS**-elements calculate the amount of thermal energy generated according to:

$$\dot{Q} = I\eta_k, \quad k \in \{act, ohm, con\}$$ (3.70)

A generic **RS**-element is shown in Figure 3.16 with electric port on the left and thermal port on the right. The generated heat is the flow variable of the pseudo-bond that leaves the electrical domain and enters the thermal domain.
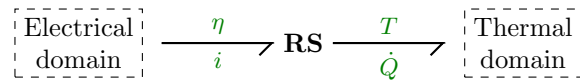
Figure 3.16: Generic thermo-electrical resistive element

Electrical dynamics are governed by the double-layer capacitance C_{dl}:

$$U_{fc} = \frac{1}{C_{dl}} \int I \, dt \tag{3.71}$$

Figure 3.17 shows the electrical part of the bond graph with three **RS** elements for each voltage loss mechanism. The heat generated due to overvoltages is directed to heat up the MEA in the thermal domain. The double-layer capacitance is represented by a capacitor **C**. The **1**-junction graphically represents Equation 3.66. Modulated source of flow **mSf** imposes the current load on the fuel cell.
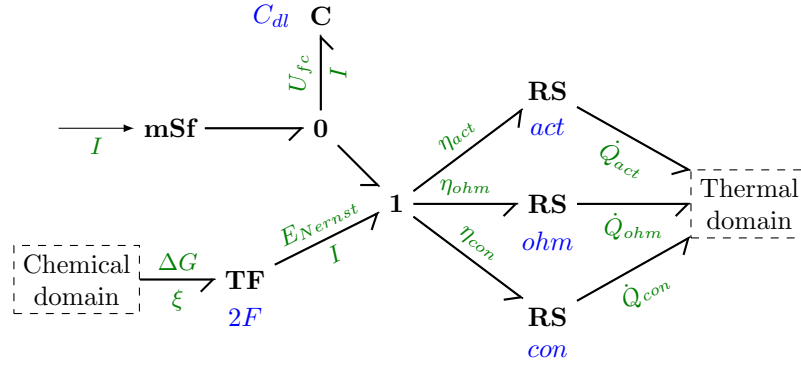
Figure 3.17: Electrical sub-model

3.5 Model Implementation

The model established in Section 3.4 needs to be implemented within modelling and simulation software in order to perform numerical simulations of the model under various conditions. When it comes to BG modelling, not many options exist to create such models. To the best of author's knowledge there is only one modern tool dedicated specifically to BG modelling currently available. This software is a commercial package called 20sim and it is geared towards modelling and simulation of mechatronic systems with bond graphs and conventional block diagrams [107].

Because of the lack of options, many researchers opt to develop ad-hoc solutions for their bond-graph needs. The Python programming language with additional packages to visualise the graphs can be used for bond graph modelling [108]. However, this approach is better suited for construction of smaller BG models than developed here.

Authors of [109] and [110] adapt Simulink block diagrams for BG models. However Simulink's signal based modelling paradigm is not ideal for BGs. Such models are causal and only contain information on the mathematical level and do not convey structural nor physical knowledge.

Alternatively, Modelica modelling language can be used to represent bond graphic elements in a object-oriented fashion [111]. Smaller Modelica models can be created with

a text editor, but in order to work with complex Modelica models, an editor for graphical manipulation of the model components is needed. A number of such editors exist and all of them include a compiler and a solver which means that they are an integrated development environment (IDE). Simulation X [112] and Dymola [113] are commercial IDEs, but an open-source OpenModelica [114] is also available online. In order to facilitate model sharing within the research community as well as wider public, the open source OpenModelica is chosen for model development here.

3.5.1 Bond Graphs in Modelica

Modelica does not have built-in support for bond graphs, but it is possible to create libraries of components that have the necessary properties [115]. The BondLib package, implemented by Cellier [116] is an open-source bond graph library that contains all the essential building blocks for BG models, such as those mentioned in Tables 3.2 to 3.4. The library contains partial base classes upon which additional single- and multi-port bond-graphic components can be built as required. Two additional libraries called MultiBondLib [117] and ThermoBondLib [118] have also been developed to extend the modelling capabilities of BondLib.

MultiBondLib implements the concept of multi-bonds as previously discussed in Section 3.2.2.2 and can be extended with additional classes of components.

ThermoBondLib library, is a domain-specific extension for modelling convective flows of matter. The library also utilises the idea of multi-bonds of encapsulating multiple power bonds into a single symbol by combining three bonds that carry pairs of true power variables: temperature (T) and entropy flow rate ($\dot{S}$), pressure (P) and volumetric flow rate ($\dot{V}$), chemical potential (μ) and mass flow rate ($\dot{m}$). Since ThermoBondLib was designed for this specific domain, their applicability is limited, so only BondLib and MultiBondLib are used in the implementation of the PEMFC model.

3.5.2 Bond Graph Model of Valves

The partial bond graph from Figure 3.9 was implemented within Modelica environment as demonstrated by Figure 3.18. In this diagram, a non-bond graphic block labelled 'Gas mix' contains Equations 3.6 to 3.11 to evaluate the partial pressures of gases. These calculated values are then used to modulate the multi-port source of effort **mSe**. The multi-port element **Rth** contains Equation 3.5 and computes the mass flow through the valve. The flow is regulated with an external signal u that can take values between 0 (fully closed) and 1 (fully open).

3.5.3 Bond Graph of Bipolar Plates

Figure 3.19 depicts a bond graph structure of the cathode bipolar plate component. The multiports 1 and 2 (drawn as a diamond ◊) are the points where the gas mixture enters
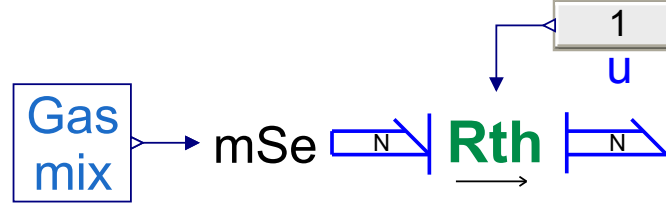
Figure 3.18: Valve component implemented with MultiBondLib.
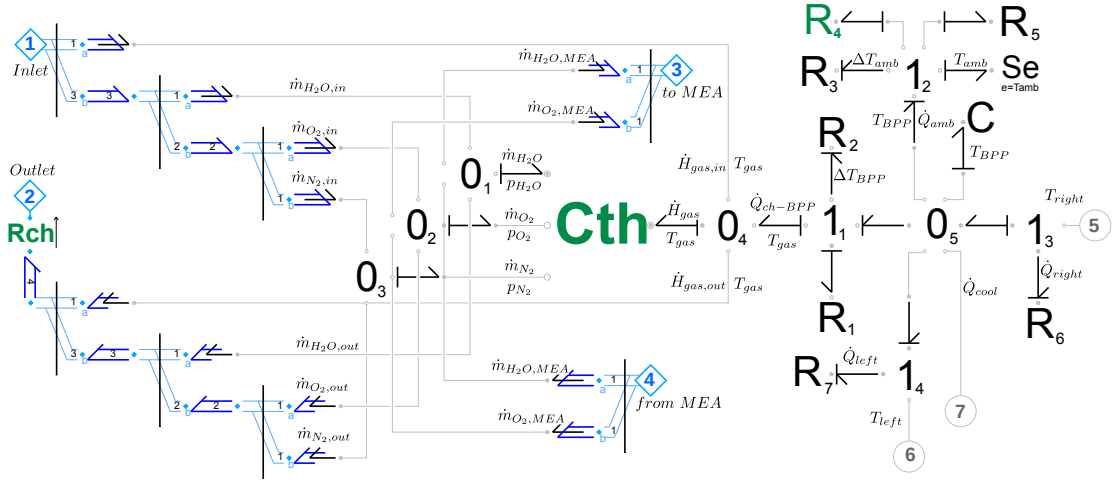
Figure 3.19: Bond graph for the cathode bipolar plate component in Modelica.

and leaves the gas flow channels of the Bipolar Plate (BPP). Three 0-junctions $\mathbf{0}_1$–$\mathbf{0}_3$ enforce the mass conservation relations of Equations 3.15 to 3.17. Since the diffusion of nitrogen is not considered in this model, only water vapour and oxygen flows to and from the MEA component as modelled by multiports 3 and 4. The thermo-hydraulic element **Cth** receives the mass flow rates of matter and computes the resulting temperature and pressure change.

The bond graph structure around junctions $\mathbf{1}_1$–$\mathbf{1}_4$ is within the thermal domain. Bond graphic elements $\mathbf{R}_{1-2}$ represent Equations 3.30 and 3.33 and compute the combined convective and conductive heat flow between the gas flow channels and the solid part of the plate ($\dot{Q}_{ch-BPP}$). Elements $\mathbf{R}_{3-5}$ calculate $\dot{Q}_{amb}$ – the amount of heat lost to the environment by conduction, convection and radiation (Equations 3.30, 3.33 and 3.34). Regular ports 5 and 6 (depicted with a circle ◯) represent points of physical contact of the plate with neighbouring layers and transfer thermal energy via conduction ($\dot{Q}_{left}$ and $\dot{Q}_{right}$). Port 7 models the convective heat exchange with the cooling channels $\dot{Q}_{cool}$.

The anode BPP is implemented in a similar fashion and depicted in Figure 3.20. The only difference to the cathode BPP is the number of chemical species in the mixture within the thermo-fluidic domain.
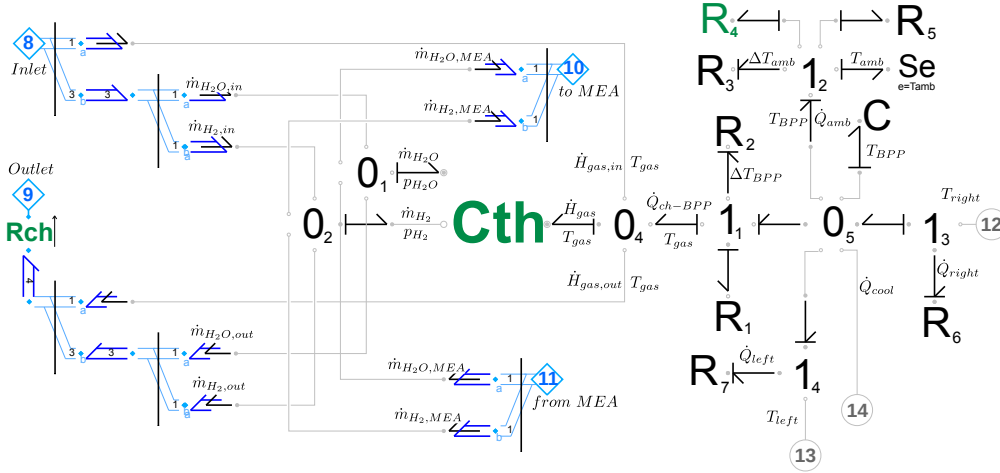
Figure 3.20: Bond graph for the anode bipolar plate component in Modelica.

3.5.4 Bond Graph of an Membrane Electrode Assembly

The complete bond graph of the MEA component incorporating all of the equations from Sections 3.4.3 and 3.4.4 is depicted in Figure 3.21. The four multi-ports 3, 4, 10 and 11 correspond to those in Figures 3.19 and 3.20 and signify the points through which the gases flow into and out the MEA. The diffusion resistances from Figure 3.12 are implemented as four multi-port resistors $\mathbf{Rd}_{1-4}$ and the corresponding mass conservation laws are enforced by junctions $\mathbf{0}_{1-4}$. Element $\mathbf{Rd}_5$ calculates the water content within the membrane and the resulting variation in the ionic resistance. Two thermo-capacitive elements $\mathbf{Cth}_{1,2}$ are additional control volumes which calculate the partial pressure of reactants at the catalyst surface. The previously shown bond graph in Figure 3.14 is implemented with three chemical transformers $\mathbf{cTF}_{1,2,3}$ and four regular transformers $\mathbf{TF}_{1-4}$ around junction $\mathbf{1}_2$. The bond graph structure shown in Figure 3.17 is implemented with three elements $\mathbf{RS}_{1-3}$ connected to junction $\mathbf{1}_1$ and the double layer capacitor $\mathbf{C}_{dl}$. The modulated source of flow $\mathbf{mSf}$ provides the demanded load current signal, while the detector of effort $\mathbf{De}$ outputs the generated voltage of the fuel cell. The temperature of the MEA is determined by the element $\mathbf{C}_1$ and two resistors $\mathbf{R}_{1,2}$ that calculate the conductive heat transfer to the BPPs. Ports 6 and 12 represent the points where the MEA and BPPs exchange thermal energy via conduction.

3.5.5 Single Cell Model

The BGs in Figures 3.19 to 3.21 are encapsulated into singular blocks and used to assemble a single cell model as shown in Figure 3.22. In this diagram, the block labelled 'Cathode BPP' is an encapsulated representation of Figure 3.19, while block 'Anode BPP' is a representation of Figure 3.20. Figure 3.21 is represented by block 'MEA', which receives current load signal and outputs cell voltage signal. The multiports 1, 2, 8 and 9 represent the points of entry and exit of the gases (same as in Figures 3.19 and 3.20). Heat transfer
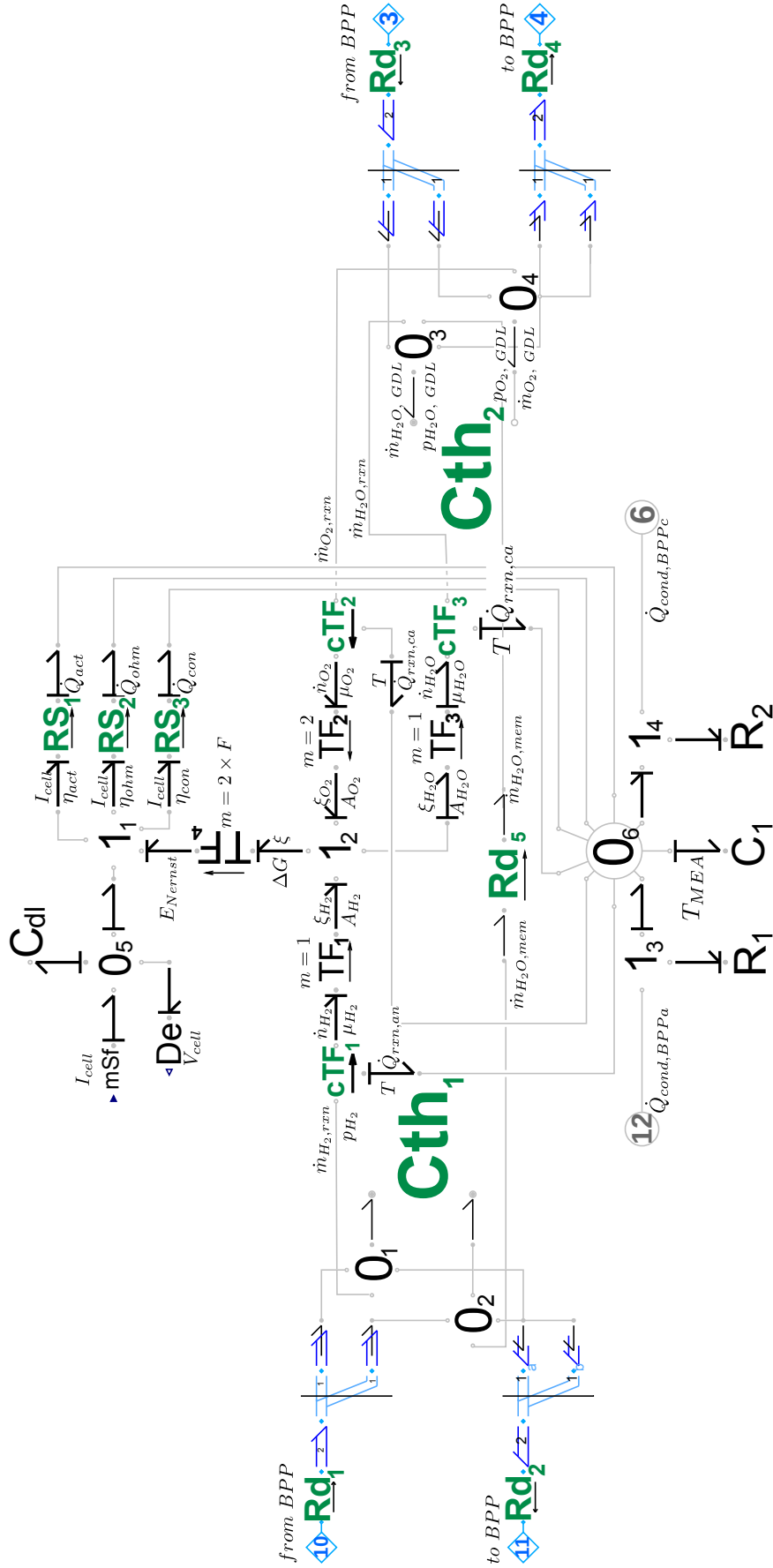
Figure 3.21: Bond graph representation of the MEA.

ports 5, 7, 13 and 14 represent the conductive heat flows with the neighbouring cells and thermal exchanges with the cooling channels. Figure 3.22 illustrates an isolated model
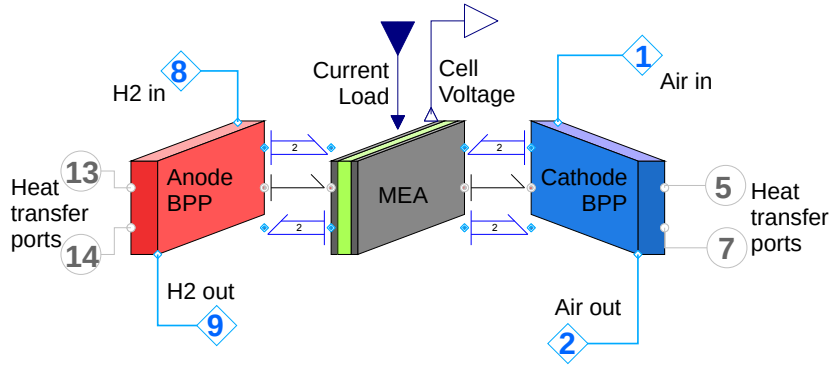
Figure 3.22: A basic single fuel cell assembly.

of a PEMFC, which is missing all the auxiliary components such as fuel supply, cooling channels and end plates. These additional components are needed in order to complete the simulation model.

3.5.6 Cooling Channels and End Plates

The cooling channels are implemented as a separate bond graph (Figure 3.23) in order to allow maximum flexibility in terms of cooling channel placement in the stack assembly. Because of this, the cooling channels bond graph has only a fluidic part and since water is used as the coolant, pseudo-bonds are only two-dimensional. The capacitive element **Cth** represents the total volume of the cooling channels, while the resistive element **Rth** calculates the mass flow rate through the channels.
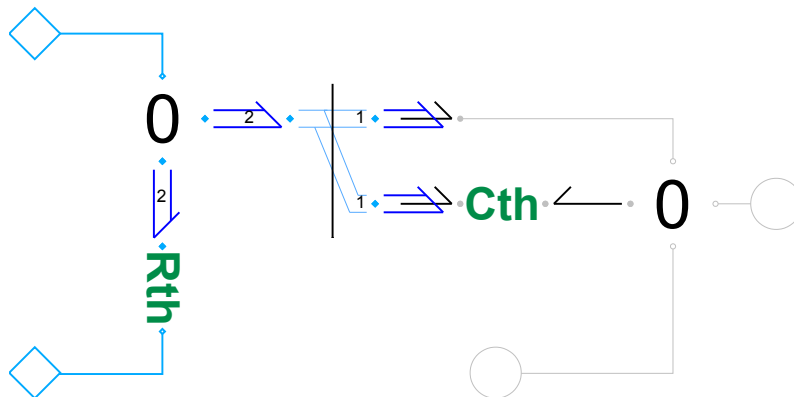
Figure 3.23: Bond graphic cooling channels components in Modelica.

The bond graph of end plates (Figure 3.24) represents only the thermal domain as the plates do not participate in any other form of power exchanges with the rest of the

components. The thermal mass of the plate is modelled by a capacitor **C**. Heat flows due
to natural convection, radiation and conduction are modelled by resistive elements $\mathbf{R}_{1-4}$.
The source of effort **Se** sets the ambient temperature.
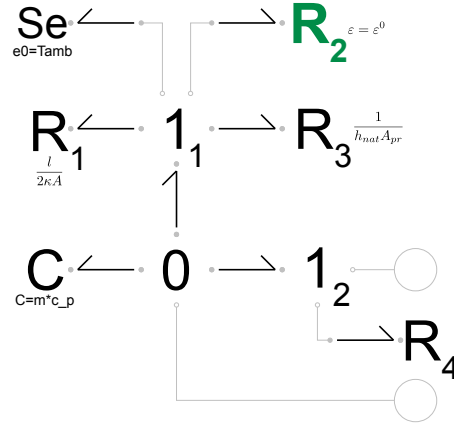
Figure 3.24: Bond-graphic endplate component in Modelica.

3.5.7 Stack Models

The BGs of components in Figures 3.22 to 3.24 are also encapsulated to create singular
blocks for each component. Using these blocks, fuel cell stacks can be constructed as shown
in Figure 3.25. In this diagram, blocks EndPlate1 and Endplate2 represent the end plates,
blocks CLoop1 and CLoop2 correspond to cooling channels. The thermal resistors $\mathbf{R}_{1-4}$
calculate convective heat transport between the cooling liquid and the solid components
of the stack. The Cell component can represent a single cell or a lumped collection of
multiple cells determined by a parameter N_{cell}. The multiports 1, 5 and 7 correspond to
the inlet flows of the gases and the coolant, while 2, 6 and 8 represent the outlet flows.
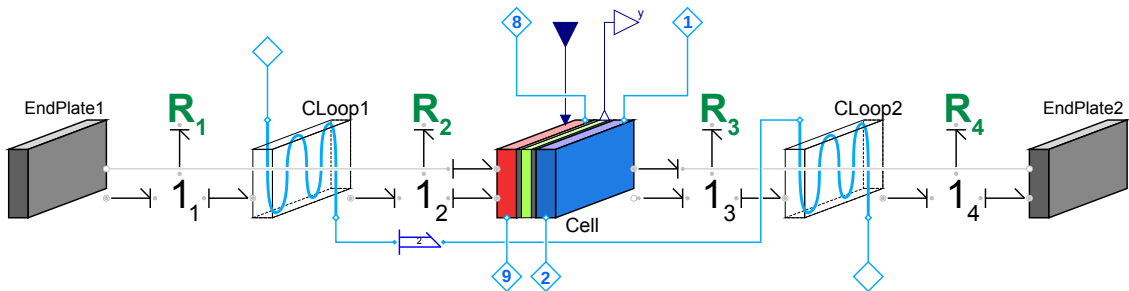
Figure 3.25: A single fuel cell stack with two cooling loops and two end plates.

The approach can be used to create models of stacks with multiple singular cells. This
is illustrated by a diagram of a 3-cell stack in Figure 3.26. Small stacks of up-to 10 cells
are easy to create with singular cell blocks. Large stacks can be separated into several
segments of lumped cells. For example, a 100-cell stack can be modelled by 5 fuel cell
blocks, each of which representing 20 cells each.
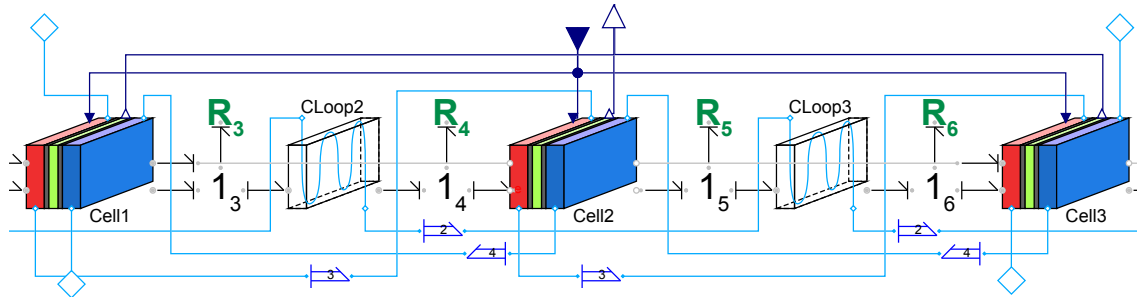
Figure 3.26: Three cell stack.
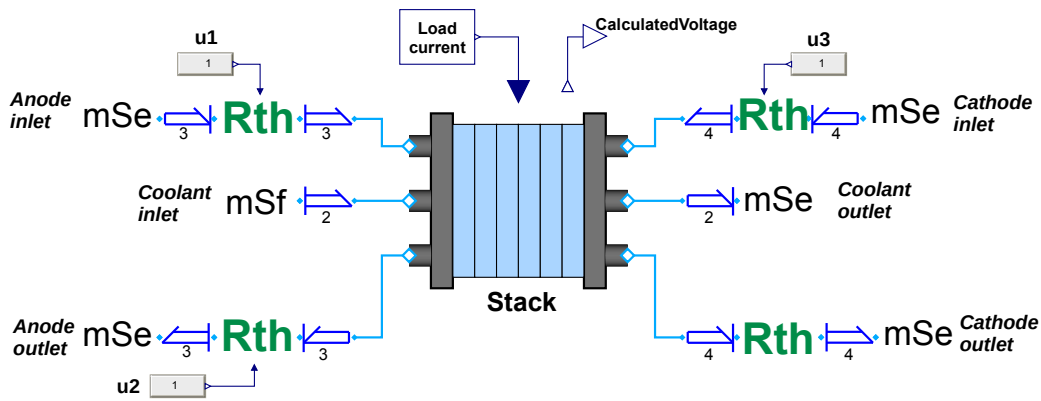
Figure 3.27: Complete simulation model.

3.5.8   Full Simulation Model

An illustration of the final simulation model is shown in Figure 3.27. Block 'Stack' is an encapsulated representation of Figure 3.25. The 4 valve elements from Figure 3.18 modulated by signals u_{1-4} control the inlet and outlet mass-flowrates of gases. The electric current input is provided by block 'Load current' and the resulting voltage response is obtained from port 'CalculatedVoltage'. The model in Figure 3.27 contains all the necessary components and only the parameters values must be set in order to produce meaningful simulation outputs.

From Sections 3.5.2 to 3.5.7 it is clear that the model has hierarchical structure as shown in Figure 3.28. The basic bond graphic elements are used to construct the main components of the stack assembly: bipolar plates, MEA, cooling channels, end plates. Encapsulating these core components and combining them together the model of a single fuel cell is created which is then augmented to create the model of a stack. Adding the balance of plant components results in the final model suitable for simulations.
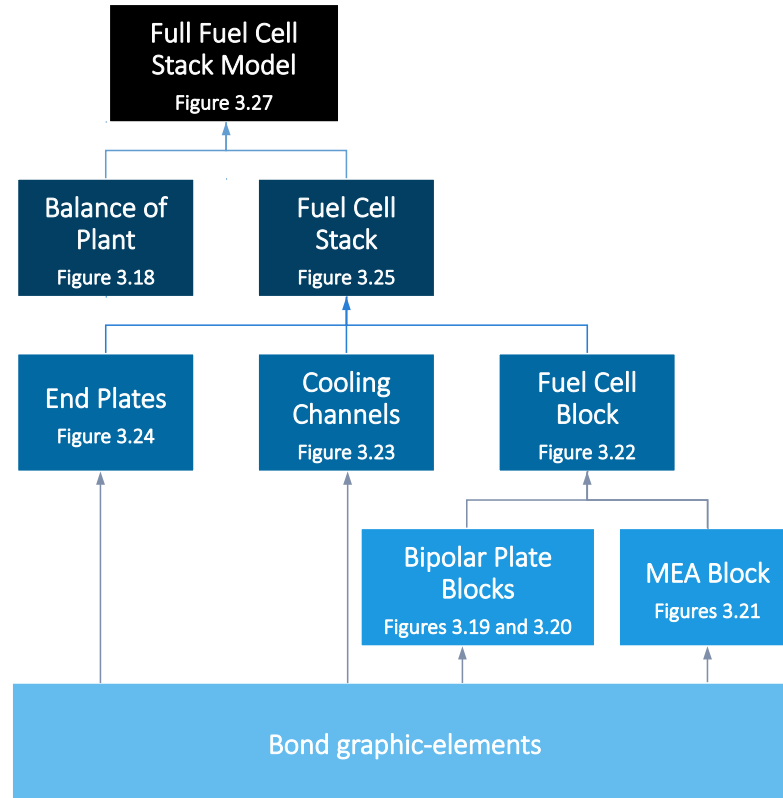
Figure 3.28: Hierarchical structure of the model

3.6 Simulation Procedure

Prior to running simulations, the initial conditions for the Ordinary Differential Equations (ODEs) within the model must be set. This means every thermal or thermo-hydraulic must have the value of initial temperature or pressure set. Additionally, the values of ambient temperature, pressure, relative humidity and the coefficient of natural convection are also needed. These parameters are listed in Table 3.7. The simulation procedure is illus-

Table 3.7: Initial and ambient parameters.

Parameter	Value	Units
Initial pressure	101325	Pa
Initial temperature	327.15	K
Ambient pressure	101325	Pa
Ambient temperature	294.15	K
Ambient RH	50	%
Coefficient of natural convection	50	W/m^2K

trated by the flow chart in Figure 3.29. The model source code is created using graphical and textual editors within OpenModelica. When the model is ready to be simulated, the translator checks if it has the same number of unknowns and equations and flattens the
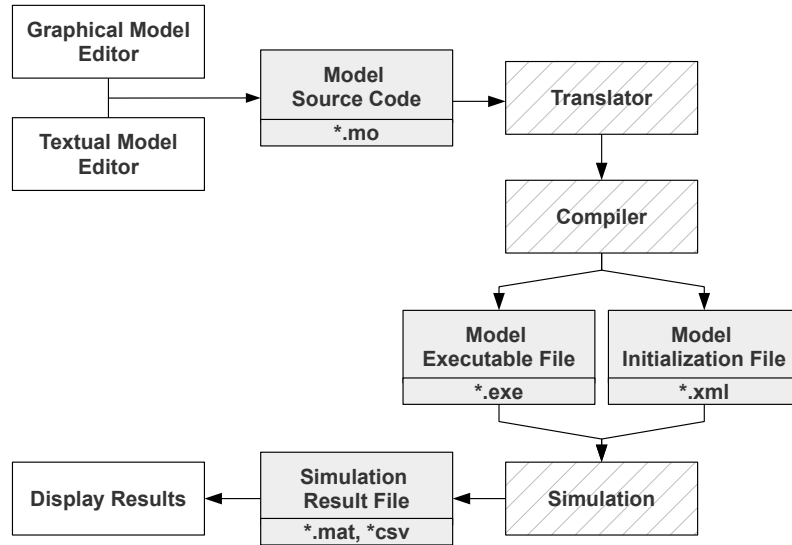
Figure 3.29: Simulation procedure with Modelica.

structure of the model in order to create a full system of equations. This is then passed to the compiler which generates binary executable and initialization files. During the simulation, the executable file reads the initial values of model parameters stored within the initialization file and performs the simulation using the OpenModelica's default Differential Algebraic System Solver (DASSL). This popular solver is well suited for simulating engineering systems which often have phenomena occurring at different time scales [119]. After the simulation is complete, the results are stored within the result file, contents of which can be viewed within OpenModelica, Dymola or Matlab.

3.7   Experimental Set-up and Parameter Identification

In order to check if the designed model is correct, the simulation results are compared to experimental data collected from a test rig. The test rig is depicted in Figure 3.30 and it consists of a PEM fuel cell stack, two gas humidifiers on both anode and cathode gas streams, pressure and temperature sensors. A water pump (not shown in the photo) provides the flow of deionized water in order to regulate the temperature of the fuel cell.

Figure 3.31 shows an array of data acquisition units which collect the measurements from the sensors and sends it to the main computer running a custom built data processing and monitoring software developed in Labview [120]. The Dynaload RBL488 Series 800W load bank [121] controlled by the computer regulates the electrical load on the fuel cell.

The fuel cell unit used in the experiments is depicted in Figure 3.32. It is a Pragma Industries Pro-RD stack which can accommodate up to 7 cells with the nominal power output of up to 470 W [122].

The bipolar plates are made of graphite with gas flow and cooling channels machined into either side of the plates as shown in Figures 3.33 and 3.34. The flow field has 7
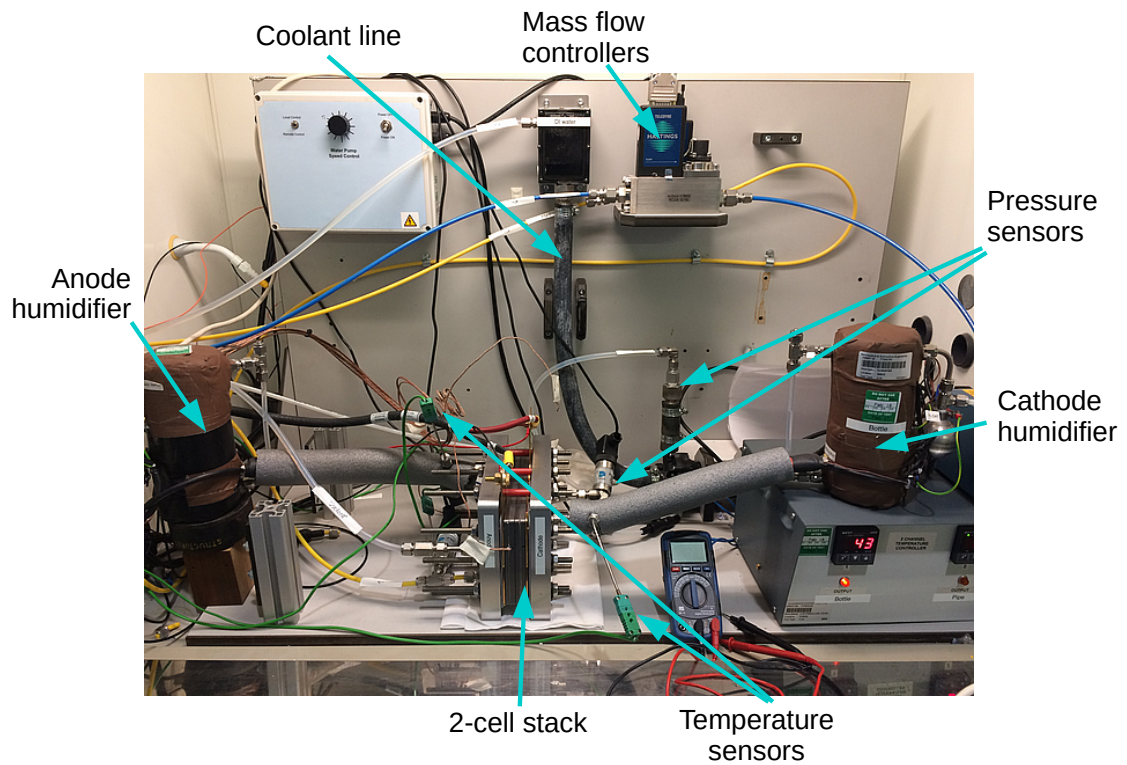
Figure 3.30: Experimental set-up with a 2-cell stack installed.
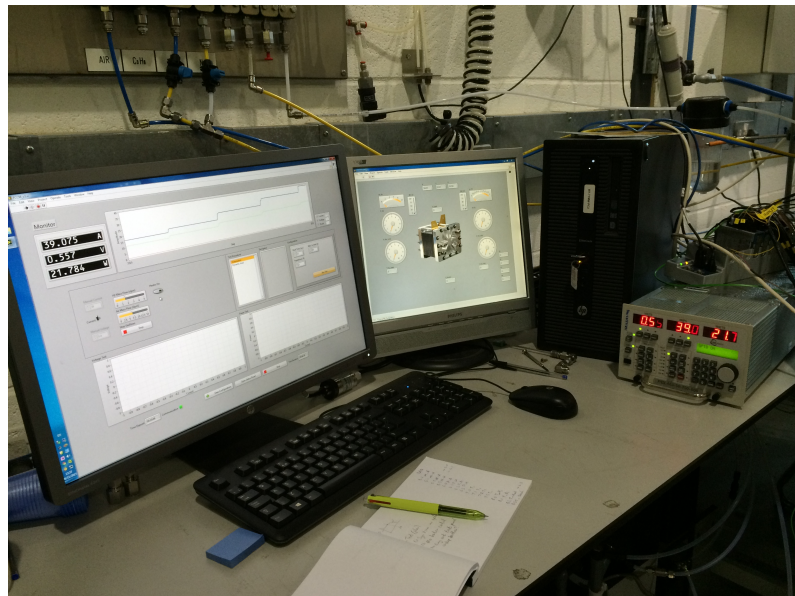
Figure 3.31: Data acquisition units, computer and the load bank.
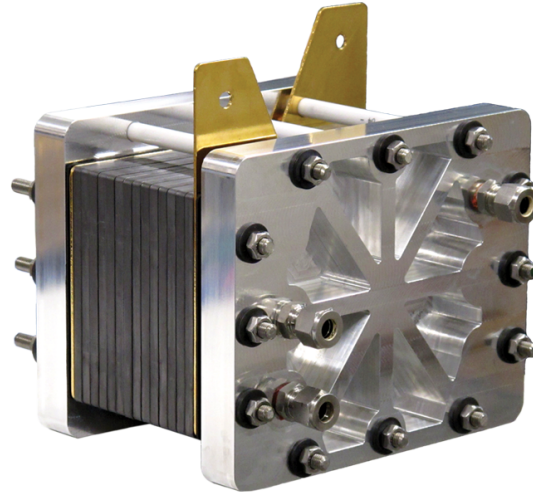
Figure 3.32: Pragma Industries Pro-RD 7-cell stack.
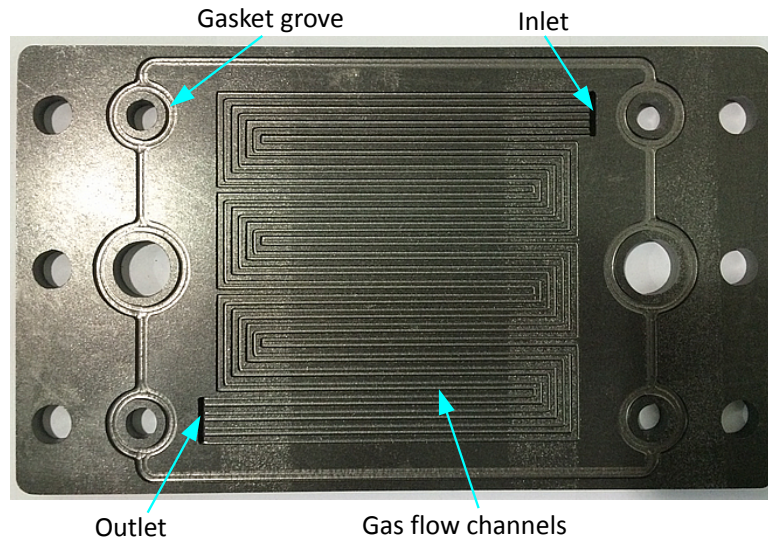
Figure 3.33: Parallel serpentine gas flow channels embedded in graphite bipolar plate.

parallel serpentine channels for both the anode and cathode sides. The geometric parameters associated with bipolar plates, gas flow and cooling channels were acquired by direct measurement while thermal characteristics of graphite were obtained from the literature. These parameters are listed in Tables 3.8 to 3.10. Additionally, the characteristics of the stack end-plates are listed in Table 3.11.

The MEA has $100\,\mathrm{cm}^2$ active area and consists of Nafion XL membrane, Sigracet 10 BC gas diffusion layer and the catalyst layer has $0.2\,\mathrm{mg/cm}^2$ Pt loading on both anode and cathode sides [122].

The first set of experiments performed was designed to determine some of the parameters of the cell not attainable from data sheets or literature. To do this, the Electrochemical Impedance Spectroscopy (EIS) technique was used. The EIS is widely used to characterize fuel cells and other electrochemical devices. The procedure consists of applying a voltage
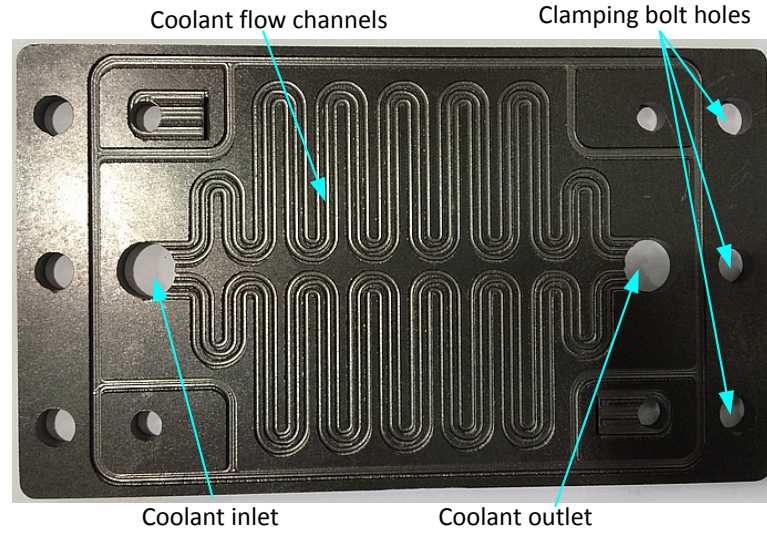
Figure 3.34: Cooling channels embedded on the back side of the graphite bipolar plate.

Table 3.8: Bipolar plate parameters.

Parameter	Value	Unit	Source
Material	Graphite		
Thickness	6×10^{-3}	m	In-situ measurement
Width	122×10^{-3}	m	In-situ measurement
Length	207×10^{-3}	m	In-situ measurement
Mass	0.243	kg	In-situ measurement
Specific heat capacity	935	J/kg K	
Thermal conductivity	52	W/m K	
Emissivity	0.9	–	
BPP thermal conductivity	120	W/mK	[123]

Table 3.9: Gas flow channels parameters.

Parameter	Value	Units	Source
Number of channels	7	–	In-situ measurement
Channel depth	1×10^{-3}	m	In-situ measurement
Channel width	1×10^{-3}	m	In-situ measurement
Distance between channels	1×10^{-3}	m	In-situ measurement

or current load of varying frequency [126]. The resulting response of the fuel cell is highly non-linear due to the fact that the impedance of the fuel cell has different dynamic responses under varying frequency of the input signal. The measurements were obtained at 10 A, 25 A and 50 A with voltage input frequency sweep from 0.2 Hz to 2000 Hz in order to observe the variation in fuel cell behaviour. During the experiments, the mass flow controllers and humidifiers for both gas lines maintained constant stoichiometry and RH. The cell operated at ambient pressure and at the temperature of 55 °C. The measured

Table 3.10: Cooling channels parameters.

Parameter	Value	Units	Source
Coolant type	De-ionized water	–	
Coolant molar mass	0.018	kg/mol	
Coolant thermal capacity	4182	J/kg K	
Coolant thermal conductivity	0.591	W/m K	
Channel depth	1×10^{-3}	m	In-situ measurement
Number of channels	6	–	In-situ measurement

Table 3.11: End plate parameters

Parameter	Value	Units	Source
Thickness	25×10^{-3}	m	In-situ measurement
Mass	1.987	kg	In-situ measurement
Specific heat capacity	500	J/kg K	
Thermal conductivity	65	W/m K	
Emissivity	0.17	–	

Table 3.12: Membrane electrode assembly properties

Parameter	Value	Units	Source
Active area	100	cm^2	[122]
GDL area	104.04	cm^2	[122]
GDL thickness (Sigracet 10 BC)	420×10^{-6}	m	[124]
GDL porosity (Sigracet 10 BC)	40	%	[124]
GDL thermal conductivity	0.3	W/mK	[124]
Exchange current density (cathode)	1×10^{-9}	A/cm^2	[16]
Pt loading anode/cathode	0.2/0.2	mg/cm^2	[122]
Membrane thickness (Nafion XL)	27.5×10^{-6}	m	[125]
Membrane dry density (Nafion XL)	1970	kg/m^3	[16]
Membrane thermal conductivity (Nafion XL)	0.13	W/mK	[]

outputs were used to create the Nyquist plots as shown in Figure 3.35. The graphs in Figure 3.35 contain important information regarding electrochemical properties of the fuel cell. For instance, the value of the double-layer capacitance C_{dl} can be estimated from the size of the impedance arcs as described by Equation 3.72 [16]:

$$C_{dl} = \frac{1}{2\pi f_{co}(R_f - R_{el})} \tag{3.72}$$

where f_{co} is the cut-off frequency, R_{el} is the combined resistance of the fuel cell and R_f is the faradic resistance. Table 3.13 summarises the values of f_{co} and R_f obtained from Figure 3.35.
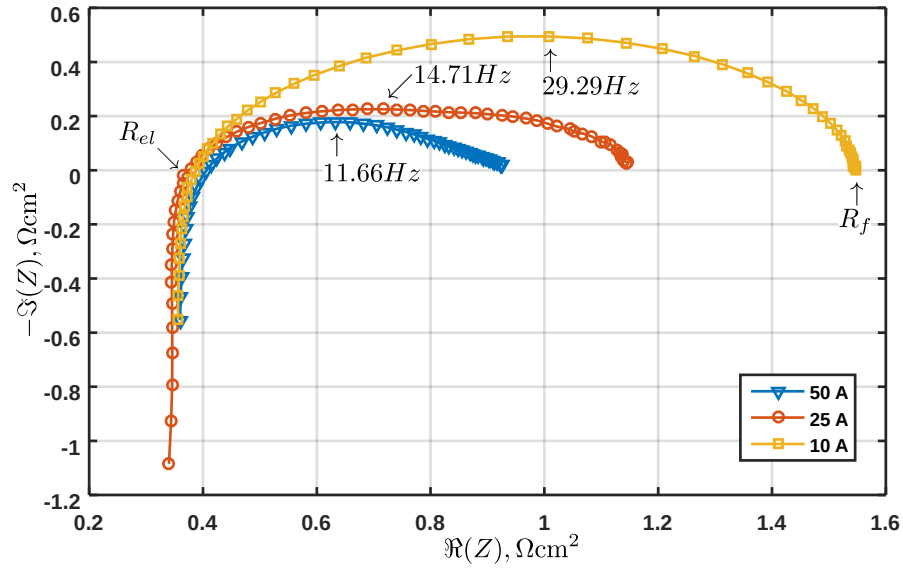
Figure 3.35: Nyquist plots of EIS measurements at 10 A, 25 A and 50 A.

Table 3.13: EIS measurements of a single cell for different current loads.

I, A	R_{el}, Ωcm^2	R_f, Ωcm^2	f_{co}, Hz	C_{dl}, F
50	0.4065	0.9256	11.66	0.026
25	0.3752	1.145	14.71	0.014
10	0.3871	1.548	29.29	0.005
Average	0.3896			0.015

Using Equation 3.72 and values obtained from Table 3.13, the average double layer capacitance $< C_{dl} >$ was found to be approximately 15 mF and the average ohmic resistance $< R_{el} >= 0.3896\,\Omega$cm^2.

A second set of measurements was used to obtain the current-voltage characteristic (also known as polarization curve) of the fuel cell. In this experiment, a two cell stack was used and steady-state operating conditions were maintained throughout. The current was gradually decreased from 75 A to 0.1 A and then increased back to 75 A in steps taking 10 s each as shown in Figure 3.36. The resulting voltage response is also shown in Figure 3.36.

Plotting voltage versus current results in the polarization curve shown in Figure 3.37. The curve provides valuable information about the performance of the fuel cell under different current loads. Matlab Curve Fitting Toolbox [127] was used to identify the values of parameters $i_0 = 3 \times 10^{-8}$ A/cm^2, $i_{loss} = 1 \times 10^{-3}$ A/cm^2, $\alpha = 0.55$.
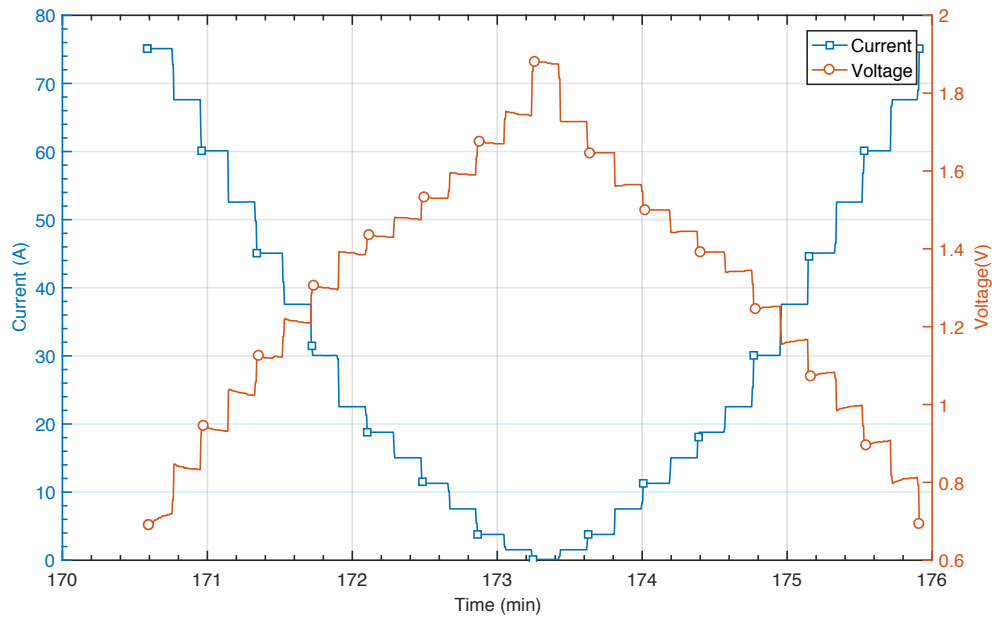
Figure 3.36: Current load profile and the resulting voltage response to obtain a polarization curve.
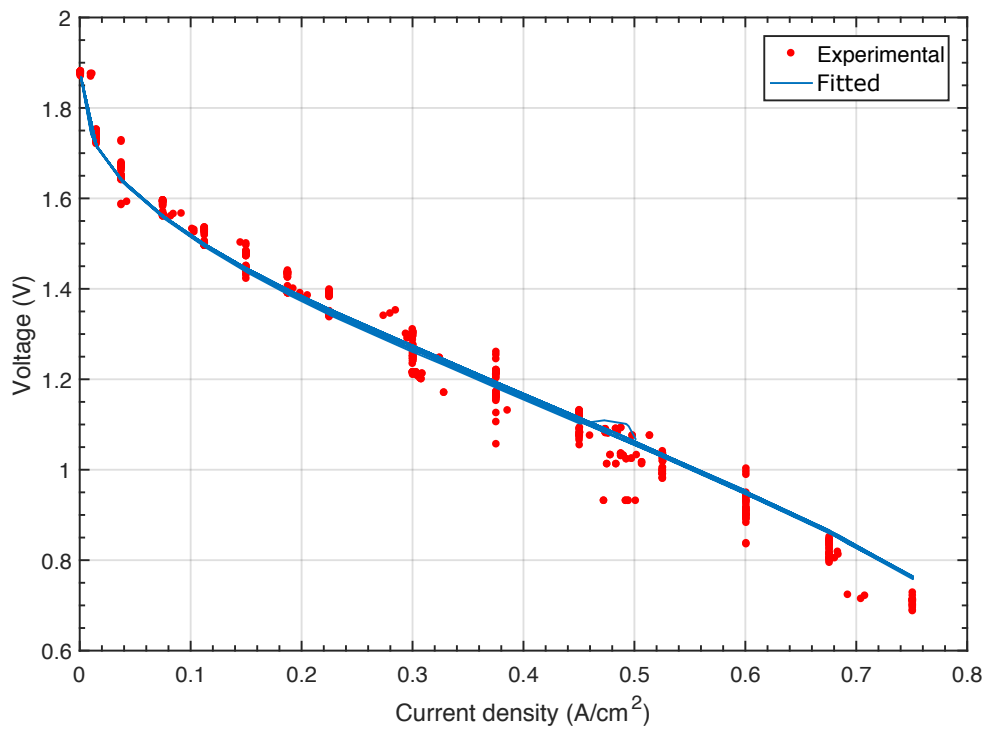
Figure 3.37: Polarisation curve of a 2-cell stack obtained experimentally and using fitted parameters.

3.8   Model Validation

On a computer with an Intel Core i5 2.2 GHz and 8 Gb RAM the model was compiled in 20 s while simulating 140 min of time as shown in Figure 3.38 took 121 s. If faster simulation performance is required, the order of the model (i.e. the total number of differential equations) can be reduced by lumping individual cells into a single block and simplifying the thermal domain dynamics by combining individual thermal masses of fuel cell layers into one. This will increase the simulation speed at the expense of model detail and accuracy.

The final experiment was designed to evaluate how the model performance compares to the experimental results. To do this, the model parameters were set to the values presented in Tables 3.8 to 3.12. During the experiment the input current was set to 5 A, 30 A and 65 A in 15 min intervals as shown in Figure 3.38. This current load profile was chosen with the aim to observe the temperature variation as a response to low (5 A), medium (30 A) and high (65 A) current loads.

The resulting experimental and simulated voltage responses are depicted in Figure 3.39a. The absolute difference between the two responses is shown in Figure 3.39b. It can be seen that during the periods 228 min to 243 min, 274 min to 289 min and 319 min to 334 min when the current load is at 65 A the error noticeably increases. This discrepancy can be explained by the fact that at higher current densities the rate of water formation is increased that leads to the flooding of the cell. However, the model was designed under the assumptions that neglect liquid water formation and, therefore, cannot account for such scenarios.

In order to evaluate how well the model represents the reality, various goodness of fit metrics can be analysed. For instance, the Mean Absolute Error (MAE) is the measure of the average distance between the measured and the approximated values which is calculated using Equation 3.73:

$$MAE = \frac{1}{n_s} \sum_{j=1}^{n_s} |y_j - \hat{y}_j| , \tag{3.73}$$
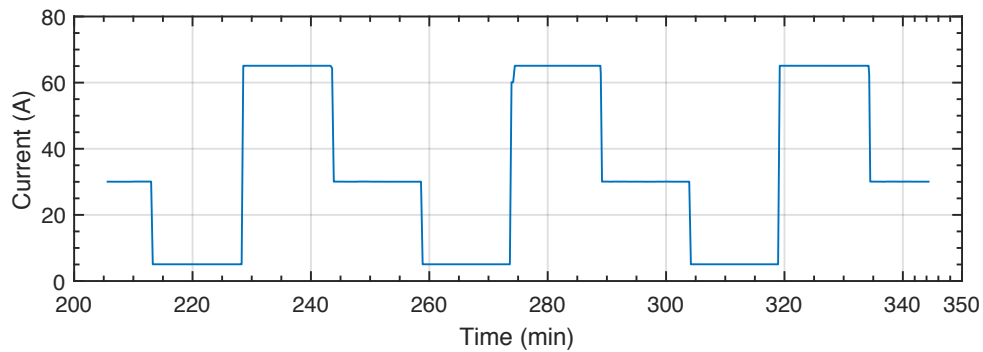
Figure 3.38: Step-wise current load.

(a)

(b)
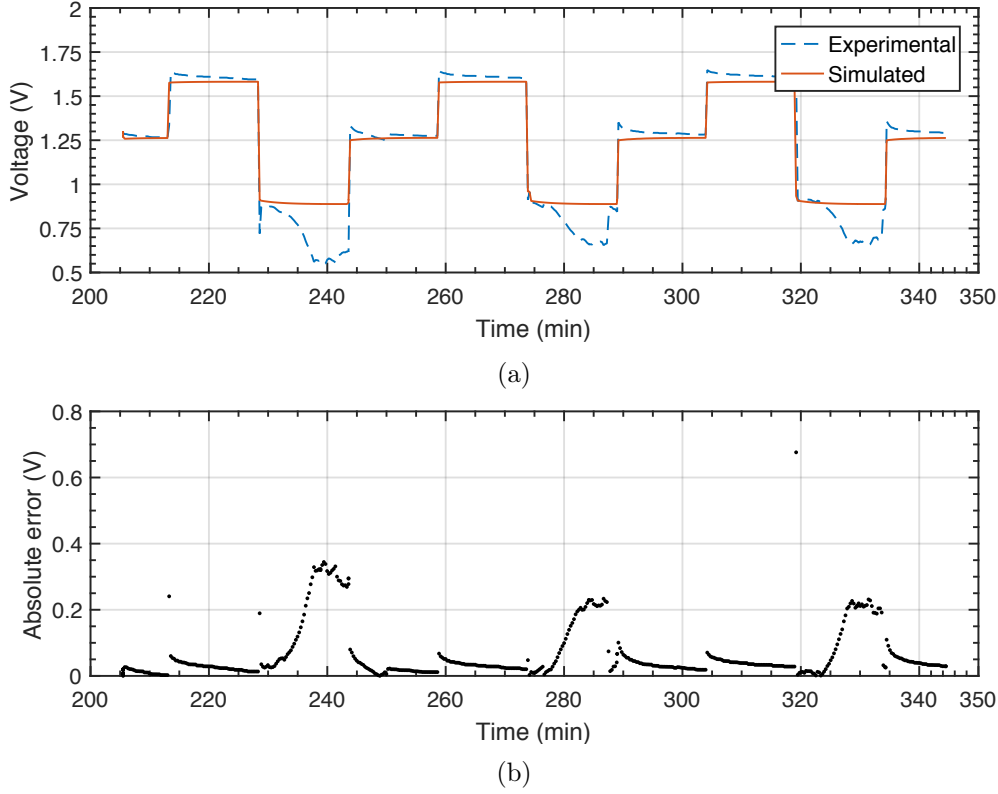
Figure 3.39: Voltage response and the corresponding absolute model error due to the step-wise current input.

where n_s is the number of samples, y_j and $\hat{y}_j$ are the experimental and simulated data points respectively. Additionally, the Mean Relative Error (MRE) evaluates the absolute error with respect to the measured values according to Equation 3.74:

$$MRE = \frac{1}{n_s} \sum_{j=1}^{n_s} \left| \frac{y_j - \hat{y}_j}{y_j} \right| \times 100\% \qquad (3.74)$$

The lower values of MAE and MRE, the better the model fits the measurements. For the data in Figure 3.39 MAE is equal to $0.0679\,\text{V}$ signifying a high degree of accuracy. However, the MRE is found to be a high $8.5149\,\%$, which reflects the discrepancies during the periods of high current loads.

The measured and simulated temperature responses due to the same current variation are depicted in Figure 3.40a. Figure 3.40b shows the values of absolute error in temperature calculations. It can be seen that the simulated temperature dynamics correspond to the experimental values well with MAE=$0.5510\,\text{K}$, MRE=$0.1668\,\%$. Both error metrics in this case signify a good agreement with experiments.
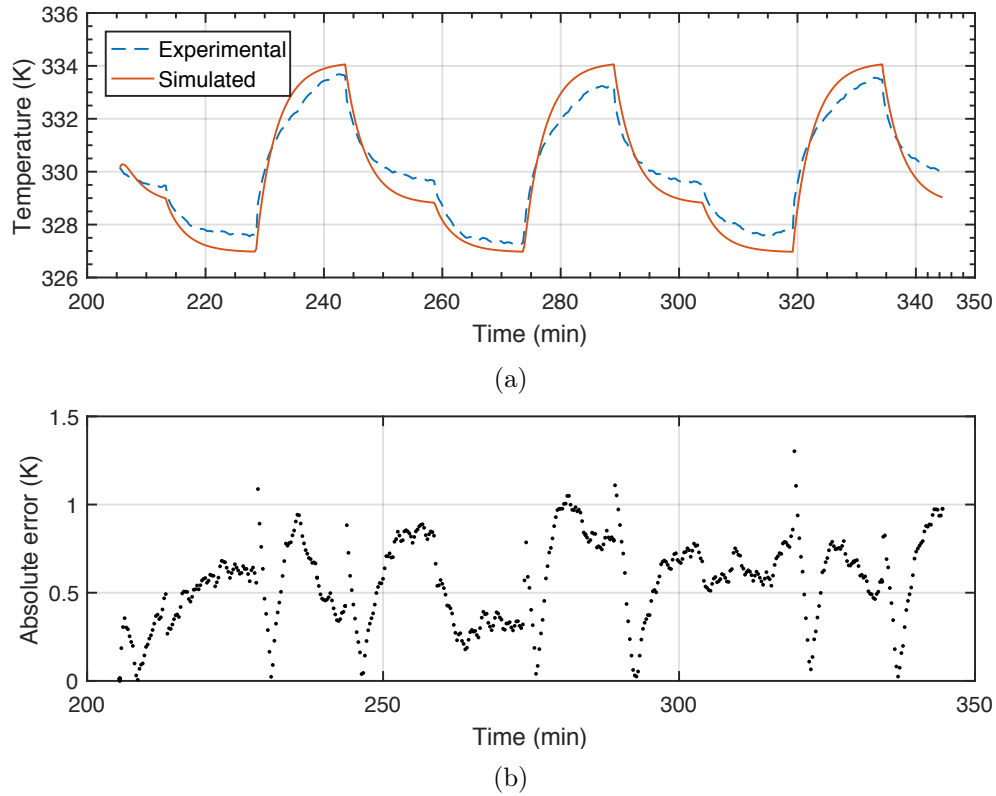
Figure 3.40: Temperature response and the corresponding absolute model error due to the step-wise current input.

3.9 Chapter Summary

The goal of this chapter was to establish the bond graph formalism for the purposes of modelling thermo-fluid systems and design a bond-graphic model of a PEM fuel cell. A general description of the approach was provided and a number of published papers on the subject was reviewed. Although bond graph formalism may seem superfluous or even arcane to a beginner at first, mastering the approach provides a unique perspective on engineering systems. The unified representation of all components allows the modeller to gain insight not only into dynamical but also into structural and causal properties of the system. It is also clear that bond graphs are very well suited for modelling fuel cell devices as demonstrated by the reviewed publications and modelling work performed in this chapter.

The designed model relies on a pseudo-bond graph representation of thermo-fluid phenomena and is implemented in Modelica modelling language. The unique feature of the model is it's hierarchical structure. Several blocks corresponding to their physical counterparts (valves, bipolar plates, cooling channels, MEAs) are created. Each block is an encapsulated model of the separate physical process and may be simulated on it's own. For example, the bipolar plate sub-model exclusively computes the pressure within the

gas flow channels and heat transfer inside the plate. This means that these physical processes can be modelled, simulated and analysed independently of other components in the system. As a result, the model topology makes the analysis of component interactions straightforward and clear.

Another innovative aspect of the proposed model is the adaptation of multi-bonds for the analysis of multi-component mixtures. This enables a streamlined graphical portrayal of the process and is highly beneficial for bond-graphic implementation of such phenomena.

In order to run model simulations, parameters were gathered from the literature and hardware descriptions. As it was demonstrated, experimental and simulation results show strong correlation between each other. Consequently, the designed model can be used as a tool for studying system behaviour in various operational scenarios, such as those demonstrated in Section 3.8.

The model can be further improved by incorporating a description of degradation mechanisms and implementation of the liquid water formation in the channels. In the rest of this thesis this model will be referred to as the Bond Graph Fuel Cell (BGFC) and in the following chapters it will be extended for reliability assessment of the fuel cell system.

Reliability Modelling of PEM Fuel Cells

4.1 Introduction

The Bond Graph Fuel Cell (BGFC) model described in Chapter 3 was designed to work under normal operating conditions without any component degradation or failures. This means that the reliability of such an idealised system is always 100 %. In reality, however, even when a fuel cell is operated under optimal operating conditions natural ageing of the fuel cell is unavoidable. Furthermore, failures of the auxiliary components can occur at unpredictable instances in time, leading to the disruption of conditions within the fuel cell and exacerbating the degradation processes. Therefore, in order to obtain a more realistic reliability estimate for the Polymer Electrolyte Membrane Fuel Cell (PEMFC) system, the model needs to take into account such deviations from the idealised behaviour. The aim of this chapter, is to discuss an approach for modelling component failure modes and degradation and extend the original BGFC model from Chapter 3 with such dynamics and create a Fault-augmented Bond Graph Fuel Cell model (F-BGFC).

This chapter is structured in the following way: Section 4.2 introduces fundamental concepts for modelling component failure behaviour. Section 4.3 is concerned with physics-based modelling of some of the key degradation mechanisms taking place within the fuel cell. Section 4.4 is focused on the discussion of estimation of the corresponding degradation parameters from the literature and experimental data. Section 4.5 provides an overview of what Petri Nets (PNs) are, their extensions and software tools. The implementation of the full F-BGFC model is described in Section 4.6. Finally, a demonstration of F-BGFC capabilities is presented in Section 4.7 through simulations of several fault scenarios and behaviours. Section 4.8 summarises and draws conclusions to this chapter.

4.2   Component Fault Models

This section presents definitions and theoretical aspects of fault modelling necessary for implementation of F-BGFC.

Although, terms *fault* and *failure* are sometimes used interchangeably in the literature, the two terms have been agreed upon to have different meanings by engineering experts. According to standard BS4778-3.2:1991, a *"fault is **a state** of an item characterised by inability to perform a required function"*. In contrast, failure is defined as **an event** that leads to *"a termination of the ability of an item to perform a required function"* [128]. This distinction is important in modelling faulty component behaviour for F-BGFC implementation.

Faults are often classified based on the origin. As such, faults may originate during design, manufacturing or assembly stages even before an item enters an active usage phase. Once the item is operational, faults related to wear-out can occur during normal operation, while wrong operation may cause faults due to excessive stress. Furthermore, faults related to maintenance, software or hardware may also take place [129].

Faults manifest themselves by altering the nominal operating condition of the system or component. This manifestation can also be classified into abrupt (step-like) or incipient (drift-like) behaviour. Abrupt faults can occur for example in gas pipelines as cracks of a welding seam and are mathematically described as proposed by [130]:

$$\mathcal{F}(t) = \begin{cases} 0, & t < t_{fault} \\ 1, & t > t_{fault}, \end{cases} \tag{4.1}$$

where $\mathcal{F}$ is the fault occurrence signature, taking values between 0 (no fault occurring) and 1 (fault has occurred). Parameter t_{fault} signifies the instance in time when the fault took place.

Incipient faults are characterised by a gradual increase of $\mathcal{F}$ during a time interval t_d. For example, gradual contamination, corrosion and plugging of heat exchanger pipes leading to the reduction of heat transfer coefficient is classed as incipient fault. Such faults can be mathematically described as follows:

$$\mathcal{F}(t) = \begin{cases} 0, & t < t_{fault} \\ (t - t_{fault})/t_d, & t < (t_{fault} + t_d) \\ 1, & t > (t_{fault} + t_d), \end{cases} \tag{4.2}$$

Figure 4.1 provides illustrative examples of the two fault types. In this diagram, both abrupt and incipient faults occur at $t_{fault} = 1$, but the incipient fault only reaches its maximum value 2 time steps later than the abrupt fault signature.

The occurrence of a fault can impose different disturbances on the process variables. Isermann [131] highlights that there are two main types of fault disturbances: additive and
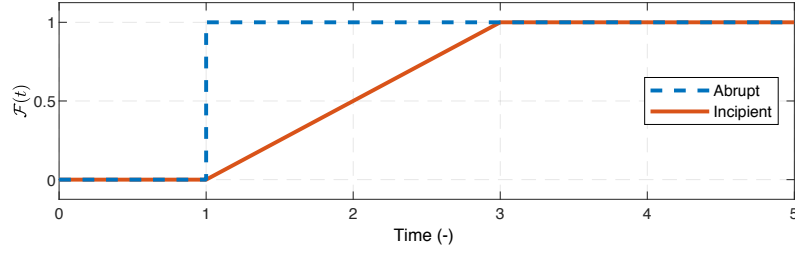
Figure 4.1: Abrupt and incipient fault signatures.

multiplicative. When a generic process variable $\mathcal{V}(t)$ is disturbed with an additive fault with magnitude m_{fa}, its altered value $\mathcal{V}_{fa}(t)$ can be expressed as follows:

$$\mathcal{V}_{fa}(t) = \mathcal{V}(t) + m_{fa} \cdot \mathcal{F}(t), \tag{4.3}$$

where m_{fa} is the magnitude parameter of the additive fault [130].

Multiplicatively disturbed variable $\mathcal{V}_{fm}(t)$ is then:

$$\mathcal{V}_{fm}(t) = \mathcal{V}(t)(1 + m_{fm} \cdot \mathcal{F}(t) - \mathcal{F}(t)), \tag{4.4}$$

where m_{fm} is the multiplicative parameter [130].

Variable t_{fault} in Equations 4.1 and 4.2 can be deterministic (i.e. it is possible to predict when a failure may occur under given operating conditions) or stochastic (i.e. such predictions are impossible). Deterministic times to failure require detailed physical models of components in order to calculate the amount of stress and degradation induced by the operating conditions. Such models are rarely available because they are difficult to create and validate. Instead, statistical modelling can be employed. This approach makes it possible to estimate the *probability* of survival or failure of a component up to a certain point in time based on historically available data.

In reliability engineering the component's time to failure is estimated using various statistical distributions such as Weibull, Exponential, Normal, Lognormal and others [132]. These continuous distributions approximate the failure rate measured in failures per unit of time and provide mathematical means of estimating the survival rates of components based solely on component's age. Corresponding formulas and illustrations for these distributions are given in Appendix B.

Among the variety of distributions, Weibull distribution is among the most commonly used in reliability analysis due to its capability to mimic many other distributions by simply adjusting its parameters [132]. The general form of a Weibull Probability Density Function (PDF) is expressed with the following 3-parameter expression:

$$f(t) = \frac{\beta}{\eta^{\beta}}(t - \gamma)^{\beta-1} \exp\left[-\left(\frac{t - \gamma}{\eta}\right)^{\beta}\right] \tag{4.5}$$

(a) PDF

(b) CDF
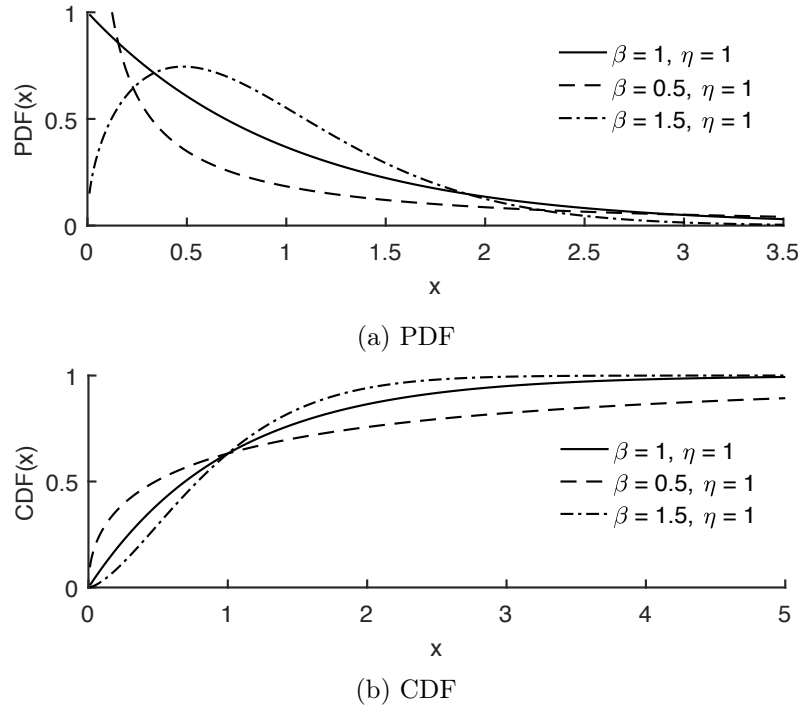
Figure 4.2: Weibull distribution for $\eta = 1$ and $\beta = 0.5, 1, 1.5$.

where β is the *shape parameter*, η is the *scale parameter* and γ is the *location parameter*. Parameter η is also known as *characteristic life* that signifies the time at which $63.2\,\%$ of the items will have failed [132]. Parameter γ determines the time interval during which no failures occur, the so-called '*failure-free interval*'. If $\gamma = 0$, the distribution is referred to as the 2-parameter Weibull (or simply Weibull) distribution. Graphically, the Weibull PDF for $\eta = 1$ and three different values of β is shown in Figure 4.2a.

In order to calculate the probability of failure before a certain time, the Weibull PDF is integrated to obtain the Cumulative Distribution Function (CDF) (also known as the *unreliability function*) as shown in Equation 4.6:

$$F(t) = 1 - R(t) = 1 - \exp\left[-\left(\frac{t - \gamma}{\eta}\right)^{\beta}\right], \tag{4.6}$$

where $R(t)$ is known as the *reliability* (or survival) function. Figure 4.2b depicts how changing β affects the CDF.

An instantaneous probability of failure of a component is called the *hazard rate* and is calculated with Equation 4.7:

$$h(t) = \frac{f(t)}{R(t)} = \frac{\beta}{t}\left(\frac{t}{\eta}\right)^{\beta} \tag{4.7}$$

The Weibull distribution is useful for describing how component hazard rate changes during its lifetime. This change is captured by the so-called *bathtub*-curve. An example of
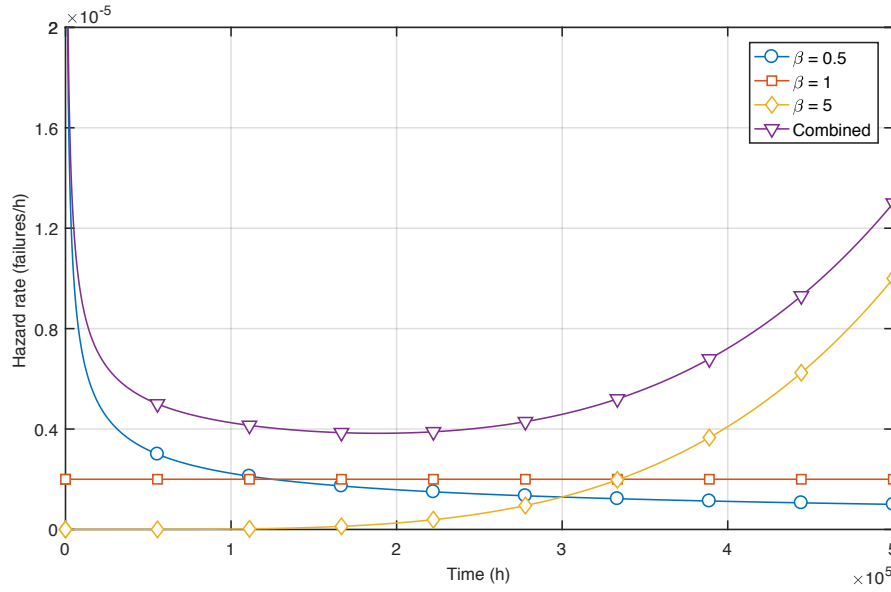
Figure 4.3: Bathtub curve representation by combination of three Weibull hazard rates with $\beta = 0.5$, $\beta = 1$ and $\beta = 5$.

such a curve for a generic component with $\eta = 5 \times 10^5$ is shown in Figure 4.3. It can be seen that from the beginning of components life to about 1×10^5 h the hazard rate rapidly decreases. This interval is commonly referred to as the period of infant mortality. Between 1×10^5 h and 3×10^5 h the hazard rate remains relatively constant and this period is known as useful life. After 3×10^5 h, the component enters the wear-out phase and the hazard rate steadily increases. Figure 4.3 also shows that the bathtub curve can be modelled by a combination of three Weibull hazard rate plots with $\beta < 1$, $\beta = 1$ and $\beta > 1$.

Once an appropriate probability distribution is selected for a component, the stochastic failures result in a discrete change of component operational state: from *'working'* to *'failed'*. Such discrete transition from one state to another can be modelled with a method called Petri nets which will be introduced in Section 4.5.

On the other hand, deterministic faults, require physics-based models of failure mechanisms in order to estimate the time to failure. Several such models of Polymer Electrolyte Membrane (PEM) fuel cell components are discussed and evaluated in the following two sections.

4.3   Fuel Cell Degradation Modelling

The process dynamics considered in the original BGFC model in Chapter 3 were only related to the operating conditions such as temperature, pressure, mass flows and electrical load, meanwhile the quantities such as catalyst active area and membrane thickness were assumed constant. As a result, under equal operating conditions, the simulated voltage output is the same at any point in time. So in order for the BGFC model to take into

account the ageing and degradation mechanisms, previously static parameters related to the properties of the Membrane Electrode Assembly (MEA) need to be made dynamic.

To differentiate between the static and dynamic quantities, superscript † is used to mark the variables that are modified to incorporate the degradation phenomena.

4.3.1   Catalyst Degradation

The activity of the cathode catalyst layer can be characterised by Equation 3.67 which estimates the magnitude of activation losses as a function of exchange i_0 and loss i_{loss} current densities and temperature T as previously outlined in Chapter 3:

$$\eta_{act} = \frac{RT}{\alpha F} \ln \left[\frac{i + i_{loss}}{i_0} \right]$$

In the BGFC model, parameters i_{loss} and i_0 were constant, but as the fuel cell ages, these parameters change in value. The rest of this section is devoted to describing the time-evolution of parameter i_0, while changes of i_{loss} are covered in Section 4.3.2. Parameter α is related to the charge transfer properties of the catalyst, however its value is often used as a fitting parameter without strict physical justification. Because of this there is no knowledge of how this parameter changes with time, so its value remains constant [87].

Exchange current density i_0 is a characteristic of the reaction rate and it is a function of temperature, partial pressure of the reactants and catalyst layer properties [15]. For the cathode electrode i_0 is expressed by Equation 4.8:

$$i_0^{\dagger} = i_0^{ref} R_f \left(\frac{p_{O_2}}{p_{O_2}^{ref}} \right)^{0.5} \exp \left[-\frac{\Delta G^*}{RT} \left(1 - \frac{T}{T^{ref}} \right) \right], \tag{4.8}$$

where $i_0^{ref} = 1 \times 10^{-9} \, \mathrm{A/cm^2}$ (according to Table 3.12) is the reference exchange current density, p_{O_2} is the partial pressure of oxygen at the catalyst layer, $p_{O_2}^{ref}$ and T^{ref} are reference pressure and temperature (according to ambient values from Table 3.7), $\Delta G^* = 66 \, \mathrm{kJ/mol}$ is the activation energy of the Oxygen Reduction Reaction (ORR). R_f is the so-called catalyst roughness factor which depends on the catalyst loading and other properties of the MEA [15]. Its value can be expressed as a ratio of the catalyst electrochemical surface area A_{ec} and nominal area of the PEMFC A_{fc}:

$$R_f = \frac{A_{ec}}{A_{fc}} \tag{4.9}$$

It is known that over time the catalyst electrochemical surface area decreases due to a process during which smaller Pt-particles agglomerate into larger ones, thus reducing the total geometric area of the catalyst particles A_{geo} [18]. The geometric and electrochemical surface areas are proportional to each other with the coefficient of proportionality is dependent on the MEA properties. Zhang and Pisu [90] assume that $A_{ec}/A_{geo} = 0.63$ and

propose a first-order Ordinary Differential Equation (ODE) to describe the degradation of the catalyst geometric area as expressed in Equation 4.10:

$$\frac{dA_{geo}}{dt} = -\Phi_A \frac{4k_1}{9V_{\text{Pt}}^2} \frac{M_{\text{Pt}}}{\rho_{\text{Pt}}} \frac{F\alpha_1}{RT} \exp\left[\frac{F}{RT}\left(\Delta\phi_c - U_1^\theta + \frac{\alpha_1 A_{geo}}{V_{\text{Pt}}}\right)\right] A_{geo}^3 \alpha_r \beta_r^2, \qquad (4.10)$$

where Φ_A is a fitting parameter, $k_1 = 10 \times 10^{-10}$ and $U_1^\theta = 1.188\,\text{V}$ are the rate constant and the standard equilibrium potential of Pt dissolution reaction respectively, $M_{Pt} = 195.1\,\text{g/mol}$ and $\rho_{\text{Pt}} = 21.45\,\text{g/cm}^3$ are the molar mass and density of Pt respectively, $\alpha_1 = 1.14 \times 10^{-10}$ is a constant parameter, parameters $\alpha_r = 1.1$ and $\beta_r = 0.038$ characterise the radius of the Pt-particle groups relative to the mean radius of the total particle population. $\Delta\phi_c$ is the phase potential difference between the electrolyte phase and the cathode phase calculated using Equation 4.11:

$$\Delta\phi_c = U_{fc} + iA_{fc}R_{ohm}, \qquad (4.11)$$

The initial value of A_{geo} is calculated using Equation 4.12 assuming that each Pt is a perfect sphere:

$$A_{geo}^0 = 4\pi r_{\text{Pt}}^2 N_{\text{Pt}}, \qquad (4.12)$$

where r_{Pt} is the average radius of Pt-particles and N_{Pt} is the number of particles in the group. Similarly, the volume of the platinum catalyst is estimated using Equation 4.13:

$$V_{\text{Pt}} = \frac{4}{3}\pi r_{\text{Pt}}^3 N_{\text{Pt}} \qquad (4.13)$$

From Equations 4.10 and 4.11 it can be seen that higher values of $\Delta\phi_c$, increase the rate of A_{geo} degradation. This, in turn, reduces the catalyst roughness factor and the exchange current density i_0. Such a decrease in i_0 consequently to the increase of activation overvoltage and drop in the voltage output.

4.3.2 Membrane Degradation

The various degradation mechanisms occurring within the polymer membrane cause it to lose its mechanical strength and charge transfer properties. Among one of the most severe degradation processes is chemical degradation at Open Circuit Voltage (OCV), which causes a significantly increased rate of fluoride (F^-) release. This leads to membrane thinning, thereby making it more susceptible to pinhole and weak-spot formation. Chandesris et al. [93] suggested the following equation to describe the rate of fluoride release v_{F^-} as a function of membrane thickness and operating conditions:

$$v_{\text{F}^-} = \Phi_{m,1} \frac{\Delta p_{\text{O}_2}}{P^{ref}} \frac{\delta_{mem}^0}{\delta_{mem}^\dagger} \exp\left[\frac{\alpha_{eq}F}{RT}U_{fc}\right] \exp\left[-\frac{\Delta G^{**}}{R}\left(\frac{1}{T} - \frac{1}{T^{ref}}\right)\right], \qquad (4.14)$$

where $\Phi_{m,1} = 1.7 \times 10^{-7}\,\mathrm{\mu g/cm^2\,h}$ is a fitting parameter, $\Delta p_{O_2} = p_{c,O_2} - p_{aO_2}$ is the difference between partial pressures of O_2 at cathode and anode sides, P^{ref} is the reference pressure, δ_{mem}^0 and δ_{mem}^* are the initial and effective thickness of the membrane, $\alpha_{eq} = 0.54$ is an equivalent transfer coefficient, $\Delta G^{**} = 75\,\mathrm{kJ/mol}$ is the activation energy of the chemical reactions causing degradation. The change in membrane thickness is then expressed in terms of v_{F^-} as follows:

$$\frac{d\delta_{mem}^\dagger}{dt} = -\Phi_{m,2}\frac{v_{F^-}}{\omega_{F^-}}\rho_{mem}, \tag{4.15}$$

where $\Phi_{m,2} = 20.8$ is a fitting parameter, $\omega_{F^-} = 0.82$ is the fraction of fluoride within Nafion and $\rho_{mem} = 0.001\,97\,\mathrm{kg/cm^3}$ is the dry density of the membrane. Equation 4.14 shows that the fluoride release rate grows exponentially with increasing voltage, which means that when the fuel cell is at OCV, the rate of membrane degradation is the highest.

The reduction of membrane thickness results in the decrease of charge transfer as well as gas diffusion paths. This leads to the increase of H_2 crossover through the membrane expressed as the loss current density $i_{loss}^\dagger$ calculated as a function of membrane thickness:

$$i_{loss}^\dagger = 2F\frac{P_{an}K_{H_2}}{\delta_{mem}^\dagger}, \tag{4.16}$$

where $K_{H_2} = 3.68 \times 10^{-16}\,\mathrm{mol/cm\,s\,Pa}$ is the permeability of H_2 through the membrane. Now, quantities $i_0^\dagger$ and $i_{loss}^\dagger$ from Equations 4.8 and 4.16 can be used to calculate a modified value of the activation losses according to Equation 4.17:

$$\eta_{act}^\dagger = \frac{RT}{\alpha F}\ln\left[\frac{i + i_{loss}^\dagger}{i_0^\dagger}\right] \tag{4.17}$$

Membrane thinning can have a positive effect on the fuel cell performance as it reduces the ionic resistance R_{ion} of the membrane, which depends on the membrane thickness δ_{mem}, membrane area A_{mem} and ionic conductivity σ as calculated by Equation 3.64. This equation is modified to take into account degrading thickness $\delta_{mem}^\dagger$ and rewritten as follows:

$$R_{ion} = A_{mem}\int_0^{\delta_{mem}^\dagger}\frac{dz}{\sigma(T,\lambda(z))} \tag{4.18}$$

The process of fluoride release is only one of several mechanisms affecting the membrane properties. In order to account for other degradation mechanisms such as mechanical and thermal stress, an empirical degradation law was implemented as suggested by Jouin et al. [87]:

$$R_{ion}^\dagger = R_{ion}\exp\left(\beta_{ion}t\right), \tag{4.19}$$

where R_{ion} is the value of membrane ionic resistance calculated using Equation 4.18 and β_{ion} is the membrane lumped degradation parameter.

Furthermore, the increase of the internal ohmic resistance of the PEMFC can also be expressed, as suggested by Jouin et al. [87] with Equation 4.20:

$$R_{ohm}^{\dagger} = R_{ohm} + \beta_{ohm}t, \tag{4.20}$$

where R_{ohm} is the initial value of the Fuel Cell (FC) ohmic resistance and β_{ohm} is the lumped degradation parameter.

Therefore, the modified expression for the ohmic losses is now according to Equation 4.21:

$$\eta_{ohm}^{\dagger} = I(R_{ion}^{\dagger} + R_{ohm}^{\dagger}) \tag{4.21}$$

4.3.3 Gas Diffusion Layer Degradation

Deterioration of the Gas Diffusion Layer (GDL) received the smallest amount of attention in the literature because it is not considered to be as critical to fuel cell performance and safety as the catalyst or the membrane. Nevertheless, structural changes within the GDLs alter the effectiveness of water removal and reactant diffusion characteristics. This increases the concentration losses as expressed by Equation 3.69:

$$\eta_{con} = \frac{RT}{z\alpha F} \ln\left[\frac{i_L}{i_L - i}\right],$$

where $i_{L,i}$ is the limiting current density as expressed by Equation 3.39:

$$i_L = \frac{zF}{RT}\frac{D_{ij}^*}{\delta_{GDL}}p_{O_2},$$

where effective binary diffusivity D_{ij}^* and GDL thickness δ_{GDL} are characterise the properties of the GDL. Since no direct, physically justified expressions of GDL degradation were found in the literature, the changes in the diffusion coefficient are calculated as suggested by Jouin et al. [87] using Equation 4.22 and δ_{GDL} is assumed constant.

$$D_{ij}^{\dagger} = D_{ij}^* + \beta_D t, \tag{4.22}$$

where D_{ij}^* is the value of diffusivity of gases through the GDL and β_D is the degradation parameter. Therefore, Equation 3.39 is modified to incorporate the degraded value of effective diffusivity:

$$i_{L,i}^{\dagger} = \frac{zF}{RT}\frac{D_{ij}^{\dagger}}{\delta_{GDL}}p_i \tag{4.23}$$

Jouin et al. [87] also suggest incorporating the increase of concentration losses by modifying Equation 3.69 with an additional degradation parameter β_B such that the modified

expression for the concentration losses is according to Equation 4.24:

$$\eta_{con}^{\dagger} = \left(\frac{RT}{z\alpha F} + \beta_B t\right) \ln\left[\frac{i_{L,i}^{\dagger}}{i_{L,i}^{\dagger} - i}\right] \tag{4.24}$$

4.3.4   Nitrogen Cross-over

Another performance reducing phenomenon occurs in fuel cell stacks with dead-end anode configuration. Since in this configuration the anode volume outlet is closed, leading to a beneficial higher H_2 utilization. However, as the cathode gases (mostly N_2) diffuse through the MEA to the anode volume the H_2 partial pressure decreases resulting in voltage output reduction. Additionally, this process leads to local starvation of the anode catalyst reaction sites, which causes carbon corrosion and further catalyst deterioration. In order to minimize the negative consequences of dead-end anode operation, periodic opening of the anode outlet valve is performed (commonly referred to as 'purging') to flush out nitrogen from the anode volume and restore high concentration of H_2.

The diffusive mass flow rate of nitrogen through the membrane $\dot{m}_{N_2,mem}$ can be described by the following equation [133]:

$$\dot{m}_{N_2,mem} = D_{N_2,mem} A_{mem} M_{N_2} \frac{\Delta p_{N_2}}{\delta_{mem}^{\dagger}}, \tag{4.25}$$

where $\Delta p_{N_2} = p_{ca,N_2} - p_{an,N_2}$ is the difference in partial pressures of nitrogen in the cathode and anode volumes, $D_{N_2 mem}$ is the diffusion coefficient of N_2 through the membrane and can be calculated from [134]:

$$D_{N_2,mem} = \frac{K_{N_2} p_{ca,N_2}}{C_{ca,N_2}}, \tag{4.26}$$

where C_{ca,N_2} is the N_2 concentration in the cathode volume and coefficient of nitrogen permeability within the membrane K_{N_2} can be calculated according to [135]:

$$K_{N_2}(\lambda, T_{cell}) = \Phi_{N_2}(0.0295 + 1.21 f_v - 1.93 f_v^2) \times 10^{-14}$$
$$\times \exp\left[\frac{\Delta G_{N_2}}{R}\left(\frac{1}{T_{ref}} - \frac{1}{T_{cell}}\right)\right], \quad (4.27)$$

where Φ_{N_2} is an empirical parameter to be identified from experiments, $\Delta G_{N_2} = 24\,\text{kJ/mol}$, $T_{ref} = 303\,\text{K}$ and f_v is the volume fraction of water inside the membrane:

$$f_v = \frac{\lambda V_w}{V_{mem} + \lambda V_w}, \tag{4.28}$$

where $V_{mem} = M_{mem}/\rho_{mem}$ and V_w is the molar volume of water within the membrane. Since the model does not include the dynamics of water condensation and evaporation, the

value of V_w is set to a constant value of 2×10^{-5}. The value of the fitting parameter Φ_{N_2} was set to 100 to represent the N_2 diffusion dynamic reported in the literature [135].

In order to include N_2 diffusion in the model, the anode bipolar plate component needs to be modified to handle the three-component mixture of gases (H_2, H_2O and N_2). To do this, the bond graph of the anode bipolar plate in Figure 3.20 was adjusted to have the same structure as the bond graph in Figure 3.19 and the necessary parameters were set to represent the inclusion of N_2 gas into the anode mixture. The MEA component was also modified by including Equations 4.25 to 4.28 within the block depicted in Figure 3.15.

4.3.5   Section Summary

This section was devoted to analysis of the theoretical foundations behind modelling deterministic faults within PEMFCs. The discussion focused on some of the well known degradation phenomena occurring within MEA constituent components: Catalyst Layers (CLs), membrane and GDLs.

The next section aims to identify the values of degradation parameters within the equations covered in this section.

4.4   Degradation Parameter Estimation

The values of degradation parameters Φ_A, β_{ion}, β_{ohm}, β_D and β_B from Equations 4.10, 4.19, 4.20, 4.22 and 4.24 need to be identified from experimental observations of a long-term durability test. For this purpose a publicly available ageing data can be used [136]. The data was obtained from a 5-cell stack with $100\,cm^2$ active area over $1150\,h$ of operation under steady-state operating conditions. During the experiment the current load was set to a constant value of $70\,A$, stack temperature maintained around $55\,°C$ with a steady coolant flow of $2\,L/min$ while anode and cathode pressures were also maintained constant at about $1.3\,bar$.

By plotting the raw measurements from this dataset it can be observed that it is noisy and contains outliers, so in order to attain better insight into the process, the data needs to be processed. Signal processing toolbox in Matlab provides the necessary tools for the task. First, any outliers can be removed by applying a Hampel filter. Next, a smoothing filter is applied to remove the noise. The resulting filtered and the raw signals of the stack output voltage are depicted in Figure 4.4. From this graph it can be observed that at the start of the durability test, the stack voltage was approximately $3.355\,V$ and over time it dropped to $3.215\,V$ at an average decay rate of $121\,\mu V\,h^{-1}$. The resulting total reduction is $0.14\,V$ or $4.17\,\%$ of the initial voltage which is well below the durability target of $10\,\%$ performance loss. Assuming the decay rate stays the same, the durability target will be reached around $2756\,h$. The dashed vertical lines in Figure 4.4 at $0\,h$, $48\,h$, $185\,h$, $348\,h$, $515\,h$, $658\,h$, $823\,h$ and $991\,h$ mark the times when the stack's state of health was characterised by current-voltage and Electrochemical Impedance Spectroscopy (EIS) measurements. It is

also worth noting that after each characterisation procedure, the voltage output recovers by approximately 29 mV on average. The eight polarization curves are shown in Figure 4.5
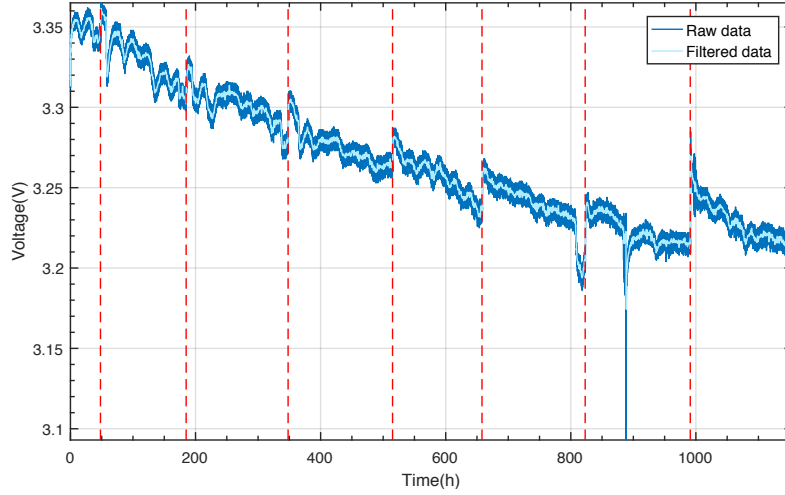
Figure 4.4: Voltage evolution over 1150 hours of steady-state operation.

and it can be clearly seen that the overall shape of the initial curve has barely changed with time. The most significant observation is the gradual shift downward almost parallel to the initial curve. Fowler et al. observed very similar changes in polarisation curves during their experiments and they concluded that this shift in the curve is due to the loss of reaction activity due to catalyst deterioration [137]. The changes in charge transfer and mass transport properties of this stack are minimal, as the shape of the polarization curve barely changes in the corresponding regions.
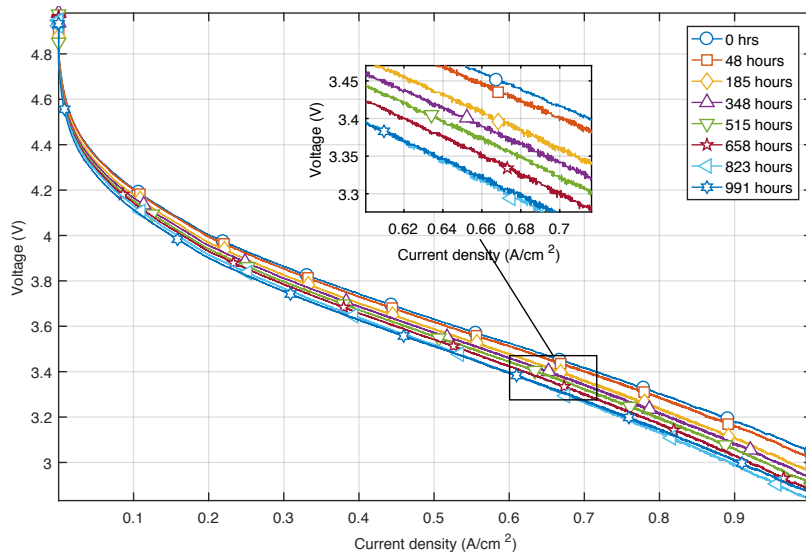
Figure 4.5: Polarization curves at 0 hours and the change over 991 hours.

Table 4.1: Estimated initial parameter values for the 5-cell stack.

Symbol	Value	Units	Source
A_{fc}	100	cm^2	[136]
α	0.55	–	Estimated
R^0_{ohm}	0.41	Ω/cm^2	Estimated
$N_{\mathrm{Pt},j}$	2.24×10^{16}	–	Estimated
$r_{\mathrm{Pt},j}$	2.6×10^{-7}	cm	[90]
A^0_{geo}	19 005	cm^2	Estimated
V_{Pt}	1.6×10^{-3}	cm^3	Estimated

The EIS measurements collected before and after each polarization curve also confirm the loss of catalytic activity. The Nyquist plots obtained from these measurements are depicted in Figure 4.6. It can be noticed that the region of ohmic resistance barely changed during the durability test and remained around $4.89\,\mathrm{m}\Omega$, while the radii of the low frequency arcs of the impedance spectra were increasing with time. This radii increase is attributed to the loss of catalytic activity.
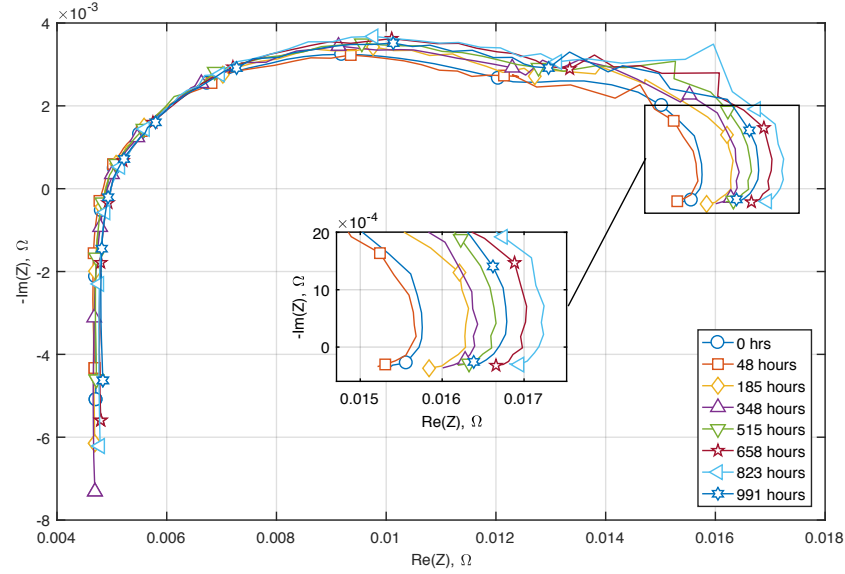
Figure 4.6: Nyquist plots of EIS measurements at 0 hours and the change over 991 hours

The initial polarization curve of Figure 4.5 can be used to estimate the initial values of parameters for Equations 4.10, 4.12, 4.13 and 4.20. The initial values for parameters estimated by manually adjusting and with the help of Matlab's Curve Fitting Toolbox are listed in Table 4.1.

Figure 4.7 shows how the fitted curve obtained by using the parameters listed in Table 4.1 compares to the experimental current-voltage characteristics of the stack. It can
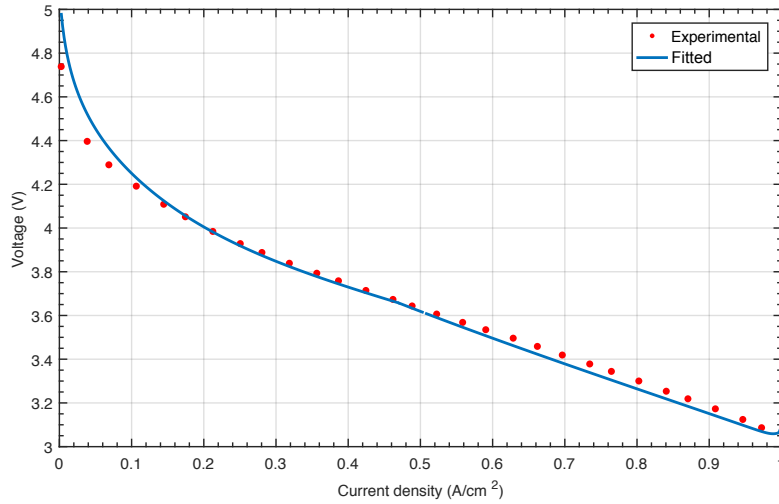
Figure 4.7: Fitted and experimental polarization curves of a 5-cell stack.

Table 4.2: Estimated degradation parameter values for the 5-cell stack.

Symbol	Value	Units	Source
β_{ohm}	5×10^{-5}	$\Omega \, h^{-1}$	Estimated
β_{ion}	5×10^{-5}	h^{-1}	Estimated
β_B	1×10^{-6}	$V \, h^{-1}$	Estimated
β_D	1×10^{-6}	$\frac{cm^2}{s} h^{-1}$	Estimated
Φ_A	25×10^5	–	Estimated

be seen that the two curves are well correlated and the corresponding goodness of fit metrics (calculated using Equations 3.73 and 3.74) demonstrate very good agreement: Mean Absolute Error (MAE)=0.03 V, Mean Relative Error (MRE)=0.88 %.

Using the parameters from Table 4.1 the degradation parameters can also be estimated by fitting the simulated voltage response to the actual voltage signal over 1100 h. Table 4.2 contains the fitted degradation parameters.

Using parameters listed in Table 4.2 the simulated voltage fits the experimental data exceptionally well with MAE being only 8×10^{-3} V, which translates into MRE of 0.25 % as shown in Figure 4.8.

4.4.1   Section Summary

The aim of this section was to identify the values of the degradation parameters within equations presented in Section 4.3. This was necessary in order to align theoretical derivations with experimental measurements. This was achieved by utilising publicly available data-set of a 5-cell PEMFC stack. First, initial values of the electrochemical parameters were identified from the stack polarization curve at the beginning of life. Next, the simulation was performed under constant temperatures, pressures, mass flows and current
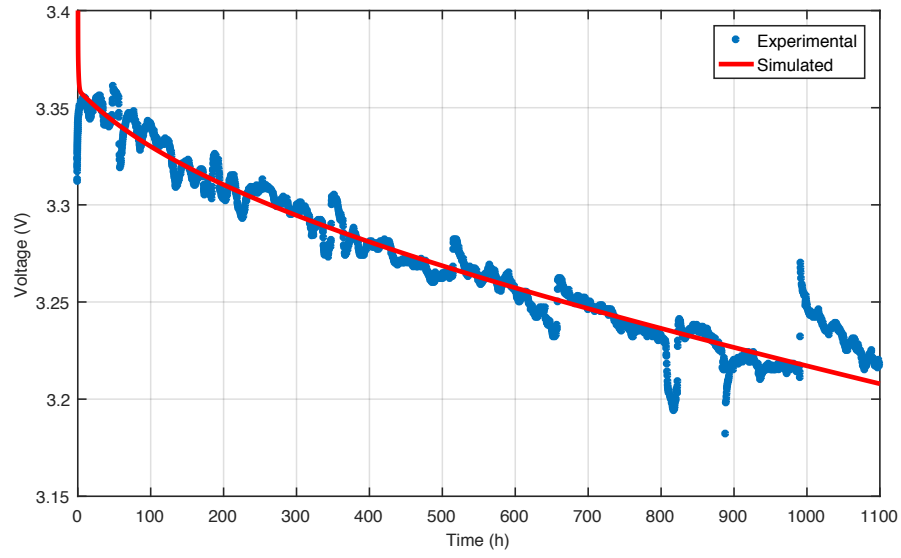
Figure 4.8: Simulated and experimental voltage degradation of a 5-cell stack over $1100\,\mathrm{h}$ of operation.

load of $70\,\mathrm{A}$. As shown in Figure 4.8 the simulated degradation output fits experimental measurements very well with calculated error metrics sufficiently low.

4.5 Petri Nets Method

PNs are a graphical and mathematical modelling tool for representation of a variety of discrete systems and processes. They were first devised by Carl Adam Petri in his PhD dissertation for modelling chemical reactions. Since then the method has been widely used in a wide range of applications including reliability and maintainability analysis [35, 138].

In general, PNs are defined as directed, weighted bipartite graphs with two types of nodes: *places* and *transitions*. The arcs of a Petri net are always between places and transitions, but never between nodes of the same type.

Graphically, places are represented by circles and transitions by squares or bars. The weighted arcs are labelled with their weight (a positive integer). The places represent different conditions or states of the system, while transitions serve as rules or events controlling the changes of state.

The overall state of the system is characterised by a procedure called '*marking*' which assigns a non-negative integer to each place of the net. A place marked with an integer m, is said to contain m '*tokens*'. Tokens may represent quantities of resources or logical conditions and are drawn as black dots within the places. In mathematical terms, a Petri net is a 5-tuple: $PN = \{P, T, A, W, M_0\}$, where:

$P = \{p_1, p_2, ..., p_m\}$ is the finite set of places,

$T = \{t_1, t_2, ..., t_m\}$ is the finite set of transitions,

$A \subseteq (P \times T) \cup (T \times P)$, is the set of arcs,

$W : A \to \{1, 2, 3, ...\}$ is the weighting of each arc,

$M_0 : P \to \{0, 1, 2, ...\}$ is the initial marking.

A basic PN with a transition between two places is depicted in Figure 4.9. In this diagram the input place of the transition is marked with one token, while the output place is not marked. The change of system state is determined by transition's '*firing*' rules:
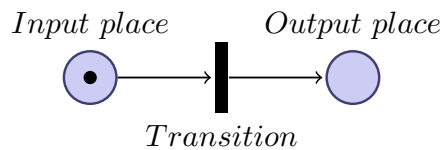
Figure 4.9: A basic Petri net with two places and a transition.

1. A transition is said to be '*enabled*' when all input places are marked with at least $w_{ia}(p, t)$ tokens, where $w_{ia}(p, t)$ is the weight of each input arc ia.

2. When all firing conditions are met and a transition is enabled it may '*fire*'. Firing of the transition removes $w_{ai}(p, t)$ tokens from the input places and marks all the output places with $w_{ao}(t, p)$ tokens, where $w_{ao}(t, p)$ is the weight of each output arc.

An example illustrating the transition firing rules applied to weighted arcs is shown in Figure 4.10. The PN depicted in Figure 4.10 represents the redox reaction of Equation 1.5

$(2\,H_2 + O_2 \longrightarrow 2\,H_2O)$, where places P_{H_2}, P_{O_2} and P_{H_2O} correspond to quantities of the corresponding chemical species. The weights of the arcs are assigned according to the stoichiometric coefficients of the reaction. Tokens within places P_{H_2}, P_{O_2} and P_{H_2O} represent units of chemical species. Transition t is enabled once at least two tokens are present in P_{H_2} and at least one is available in P_{O_2}, as shown in Figure 4.10a. Transition t removes two tokens from P_{H_2} and one from P_{O_2} to generate two tokens in place P_{H_2O}, as shown in Figure 4.10b.

(a) Transition t enabled   (b) Transition t fired
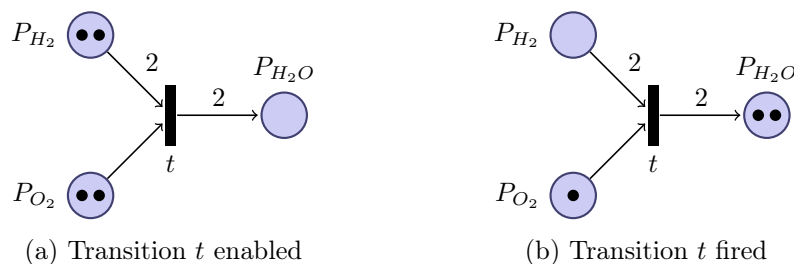
Figure 4.10: Petri net transition firing example

The logical rules of transition firing can be altered by incorporating inhibit arcs – a special type of arc that enables transitions to fire only when the corresponding input place contains less tokens than the weight of the inhibit arc. In other words, if the weight of inhibit arc is unity, the inhibited transition will only fire when the input place contains zero tokens. Pictorially, an inhibit arc is shown with a circle instead of an arrow head.

4.5.1   Petri Net Extensions

There are many additional properties that can be added to the Petri nets to expand their modelling capabilities and flexibility.

4.5.1.1   Timed Petri Nets

The basic definition of the PN provided above can be augmented with the concept of time. Transitions of such '*timed*' PNs must stay enabled for a certain period of time before they can fire. This allows the creation of Petri net models more relevant to real processes. Furthermore, the firing intervals can be sampled from a random probability distribution. PNs in which the firing interval is defined by such a random variable are called Stochastic Petri Nets (SPNs).

4.5.1.2   Coloured Petri Nets

In modelling various processes with Petri nets, tokens often mean different quantities such as resources, goods or people. So it is desirable to incorporate additional information about these quantities into the model. Therefore the classical definition of tokens is extended with '*colours*' (or attributes) such as ID number, name or date. In a Coloured Petri Net (CPN)

(a) Discrete   (b) Continuous
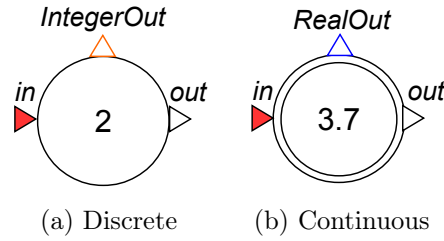
Figure 4.11: Petri net places in PNlib 2.0.

transitions can manipulate the data stored within tokens and can have different firing rules depending on the token colour.

Volovoi [139] proposed a special type of coloured tokens for modelling degradation processes called '*ageing*' tokens. These tokens hold information about historic degradation processes that occur in the system.

4.5.1.3   Hierarchical Petri Nets

When representing complex systems with Petri nets, the overall models become large and difficult to maintain. So in order to make it easier to manage large PNs, it is advantageous to separate the large net into smaller sub-nets and employ hierarchy within the Petri net.

4.5.2   Petri Net Tools

Several programs dedicated to PN modelling can be found on-line, but they are often limited in functionality, so many researchers prefer to code a required ad-hoc implementation of PNs [43, 44, 45], which can be a time-consuming and error-prone endeavour.

Since the BGFC model was already implemented in the Modelica environment, it was desirable to have the Petri net functionality implemented within the same environment. Thankfully, Modelica language has the capability for the implementation of states and transitions. One open-source library called PNlib implemented by Proß and Bachmann [140] contains a set of classes for representation of Generalised Stochastic Petri Net (GSPN) and can be easily extended with additional functionality. It was initially developed for modelling biological systems, but the implementation is generic enough to be used in other applications. The library includes two types of places: discrete and continuous (illustrated in Figure 4.11). Each place has input and output ports (labelled 'in' and 'out' in Figure 4.11) for connecting input and output arcs respectively. Additionally, an external connector port is used to output the current marking of the place, what can be used to transfer the current state of the PN to other parts of the model. Since the discrete places can only contain any non-negative integer number ($\mathbb{N} = 0, 1, 2, ...$) of tokens this external connector (labelled 'IntegerOut') transmits integer values. The discrete place in Figure 4.11a is shown to contain 2 tokens, so the value of IntegerOut is also 2. Continuous places, on the other hand can store any non-negative real number ($\mathbb{R}$) of tokens. Correspondingly, the external connector (labelled 'RealOut') transmits real values. The

(a) Discrete   (b) Stochastic   (c) Continuous
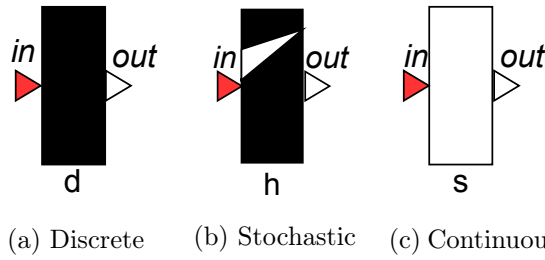
Figure 4.12: Petri net transitions in PNlib 2.0.

(a) Test arc   (b) Inhibit arc   (c) Read arc
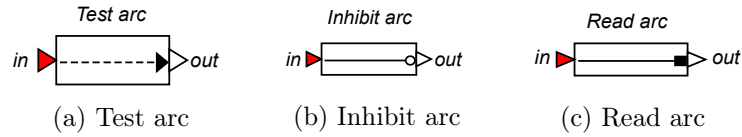
Figure 4.13: Petri net arcs in PNlib 2.0.

continuous place in Figure 4.11b contains 3.7 tokens, so the value of RealOut is also 3.7. Furthermore, each place has a set of parameters such as initial, minimum and maximum number of tokens, reset conditions, and others.

The library includes three types of transitions as depicted in Figure 4.12: discrete, stochastic and continuous. Similar to the places, each transition in PNlib has input/output ports and a set of parameters that determine their firing interval. The discrete transitions (illustrated Figure 4.12a) fire after a pre-determined amount of time defined by a parameter d. Stochastic transitions perform a similar function, but fire after a period of time obtained from a statistical distribution. The firing interval of the stochastic transition depicted in Figure 4.12b is governed by an exponential distribution with parameter h. The continuous transitions (Figure 4.12c) allow the flow of tokens between the continuous places with a speed determined by parameter s. Furthermore, each transition has a set of parameters that specify additional firing conditions and the weights of the input and output arcs.

Alongside regular arcs, PNlib includes three additional types of arcs as shown in Figure 4.13: test, inhibit and read. Test arc (Figure 4.13a) only allows a transition to fire when the marking of a place exceeds a certain predefined value. Inhibit arcs (Figure 4.13b) allow a transition to fire only when the marking of a place is lower than some predefined value. Read arcs (Figure 4.13c), however, only pass the information regarding a place marking, but cannot transfer tokens under any conditions.

All in all, the PNlib library provides all the basic building blocks for implementing GSPNs, making it an ideal tool for modelling hybrid dynamic systems, since the interaction between the continuous physical process and the discrete state transitions can be implemented seamlessly within a single Modelica model.

The next section is dedicated to the application of the degradation modelling concepts from Sections 4.2 to 4.5 to create the Fault-augmented BGFC.

(a) One failure mode.   (b) Two failure modes.
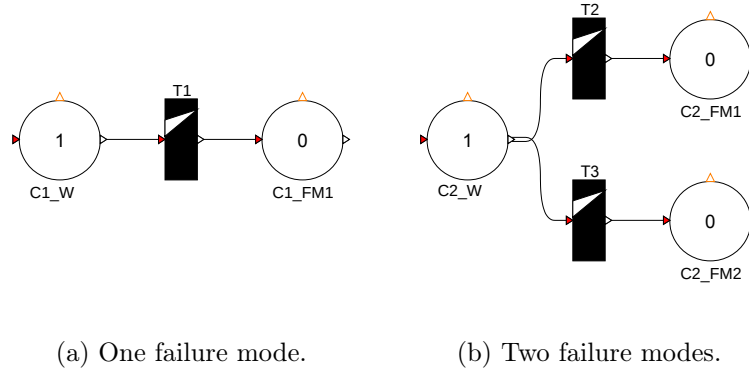
Figure 4.14: Petri net representation of generic component failure modes using PNlib.

4.6   Implementation of the Fault-Augmented Model

Deterministic degradation is accounted for by encoding Equations 4.17, 4.21, 4.24 and 4.25 into the relevant bond-graphic blocks within the model. Parameter values are set according to Tables 4.1 and 4.2.

Stochastic behaviour of auxiliary components is modelled using the PN method in accordance to reliability engineering nomenclature outlined in Section 4.2 and British Standard 62551:2012 [35]. Component operational states (working or failed) are represented by PN states, while failures are modelled as transitions.

An illustrative example in Figure 4.14a contains Petri net states C1_W and C1_FM1 representing working (W) and failed (FM1) states of a generic component C1. When stochastic transition T1 fires it moves the token from C1_W to C1_FM1, thus representing a failure event.

In [35], however, components are assumed to have only one *'failure mode'*, i.e. components fail in only one certain way. In reality, many components can have multiple failure modes, each of which affects the overall system in a different way. If a component C2 has two failure modes (e.g. FM1 and FM2), PN representation in Figure 4.14b can be utilised. When either of the transitions T2 or T3 fires, the token marking working state C2_W will be moved to the state corresponding to a respective failure mode (C2_FM1 or C2_FM2). Depending on a specific component, additional failure modes can be added in a similar fashion.

In order to introduce the interaction between the PN modules and the deterministic model, the state of the PN needs to be translated into a set of the disturbed variables $\mathcal{V}(t)$. To do that, Equations 4.1 and 4.2 are implemented in Modelica using a block called TriggeredTrapezoid from Modelica Standard Library (MSL) located in package Modelica.Blocks.Logical. This block has one boolean input and one real output, but the output of a discrete PN place is given in integer values, so an integerToBoolean conversion block is added.
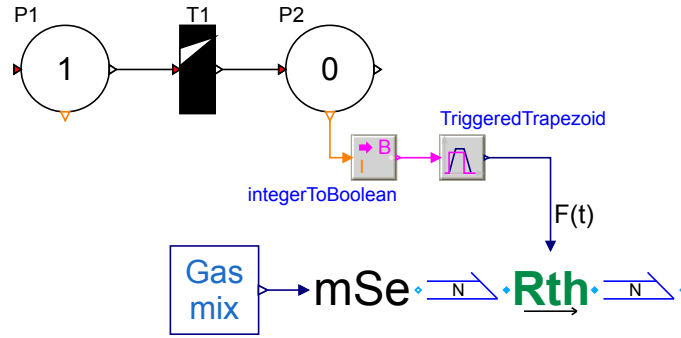
Figure 4.15: Arrangement of blocks to translate the PN states into the fault behaviour.

The resulting arrangement of blocks to translate the state of the PN module into the BGFC model is shown in Figure 4.15. This illustrative example shows how the state of a H_2 solenoid valve within fuel supply sub-system can be influenced by the PN module. Since the valve has only one failure mode, it is modelled by a PN module with one transition T1 and two states P1 and P2. The state of the component is interpreted from the presence or absence of token within P2 through blocks integerToBoolean and TriggeredTrapezoid, which generates the fault signal $\mathcal{F}(t)$. This signal serves as an input to a valve represented by bond-graphic block **Rth** and increases the valve resistance and consequently reducing its throughput.

Individual PN modules like those depicted in Figure 4.14 are implemented for each Balance of Plant (BoP) component in PEMFC system according to the Failure Modes and Effect Analysis (FMEA) table from [27]. Table 4.3 contains the list of components grouped by the corresponding sub-system and their respective failure modes.

The default transition classes in PNlib allow sampling from the exponential distribution, but in order to allow for generality, the Weibull distribution was added. The stochastic transition firing interval t_{fire} can be defined by rearranging and taking the logarithm of both sides of Equation 4.6:

$$t_{fire} = \eta \times [-\ln(R(t))]^{1/\beta} + \gamma, \tag{4.29}$$

where $R(t)$ takes values in the interval $[0, 1]$. The values of parameters β and η are gathered from the literature [141, 142] and listed in Table 4.3 along with the corresponding failure modes for the components. The values of parameter γ are set to be 0 for all the components under the assumption that every component begins ageing at the start of system exploitation.

It is important to note that $\beta = 1$ for all the failure modes due to the fact that the reliability data is usually gathered under the assumption of constant failure rate. This assumption is justified if early life failures are eliminated by extensive testing before installation, while end-of-life failures are also eliminated because a component is assumed to be

Table 4.3: Component failure modes.

Sub-system	Component	Failure Mode	β	η, 10^6 h	Source
Fuel supply	H$_2$ safety relief valve	Fails to function	1	0.2	[142]
	H$_2$ solenoid valve	Fails to function	1	0.2	ibid.
Fuel processing	Low-pressure H$_2$ filter	Restrict or limit flow	1	1	ibid.
	H$_2$ humidifier	Leak or rupture	1	0.004	ibid.
		Leak or rupture	1	0.01	ibid.
Air supply	Air blower	Fails to function	1	0.04	ibid.
	Air compressor	Fails to function	1	0.008	ibid.
	Air flow meter	Fails to function	1	0.05	ibid.
	Air line	Leak or rupture	1	1	ibid.
Air processing	Air filter	Restrict or limit flow	1	1	ibid.
		Hole in filter media	1	1	ibid.
	Air humidifier	Leak or rupture	1	0.004	ibid.
Thermal Management	Radiator	Restrict or limit flow	1		ibid.
		Fails to function	1		ibid.
	Coolant pump	Fails to function	1	0.1	[141]
		Leak or rupture	1	0.01	[142]
	Coolant line	Leak or rupture	1	1	ibid.

replaced before it reaches that point in its lifetime. Additionally, this reliability data is obtained from several reliability databases such as OREDA, NPRD and MIL [143, 144, 145] which contain reliability metrics for a generic set of components without adjustment of a specific field of application.

Each BoP component listed in Table 4.3 is represented with a separate PN module with $N+1$ places and N transitions, where N is the number of failure modes of the component. Figure 4.16 shows all 13 modules grouped into three main sub-systems: air supply and processing, fuel supply and processing and thermal management.

Different failure modes of different components within the same sub-system can have detrimental effect on the same variable in the system. For example, blockages of the air filter or pipe would have similar effect to a leak in the humidifier in terms of reducing the air flow rate. Therefore, the failure signal $\mathcal{F}$ can be chosen from all the failure modes affecting the same process variable and passed to the BGFC model. In order to pass only one signal to the affected bond-graphic block, blocks labelled multiSwitch and extractor are included in Figure 4.16. Block multiSwitch determines which failure mode of which component was activated depending on its index, while extractor block passes the value of $\mathcal{F}$ corresponding to that index to the BGFC model.

(a) Air supply and processing sub-system.

(b) Thermal management sub-system.
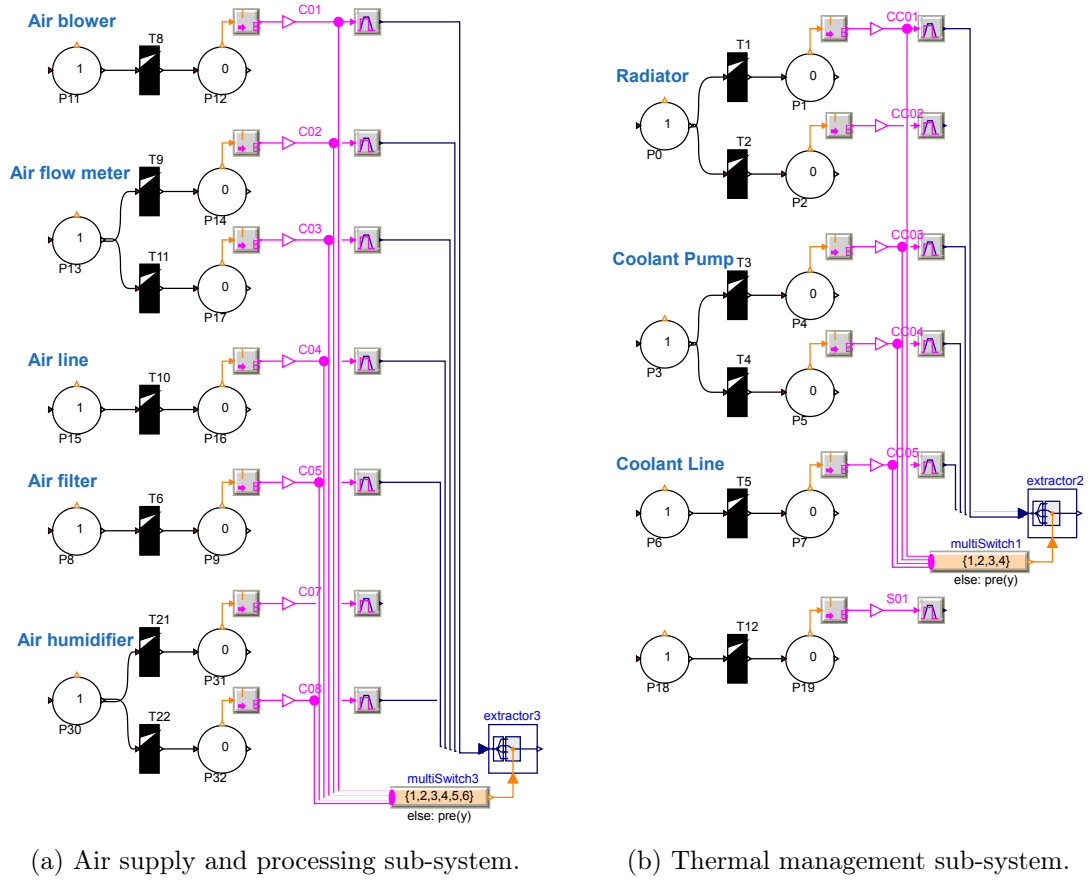
Figure 4.16: Petri net modules for auxiliary sub-systems.

(c) Fuel supply and processing sub-system.
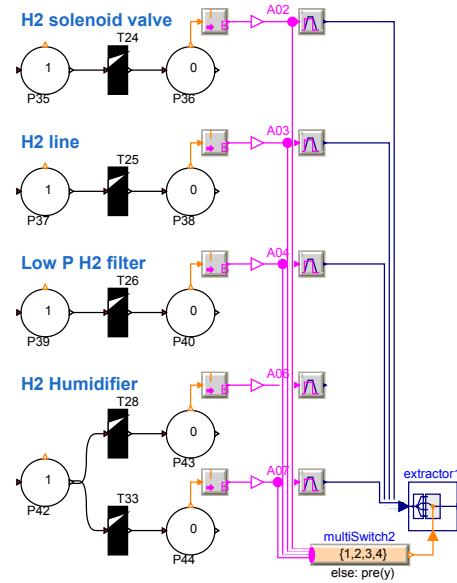
Figure 4.16: (Cont.) Petri net modules for auxiliary sub-systems.

All the PN modules in Figure 4.16 were encapsulated into a single block Failure Modes
as seen in Figure 4.17, which shows the complete F-BGFC model. Additionally, a pulse-
signal was added to control the state off the purge valve, which periodically opens and
closes it.
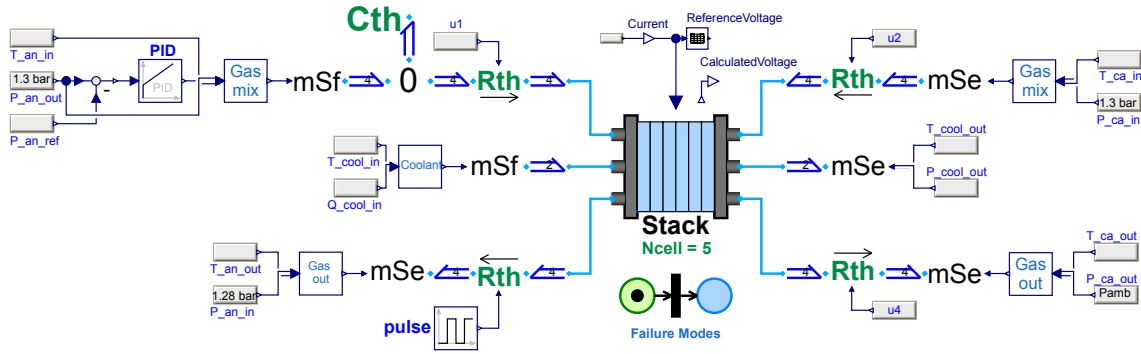
Figure 4.17: Full diagram of the Fault-augmented Bond Graph Fuel Cell (F-BGFC) model.

In summary, the resulting F-BGFC model incorporates two sub-models: physics-based
model of the FC stack that includes degradation mechanisms within the MEA and the
event-based PN model of the stack auxiliary sub-systems. The interaction between the sub-
models is implemented by translating the state of the PN modules into the corresponding
physical variables such as flow rate, pressure, temperature and current load by means of
supplementary blocks (TriggeredTrapezoid). In other words the designed PN modules do
not represent actual physical dynamics of each modelled component (pumps, valves, filters,
etc.) but rather function as an interpreters of the component working/failure states into
the change of physical variables within the stack. Subsequent change in physical variables
affects the operational regime of the fuel cell, thereby changing the degradation rates of
the catalyst, membrane, the gas diffusion layer and the rate of nitrogen cross-over.

For example, events resulting in the reduction of the coolant flow rate (e.g. failure
of the coolant pump or leaks in the coolant line) can result in the increase of stack tem-
perature. Such a rise in the stack temperature will not only boost the rate of the redox
reaction, but also increase the rate of catalyst and membrane degradation (as described
by Equations 4.10 and 4.15).

The following section will show several examples of failure scenarios that are possible
to be simulated using the full F-BGFC model.

4.7   Simulation of Failure Scenarios

This section demonstrates simulation outputs of several scenarios and degradation mech-
anisms obtained from the F-BGFC model. All the simulations discussed in this section
use the same workflow and initialization values as previously discussed in Section 3.6. Cell
dimensions and material parameters were left unchanged, but stack sizes different in order
to show flexibility of the modular modelling approach.
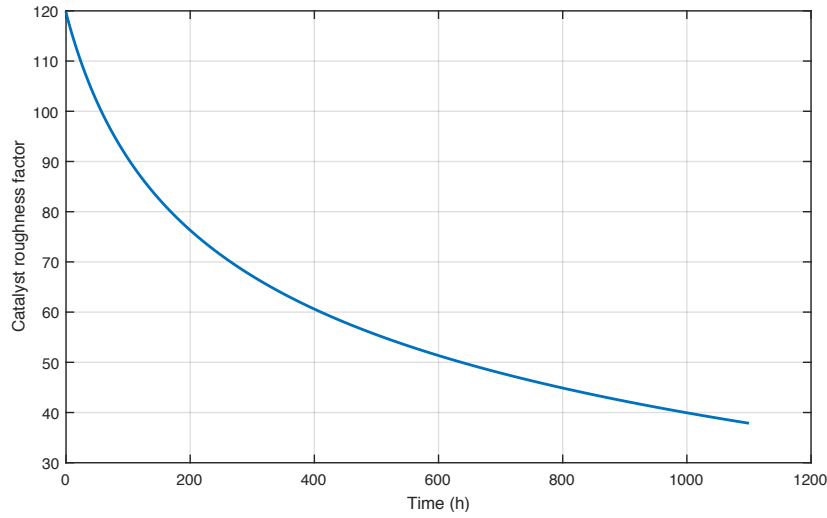
Figure 4.18: Catalyst ageing.

Normal operational conditions were defined to be the same as in the ageing data set discussed in Section 4.4 in order to keep the values of the identified degradation parameters unchanged.

In the first scenario, no component faults were introduced and instead, the degradation of catalyst active surface area was observed in the absence of any external disturbances. This is shown in Figure 4.18 and it can be seen that the rate of ageing shows exponential behaviour in line with Equation 4.10. Despite the slow-down in the degradation rate, the first 1000 h of operation show a significant reduction in roughness factor from 120 to 40.

The second scenario aims to demonstrate how high operational voltage exacerbates the rate of fluoride loss and leads to membrane thinning. In this simulation, a single cell-assembly was operating at constant voltage until 40 h when a fault representing a short-circuit was injected into the current demand signal. The simulation output depicted in Figure 4.19 shows how the fuel cell voltage abruptly increased from 0.57 V to OCV of 1.08 V at the time of failure event. The same diagram shows how membrane thickness begins to fall over the next 190 h. When membrane thickness reaches 0, the simulation is stopped as the formed pinhole signifies the death of the PEMFC.

In the third scenario, the consequences of increasing coolant temperature within a 5-cell stack were investigated. The simulation was setup to introduce an incipient radiator failure (due to e.g. loss of heat exchanging properties) leading to gradual temperature increase starting at 40 min. The results of this simulation are shown in Figure 4.20. The coolant temperature increases from 328 K to 347 K over 30 min of operation as shown in Figure 4.20a. This lead to the reduction of voltage output from approximately 3.75 V to 3.54 V. This drop in performance occurs due the reduction of water content within the fuel cell, leading to the increase of area-specific resistance (ASR) of the membrane as shown in Figure 4.20b. This, in turn, causes the increase of ohmic losses and thus the drop in voltage.
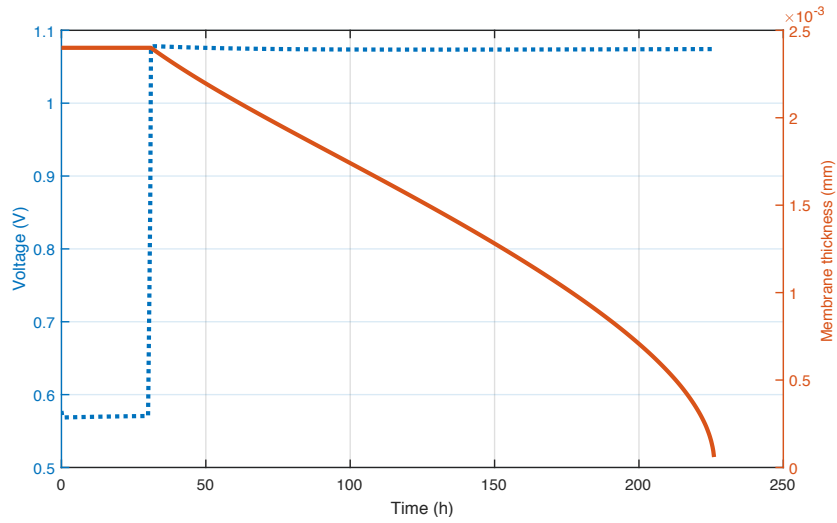
Figure 4.19: Membrane thinning at OCV.
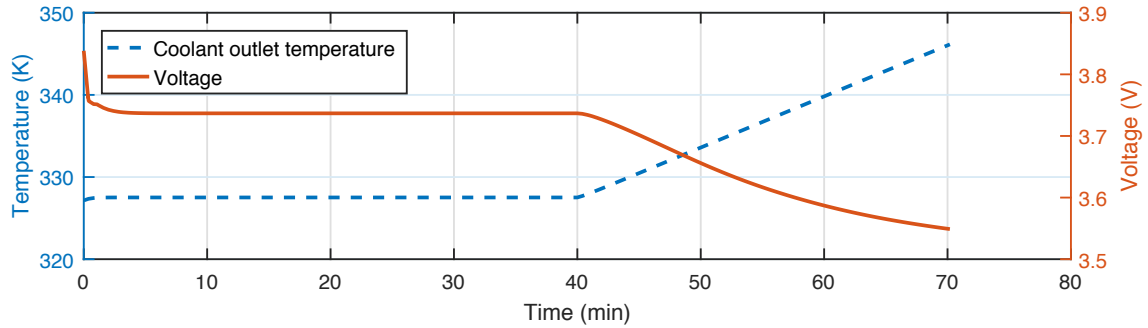
(a) The change in stack voltage due to the increase in fuel cell temperature due to the increased coolant temperature.
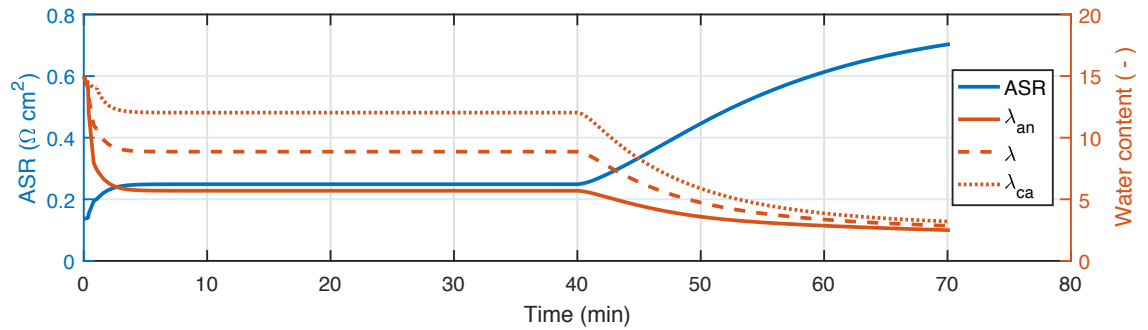
(b) The change in the membrane area specific resistance (ASR) and water content (λ) distribution.

Figure 4.20: Changes in fuel cell performance due to the increase of coolant temperature.
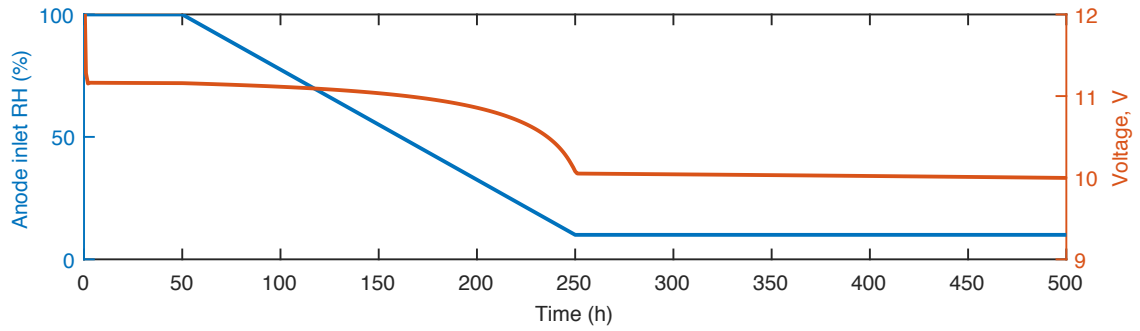
Figure 4.21: Influence of anode inlet relative humidity loss on the stack voltage output.
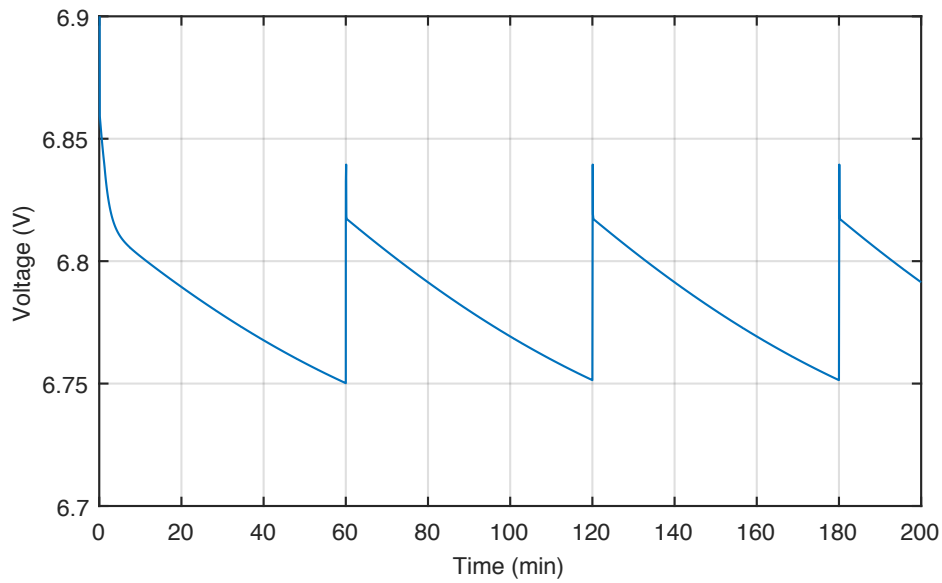
Figure 4.22: Voltage dynamics during anode dead-end operation with purging cycles.

The gradual loss of external humidification of H_2 supply due to a leak within the humidifier and its effect on the voltage output of a 15-cell stack was also investigated. Figure 4.21 shows how a failure initiated at $50\,h$ lead to the to drop of Relative Humidity (RH) from $100\,\%$ to $10\,\%$ over $200\,h$. The lack of resulting membrane humidification caused a voltage drop of approximately $1\,V$ is shown on the same figure.

If a PEMFC stack operates in dead-end fuel supply mode, it requires periodic purging in order to vent the accumulated N_2 from the anode volume. In order to observe the voltage fluctuations occurring due to the changing H_2 concentrations, another simulation was performed. Figure 4.22 shows a simulated example of voltage dynamics within a 7-cell stack operating under constant current load and with purging events occurring every $60\,min$. It can be observed that as a result of the purging cycles, the voltage alternates between $6.82\,V$ and $6.75\,V$.

Simulations performed in this section demonstrate the vastly expanded capability of the F-BGFC model compared to the original model. Not only continuous degradation

behaviour can be evaluated and investigated, but also discrete events of component failures can be captured and their consequences analysed.

4.8   Chapter Summary

The focus of this chapter was to discuss and implement the possible modifications to the original fuel cell model of Chapter 3 in pursuance of allowing the simulation of various component failure mechanisms.

The resulting F-BGFC model has three main novel contributions to this field of study. Firstly, the combination of performance degradation mechanisms such as membrane thinning, nitrogen cross-over, loss of catalyst surface area, increase of the FC internal resistance and loss of mass transport properties of the GDLs was not previously seen in a published model before.

Secondly, the parameters identified from the ageing data provide a useful insight into the degradation processes within PEMFC and can serve as the baseline for other models and hardware configurations under similar operational conditions.

Thirdly, the novelty of such implementation is in the seamless hybridization between deterministic and statistical processes within one integrated model. The unique properties of the resulting model were demonstrated through a set of fault simulation scenarios in Section 4.7.

The following chapter will discuss what additional alterations are required to be implemented for the model to be used in dynamic reliability analysis.

Reliability Analysis

Contents

5.1 Introduction

Simulation-based reliability analysis relies on the method called Monte Carlo simulation, which is often used when the model contains a high degree of uncertainty in its parameters and provides the means to analyse a wide number of possible scenarios of system life-time evolution. The method consists of iteratively generating a set of random input parameters, then using them to evaluate the deterministic model and recording the outputs. After completing a large number of simulations, statistical information about the system performance and its reliability characteristics can be gathered and assessed.

This chapter is devoted to discussion of several practical aspects of Monte Carlo simulations, followed by the analysis of the simulation results. First, the problem of setting the appropriate time-step for lifetime simulations is addressed in Section 5.2. Uncertainty in parameter estimation is discussed in Section 5.3. Section 5.4 covers the steps required to setup Monte Carlo simulations and the results are discussed in Section 5.5.

5.2 Considerations for Lifetime Simulations

The multiple physical phenomena occurring within Polymer Electrolyte Membrane Fuel Cells (PEMFCs) have various dynamics and span a very large range of time-scales from micro-seconds to days and months. Charge transfer and double-layer capacitance effects span the time-scale 1×10^{-6} s to 1 s, gas diffusion, fluid dynamics and membrane humidification are approximately 3×10^{-3} s to 1×10^4 s, while heat transfer phenomena occur between 2×10^1 s and 3×10^4 s. The degradation and ageing mechanisms, however span 2×10^4 s to 1×10^8 s time-scales [146]. Such a wide range of time-constants within a system needs to be taken into account when simulating the lifetime of the system.

The original BGFC model described in Chapter 3 was designed to operate at time-scales from seconds to minutes, so when performing evaluation of the model equations,

each simulation time-step T_s was equal to $1\,\mathrm{s}$. However, the extended F-BGFC model from Chapter 4 includes the description of some of the degradation mechanisms that take place at much larger time-scales. This means that for the simulation to capture all the relevant model dynamics over extended periods of time (such as the target lifetime of $5000\,\mathrm{h}$), it would be needed to run the simulation for $5000 \times 1\,\mathrm{h} = 5000 \times 3600\,\mathrm{s} = 18\,000\,000\,\mathrm{s}$ or $18\,000\,000$ time-steps. This results in very time-consuming and computationally inefficient solutions.

This problem of establishing an appropriate simulation time-step when simulating systems exhibiting dynamics at various time-scales is a known issue and was addressed by other researchers in the field of physics-based modelling. Hmam et al. [147] developed an algorithm to determine the simulation step-size adaptively in order to significantly speed-up the evaluation of the performance degradation of an energy storage unit over its 20 year-lifetime. This approach assumes the usage profile for the system is known in advance and the algorithm first evaluates the solution over a basic repeating interval (i.e. 1 day) and extrapolates the results to a larger time-interval (i.e. week or month). The model parameters are then updated to represent the degradation and the next iteration begins in the same manner until the simulation finish time is reached. The authors were able to achieve a reduction of the simulation time by a factor of 100 by using their adaptive algorithm compared to a non-adaptive one. However, such an approach requires a way of interacting with the solver during the simulation, which is not directly available in the default Modelica solver and the development of such an algorithm from scratch is outside the scope of this thesis.

Another approach to solve the problem is to separate the overall model into different sections according to the physical domain or the corresponding dynamics and use different solvers with different simulation step sizes for each model segment. These individual solvers are then coupled such that at certain points in time they exchange the values of state variables in order to produce a consistent solution. Thiele et al. [148] suggest using a custom Modelica library called MULTIRATE in order to implement such model segmentation and simulation. Unfortunately, the library is not included in the standard Modelica installations, nor is it currently available on-line.

Consequently, modifications to the solver routines are not feasible at this point and an alternative solution is proposed by adjusting the model dynamics. Firstly, the model order can be reduced by removing insignificant dynamic states. As already mentioned, double-layer capacitance effects occur under a micro-second scale, and the long-term changes in its behaviour are assumed constant and not taken into consideration in degradation modelling, hence this dynamic element can be removed. Secondly, time-constants of thermal domain dynamics can be scaled up from seconds to hours such that they take place much faster relative to the overall lifetime. This scaling is done by multiplying all thermal domain time constants by a factor of 1/3600 in order to convert the values from a time-scale of seconds into hours.

However, this kind of time-constant scaling is not suitable for the fluidic domain in the current model. This is because the channel capacitances are already small enough so that when applying the scaling yields such small time-constants, the dynamic response becomes instantaneous and leads to the solver's inability to efficiently resolve the calculations. At the same time, removing the dynamic behaviour in the fluidic domain from the model would mean setting the gas pressures to be constant, thus invalidating key calculations of the model, such as changes in membrane humidification. Therefore, fluid dynamics of the model are left unaltered.

5.3 Parameter Uncertainty

The degradation parameters identified in the previous chapter (Table 4.2) are highly uncertain and strictly speaking cannot be used when attempting to simulate the behaviour of a different fuel cell stack even under similar operational conditions. The uncertainty comes from many sources such as natural unit-to-unit variability occurring during component manufacturing, assembly and operation. Furthermore, the values of these parameters often cannot be directly measured.

Monte Carlo simulation accounts for the uncertainty in estimation by sampling the values of these parameters from various statistical distributions. Many types of such distributions exist, such as the already mentioned Weibull, exponential, uniform, normal and many others. Each of the distributions has a unique set of properties and can be used in various applications. The Monte Carlo (MC) approach is indifferent to the type of a distribution used, so the choice of the parameter distribution can be guided by the experimental measurements and expert knowledge. Noguer et al. [149] distinguish three types of parameter uncertainty: optimistic (normal distribution), pessimistic (uniform distribution) and realistic (Weibull distribution). The parameters and equations for each of these distributions are provided in Appendix B.

Assuming the process of catalyst deposition on the Membrane Electrode Assembly (MEA) is well established and consistent from one item to another, then the roughness factor of the catalyst can be assumed to follow a normal distribution (since small deviations from an ideal process are inevitable). As a consequence, under equal operating conditions, the catalyst degradation rate would also correspond to the normal distribution. Therefore, the parameter Φ_A from Equation 4.10 is assumed to be normally distributed with the mean value of 25×10^5 as defined in Table 4.2. The value of the corresponding standard deviation is set to be not too high and not too small at $10\,\%$ of the mean value.

Similarly, the uncertainty of parameters β_{ion}, β_{ohm}, β_D and β_B can be assumed to be normal. However, the normal distribution is defined on the range $(-\infty, \infty)$, but the degradation laws in Equations 4.19, 4.20, 4.22 and 4.24 are defined in such a way that the values of these parameters need to be non-negative (otherwise the performance of the fuel cell will be increasing with time). Therefore, the original distribution can be truncated at

Table 5.1: Degradation distributions characteristics.

Parameter	Units	Distribution	Interval	Estimated μ	Suggested σ
δ_{mem}^0	m	Uniform	$[0, 27.5 \times 10^{-6}]$	–	–
Φ_A	–	Normal	$(-\infty, \infty)$	25×10^5	25×10^4
β_{ohm}	$\Omega\,\mathrm{h}^{-1}$	Truncated normal	$[0, \infty)$	5×10^{-5}	1.25×10^{-5}
β_{ion}	h^{-1}	Truncated normal	$[0, \infty)$	5×10^{-5}	1.25×10^{-5}
β_B	$\mathrm{V\,h}^{-1}$	Truncated normal	$[0, \infty)$	1×10^{-6}	2.5×10^{-7}
β_D	$\frac{\mathrm{cm}^2}{\mathrm{s}}\mathrm{h}^{-1}$	Truncated normal	$[0, \infty)$	1×10^{-6}	2.5×10^{-7}

0 to obtain a truncated normal distribution on the interval $[0, \infty)$ [150]. In comparison to the catalyst deterioration process, there is not enough knowledge to justify higher degree of certainty, so the standard deviation of these parameters is set at 25 % of the mean value.

The variation of the initial membrane thickness is also investigated. Imperfections in the Bipolar Plate (BPP) and MEA components can create local mechanical deformations and stress within the fuel cell. Additionally, during the stack assembly process, manufacturing errors can lead to further defects. Therefore it can be assumed that there is a non-zero chance of the membrane over-compression or even puncture. As a consequence, the uncertainty of the initial value of parameter δ_{mem} is pessimistic and follows the uniform distribution defined on the interval $[0, \delta_{mem}]$. Based on the parameter values identified in Table 4.2, Table 5.1 lists the same parameters with the corresponding distribution types and their suggested characteristic properties. Sampling a random number from a statistical distribution can be done using the '*inverse transform sampling method*' [132]. The method computes the value of the inverse cumulative distribution function (the so-called quantile function) by taking values of probability (between 0 and 1) as inputs. These input values are randomly generated by dedicated algorithms.

5.3.1 Random Number Generation

Modelica Standard Library (MSL) 3.2.2 comes with a package Math.Random.Generators that contains a set of three Pseudo-Random Number Generators (PRNGs) called xor-shift64*, xorshift128+ and xorshift1024* which were initially developed by Marsaglia [151] and later extended by Vigna [152]. These generators differ from each other (among other properties) by their respective period lengths denoted in their names: 2^{64}, 2^{128} and 2^{1024}. The period length determines the amount of random numbers generated before the sequence begins to repeat. It is highly unlikely that more than 2^{64} simulations will be performed, and therefore the xorshift64* generator is used in this work.

The inverse transform sampling method for generating parameter values according to the truncated normal distribution is implemented as a Modelica function shown in Listing 5.1. The code in Listing 5.1 relies on two functions within MSL 3.2.2, definitions of which are imported in lines 2 and 3. The truncated normal quantile function is imported under label '`distr`', while the function that generates pseudo-random numbers is imported

Listing 5.1: Modelica function to sample a random number from the truncated normal distribution.

```
1  function normalT
2    import distr = Modelica.Math.Distributions.TruncatedNormal.quantile;
3    import rnd = Modelica.Math.Random.Generators.Xorshift64star.random;
4    input Real y_min;
5    input Real y_max;
6    input Real y_mean;
7    input Real y_sigma;
8    input Integer seed;
9    output Real r;
10  protected
11    Integer stateIn[2]={seed,seed};
12    Integer state[2];
13    Real r_raw;
14  algorithm
15    (r_raw, state) := rnd(stateIn);
16    r := distr(r_raw, y_min, y_max, y_mean, y_sigma);
17  end normalT;
```

under label 'rnd'. The characteristic parameters such as thresholds (y_min and y_max) and the mean y_mean and standard variation y_sigma of the original normal distribution are inputs to the function as shown in lines 4-7. An additional input variable seed in line 8 is used to define the input state of the random number generator (stateIn) in line 11. Key-word 'protected' ensures that the variables in lines 11-13 are not saved to the results file as they do not have any practical purpose. The equation in line 15 yields a uniformly-distributed random number in the range [0; 1] and saves it in a variable called 'r_raw'. The equation in line 16 takes the generated random number and maps it onto the distribution with given characteristic parameters.

Random number generation is not only used to create randomized parameter values, it is also used to make sure the stochastic Petri net transitions discussed in Chapter 4 fire at different intervals of time during each iteration of the model execution. In order to ensure the PRNG receives a new seed each simulation, the lines of code shown in Listing 5.2 must be included at the top level of the model.

Listing 5.2: Modelica code to generate a new seed for the random number generator.

```
1  inner Modelica.Blocks.Noise.GlobalSeed globalSeed(useAutomaticSeed=true);
2  inner PNlib.Settings settings(globalSeed=globalSeed.seed);
```

Line 1 in Listing 5.2 includes a Modelica object globalSeed of class GlobalSeed from package Modelica.Blocks.Noise and sets its boolean parameter useAutomaticSeed to true. This ensures a new seed is generated each time the model is simulated. Line 2 includes an object settings of class Settings from PNlib library and sets its parameter globalSeed to seed from the defined in line 1 object globalSeed.

5.4   Simulation Design

The last prerequisite for Monte Carlo simulations is to set up the simulation procedure by defining the model inputs, setting the number of algorithm iterations and establishing at what point is it sufficient to stop an iteration.

In order to investigate the effect of changing operating conditions on the reliability of the Fuel Cell System (FCS), three cases are investigated:

1. Baseline simulation scenario designed to observe the effect of parameter uncertainty on the voltage degradation rate which was found to be $121\,\mu V\,h^{-1}$ under the same operating conditions as in [136]. That is constant values of pressures, temperatures, mass flows and current load (70 A) are set.

2. The second scenario aims to observe the effect of purging events on fuel cell reliability. The operating conditions are kept the same, except the anode side of the stack was operating in dead-end mode (as described in Section 4.3.4), thus requiring periodic purging of the anode compartment.

3. The third scenario aims to investigate the effects of dynamic current load on the system reliability. Same operating conditions were kept, except for the current load which was set to be varying dynamically between 0 A and 100 A according to the New European Drive Cycle (NEDC) as shown in Figure 5.1. Such dynamic input is designed to mimic a more realistic environment where the stack undergoes multiple potential, humidity, temperature and start-stop cycles. The range of current variation was chosen to capture the full spectre of voltage loss mechanisms (i.e. to capture the full range of the polarization curve).

For each of the simulation scenarios, the stop time was set to 5000 h (since the durability target is 5000 h). However, due to degradation the voltage output can drop below the recommended durability threshold of 10 % before the simulation reaches its final stopping time. Therefore, the simulations can be stopped when the calculated voltage reaches this threshold. In order to do that, there needs to be a reference value against which to compare. This can be implemented within the model by including a look-up table with the polarization curve of the fuel cell stack at the beginning of life. Modelica block `CombiTable1D` from package `Modelica.Blocks.Tables` is used for this purpose. It takes the current load as input and outputs the corresponding voltage of the stack at the beginning of life. Once the threshold is reached, a command to stop the simulation can be executed as shown in Listing 5.3.

The code in Listing 5.3 contains a statement to check whether a specified condition (i.e. degradation limit reached) was met and if it was, terminate the simulation and issue a message describing the reason for termination.

There is no single way of selecting the total number of Monte Carlo iterations since the output depends on the desired accuracy and the variance of parameters within the model
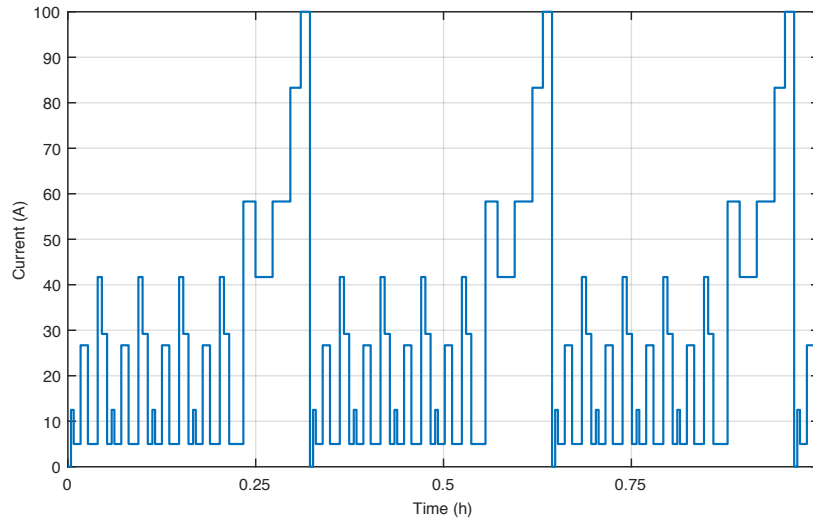
Figure 5.1: Dynamic current load profile consisting of repeating New European Drive Cycles (NEDCs).

Listing 5.3: Modelica code to terminate the simulation.

```
1  when condition==true then
2    terminate("terminationMessage");
3  end when;
```

[132]. In order to identify the stopping point, it was decided to run a large number of simulations and record the change in mean survival time of the system with every iteration of the Monte Carlo simulation. The resulting graph after 500 iterations is depicted in Figure 5.2. This graph shows that after the initial oscillations during the first 200 iterations, the mean survival time converged at approximately 2470 h. Therefore it is sufficient to stop the algorithm execution when such convergence is reached. However, because the model contains different sub-systems, it is beneficial to perform larger number of simulations in order to obtain a more detailed insight into the different failure modes of the system. Because of this, the Monte Carlo algorithm was stopped after 500 iterations were completed and the data was processed.

The model code is modified to include the parameter uncertainties and termination conditions. It is then recompiled to generate the updated executable and initialization files. The Monte Carlo simulation is set-up using the Matlab environment and the process logic is illustrated in Figure 5.3. Matlab repeatedly calls the model executable file for nSim simulations. After an individual simulation is complete, the necessary information such as the calculated stack voltage and the failure modes are extracted from the result file and stored in an output file for future analysis. This process is repeated until the total number of simulations (nSim) is completed.
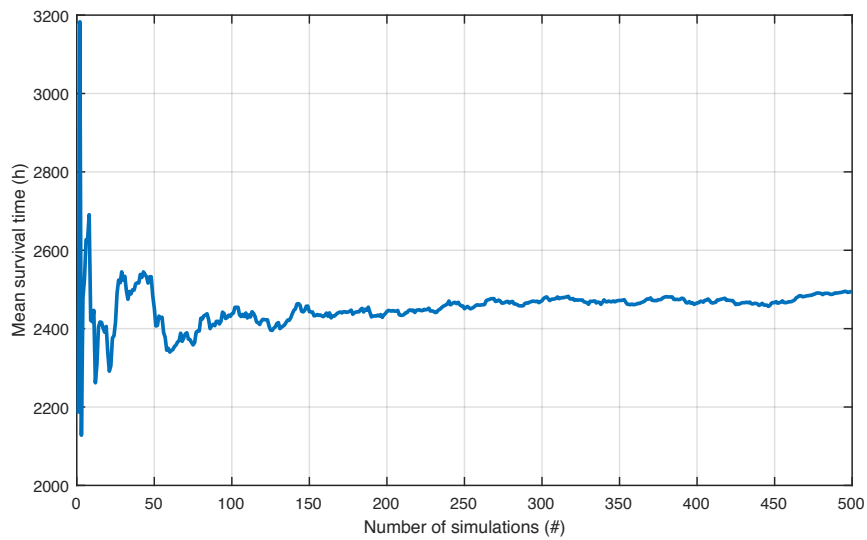
Figure 5.2: Mean survival time versus the number of Monte Carlo runs.
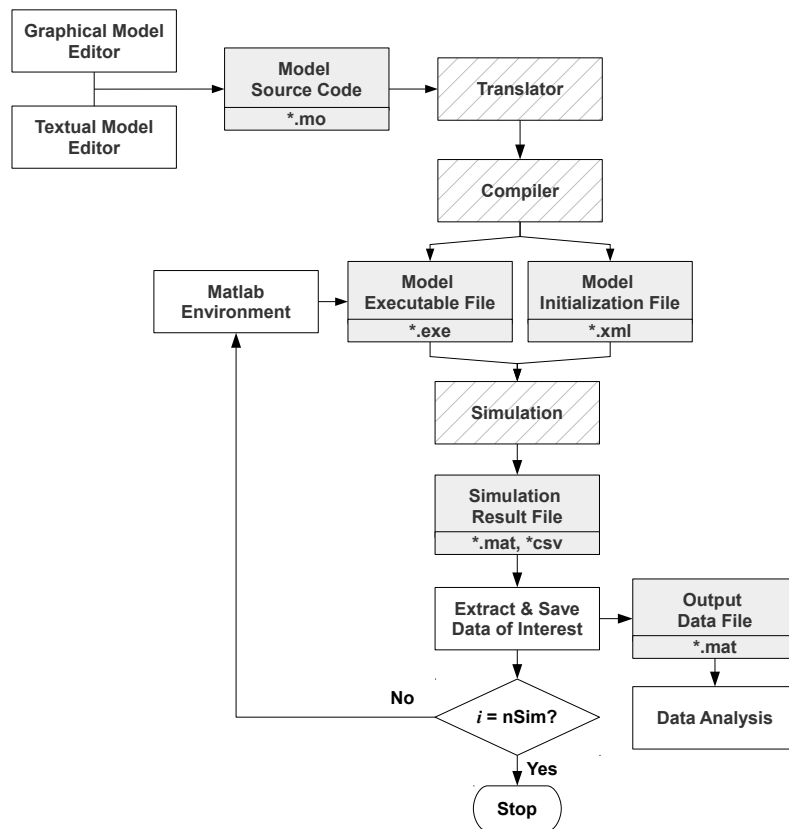
Figure 5.3: Monte Carlo simulation flow-chart.

5.5   Simulation Results and Analysis

After the defined number of simulations (nSim) is complete, the collected data is sorted and expressed as shown in Table 5.2. Each simulation run constitutes an individual observation.

The first column contains the observation numbers, the entries in the second column signify whether the fuel cell system failed (F) or survived until the cut-off point of 5000 h and was suspended (S). Since the failure times of the suspended runs are unknown, these values are censored and not included in the analysis. The last column in this table signifies the corresponding system failure mode as denoted by the sub-system name or labelled as 'unknown' if an observation was suspended. The collected life-time data in Table 5.2 can

Table 5.2: Times to failure table.

Observation Number	State	Failure Time (h)	Failure Mode
1	F	1395	Thermal management
2	F	2487	Fuel supply
3	F	1693	Stack
4	S	5000	Unknown
. . .	. . .	. . .	. . .
500	F	3152	Air supply

be analysed using one of many dedicated software packages such as Minitab [153], R [154], Weibull++ [155] and others. Minitab is used here to analyse the generated data because of advanced and automated capabilities for parametric and non-parametric lifetime data analysis.

The 500 baseline runs resulted in 6 suspensions and 494 failures, among which 326 are attributed to the degradation of the stack, 54 are due to failures within the fuel supply and processing sub-system, 69 occurred within the air supply and processing sub-system and 45 were due to failures within thermal management equipment. This makes it clear that the fuel cell stack is the most vulnerable component in the whole system.

Further analysis can begin with plotting the histogram of the times to failure as shown in Figure 5.4. This histogram reveals a pattern for failure occurrences of the system. It can be seen that although there are some early-life failures (up to 1600 h to 1800 h), the majority of failures take place between approximately 2000 h and 3400 h. After 3400 h the frequency decreases and falls off to almost 0 by 5000 h.

Histograms of the times to failure of the individual sub-systems are shown in Figure 5.5. It can be seen from Figure 5.5d that the system unreliability throughout lifetime is overwhelmingly determined by the fuel cell stack unreliability. Balance of Plant (BoP) components do contribute to system failures, but not nearly as much as the stack as observed from Figures 5.5a to 5.5c.

One drawback of analysing the data using histograms is that they can appear very different for different widths of the columns. A better way of analysing such data is by plotting an empirical Cumulative Distribution Function (eCDF). It provides a normalised overview of the survival data by calculating the cumulative sum of all the columns in the histogram and expressing it as a proportional value between 0 and 1. Mathematically, it can be calculated using the Kaplan-Meyer estimator, which is given by Equation 5.1 [156]:
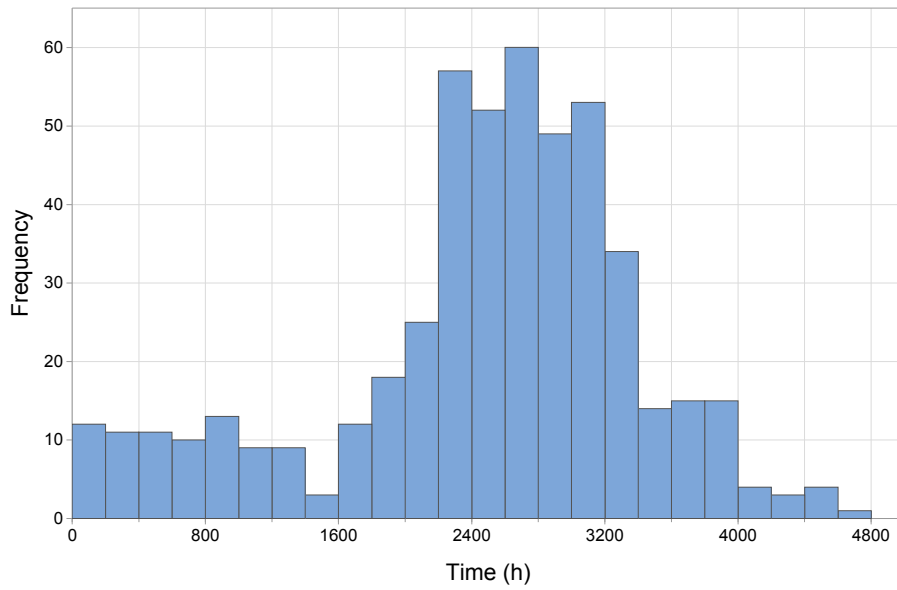
Figure 5.4: Histogram of system times to failure under constant 70 A load.

(a) Fuel supply sub-system

(b) Air supply sub-system

(c) Thermal management sub-system

(d) Fuel cell stack sub-system
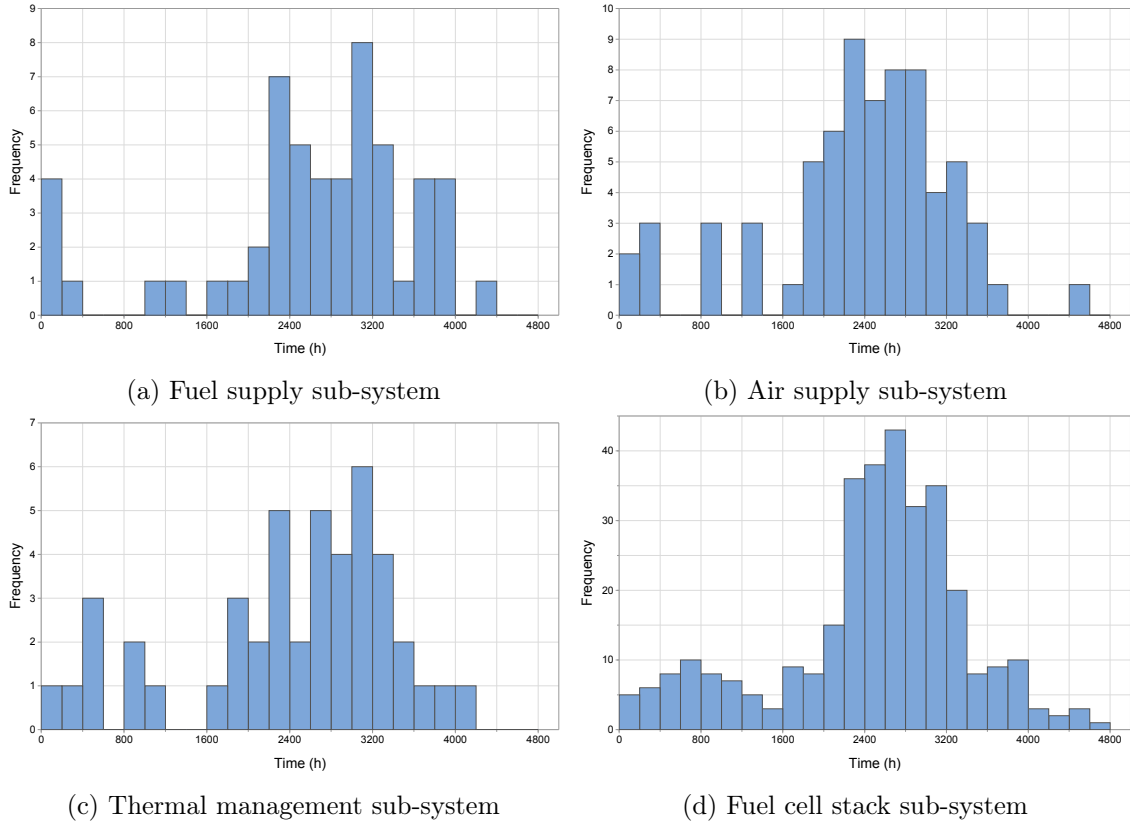
Figure 5.5: Histograms of sub-systems time-to-failure.
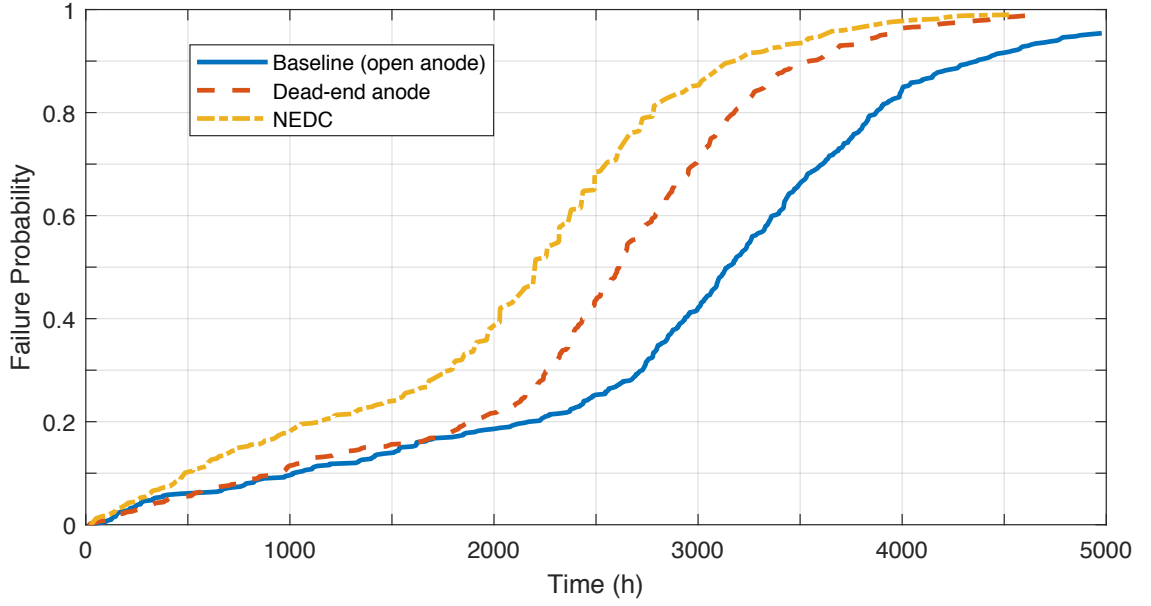
Figure 5.6: Empirical CDFs under different current load profiles and operating modes.

$$\hat{R}(t) = \prod_{i:t_i \leq t} \left(1 - \frac{d_i}{n_i}\right), \tag{5.1}$$

where t_i is the time when at least one event happened, d_i is the number of the events that happened at time t_i and n_i is the number of surviving items.

Calculated eCDFs for each of the simulated cases is shown in Figure 5.6. By observing the baseline eCDF, it can be seen that the probability of system failure by 2000 h is approximately 19 %, but by 4000 h the probability soars to 84 %. Only 5 % of the population survive to 5000 h. The mean and median survival times for this case are 2979 h and 3147 h respectively. The change in slope of the eCDF after 2000 h is likely due to occurrence of two different failure modes within the stack.

The eCDF of the purging scenario shows worse reliability characteristics. In this case at 2000 h the probability of failure is 22 %, but by 4000 h it is at 97 % with probability of system survival to 5000 h practically 0. The mean and median survival times for this case are 2494 h and 2613 h respectively. An apparent increase in the failure probability can be seen after 2000 h, while unreliability in the early life remains almost the same as baseline. This observation is explained by the fact that each purging event subjects the membrane to additional mechanical stress caused by the periodic and abrupt pressure variations, thereby contributing to membrane degradation and failures.

The third eCDF calculated from MC simulations under dynamic current load also yields worse reliability performance. At 2000 h, the probability of failure is 40 % and at 4000 h it reaches 97 %. The mean and median survival times for this case are 2083 h and 2204 h respectively. Such poor survivability of the system compared to the baseline is explained

by the fact that the stack is operating in very intensive conditions, with large voltage variations constantly occurring as a result of repeating NEDC cycles.

The difference between reliability characteristics of the three investigated scenarios displayed in Figure 5.6, demonstrates the capability of the F-BGFC model to calculate the dynamic reliability characteristics of PEMFC systems under varying operating conditions. This is significant because it shows that the modelling approach proposed in this thesis can be used to evaluate the reliability metrics of PEMFCs systems under various operating conditions and control strategies.

Since the model was developed using open-source libraries and software, potential alterations can easily be implemented without requiring third-party licenses and tools. The model can be extended to take into account daily and seasonal variations of ambient air temperature and humidity in different geographical locations. Using the model, a system designer can change the hardware configuration and set the corresponding reliability characteristics of the auxiliary components, define a different duty cycle (for example defined by automotive drive profiles such as WLTP, US06, etc.) and specify the climatic conditions. Performing another set of MC simulations using reconfigured model will yield a new dynamic reliability characteristic specific to the given model configuration. Comparing the obtained dynamic reliability metrics for different system configurations can guide improvements in hardware design, control and maintenance strategy optimisation, as well as help with defining a more informed warranty policy.

The control strategy can be adjusted by balancing the performance with reliability in a given system configuration at a defined point in lifetime of the system. The maintenance strategy can also be adjusted by taking into account the changes in eCDF slope by increasing (or decreasing) the frequency of maintenance checks as appropriate. This will ensure that components are fixed and replaced on time, and any Fuel Cell (FC) degradation mitigated, thereby extending the lifetime of the system. Additionally, the knowledge of how reliable a given design will last under given ambient and operational conditions can inform the company on better warranty policy. Longer warranty periods will boost consumer confidence in the technology and assist with price formation for the given design.

In other words, for a given climate and hardware configuration and given point in lifetime of the system, the proposed analysis can help with answering the following questions:

- Can sacrificing $X\%$ in performance provide $Y\%$ improvement in reliability? Is it acceptable?

- What hardware configuration offers the best trade-off between performance, cost and reliability?

- How frequent should maintenance checks be?

- How long should the optimal warranty period be?

5.6 Summary and Conclusions

This chapter demonstrated the application of the developed modelling approach for novel condition-based dynamic reliability analysis. The main contribution of this chapter lies in the description of necessary steps required for performing dynamic reliability analysis and demonstrating the results of such simulations.

Three MC simulation scenarios were designed to observe the effects of changing operating conditions on reliability of the system. The results show clear influence of both purging and load cycles on longevity of the PEMFC stack. While the effects of purging events become more pronounced after 2000 h, loading cycles have clear negative influence throughout the system lifetime.

System reliability is shown to be low for all three cases, showing the worst case scenario of system lifetime. Probability of survival at the target time of 5000 h was found to be 5 %, while the other two cases exhibit even lower probability. This is due to harsh operating conditions imposed on the stack. In reality, the stack will not be subjected to constant loads for extended periods of time. Likewise, dynamic loads in real vehicles occur only when driving.

The results can be used to define a more robust maintenance strategy. Such a schedule will dedicate more frequent checks of all the system components and especially the stack after 2000 h lifetime threshold.

During such maintenance checks, auxiliary components can be fixed and the stack cells exhibiting poor voltage output replaced, thereby improving overall system reliability and lifetime.

The simulation results also showed the detrimental effect of the purging cycles on the stack lifetime due to the additional mechanical stress on the membrane. It is important to note that the choice between open or dead-end anode configuration depends on the design requirements (fuel efficiency targets, components costs, etc.) and must be decided at the initial stages of the design. Therefore, these operational modes cannot be changed during system operation. Nevertheless, such reliability analysis can guide decision making process during the design phase. A designer can set the desired operating conditions and modes for the fuel cell system, define the reliability characteristics of the constituent components and perform the dynamic reliability analysis. Comparing different system configurations with given components and conditions, the designer can obtain the optimal design that maximises not only performance and costs, but also long-term reliability of the system.

Conclusions and Future Work

6.1 Summary and Discussion

The five objectives set out for this thesis in Section 1.5 were successfully achieved. The work conducted in order to fulfil these objectives covers multiple fields of study from electrochemistry and various methods of mathematical modelling of continuous and discrete systems to probabilistic analysis of failure occurrences.

The first objective was to gain understanding of operational principles, structure and durability issues was achieved in the introductory Chapter 1. Although the fundamental structure of Polymer Electrolyte Membrane Fuel Cells (PEMFCs) and the operational principles are fairly simple, the underlying causes for degradation and performance deterioration are complex and not always well understood. Additionally, the full set of auxiliary components necessary for PEMFC system operation introduce further points of failure and unreliability.

The second objective was achieved through the literature review conducted in Chapter 2. It made it clear that classical techniques of survival analysis such as Fault Tree Analysis (FTA) or Petri Nets (PNs) are unable to capture changing reliability metrics of PEMFC systems in various operating conditions on their own. Consequently, the inclusion of physics-based models of the system in the analysis was deemed necessary. Further review of literature dedicated to physics-based modelling of PEMFCs revealed the bond graph method as one of the most suitable modelling methods for PEMFCs. As a result, of this literature review, a combined modelling approach that captures both physics-based behaviour and reliability performance was proposed and developed.

The third objective was to develop a fuel cell model capable of reproducing system behaviour under dynamic operational conditions. This objective was achieved in Chapters 3 and 4. The model development consisted of two major parts: fault-free modelling and fault-augmentation. The fault-free model (BGFC) was created using an object-oriented modelling language Modelica and has a unique modular and hierarchical structure. Such model architecture makes it possible to create fuel cell stack models of various sizes and

configurations. Furthermore, the novel use of multi-bonds within the model provides another level of flexibility, as the interactions with additional chemical species can be also captured by the model. The BGFC model laid the foundation for the development of fault-augmented model (F-BGFC). This extended model incorporates deterministic degradation behaviour of the fuel cell as well as stochastic failures of auxiliary equipment such as valves and pumps. Such stochastic behaviour was modelled with a different modelling method called Petri nets. The innovative structure of this model makes it possible to capture a wide array of system behaviours by seamlessly integrating continuous and discrete-time dynamics in a single system representation.

The fourth objective was to experimentally validate the model to ensure it represents the real behaviour of the system. This was completed alongside model development in Chapters 3 and 4. First, the experimental procedure was described in and the collected measurements were used to identify the parameters to fit the polarization curve. An additional test was conducted to ensure the model is capable of capturing dynamic behaviour of the system. A good agreement was demonstrated and error metrics were found to be sufficiently low.

Finally, the last objective was achieved in Chapter 5, which showed how the developed model can be further extended to make it suitable for Monte Carlo simulations and subsequent dynamic reliability analysis. The final results show how probability of system failure changes throughout the system lifetime. It was found that the majority of PEMFC system failures occurred due to the stack failures. Additionally, it was observed that after approximately 2000 h, system unreliability drastically increases with time. The change in the failure rate is attributed to different failure modes within the fuel cell stack. Simulations performed under different operational modes (i.e. dead-end anode) showed that the effect of purge events has detrimental effect on the system reliability because of the additional mechanical stress. Dynamic loads were also found to have negative effect on system reliability. As a result, the modelling efforts performed in this thesis demonstrate the capability of this novel modelling structure to be used to perform innovative dynamic reliability analysis. The results of such analysis can prove to be essential for appropriate maintenance planning as well as more accurate warranty estimates in different climates and conditions.

6.2 Conclusions and Major Contributions

The work conducted during this research project resulted in four original contributions to knowledge:

1. Identified the knowledge gap in the literature.

   Classical reliability techniques such as FTA have been used before to for PEMFC systems analysis. However, such techniques don't take into account the effects of changing system dynamics due to failures and degradation on the overall failure

rate. Dynamic Probabilistic Risk Assessment (DPRA) is a field of study that aims to circumvent these limitations by incorporating a physics-based model of the system into analysis. Although this concept was first introduced in mid-1990s, the primary area for application of DPRA methods has been the reliability and safety analysis of nuclear power plants, and it hasn't found widespread adoption in other engineering applications. This thesis, therefore, contributes to both DPRA and PEMFC fields by exploring the previously unexamined area of research in conjunction of the two fields.

2. Proposed an approach to extending bond graph modelling of PEMFCs.

   Bond graphs have been extensively used for PEMFC modelling before, but quite often the modellers adopt several simplifying assumptions such as constant membrane humidification and assume single-component gas mixtures. Additionally, the majority of published models were developed using commercial software and tend to be difficult to interpret due to the absence of model hierarchy. The modelling approach proposed in this thesis adopts multi-bonds in order to incorporate multi-component mixtures of gases, thereby enabling the calculations of dynamic humidification within the membrane and nitrogen cross-over phenomenon. The model was also developed using open-source software in order to eliminate any barriers in terms of access to modelling tools. Furthermore, the modular component-based model architecture ensures better understanding of physical processes occurring within each section of the model. The model design and validation were published in a high profile peer-reviewed journal.

3. Proposed a novel approach and modelling tools to implement fault-augmented model of the fuel cell.

   Previously published papers on degradation modelling of fuel cell internal components (catalyst layers, membrane and gas diffusion layers) focused on individual phenomena and were not combined in a single model to such detail prior to work carried out in this thesis. Additionally, an innovative approach to modelling auxiliary component failures through hybridisation of the stochastic Petri nets with the bond graphic model created a novel fault-augmented model of the fuel cell. Such a model is capable of calculating the performance of the PEMFC system not only in nominal operating conditions, but also during long-term degradation and component failure events such as cooling system failure, short-circuit and others. Overall, the proposed modelling technique paves the way to a more realistic representation of fuel cell system behaviour in dynamic operating conditions.

4. Provided a description of necessary steps to prepare the model for Monte Carlo simulations and performed subsequent reliability analysis.

The developed fault-augmented model can only evaluate system behaviour from deterministic point of view (i.e. same initial conditions lead to the same solution), however due to uncertain nature of reliability predictions, the model needs to be adjusted to take into account the parameter uncertainty. As a result, a number of model parameters were replaced by corresponding statistical distributions and a workflow to perform Monte Carlo simulations have been proposed.

To conclude, the overall modelling technique presented in this thesis can be used to perform dynamic reliability analysis for a given hardware configuration of the PEMFC system under defined operational conditions. By evaluating system's dynamic reliability metrics over multiple designs and conditions, engineers can make more informed decisions about component choices and control and maintenance strategies. Subsequent increase in system reliability will ensure higher customer satisfaction, leading to higher rates of adoption and societal acceptance of the Fuel Cell Electric Vehicle (FCEV) technology and ultimately to the reduction of CO_2 emissions from the transportation sector.

6.3 Suggestions for Future Work

The work conducted in this dissertation demonstrates the conceptual application of dynamic reliability modelling to automotive PEMFC systems. However, there can be several improvements implemented in the model to extend it to wider fuel cell applications and ensure better prediction accuracy. Generally speaking, such improvements can be achieved by incrementally relaxing modelling assumptions and experimentally validating the obtained results.

6.3.1 Improvements to failure-free models

The designed BGFC model in its current form consists of a set of modular components organised in an library. Each fuel cell component inherits a set of parameters describing its dimension and major material properties. This makes it possible to model fuel cell stacks of various sizes for different application areas (automotive, stationary, portable and aerospace).

However, the developed library does not include physics-based models of powertrain components, power electronics, secondary power sources (e.g. batteries, super-capacitors), vehicle dynamics and others. Extending the library with these models and incorporating them into the BGFC will result in a more realistic representation of electrical loads on the PEMFC stack. Certain fuel cell systems operate by reforming hydro-carbon fuels into hydrogen, so models of fuel reformers can also be added to the library.

Incorporation of water phase transitions within the bipolar plate channels and Membrane Electrode Assembly (MEA) layers will provide better insight into how changes in operating conditions affect output performance of the stack.

Furthermore, PEMFCs can operate in reversible mode - splitting the water into hydrogen and oxygen, but current version of the model only allows redox reaction for power generation. Therefore, reconfiguring the bond graph structure to incorporate reverse reaction can be another avenue for future work.

Additionally, the fault-free bond graphic model can be used to evaluate fault detection and identification algorithms by utilising the causal properties of bond graphs [157, 158].

6.3.2 Improvements to failure modelling

Improvements to failure modelling reported in Chapter 4 can be achieved by validating the models using the data obtained from real driving conditions. Such a data will help with adjusting the estimated parameter values and uncertainties. An additional set of experiments can be conducted to validate the failure behaviour models of the auxiliary components.

Current simulations were performed under the assumption that the auxiliary component failure times are independent of the operating conditions, i.e. only time-dependent. Incorporating condition-dependent failure behaviour of the components will improve the prediction accuracy, but it requires much more detailed physics-based component modelling. Alternatively, the reliability characteristics of BoP components can be replaced with data obtained from an automotive application instead of using the data from databases for components used in off-shore oil rigs.

Moreover, Petri net modelling of component failures can be elaborated to include various maintenance processes. Additional transitions and states representing availability of spare parts and maintenance crew during the lifetime of the system can be easily incorporated.

6.3.3 Improvements to the dynamic reliability analysis

Current simulations were performed under the assumption of constant ambient air temperature and humidity. Incorporating daily and seasonal changes of ambient conditions into the model is another avenue for method extension. Such analysis will be useful for adapting control strategy and maintenance schedules based on the local climate conditions.

Furthermore, performing the dynamic reliability analysis under more realistic duty cycles will provide an even better insight into system reliability for a given configuration and operating conditions.

Appendices

Modelica Code

A.1 Organising Modelica Packages

Any Modelica library is stored in a textual file with extension *.mo that has a general syntax as shown in Listing A.1. The description of any library or package begins with a keyword `package` (Line 1) followed by a chosen library name (`libraryName`). A library can contain as many packages as needed, each of which can consist of any number of component models. In Listing A.1, packages `packageName1` and `packageName2` are defined to contain `componentName` and `blockName` model respectively.

Listing A.1: Code of a generic Modelica library.

```
1   package libraryName
2     package packageName1;
3       model componentName
4       ...
5       end componentName;
6     end packageName1;
7     package packageName2;
8       block blockName
9       ...
10      end blockName;
11    end packageName2;
12  end libraryName;
```

The definition of a component class begins with either keyword `model` or `block` as shown in Listing A.2. Since Modelica is an object-oriented language, such features as inheritance play a large role in model development. This is why any component class can inherit properties of other classes. Inheritance is signified with keyword `extends` in line 2 of Listing A.2. A component class can contain definitions of multiple variables and parameters as defined in lines 3 to 9. Keyword `equation` signifies the beginning of the section of the code containing all the necessary equations within the component.

More complex simulation models may consist of many constituent components, which are instantiated into the larger model by specifying the class of the object and its name. Listing A.3 provides a generic syntax of such component definitions. Lines 2 and 3 in Listing A.3 define the two objects `Component_Name` and `Block_Name`. The interaction of the two objects is coded by equating output connector `outPort` to the input connector `inPort` using command `connect` in line 6.

Listing A.2: Modelica code of a generic component

```
1  model componentName
2    extends libraryName.packageName.className;
3    constant Real constName;
4    parameter Integer parName;
5    Real varName;
6    input Real inName;
7    Modelica.SIunits.Length a;
8    Modelica.SIunits.Length b;
9    Modelica.SIunits.Area S;
10   ...
11 equation
12   S = a * b;
13   ...
14   annotation(Icon(graphics={...}), Diagram(graphics={...}));
15 end componentName;
```

Listing A.3: Modelica code of a generic simulation model

```
1  model modelName
2    libraryName.packageName1.componentName Component_Name annotation(...);
3    libraryName.packageName2.blockName Block_Name annotation(...);
4    ...
5  equation
6    connect(Block_Name.outPort, Component_Name.inPort) annotation(...);
7    ...
8    annotation(experiment(StartTime=0, StopTime=100));
9  end modelName;
```

A.2   PEMBondLib Library

During the design of the model described in this thesis a dedicated Modelica library called 'PEMBondLib' was created. The library contains multiple of packages of bond graphic and non-bond graphic components containing all the equations outlined in Chapters 3 to 5. The following listings contain the code of the crucial blocks within the model.

Listing A.4: Code for a thermo-fluidic restrictor calculating the pressure drop within the channels for a mixture of 3 gases

```
1  model Rth_ca
2    extends MultiBondLib.Interfaces.TwoPort;
3    Modelica.Blocks.Interfaces.RealInput u annotation(...);
4    parameter Integer Ncell;
5    parameter Integer ch_N=ParamBPP.chC_N;
6    parameter Modelica.SIunits.ThermalConductivity lambda=0.0253;
7    parameter Modelica.SIunits.Length ch_a=ParamBPP.chC_a "Channel depth";
8    parameter Modelica.SIunits.Length ch_b=ParamBPP.chC_b "Channel width";
9    parameter Modelica.SIunits.Length ch_L=ParamBPP.chC_L*Ncell;
```

```
10    parameter Modelica.SIunits.Area ch_S=ch_N*ch_L*(ch_b + 2*ch_a);
11    final parameter Real alpha=ch_b/ch_a;
12    final parameter Modelica.SIunits.Length Dh=4*(ch_a*ch_b)/(2*(ch_a +
          ch_b));
13    final parameter Modelica.SIunits.Area ch_A=ch_a*ch_b;
14    Real fRe(unit="1");
15    Modelica.SIunits.Pressure Pu "Total upstream pressure";
16    Modelica.SIunits.Pressure Pd "Total downstream pressure";
17    Modelica.SIunits.Pressure dP "Pressure difference";
18    Modelica.SIunits.Pressure pu[size(e1, 1) - 1] "Partial upstream
          pressures";
19    Modelica.SIunits.Pressure pd[size(e1, 1) - 1] "Partial downstream
          pressure";
20    Modelica.SIunits.Temperature Tu "Upstream temperature";
21    Modelica.SIunits.Temperature Td "Downstream temperature";
22    Modelica.SIunits.MoleFraction x[size(e1, 1) - 1] "Molar fractions of
          components";
23    Modelica.SIunits.MassFraction w[size(e1, 1) - 1] "Mass fractions of
          components";
24    Modelica.SIunits.MassFlowRate m_t_dot "Total upstream mass flow";
25    Modelica.SIunits.MassFlowRate m_dot[size(e1, 1) - 1] "Partial upstream
          mass flows";
26    Modelica.SIunits.Velocity v "Mean velocity of gas flow";
27    Modelica.SIunits.VolumeFlowRate Q_t_dot "Volumetric flow rate";
28    Real Q_t_dot_lmin(unit="l/min") "Volumetric flow rate (l/min)";
29    Modelica.SIunits.EnthalpyFlowRate H_dot "Enthalpy flow rate";
30    Modelica.SIunits.MolarMass M_mix "Molar mass of the mixture";
31    Modelica.SIunits.Density Rho_mix "Density of the mixture";
32    Modelica.SIunits.SpecificHeatCapacity cp_mix "Heat capacity of the
          mixture";
33    Modelica.SIunits.DynamicViscosity mu_mix "Dynamic viscosity of the gas
          mixture";
34    Modelica.SIunits.PrandtlNumber Pr "Prandtl Number";
35    Modelica.SIunits.ReynoldsNumber Re "Reynolds Number";
36    Modelica.SIunits.NusseltNumber Nu "Nusselt Number";
37    Modelica.SIunits.CoefficientOfHeatTransfer h_forced "Coefficient of
          forced convection";
38  protected
39    outer MultiBondLib.Defaults MBG_defaults;
40    outer PEMBondLib.Initialization.ParametersBPP ParamBPP;
41    PEMBondLib.Substances.Gases.Steam G1;
42    PEMBondLib.Substances.Gases.Oxygen G2;
43    PEMBondLib.Substances.Gases.Nitrogen G3;
44    parameter Integer Nmix=3;
45    constant Real pi=Modelica.Constants.pi;
46    constant Real R=Modelica.Constants.R;
47    parameter Modelica.SIunits.MolarMass MM[Nmix]={G1.M,G2.M,G3.M} "Molar
          masses of gases";
48    parameter Modelica.SIunits.SpecificHeatCapacityAtConstantVolume
          cv[Nmix]={G1.cv,G2.cv,G3.cv};
```

```modelica
49     parameter Modelica.SIunits.SpecificHeatCapacityAtConstantPressure
           cp[Nmix]={G1.cp,G2.cp,G3.cp};
50     parameter Modelica.SIunits.DynamicViscosity
           mu0v[Nmix]={G1.mu0,G2.mu0,G3.mu0} "Reference viscosity values";
51     parameter Modelica.SIunits.Temperature T0v[Nmix]={G1.T0,G2.T0,G3.T0}
           "Reference temperature for viscosity calculations";
52     parameter Real nv[Nmix]={G1.n,G2.n,G3.n} "Parameter for viscosity
           calculations";
53   equation
54     Tu = e1[1];
55     pu[:] = e1[2:end];
56     Td = e2[1];
57     pd[:] = e2[2:end];
58     Pu = sum(pu[i] for i in 1:size(pu, 1));
59     Pd = sum(pd[i] for i in 1:size(pu, 1));
60     dP = Pu - Pd;
61     for i in 1:size(pu, 1) loop
62       x[i] = pu[i]/Pu;
63     end for;
64     for i in 1:size(x, 1) loop
65       w[i] = x[i]*MM[i]/M_mix;
66     end for;
67     M_mix = sum(x[i]*MM[i] for i in 1:size(x, 1));
68     Rho_mix = Pu*M_mix/(R*Tu);
69     cp_mix = sum(x[i]*cp[i] for i in 1:size(x, 1));
70     mu_mix = PEMBondLib.Functions.DynViscGasMix(Tu, x, MM, mu0v, T0v, nv);
71     v = (u*ch_N*dP*Dh^2)/(2*ch_L*fRe*mu_mix);
72     Q_t_dot = m_t_dot/Rho_mix;
73     Q_t_dot_lmin = 60000*Q_t_dot;
74     v = Q_t_dot/(ch_a*ch_b);
75     fRe = 24*(1 - 1.3553*alpha + 1.9467*alpha^2 - 1.7012*alpha^3 +
           0.9564*alpha^4 - 0.2537*alpha^5);
76     for i in 1:size(x, 1) loop
77       m_dot[i] = w[i]*m_t_dot;
78     end for;
79     H_dot = m_t_dot*cp_mix*Tu;
80     Pr = cp_mix*mu_mix/lambda;
81     Re = Rho_mix*Dh*abs(v)/mu_mix;
82     Nu = 3.657 + (0.0677*(Re*Pr*(Dh/ch_L))^1.33)/(1 +
           0.1*Pr*(Re*Dh/ch_L)^0.3);
83     h_forced = Nu*lambda/Dh;
84     f1[1] = H_dot;
85     f1[2:end] = m_dot[:];
86     f2[1] = H_dot;
87     f2[2:end] = m_dot[:];
88     annotation (...);
89   end Rth_ca;
```

Listing A.5: Thermo-fluidic capacitor for a mixture of 3 gases.

```
 1  model CCca
 2    import SI = Modelica.SIunits;
 3    BondLib.Interfaces.BondCon_b port_th "Thermal port" annotation(...);
 4    BondLib.Interfaces.BondCon_b port_mat1 "Material port" annotation(...);
 5    BondLib.Interfaces.BondCon_b port_mat2 "Material port" annotation(...);
 6    BondLib.Interfaces.BondCon_b port_mat3 "Material port" annotation(...);
 7    Substances.Gases.Steam G1 "Water vapour characteristic parameters";
 8    Substances.Gases.Oxygen G2 "Oxygen characteristic parameters";
 9    Substances.Gases.Nitrogen G3 "Nitrogen characteristic parameters";
10    constant Real R=Modelica.Constants.R;
11    parameter SI.Volume V "Volume of the cathode chamber";
12    parameter SI.MoleFraction x0[Nmix] "Initial molar fractions
          (Steam,H2,O2,N2)";
13    final parameter SI.Pressure P0=world.P0 "Pressure inside the cathode
          chamber";
14    final parameter SI.Temperature T0=world.T0 "Temperature";
15    final parameter Integer Nmix=3 "Nmix-component mixture of ideal gases";
16    final parameter SI.SpecificHeatCapacityAtConstantVolume
          cv[Nmix]={G1.cv,G2.cv,G3.cv};
17    final parameter SI.SpecificHeatCapacityAtConstantPressure
          cp[Nmix]={G1.cp,G2.cp,G3.cp};
18    final parameter SI.MolarMass MM[Nmix]={G1.M,G2.M,G3.M} "Molar masses of
          gases";
19    final parameter SI.Mass m0_t=P0*V*M0/(R*T0) "Initial total Mass of the
          mixture";
20    final parameter SI.SpecificHeatCapacityAtConstantVolume
          cv_mix0=sum(x0[i]*cv[i] for i in 1:Nmix);
21    final parameter SI.Enthalpy H0=m0_t*T0*cv_mix0;
22    SI.Temperature T "Temperature";
23    SI.Pressure P "Total pressure";
24    SI.Mass m_t "Total mass";
25    SI.Mass m[Nmix] "Individual masses of components";
26    SI.Pressure p[Nmix] "Pressure";
27    SI.MoleFraction x[Nmix] "Molar fractions of components";
28    SI.MassFraction w[Nmix] "Mass fractions of components";
29    SI.Enthalpy H(start=H0) "Energy";
30    SI.SpecificHeatCapacity cv_mix "Heat Capacity";
31    SI.Density RhoMix "Density of the mixture";
32  protected
33    outer Initialization.World world;
34  initial equation
35    for i in 1:Nmix loop
36      m[i] = x0[i]*m0_t*MM[i]/M0;
37    end for;
38  equation
39    der(m[1]) = port_mat1.f;
40    der(m[2]) = port_mat2.f;
41    der(m[3]) = port_mat3.f;
```

```
42    der(H) = port_th.f;
43    m_t = sum(m[i] for i in 1:Nmix);
44    for i in 1:Nmix loop
45       w[i] = m[i]/m_t;
46       x[i] = w[i]/MM[i]/sum(w[j]/MM[j] for j in 1:Nmix);
47    end for;
48    P*V = sum(m[i]/MM[i] for i in 1:Nmix)*R*T;
49    RhoMix = m_t/V;
50    cv_mix = sum(x[i]*cv[i] for i in 1:Nmix);
51    H = T*m_t*cv_mix;
52    for i in 1:Nmix loop
53       p[i] = x[i]*P;
54    end for;
55    port_mat1.e = p[1];
56    port_mat2.e = p[2];
57    port_mat3.e = p[3];
58    port_th.e = T;
59    annotation(...);
60  end CCca;
```

A.2.1   Code for calculating diffusion phenomena.

Listing A.6: Gas diffusion layer block at the cathode side

```
1  model Rdiff_ca "2-port restrictor for calculation of diffusion mass flow
       rate through the GDL"
2     extends MultiBondLib.Interfaces.TwoPort(MultiBondCon1(n=2),
          MultiBondCon2(n=2));
3     import SI = Modelica.SIunits;
4     input SI.Temperature T;
5     PEMBondLib.Substances.Gases.Steam G1;
6     PEMBondLib.Substances.Gases.Oxygen G2;
7     constant Real F=Modelica.Constants.F;
8     constant Real R=Modelica.Constants.R;
9     constant Real Inf=Modelica.Constants.inf;
10    parameter SI.DiffusionLength t_GDL=ParamMEA.t_gdl;
11    final parameter SI.DiffusionArea Adiff=ParamMEA.A_gdl;
12    final parameter Integer z=2;
13    final parameter Real Agdl(unit="cm2") = 104.04;
14    final parameter Real sigma=0.4;
15    final parameter Real sigma_p=0.11;
16    final parameter Real alpha_d=0.785;
17    final parameter Real m=1.5;
18    final parameter Real D_WO(unit="cm2/s") = 0.282;
19    parameter Real b_D=0 "Diffussivity increase factor";
20    parameter Real b_D_min=1;
21    parameter Real b_D_max=1;
22    parameter Real b_D_mean=b_D;
```

```
23    parameter Real b_D_sigma=1;
24    Real b_D_distr;
25    SI.Pressure Pu;
26    SI.Concentration CR "Molar concentration of the reactant";
27    SI.Pressure pu[size(e1, 1)];
28    SI.Pressure pd[size(e2, 1)];
29    SI.MassFlowRate m_dot[size(f1, 1)];
30    Real D12(unit="cm2/s") "Binary diffusion coefficient in empty medium";
31    Real Deff(unit="cm2/s") "Effective diffusion coefficient considering
          porosity and water saturation";
32    Real i_L(unit="A/cm2") "Limiting current density";
33  protected
34    final parameter Real MM[2]={G1.M,G2.M};
35    final parameter Real TC[2]={G1.Tc,G2.Tc};
36    final parameter Real PC[2]={G1.Pc,G2.Pc};
37    outer PEMBondLib.Initialization.ParametersMEA ParamMEA;
38    outer Modelica.Blocks.Noise.GlobalSeed globalSeed;
39    final parameter Integer seed=globalSeed.seed;
40  equation
41    pu = e1[:];
42    pd = e2[:];
43    Pu = sum(pu[i] for i in 1:size(e1, 1));
44    CR = pu[2]/(R*T);
45    D12 = PEMBondLib.Functions.BiDiffusion(MM[1], MM[2], TC[1], TC[2],
          PC[1], PC[2], T, Pu, "polar");
46    b_D_distr = PEMBondLib.Functions.Distributions.normalT(0, Inf, b_D_mean,
          b_D_sigma, seed);
47    if globalSeed.enableNoise == true then
48      Deff = D12*sigma*((sigma - sigma_p)/(1 - sigma_p))^alpha_d*(1 - Sw)^m
            - b_D_distr*OnTime;
49    else
50      Deff = D12*sigma*((sigma - sigma_p)/(1 - sigma_p))^alpha_d*(1 - Sw)^m
            - b_D*OnTime;
51    end if;
52    pd[1] = pu[1] - m_dot[1]*R*T*t_GDL/(Deff*Agdl*MM[1]*1e-8);
53    pd[2] = pu[2] - m_dot[2]*R*T*t_GDL/(Deff*Agdl*MM[2]*1e-8);
54    i_L = 4*F*Deff*CR*1e-6/(t_GDL*100);
55    f1[1] = m_dot[1];
56    f2[1] = m_dot[1];
57    f1[2] = m_dot[2];
58    f2[2] = m_dot[2];
59    annotation(...);
60  end Rdiff_ca;
```

Listing A.7: Code of the membrane diffusion block.

```
1  model RSmemN2
2    extends BondLib.Interfaces.TwoPort;
3    input Modelica.SIunits.Temperature Tmem;
```

```modelica
4     input Modelica.SIunits.Current I;
5     input Modelica.SIunits.Pressure p_O2;
6     input Modelica.SIunits.Pressure p_an_H2;
7     input Modelica.SIunits.Voltage Vcell;
8     input Modelica.SIunits.Time OnTime;
9     parameter Integer Ncell=1 "Number of cells";
10    parameter Integer TC=1 "Scaling factor";
11    parameter Modelica.SIunits.MolarMass M =
          PEMBondLib.Substances.Gases.Steam.M;
12    parameter Modelica.SIunits.Density Rho_mem = ParamMEA.rho_mem "Dry
          density of Nafion";
13    parameter Real rho_cm3(unit="kg/cm3") = 0.00197 "Dry density of Nafion";
14    parameter Modelica.SIunits.MolarMass M_mem = ParamMEA.M_mem_dry
          "Equivalent weight of Nafion";
15    parameter Modelica.SIunits.DiffusionLength t_mem = ParamMEA.t_mem
          "Membrane thickness";
16    parameter Modelica.SIunits.DiffusionLength t_GDL = ParamMEA.t_gdl "GDL
          thickness";
17    parameter Modelica.SIunits.Area A_mea=ParamMEA.A_mea;
18    parameter Real Afc(unit="cm2")=100 "Nominal fuel cell area";
19    parameter Real zmin(unit="cm") = 0;
20    parameter Real zmax(unit="cm") = t_mem*100 "Thickness of the membrane";
21    parameter Real s1(unit="1") = 0.005193;
22    parameter Real s2(unit="1") = 0.00326;
23    parameter Real A1(unit="ug/(h.cm2)") = 1.7e-7;
24    parameter Real A2(unit="1") = 20.8;
25    parameter Real t_0_hole(unit="cm") = 25e-4 "Initial membrane thickness
          inside the weaker region";
26    parameter Real K_H2(unit="mol/(Pa.cm.s)") = 3.68e-16 "H2 permeability in
          Nafion";
27    parameter Real alpha_eq=0.54 "Equivalent transfer coefficient";
28    parameter Real wF=0.82 "Mass fraction of fluorine in Nafion";
29    parameter Real Ea(unit="J/mol") = 75000 "Equivalent activation energy
          for all the different reactions";
30    parameter Modelica.SIunits.Pressure Pref=101325;
31    parameter Modelica.SIunits.Temperature Tref=273.15 + 95;
32    parameter Real zhole(unit="cm") = 0.0023;
33    parameter Real zhole_min(unit="cm") = 0;
34    parameter Real zhole_max(unit="cm") = zmax;
35    parameter Real zhole_mean=zhole;
36    parameter Real zhole_sigma=1;
37    parameter Modelica.SIunits.MolarEnergy E_N2=24000;
38    parameter Real Vmem=M_mem/Rho_mem "Dry membrane volume";
39    parameter Real alpha_N2=1;
40    parameter Real M_N2 = PEMBondLib.Substances.Gases.Nitrogen.M;
41    parameter Real Vw=2e-5;
42    Modelica.SIunits.MassFlowRate m_dot_drag "Mass flow of water due to
          electro-osmotic drag";
43    Modelica.SIunits.MassFlowRate m_dot_bd "Mass flow of water due to dack
          diffusion";
```

```
44   Modelica.SIunits.MassFlowRate m_dot_net "Total water flow across
        memebrane";
45   Modelica.SIunits.Pressure p_an;
46   Modelica.SIunits.Pressure p_ca;
47   Modelica.SIunits.Pressure Psat;
48   Modelica.SIunits.Pressure Pan;
49   Modelica.SIunits.Pressure p_an_N2;
50   Modelica.SIunits.Pressure p_ca_N2;
51   Modelica.SIunits.MassFlowRate m_dot_N2;
52   Modelica.SIunits.Concentration C_ca_N2;
53   Modelica.SIunits.DiffusionCoefficient D_N2;
54   Real i(unit="A/cm2") "Cell current density";
55   Real a_an(unit="1") "Water activity on anode side";
56   Real a_ca(unit="1") "Water activity at cathode side";
57   Real lambda_an(unit="1") "Water content in membrane at anode side";
58   Real lambda_ca(unit="1") "Water content in membrane at cathode side";
59   Real lambda(unit="1") "Mean water content in the membrane";
60   Real D_lambda(unit="cm2/s") "Effective diffusivity coefficient";
61   Real Dw(unit="cm2/s") "Water diffusivity";
62   Real nd(unit="1") "Electro-osmotic drag coefficient";
63   Real ASR(unit="Ohm.cm2") "Area specific resistance";
64   Real sigma_an(unit="S/cm") "Electrolytic conductivity at anode side of
        the membrane";
65   Real sigma_ca(unit="S/cm") "Electrolytic conductivity at cathode side of
        the membrane";
66   Real alpha(unit="1");
67   Real C(unit="1");
68   Real K, X1, X2, X3, Y1, Y2;
69   Real zmax_eff(unit="cm", start=zmax) "Effective thickness of the
        membrane";
70   Real zhole_distr;
71   Real zhole_eff(unit="cm") "Effective thickness of the weak area of the
        membrane";
72   Real FRR "Fluoride release rate";
73   Real FRR_hole;
74   Real i_loss(unit="A/cm2") "Leak current density due to H2 crossover";
75   Real k(unit="mol/(Pa.m.s)");
76   Real fv;
77 protected
78   outer PEMBondLib.Initialization.ParametersMEA ParamMEA;
79   outer Modelica.Blocks.Noise.GlobalSeed globalSeed;
80   final parameter Integer seed=globalSeed.seed;
81   constant Real F=Modelica.Constants.F;
82   constant Real R=Modelica.Constants.R;
83   constant Real eps=Modelica.Constants.eps;
84   constant Real Inf=Modelica.Constants.inf;
85 public
86   BondLib.Interfaces.BondCon_b portM_an_N2 annotation(Placement(...));
87   BondLib.Interfaces.BondCon_b portM_ca_N2 annotation(Placement(...));
88 initial equation
```

```
89     zhole_eff = zhole_distr;
90   equation
91     p_an = e1;
92     p_ca = e2;
93     p_an_N2 = portM_an_N2.e;
94     p_ca_N2 = portM_ca_N2.e;
95     Pan = p_an + p_an_H2 + p_an_N2;
96     i = I/A_mem;
97     zhole_distr = PEMBondLib.Functions.Distributions.normalT(zhole_min,
           zhole_max, zhole_mean, zhole_sigma, seed);
98     Psat = Modelica.Media.Air.MoistAir.saturationPressure(Tmem);
99     a_an = p_an/Psat;
100    a_ca = p_ca/Psat;
101    if 0 < a_an and a_an < 1 then
102      lambda_an = 0.043 + 17.81*a_an - 39.85*a_an^2 + 36*a_an^3;
103    else
104      lambda_an = 14 + 1.4*(a_an - 1);
105    end if;
106    if 0 < a_ca and a_ca <= 1 then
107      lambda_ca = 0.043 + 17.81*a_ca - 39.85*a_ca^2 + 36*a_ca^3;
108    elseif a_ca > 1 and a_ca <= 3 then
109      lambda_ca = 14 + 1.4*(a_ca - 1);
110    else
111      lambda_ca = 16.8;
112    end if;
113    lambda = (lambda_an + lambda_ca)/2;
114    D_lambda = (2.563 - 0.33*lambda + 0.0264*lambda^2 -
           0.000671*lambda^3)*1e-6;
115    Dw = D_lambda*exp(2416*(1/303 - 1/Tmem));
116    nd = 0.0029*lambda^2 + 0.05*lambda - 3.4e-19;
117    FRR = if ON then (A1/2)*(p_O2/Pref)* (zmax/zmax_eff)*
           exp(alpha_eq*F*Vcell/(Ncell*R*Tmem))* exp(-(Ea/R)*(1/Tmem - 1/Tref))
           else 0;
118    FRR_hole = if ON then (A1/2)*(p_O2/Pref)* (zhole/zhole_eff)*
           exp(alpha_eq*F*Vcell/(Ncell*R*Tmem))* exp(-(Ea/R)*(1/Tmem - 1/Tref))
           else 0;
119    der(zmax_eff) = -1e-9*A2*FRR/(wF*rho_cm3);
120    der(zhole_eff) = -1e-9*A2*FRR_hole/(wF*rho_cm3);
121    when zmax_eff <= 0 or zhole_eff <= 0 then
122      terminate("Membrane thickness degraded to 0");
123    end when;
124    i_loss = 2*F*Pan*K_H2*(zmax_eff +
           500*zhole_eff)/(501*zmax_eff*zhole_eff);
125    X2 = (Dw*A_mem*M*rho_cm3)/M_mem;
126    K = exp(1268*((1/303) - (1/Tmem))) "Temperature effect on conductivity";
127    if I < 1e-5 then
128      X1 = 0;
129      X3 = 0;
130      m_dot_net = X2*(lambda_an - lambda_ca)/(Ncell*zmax_eff);
131      alpha = 0;
```

```
132     C = 0;
133     Y1 = 0;
134     Y2 = 0;
135     sigma_an = (s1*lambda_an - s2)*K;
136     sigma_ca = (s1*lambda_ca - s2)*K;
137     ASR = (Ncell*zmax_eff)/sigma_an "ASR when I=0";
138   else
139     X1 = (nd*I*M)/(22*F);
140     X3 = (I*M)/(2*F*X2);
141     m_dot_net = X1*(lambda_an*exp(X1*Ncell*zmax_eff/X2) -
                lambda_ca)/(exp(X1*Ncell*zmax_eff/X2) - 1);
142     lambda_an = (X2*X3*alpha/X1) - (C/X1)*exp(X1*zmin/X2);
143     lambda_ca = (X2*X3*alpha/X1) - (C/X1)*exp(X1*Ncell*zmax_eff/X2);
144     Y1 = (s1*K*X2*X3*alpha)/X1 - (s2*K);
145     Y2 = -(s1*K*C)/X1;
146     sigma_an = Y1 + Y2;
147     sigma_ca = Y1 + Y2*exp(X1*Ncell*zmax_eff/X2);
148     ASR = Ncell*zmax_eff/Y1 + (X2/(X1*Y1))*log(sigma_an/sigma_ca) "ASR
                when I!=0";
149   end if;
150   m_dot_drag = ((nd*lambda)/11)*(I/(2*F))*M;
151   m_dot_bd = Dw*A_mem*M*rho_cm3*(lambda_an -
            lambda_ca)/(Ncell*zmax_eff*M_mem);
152   k = alpha_N2*(0.0295 + 1.21*fv -
            1.93*fv^2)*10^(-14)*exp((E_N2/R)*(1/Tref - 1/Tmem));
153   fv = lambda*Vw/(Vmem + lambda*Vw);
154   C_ca_N2 = p_ca_N2/(R*Tmem);
155   D_N2 = k*p_ca_N2/C_ca_N2;
156   m_dot_N2*R*Tmem*(Ncell*zmax_eff*0.01)/(TC*D_N2*A_mea*M_N2) = p_ca_N2 -
            p_an_N2;
157   f1 = m_dot_net;
158   f2 = m_dot_net;
159   portM_an_N2.f = m_dot_N2;
160   portM_ca_N2.f = m_dot_N2;
161   annotation(...);
162 end RSmemN2;
```

A.2.2 Chemical transformation

Listing A.8: Code for the chemical tranformer.

```
1 model cTF_H "Chemicatl transformation block"
2   extends PEMBondLib.Interfaces.ThreePort;
3   constant Real R=Modelica.Constants.R;
4   PEMBondLib.Substances.Gases.Hydrogen G1 "Hydrogen thermodynamic
        properties";
5   final parameter Modelica.SIunits.Temperature Tref=world.Tref "Reference
        temperature";
```

```
 6    final parameter Modelica.SIunits.Pressure Pref=world.Pref "Reference
          Pressure";
 7    Modelica.SIunits.Temperature T "Temperature";
 8    Modelica.SIunits.Pressure p "Partial pressure";
 9    Modelica.SIunits.ChemicalPotential mu "Chemical potential";
10    Modelica.SIunits.MolarEnthalpy dh "Enthalpy change due to reaction";
11    Modelica.SIunits.MolarEntropy ds "Entropy change due to reaction";
12    Modelica.SIunits.MolarFlowRate n_dot "Molar flow rate of reactants";
13    Modelica.SIunits.MassFlowRate m_dot "Mass flow rate of reactants";
14  protected
15    outer Initialization.World world;
16    parameter Modelica.SIunits.SpecificHeatCapacity cp=G1.cp;
17    parameter Modelica.SIunits.MolarMass M=G1.M;
18  equation
19    p = e1;
20    m_dot = f1;
21    T = e3;
22    m_dot = G1.M*n_dot;
23    dh = G1.h0 + M*cp*(T - 298);
24    ds = G1.s0 + M*cp*log(T/298);
25    mu = dh - T*ds + R*T*log(p/Pref);
26    f2 = n_dot;
27    e2 = mu;
28    f3 = T*ds*n_dot;
29    annotation(...);
30  end cTF_H;
```

A.2.3   Voltage Losses

Listing A.9: Code for the activation losses block

```
 1  model RSa "Two-port thermo-electrical resistor for activation losses"
 2    extends BondLib.Interfaces.TwoPort;
 3    input Modelica.SIunits.Pressure p_O2;
 4    input Modelica.SIunits.Pressure p_H2;
 5    input Modelica.SIunits.Voltage Vcell;
 6    input Real i_loss;
 7    input Real Rohm(unit="Ohm.cm2");
 8    parameter Integer Ncell;
 9    parameter Real Afc(unit="cm2")=100 "Nominal fuel cell area";
10    parameter Real alpha_e "Exchange coefficient";
11    parameter Real alpha_a;
12    parameter Real alpha_c;
13    parameter Real i_0(unit="A/cm2") = 1e-9 "Reference cathode exchange
          current density";
14    parameter Real i_0_an(unit="A/cm2") = 3e-3;
15    parameter Real dG_O2(unit="J/mol") = 66000 "Activation energy of ORR";
16    parameter Real k1=10e-10;
17    parameter Real M_Pt(unit="g/mol") = 195.1;
```

```
18    parameter Real rho_Pt(unit="g/cm3") = 21.45;
19    parameter Real alpha_1(unit="1") = 1.14e-10;
20    parameter Real alpha_r(unit="1") = 1.1;
21    parameter Real beta_r(unit="1") = 0.038;
22    parameter Real U_theta(unit="V") = 1.18;
23    parameter Real delta_CL(unit="cm") = 0.0065;
24    parameter Real N_Pt(unit="1") = 2.24e16;
25    parameter Real R_Pt(unit="cm") = 2.6e-7;
26    parameter Real V_Pt(unit="cm3") = N_Pt*4*pi*R_Pt^3/3;
27    parameter Real Phi_A=25e5;
28    parameter Real Phi_A_mean=Phi_A;
29    parameter Real Phi_A_sigma=0.1*Phi_A_mean;
30    Modelica.SIunits.Voltage eta_act "Total activation overvoltage";
31    Modelica.SIunits.Voltage eta_act_ca "Activation overvoltage of ORR";
32    Modelica.SIunits.Voltage eta_act_an "Activation overvoltage of HOR";
33    Modelica.SIunits.Current I "Cell current load";
34    Modelica.SIunits.Temperature T "Temperature";
35    Real i(unit="A/cm2") "Cell current density";
36    Real i_ex_ca(unit="A/cm2") "Cathode exchange current density";
37    Real dPhi_c(unit="V");
38    Real Aec(unit="cm2");
39    Real Ageo(unit="cm2");
40    Real Rf "Roughness factor";
41    Real Phi_A_distr;
42  protected
43    outer PEMBondLib.Initialization.ParametersMEA ParamMEA;
44    outer PEMBondLib.Initialization.World world;
45    outer Modelica.Blocks.Noise.GlobalSeed globalSeed;
46    final parameter Integer seed=globalSeed.seed;
47    final parameter Modelica.SIunits.Temperature Tref=world.Tref;
48    final parameter Modelica.SIunits.Pressure Pref=world.Pref;
49    constant Real F=Modelica.Constants.F;
50    constant Real R=Modelica.Constants.R;
51    constant Real pi=Modelica.Constants.pi;
52    constant Real eps=Modelica.Constants.eps;
53    constant Real Inf=Modelica.Constants.inf;
54    Real u_c, u_theta;
55  initial equation
56    Ageo = 4*pi*R_Pt^2*N_Pt;
57  equation
58    I = f1;
59    T = e2;
60    i = I/Afc;
61    dPhi_c = Vcell/Ncell + I*Rohm/Afc;
62    u_c = exp(F*dPhi_c/(R*T));
63    u_theta = exp(F*U_theta/(R*T));
64    Aec/Ageo = 0.63;
65    Rf = Aec/Afc;
66    Phi_A_distr = PEMBondLib.Functions.Distributions.normal(Phi_A_mean,
          Phi_A_sigma, seed);
```

```
67    if globalSeed.enableNoise == true then
68      der(Ageo) = -((4*Phi_A_distr*k1)/(9*V_Pt^2)) * (u_c/u_theta) *
             (M_Pt/rho_Pt) * (F*alpha_1/(R*T)) *
             exp(F*alpha_1*Ageo/(R*T*3*V_Pt)) * Ageo^3 * alpha_r * beta_r^2;
69    else
70      der(Ageo) = -((4*Phi_A*k1)/(9*V_Pt^2)) * (u_c/u_theta) * (M_Pt/rho_Pt)
             * (F*alpha_1/(R*T)) * exp(F*alpha_1*Ageo/(R*T*3*V_Pt)) * Ageo^3 *
             alpha_r * beta_r^2;
71    end if;
72    i_ex_ca = i_0*Rf*(p_O2/Pref)^0.5*exp(-(1 - T/Tref)*(dG_O2/(R*T)));
73    eta_act_an = if i < eps then 0 else
             p_stack*Ncell*R*T/(alpha_a*2*F)*log((i + i_loss)/i_0_an);
74    eta_act_ca = if i < eps then 0 else
             p_stack*Ncell*R*T/(alpha_c*4*F)*log((i + i_loss)/i_ex_ca);
75    eta_act = eta_act_ca + eta_act_an;
76    e1 = eta_act;
77    f2 = I*eta_act;
78    annotation (preferredView="text", ...);
79  end RSa;
```

Listing A.10: Code for the ohmic losses block.

```
1   model RSo "Two-port thermo-electrical resistor for ohmic losses"
2     extends BondLib.Interfaces.TwoPort;
3     input Real ASR(unit="Ohm.cm2") "Area-specific resistance of the
           membrane";
4     parameter Integer Ncell;
5     parameter Afc(unit="cm2")=ParamMEA.A_fc "Nominal fuel cell area";
6     parameter Real Ri_0(unit="Ohm.cm2") = ParamMEA.Ri_mem "Initial internal
           ohmic resistance";
7     parameter Real b_i(unit="Ohm.cm2/s") = b_i "Internal resistance increase
           factor due to degradation";
8     parameter Real b_i_min=0;
9     parameter Real b_i_max=Inf;
10    parameter Real b_i_mean=b_i;
11    parameter Real b_i_sigma=1e-3;
12    parameter Real b_ion = b_ion "Ionic resistance increase factor due to
           degradation";
13    parameter Real b_ion_min=0;
14    parameter Real b_ion_max=Inf;
15    parameter Real b_ion_mean=b_ion;
16    parameter Real b_ion_sigma=1e-3;
17    Modelica.SIunits.Current I "Cell current";
18    Modelica.SIunits.Voltage eta_ohm "Ohmic overvoltage";
19    Modelica.SIunits.Temperature T "Temperature";
20    Real i(unit="A/cm2") "Cell current density";
21    Real Ri(unit="Ohm.cm2") "Effective internal resistance";
22    Real ASReff(unit="Ohm.cm2") "Effective area sepecific resistance";
23    Real b_ion_distr;
```

```
24    Real b_i_distr;
25  protected
26    outer Initialization.ParametersMEA ParamMEA;
27    outer Modelica.Blocks.Noise.GlobalSeed globalSeed;
28    final parameter Integer seed=globalSeed.seed;
29    constant Real Inf=Modelica.Constants.inf;
30  equation
31    I = f1;
32    T = e2;
33    i = I/Afc;
34    b_i_distr = PEMBondLib.Functions.Distributions.normalT(0, Inf, b_i_mean,
          b_i_sigma, seed);
35    b_ion_distr = PEMBondLib.Functions.Distributions.normalT(0, Inf,
          b_ion_mean, b_ion_sigma, seed);
36    Ri = if globalSeed.enableNoise == true then Ri_0 + b_i_distr*OnTime else
          Ri_0 + b_i*OnTime;
37    ASReff = if globalSeed.enableNoise == true then
          ASR*exp(b_ion_distr*OnTime) else ASR*exp(b_ion*OnTime);
38    eta_ohm = I*(Ri + ASReff)/Amem;
39    e1 = eta_ohm;
40    f2 = eta_ohm*I;
41    annotation(preferredView="text", ...);
42  end RSo;
```

Listing A.11: Code for the concentration losses block

```
1  model RSc "Two-port thermo-electrical resistor for concentration losses"
2    extends BondLib.Interfaces.TwoPort;
3    import normT = PEMBondLib.Functions.Distributions.normalT;
4    input Real i_L(unit="A/cm2") = 1 "Limiting current density";
5    input Real i_L_an(unit="A/cm2") = 1 "Limiting current density at anode
          electrode";
6    parameter Integer Ncell;
7    parameter Real b_C=0;
8    parameter Real b_C_min=0;
9    parameter Real b_C_max=0.1;
10   parameter Real b_C_mean=b_C;
11   parameter Real b_C_sigma=1;
12   Real b_C_distr;
13   final parameter Integer z=2;
14   final parameter Afc(unit="cm2")=ParamMEA.A_fc "Nominal fuel cell area";
15   Modelica.SIunits.Current I "Cell current load";
16   Real i(unit="A/cm2") "Cell current density";
17   Real di_an(unit="A/cm2");
18   Real di_ca(unit="A/cm2");
19   Modelica.SIunits.Voltage eta_con_ca "Concentration overvoltage";
20   Modelica.SIunits.Voltage eta_con_an "Concentration overvoltage";
21   Modelica.SIunits.Voltage eta_con;
22   Modelica.SIunits.Temperature T "Temperature";
```

```
23  protected
24    outer PEMBondLib.Initialization.ParametersMEA ParamMEA;
25    outer Modelica.Blocks.Noise.GlobalSeed globalSeed;
26    final parameter Integer seed=globalSeed.seed;
27    constant Real R=Modelica.Constants.R;
28    constant Real F=Modelica.Constants.F;
29    constant Real Inf=Modelica.Constants.inf;
30  equation
31    I = f1;
32    T = e2;
33    i = I/Afc;
34    di_ca = i_L - i;
35    di_an = i_L_an - i;
36    b_C_distr = normT(0, Inf, b_C_mean, b_C_sigma, seed);
37    if globalSeed.enableNoise == true then
38      eta_con_an = if di_an <= 1e-6 then 1e2 else -p_stack*(Ncell*R*T/(2*F)
              + b_C_distr*OnTime)*log(1 - (i/i_L_an));
39      eta_con_ca = if di_ca <= 1e-6 then 1e2 else -p_stack*(Ncell*R*T/(4*F)
              + b_C_distr*OnTime)*log(1 - (i/i_L));
40    else
41      eta_con_an = if di_an <= 1e-6 then 1e2 else -p_stack*(Ncell*R*T/(2*F)
              + b_C*OnTime)*log(1 - (i/i_L_an));
42      eta_con_ca = if di_ca <= 1e-6 then 1e2 else -p_stack*(Ncell*R*T/(4*F)
              + b_C*OnTime)*log(1 - (i/i_L));
43    end if;
44    eta_con = eta_con_an + eta_con_ca;
45    e1 = eta_con;
46    f2 = I*eta_con;
47    annotation (preferredView="text", ...);
48  end RSc;
```

A.2.4   Calculating Diffusion Coefficient

In order to calculate the diffusion coefficient according to Equation 3.37, a dedicated Modelica function provided in Listing A.12 was created. This function relies on Equation A.1 and calculates the coefficient of diffusivity between two gases. The coefficient depends on the types of gases involved.

$$D_{ij} = \frac{a}{P} \left(\frac{T}{\sqrt{T_{ci}T_{cj}}} \right)^b (P_{ci}P_{cj})^{1/3}(T_{ci}T_{cj})^{5/12} \left(\frac{1}{M_i} + \frac{1}{M_j} \right)^{1/2} \tag{A.1}$$

Lines 3-11 in Listing A.12 contain the inputs into the function. These include the critical properties of gases, temperature and pressure of the mixture and the types of gases (polar or nonpolar) in the mixture. Keyword `protected` in line 13 signifies that the constants defined in lines 14-17 are internal to the function and cannot be modified externally. The lines 19-24 contain the equation to calculate the diffusion coefficient depending on the type of gases involved.

Listing A.12: Function to calculate the binary diffusion coefficient of two gases

```
1  function BiDiffusion
2    import SI = Modelica.SIunits;
3    input SI.MolarMass M1 "Molar mass of gas 1";
4    input SI.MolarMass M2 "Molar mass of gas 2";
5    input SI.Temperature Tc1 "Critical temperature of gas 1";
6    input SI.Temperature Tc2 "Critical temperature of gas 2";
7    input SI.Pressure pc1 "Critical pressure of gas 1";
8    input SI.Pressure pc2 "Critical pressure of gas 2";
9    input SI.Temperature T "Temperature";
10   input SI.Pressure P "Pressure";
11   input String PairType;
12   output Real D12;
13 protected
14   constant Real an=2.745e-4 "Nonpolar - nonpolar gas pair";
15   constant Real bn=1.832 "Nonpolar - nonpolar gas pair";
16   constant Real ap=3.640e-4 "Polar - nonpolar gas pair";
17   constant Real bp=2.334 "Polar - nonpolar gas pair";
18 algorithm
19   if PairType == "polar" then
20     D12 := (ap/P) * ((T/sqrt(Tc1*Tc2))^bp) * ((pc1*pc2)^(1/3)) *
             ((Tc1*Tc2)^(5/12)) * (((1/M1)+(1/M2))^(1/2));
21   elseif PairType == "nonpolar" then
22     D12 := (an/P)*((T/sqrt(Tc1*Tc2))^bn) * ((pc1*pc2)^(1/3)) *
             ((Tc1*Tc2)^(5/12)) * (((1/M1)+(1/M2))^(1/2));
23   else
24     assert(PairType <> "polar" and PairType <> "nonpolar", "Invalid
             input", AssertionLevel.warning);
25   end if;
26 end BiDiffusion;
```

A.2.5 Dynamic viscosity of gas mixtures

Another function to calculate the dynamic viscosity of gas mixtures μ_{mix} can is written based on the following equation [16]:

$$\mu_{mix} = \sum_{i=1}^{N} \frac{x_i \mu_i}{\sum_{j=1}^{N} x_j \Phi_{ij}}, \tag{A.2}$$

where N is the number of gases in the mixture, x_i is the molar fraction of each gas, and μ_i is the viscosity of individual gases calculated according to:

$$\mu_i = \mu_{i,0} \left(\frac{T}{T_0} \right)^n, \tag{A.3}$$

where $\mu_{i,0}$ is the dynamic viscosity of the gas at reference conditions. The quantity Φ_{ij} is calculated according to Equation A.4:

$$\Phi_{ij} = \frac{1}{\sqrt{8}} \left(1 + \frac{M_i}{M_j}^{-1/2} \right) \left[1 + \left(\frac{\mu_i^{1/2}}{\mu_j} \right) \left(\frac{M_i}{M_j} \right)^{1/4} \right]^2, \tag{A.4}$$

where values of parameters $\mu_{i,0}$, T_0 and n for each gas are defined in Table A.1.

Table A.1: Reference values of dynamic viscosity for each gas [16].

Gas	μ_0, 1×10^{-6} kg/m s	T_0, K	n
H_2	8.411	273	0.68
O_2	19.19	273	0.69
N_2	16.63	273	0.67
H_2O_{vap}	11.2	350	1.15

Listing A.13: Function to calculate dynamic viscosity of any gas mixture

```
1  function DynViscGasMix
2    import SI = Modelica.SIunits;
3    input SI.Temperature T;
4    input SI.MoleFraction X[:];
5    input SI.MolarMass M[:];
6    input SI.DynamicViscosity mu0[:];
7    input SI.Temperature T0[:];
8    input Real n[:];
9    output SI.DynamicViscosity muMix;
10 protected
11   Real mu[size(X, 1)];
12   Real F[size(X, 1), size(X, 1)];
13 algorithm
14   for i in 1:size(X, 1) loop
15     mu[i] := mu0[i]*(T/T0[i])^n[i];
16   end for;
17   for i in 1:size(X, 1) loop
18     for j in 1:size(X, 1) loop
19       F[i, j] := 0.353/sqrt(1 + M[i]/M[j]) * (1 + sqrt(mu[i]/mu[j]) *
                sqrt(sqrt(M[i]/M[j])))^2;
20     end for;
21   end for;
22   muMix := sum(X[i]*mu[i]/sum(X[j]*F[i, j] for j in 1:size(X, 1)) for i in
             1:size(X, 1));
23 end DynViscGasMix;
```
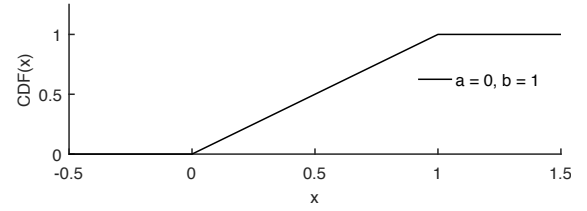
Continuous Distribution Functions

This appendix contains a definitions, parameters and illustrations of commonly used distributions [159, 160, 161].

Uniform Distribution

Parameters: lower limit a and upper limit b.

$$f(x) = \begin{cases} \frac{1}{b-a} & a \leq t \leq b \\ 0 & \text{otherwise} \end{cases}$$

$$F(x) = \frac{x-a}{b-a}$$
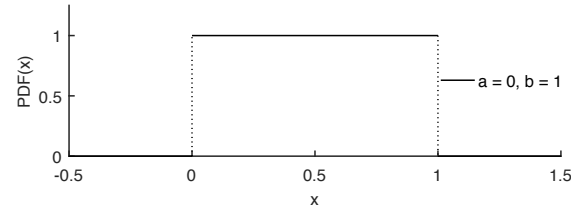
Normal Distribution

Parameters: mean μ and standard deviation σ.

$$f(x) = \frac{1}{\sigma\sqrt{2\pi}} \exp\left[-\frac{(x-\mu)^2}{2\sigma^2}\right]$$

$$F(x) = \Phi\left(\frac{x-\mu}{\sigma}\right)$$

$$\Phi(x) = \frac{1}{\sqrt{2}} \int_0^x \exp\left(-\frac{t^2}{2}\right) dt$$

where $\Phi(x)$ is the Cumulative Distribution Function (CDF) of the the standard normal distribution with $\mu = 0$ and $\sigma = 1$:

Truncated Normal Distribution

Parameters: mean μ, standard deviation σ, lower limit a and upper limit b.

$$f(x) = \frac{\phi\left(\frac{x-\mu}{\sigma}\right)}{\sigma\left(\Phi\left(\frac{b-\mu}{\sigma}\right) - \Phi\left(\frac{a-\mu}{\sigma}\right)\right)}$$

$$F(x) = 1 - \int_{-\infty}^{x} f(x)dx$$
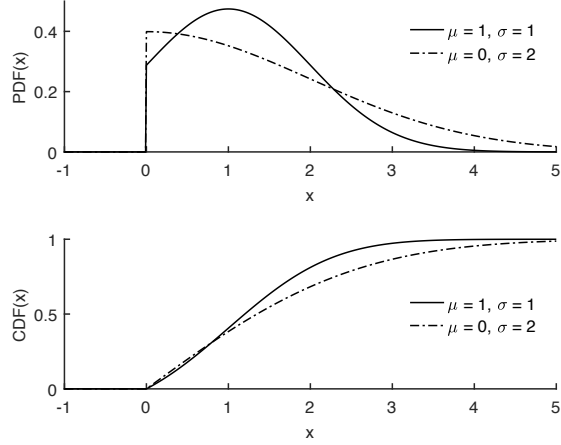
where $\phi(\frac{x-\mu}{\sigma})$ is the Probability Density Function (PDF) of the normal distribution.
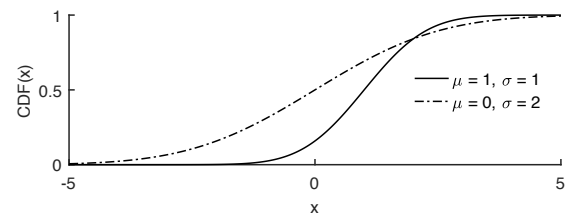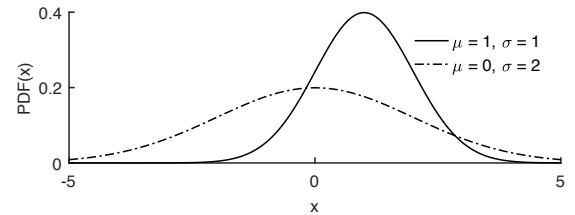
Lognormal Distribution

Parameters: mean μ and standard deviation σ.

$$f(x) = \frac{1}{\sigma x \sqrt{2\pi}} \exp\left[-\frac{(\ln(t) - \mu)^2}{2\sigma^2}\right]$$
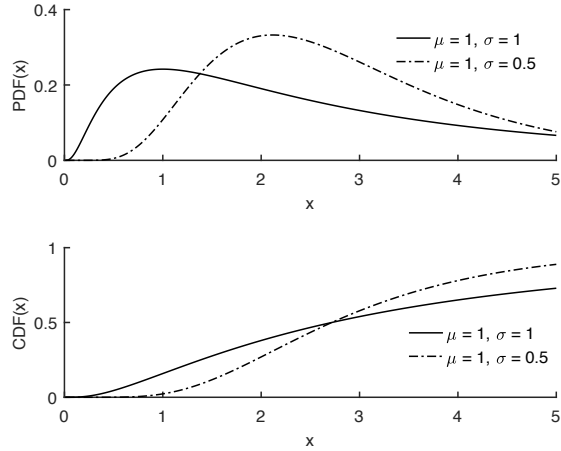
$$F(x) = \int_{x}^{\infty} f(x)dx$$

Exponential Distribution

Parameter: failure rate λ.

$$f(x) = \lambda \exp(-\lambda x)$$

$$F(x) = \int_x^\infty f(x)dx$$
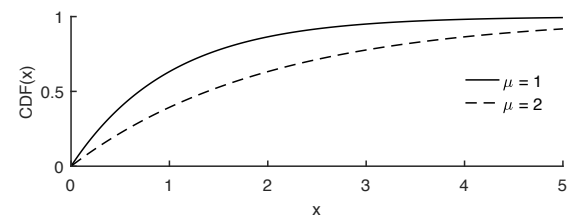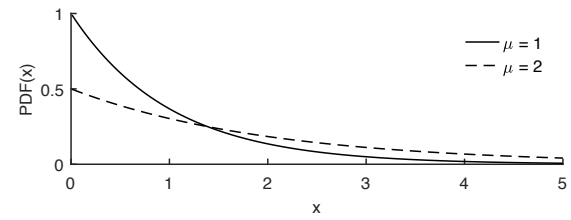
References

[1] United Nations Framework Convention on Climate Change (UNFCCC), Paris Agreement (2015).
URL `http://unfccc.int/paris{_}agreement/items/9485.php`

[2] NASA, Global Temperature (2017).
URL `https://climate.nasa.gov/vital-signs/global-temperature/`

[3] United States Environmental Protection Agency, Climate Change Indicators: Atmospheric Concentrations of Greenhouse Gases (2017).
URL `https://www.epa.gov/climate-indicators/climate-change-indicators-atmospheric-co`

[4] Intergovernmental Panel on Climate Change (IPCC), Fifth Assessment Report (2013).
URL `http://www.ipcc.ch/report/ar5/`

[5] M. Nachmany, S. Fankhauser, J. Setzer, A. Averchenkova, Global trends in climate change legislation and litigation, Tech. rep. (2017).

[6] National Statistics, Final UK greenhouse gas emissions national statistics: 1990-2015 (2017).
URL `https://www.gov.uk/government/statistics/final-uk-greenhouse-gas-emissions-national-statistics-1990-2015`

[7] Department for Transport, Vehicles Statistics (2017).
URL `https://www.gov.uk/government/collections/vehicles-statistics`

[8] U.S. Department of Energy – Fuel Cell Technologies Office, Fuel Cell Technologies Office Multi-Year Research, Development, and Demonstration Plan, Tech. rep. (2016).

[9] D. Stolten, R. C. Samsun, N. Garland (Eds.), Fuel Cells: Data, Facts, and Figures, John Wiley & Sons, 2016.

[10] British Standard, BS 4778-3.1:1991 Quality Vocabulary (1991).

[11] P. Pei, H. Chen, Main factors affecting the lifetime of Proton Exchange Membrane fuel cells in vehicle applications: A review, Applied Energy 125 (2014) 60–75. `doi:10.1016/j.apenergy.2014.03.048`.
URL `http://www.sciencedirect.com/science/article/pii/S0306261914002797`

[12] M. Ball, M. Wietschel, The future of hydrogen – opportunities and challenges, International Journal of Hydrogen Energy 34 (2) (2009) 615–627. `doi:10.1016/j.`

ijhydene.2008.11.014.
URL http://linkinghub.elsevier.com/retrieve/pii/S0360319908015061

[13] J. M. Thomas, W.R. Grove and the Fuel Cell, Philosophical Magazine 92 (31) (2012) 3757–3765. doi:10.1080/14786435.2012.691216.

[14] W. Grubb, L. Niedrach, Batteries with Solid Ion-Exchange Membrane Electrolytes, Journal of Electrochemical Society 107 (2) (1960) 131–135.

[15] F. Barbir, PEM Fuel Cells: Theory and Practice, Academic Press, 2013.
URL http://books.google.com/books?hl=en{&}lr={&}id=elO7n4Z6uLoC{&}pgis=1

[16] R. O'Hayre, S.-W. Cha, F. B. Prinz, W. Colella, Fuel Cell Fundamentals, 3rd Edition, John Wiley & Sons, 2016.

[17] B. Huang, Y. Chatillon, C. Bonnet, F. Lapicque, S. Leclerc, M. Hinaje, S. Raël, Experimental investigation of pinhole effect on MEA/cell aging in PEMFC, International Journal of Hydrogen Energy 38 (1) (2013) 543–550. doi:10.1016/j.ijhydene.2012.09.058.

[18] H. Wang, H. Li, X.-Z. Yuan, PEM Fuel Cell Failure Mode Analysis, CRC Press, 2011.

[19] X. Cheng, Z. Shi, N. Glass, L. Zhang, J. Zhang, D. Song, Z.-S. Liu, H. Wang, J. Shen, A review of PEM hydrogen fuel cell contamination: Impacts, mechanisms, and mitigation, Journal of Power Sources 165 (2) (2007) 739–756.

[20] H. Li, S. Knights, Z. Shi, J. W. Van Zee, J. Zhang (Eds.), Proton exchange membrane fuel cells : contamination and mitigation strategies, CRC Press, 2010.

[21] X. Li, I. Sabir, Review of bipolar plates in PEM fuel cells: Flow-field designs, International Journal of Hydrogen Energy 30 (4) (2005) 359–371. doi:10.1016/j.ijhydene.2004.09.019.
URL http://linkinghub.elsevier.com/retrieve/pii/S0360319904003453

[22] X. Li, I. Sabir, J. Park, A flow channel design procedure for PEM fuel cells with effective water removal, Journal of Power Sources 163 (2) (2007) 933–942. doi:10.1016/j.jpowsour.2006.10.015.
URL http://linkinghub.elsevier.com/retrieve/pii/S0378775306020556

[23] P. Rama, R. Chen, J. Andrews, A review of performance degradation and failure modes for hydrogen-fuelled polymer electrolyte fuel cells, Proceedings of the Institution of Mechanical Engineers, Part A: Journal of Power and Energy 222 (5) (2008) 421–441. doi:10.1243/09576509JPE603.
URL http://pia.sagepub.com/lookup/doi/10.1243/09576509JPE603

[24] M. M. Mench, E. C. Kumbur, T. N. Veziroglu, Polymer Electrolyte Fuel Cell Degradation, Academic Press, 2011.

[25] SAE International, SAE J2615 Testing Performance of Fuel Cell Systems for Automotive Applications (2005).

[26] British Standard, BS EN 60812:2006 Analysis techniques for system reliability – procedure for failure mode and effects analysis (FMEA) (2006). `doi:10.1520/E2019-03R13.Copyright`.

[27] US Department of Transportation, Failure Modes and Effects Analysis for Hydrogen Fuel Cell Vehicles – Subtask 1, Tech. Rep. February (2009).

[28] British Standard, BS EN 61025:2007 Fault Tree Analysis (FTA) (2007).

[29] N. Yousfi Steiner, D. Hissel, P. Moçotéguy, D. Candusso, D. Marra, C. Pianese, M. Sorrentino, Application of Fault Tree Analysis to Fuel Cell diagnosis, Fuel Cells 12 (2) (2012) 302–309. `doi:10.1002/fuce.201100072`.
URL `http://doi.wiley.com/10.1002/fuce.201100072`

[30] L. Placca, R. Kouta, Fault tree analysis for PEM fuel cell degradation process modelling, International Journal of Hydrogen Energy 36 (19) (2011) 12393–12405. `doi:10.1016/j.ijhydene.2011.06.093`.

[31] S. Collong, R. Kouta, Fault tree analysis of proton exchange membrane fuel cell system safety, International Journal of Hydrogen Energy 40 (25) (2015) 8248–8260. `doi:10.1016/j.ijhydene.2015.04.101`.

[32] K. Brik, F. Ben Ammar, A. Djerdir, A. Miraoui, Causal and Fault Trees Analysis of Proton Exchange Membrane Fuel Cell Degradation, Journal of Fuel Cell Science and Technology 12 (5) (2015) 051002. `doi:10.1115/1.4031584`.

[33] P. Rama, R. Chen, J. Andrews, Failure analysis of polymer electrolyte fuel cells., in: Society of Automotive Engineers, [Special Publication] SP, Vol. SP-2167, 2008, pp. 109–125.

[34] M. Whiteley, S. Dunnett, L. Jackson, Failure Mode and Effect Analysis, and Fault Tree Analysis of Polymer Electrolyte Membrane Fuel Cells, International Journal of Hydrogen Energy 41 (2) (2015) 1187–1202. `doi:10.1016/j.ijhydene.2015.11.007`.

[35] British Standard, BS EN 62551:2012 Analysis Techniques for Dependability – Petri Net Techniques (2012).

[36] C. Wieland, O. Schmid, M. Meiler, A. Wachtel, D. Linsler, Reliability computing of polymer-electrolyte-membrane fuel cell stacks through Petri nets, Journal of Power Sources 190 (1) (2009) 34–39. `doi:10.1016/j.jpowsour.2008.10.010`.

[37] M. Whiteley, A. Fly, J. Leigh, S. Dunnett, L. Jackson, Advanced reliability analysis of Polymer Electrolyte Membrane Fuel Cells using Petri-Net analysis and fuel cell modelling techniques, International Journal of Hydrogen Energy 40 (35) (2015) 11550–11558. `doi:10.1016/j.ijhydene.2015.01.154`.

[38] M. Marseguerra, E. Zio, J. Devooght, P. Labeau, A concept paper on dynamic reliability via Monte Carlo simulation, Mathematics and Computers in Simulation 47 (1998) 371–382. `doi:10.1016/S0378-4754(98)00112-8`.

[39] P. Labeau, C. Smidts, S. Swaminathan, Dynamic reliability: towards an integrated platform for probabilistic risk assessment, Reliability Engineering & System Safety 68 (3) (2000) 219–254. `doi:10.1016/S0951-8320(00)00017-X`.

[40] M. H. Davis, Piecewise-Deterministic Markov Processes : A General Class of Non-Diffusion Stochastic Models, Journal of the Royal Statistical Society 46 (3) (1984) 353–388.

[41] M. Bouissou, H. Elmqvist, M. Otter, A. Benveniste, R. Edf, G. D. Gaulle, E. C. Paris, G. Voie, C. Malabry, Efficient Monte Carlo Simulation of Stochastic Hybrid Systems, in: 10th International Modelica Conference, Lund, Sweden, 2014, pp. 715–725. `doi:10.3384/ECP14096715`.

[42] F. Chiacchio, D. D'Urso, G. Manno, L. Compagno, Stochastic hybrid automaton model of a multi-state system with aging: Reliability assessment and design consequences, Reliability Engineering & System Safety 149 (2016) 1–13. `doi:10.1016/j.ress.2015.12.007`.

[43] D. Codetta-Raiteri, A. Bobbio, Evaluation of a benchmark on dynamic reliability via Fluid Stochastic Petri Nets, in: Proceedings of the 7th international workshop on performability modeling of computer and communication systems, 2005, pp. 52—-55.

[44] D. Codetta-Raiteri, A. Bobbio, Solving dynamic reliability problems by means of ordinary and Fluid Stochastic Petri Nets, Advances in Safety and Reliability - Proceedings of the European Safety and Reliability Conference, ESREL 2005 1 (2005).

[45] C. Fecarotti, J. Andrews, R. Chen, A Petri net approach for performance modelling of polymer electrolyte membrane fuel cell systems, International Journal of Hydrogen Energy 41 (28) (2016) 12242–12260. `doi:10.1016/j.ijhydene.2016.05.138`.

[46] G. Manno, A. Zymaris, N. Kakalis, F. Chiacchio, F. Cipollone, L. Compagno, D. D'Urso, N. Trapani, Dynamic reliability analysis of three nonlinear aging components with different failure modes characteristics, in: Safety, Reliability and Risk Analysis: Beyond the Horizon, 2013, pp. 3047–3055.

[47] C. Schallert, Incorporation of Reliability Analysis Methods with Modelica, 2008, pp. 103—-112.

[48] A. Biyikoglu, Review of proton exchange membrane fuel cell models, International Journal of Hydrogen Energy 30 (11) (2005) 1181–1212. `doi:10.1016/j.ijhydene.2005.05.010`.
URL `http://linkinghub.elsevier.com/retrieve/pii/S0360319905001898`

[49] D. Cheddie, N. Munroe, Review and comparison of approaches to proton exchange membrane fuel cell modeling, Journal of Power Sources 147 (1-2) (2005) 72–84. `doi:10.1016/j.jpowsour.2005.01.003`.
URL `http://linkinghub.elsevier.com/retrieve/pii/S0378775305000765`

[50] K. Haraldsson, K. Wipke, Evaluating PEM Fuel Cell System Models, Journal of Power Sources 126 (1) (2004) 88–97.
URL `http://www.sciencedirect.com/science/article/pii/S0378775303010061`

[51] D. Hissel, C. Turpin, S. Astier, L. Boulon, a. Bouscayrol, A review of existing modelling methodologies for PEM fuel cell systems, Fdfc (October 2015) (2008).
URL `http://hal.archives-ouvertes.fr/hal-00369704/`

[52] J. Kofránek, M. Mateják, P. Privitzer, M. Tribula, Causal or Acausal Modelling: Labour for Humans or Labour for Machines, in: Technical Computing Prague 2008, Prague, 2008, pp. 1—-16.

[53] A. A. Franco, P. Schott, C. Jallut, B. Maschke, A Multi-Scale Dynamic Mechanistic Model for the Transient Analysis of PEFCs, Fuel Cells 7 (2) (2007) 99–117. `doi:10.1002/fuce.200500204`.
URL `http://doi.wiley.com/10.1002/fuce.200500204`

[54] T. E. Springer, T. A. Zawodzinski, S. Gottesfeld, Polymer Electrolyte Fuel Cell Model, Journal of the Electrochemical Society 138 (8) (1991) 2334–2342.

[55] J. C. Amphlett, R. M. Baumert, R. F. Mann, B. A. Peppley, P. R. Roberge, T. J. Harris, Performance Modeling of the Ballard Mark IV Solid Polymer Electrolyte Fuel Cell I. Mechanistic Model Development, Journal of The Electrochemical Society 142 (1) (1995) 1. `doi:10.1149/1.2043866`.
URL `http://jes.ecsdl.org/content/142/1/1.abstract`

[56] J. C. Amphlett, R. M. Baumert, R. F. Mann, B. A. Peppley, P. R. Roberge, T. J. Harris, Performance Modeling of the Ballard Mark IV Solid Polymer Electrolyte Fuel Cell II. Empirical Model Development, Journal of The Electrochemical Society 142 (1) (1995) 9. `doi:10.1149/1.2043959`.

[57] A. Rowe, X. Li, Mathematical modeling of proton exchange membrane fuel cells, Journal of Power Sources 102 (1-2) (2001) 82–96. `doi:10.1016/S0378-7753(01)00798-4`.
URL `http://www.sciencedirect.com/science/article/pii/S0378775301007984`

[58] A. J. del Real, A. Arce, C. Bordons, Development and experimental validation of a PEM fuel cell dynamic model, Journal of Power Sources 173 (1) (2007) 310–324. `doi:10.1016/j.jpowsour.2007.04.066`.
URL `http://www.sciencedirect.com/science/article/pii/S0378775307008981`

[59] S.-K. Park, S.-Y. Choe, Dynamic modeling and analysis of a 20-cell PEM fuel cell stack considering temperature and two-phase effects, Journal of Power Sources 179 (2) (2008) 660–672. `doi:10.1016/j.jpowsour.2008.01.029`.
URL `http://www.sciencedirect.com/science/article/pii/S0378775308001031`

[60] J. T. Pukrushpan, H. Peng, A. G. Stefanopoulou, Control-Oriented Modeling and Analysis for Automotive Fuel Cell Systems, Journal of Dynamic Systems Measurement and Control-Transactions of the Asme 126 (1) (2004) 14–25. `doi:10.1115/1.1648308`.

[61] M. Schultze, J. Horn, A Control Oriented Simulation Model of an Evaporation Cooled Polymer Electrolyte Membrane Fuel Cell System, in: 18th IFAC World Congress, Milan, Italy, 2011.

[62] J. Macedo-Valencia, J. M. Sierra, S. J. Figueroa-Ramirez, S. E. Diaz, M. Meza, 3D CFD modeling of a PEM fuel cell stack, International Journal of Hydrogen Energy 41 (48) (2016) 23425–23433. `doi:10.1016/j.ijhydene.2016.10.065`.

[63] M. J. Khan, M. T. Iqbal, Modelling and Analysis of Electro-chemical, Thermal, and Reactant Flow Dynamics for a PEM Fuel Cell System, Fuel cells 5 (4) (2005) 463–475.

[64] B. Blunier, A. Miraoui, Modelling of fuel cells using multi-domain VHDL-AMS language, Journal of Power Sources 177 (2) (2008) 434–450. `doi:10.1016/j.jpowsour.2007.11.002`.
URL `http://www.sciencedirect.com/science/article/pii/S0378775307024329`

[65] F. Gao, B. Blunier, A. Miraoui, A. El-Moudni, Cell layer level generalized dynamic modeling of a PEMFC stack using VHDL-AMS language, International Journal of Hydrogen Energy 34 (13) (2009) 5498–5521. `doi:10.1016/j.ijhydene.2009.04.069`.
URL `http://www.sciencedirect.com/science/article/pii/S0360319909006533`

[66] M. A. Rubio, A. Urquia, S. Dormido, Dynamic modelling of PEM fuel cells using the FuelCell Lib Modelica library, Mathematical and Computer Modelling of Dynamical Systems 16 (3) (2010) 165–194. `doi:10.1080/13873954.2010.506758`.
URL `http://www.tandfonline.com/doi/abs/10.1080/13873954.2010.506758`

[67] K. L. Davies, C. J. Paredis, C. L. Haynes, Library for First-Principle Models of Proton Exchange Membrane Fuel Cells in Modelica, in: 9th International Modelica Conference, Munich, Germany, 2012, pp. 115–124. `doi:10.3384/ecp12076115`.

[68] K. L. Davies, Declarative Modeling of Coupled Advection and Diffusion as Applied to Fuel Cells, Ph.D. thesis, Georgia Institute of Technology (2014).

[69] P. Gawthrop, G. Bevan, Bond-Graph Modeling, IEEE Control Systems Magazine 27 (2) (2007) 24–45. `doi:10.1109/MCS.2007.338279`.
URL `http://ieeexplore.ieee.org/lpdocs/epic03/wrapper.htm?arnumber=4140745`

[70] A. K. Samantaray, B. Ould Bouamama, Model-based Process Supervision, Springer, 2008.

[71] D. Karnopp, D. L. Margolis, R. C. Rosenberg, System Dynamics: Modeling and Simulation and Control of Mechatronic Systems, 4th Edition, John Wiley & Sons, Inc., 2012.

[72] R. Saisset, G. Fontes, C. Turpin, S. Astier, Bond Graph model of a PEM fuel cell, Journal of Power Sources 156 (1) (2006) 100–107. `doi:10.1016/j.jpowsour.2005.08.040`.

[73] D. Mzoughi, H. Allagui, A. Bouaicha, A. Mami, Modeling and testing of a 1.2-kW Nexa fuel cell using bond graph methodology, IEEJ Transactions on Electrical and Electronic Engineering 10 (5) (2015) 527–538. `doi:10.1002/tee.22116`.
URL `http://doi.wiley.com/10.1002/tee.22116`

[74] C. Peraza, J. G. Diaz, F. J. Arteaga-Bravo, C. Villanueva, F. Gonzalez-Longatt, Modeling and simulation of PEM fuel cell with bond graph and 20sim, 2008 American Control Conference (2008) 5104–5108`doi:10.1109/ACC.2008.4587303`.
URL `http://ieeexplore.ieee.org/lpdocs/epic03/wrapper.htm?arnumber=4587303`

[75] S. Rabih, C. Turpin, S. Astier, Bond Graph model of a PEM fuel cell stack, in: ICREPQ08-international conference on renewable energy and power quality, Santander, Spain, 2008, pp. 1–6.
URL `http://scholar.google.com/scholar?hl=en{&}btnG=Search{&}q=intitle:Bond+Graph+model+of+a+PEM+fuel+cell+stack{#}0`

[76] B. A. Mccain, A. G. Stefanopoulou, Order Reduction for a Control-Oriented Model of the Water Dynamics in Fuel Cells, in: Fourth International Conference on Fuel Cell Science, Engineering and Technology, Irvine, California, USA, 2006, pp. 1–9.

[77] K. Bruun, Bond Graph Modelling of Fuel Cells for Marine Power Plants, Ph.D. thesis, Norwegian University of Science and Technology (NTNU) (2009).

[78] D. Mzoughi, H. Allagui, N. Khili, A. Mami, Bond graph modeling and control of a single PEM cell, in: 6th International Renewable Energy Congress (IREC), 2015.

[79] Y. Hung, P. Lin, C. Wu, C. Hong, Real-time dynamic modeling of hydrogen PEM-FCs, Journal of the Franklin Institute 345 (2) (2008) 182–203. `doi:10.1016/j.jfranklin.2007.08.004`.
URL `http://www.sciencedirect.com/science/article/pii/S0016003207000804`

[80] P. Vijay, A. Samantaray, A. Mukherjee, A bond graph model-based evaluation of a control scheme to improve the dynamic performance of a solid oxide fuel cell, Mechatronics 19 (4) (2009) 489–502. `doi:10.1016/j.mechatronics.2008.11.016`.

[81] P. Vijay, A. K. Samantaray, A. Mukherjee, On the rationale behind constant fuel utilization control of solid oxide fuel cells, Proceedings of the Institution of Mechanical Engineers, Part I: Journal of Systems and Control Engineering 223 (2) (2009) 229–252. `doi:10.1243/09596518JSCE650`.
URL `http://pii.sagepub.com/lookup/doi/10.1243/09596518JSCE650`

[82] Q. Yang, A. Aitouche, B. Ould-Bouamama, Structural Diagnosability of Fuel Cell Stack System Based on Bond Graph Tool, IFAC Proceedings Volumes 42 (8) (2009) 728–733. `doi:10.3182/20090630-4-ES-2003.00121`.
URL `http://linkinghub.elsevier.com/retrieve/pii/S1474667016358645`

[83] C. Robin, M. Gerard, J. D'Arbigny, P. Schott, L. Jabbour, Y. Bultel, Development and experimental validation of a PEM fuel cell 2D-model to study heterogeneities effects along large-area cell surface, International Journal of Hydrogen Energy 40 (32) (2015) 10211–10230. `doi:10.1016/j.ijhydene.2015.05.178`.

[84] M. W. Fowler, R. F. Mann, J. C. Amphlett, B. A. Peppley, P. R. Roberge, Incorporation of voltage degradation into a generalised steady state electrochemical model for a PEM fuel cell, Journal of Power Sources 106 (1) (2002) 274–283.
URL `http://www.sciencedirect.com/science/article/pii/S0378775301010291`

[85] R. F. Mann, J. C. Amphlett, M. A. I. Hooper, H. M. Jensen, B. A. Peppley, P. R. Roberge, Development and application of a generalised steady-state electrochemical model for a PEM fuel cell, Journal of Power Sources 86 (1) (2000) 173–180.

[86] M. Jouin, R. Gouriveau, D. Hissel, M. C. Péra, N. Zerhouni, PEMFC aging modeling for prognostics and health assessment, IFAC-PapersOnLine 48 (21) (2015) 790–795. `doi:10.1016/j.ifacol.2015.09.623`.

[87] M. Jouin, R. Gouriveau, D. Hissel, M. C. Pera, N. Zerhouni, Degradations analysis and aging modeling for health assessment and prognostics of PEMFC, Reliability Engineering and System Safety 148 (2016) 78–95. `doi:10.1016/j.ress.2015.12.003`.

[88] U. Reimer, B. Schumacher, W. Lehnert, Accelerated Degradation of High-Temperature Polymer Electrolyte Fuel Cells: Discussion and Empirical Modeling,

Journal of the Electrochemical Society 162 (1) (2015) F153–F164. `doi:10.1149/2.0961501jes`.
URL `http://jes.ecsdl.org/cgi/doi/10.1149/2.0961501jes`

[89] X. Zhang, D. Yang, M. Luo, Z. Dong, Load profile based empirical model for the lifetime prediction of an automotive PEM fuel cell (2017). `doi:10.1016/j.ijhydene.2017.02.146`.

[90] X. Zhang, P. Pisu, Prognostic-oriented Fuel Cell Catalyst Aging Modeling and Its Application to Health-Monitoring and Prognostics of a PEM Fuel Cell, International Journal of Prognostics and Health Management (2014) 1–16.

[91] C. Robin, M. Gerard, A. A. Franco, P. Schott, Multi-scale coupling between two dynamical models for PEMFC aging prediction, International Journal of Hydrogen Energy 38 (11) (2013) 4675–4688. `doi:10.1016/j.ijhydene.2013.01.040`.

[92] C. Robin, M. Gérard, M. Quinaud, J. D'Arbigny, Y. Bultel, Proton exchange membrane fuel cell model for aging predictions: Simulated equivalent active surface area loss and comparisons with durability tests, Journal of Power Sources 326 (2016) 417–427. `doi:10.1016/j.jpowsour.2016.07.018`.

[93] M. Chandesris, R. Vincent, L. Guetaz, J. S. Roch, D. Thoby, M. Quinaud, Membrane degradation in PEM fuel cells: From experimental results to semi-empirical degradation laws, International Journal of Hydrogen Energy 42 (12) (2017) 8139–8149. `doi:10.1016/j.ijhydene.2017.02.116`.
URL `http://dx.doi.org/10.1016/j.ijhydene.2017.02.116`

[94] Y. Zhou, Y. Luo, S. Yu, K. Jiao, Modeling of cold start processes and performance optimization for proton exchange membrane fuel cell stacks, Journal of Power Sources 247 (2014) 738–748. `doi:10.1016/j.jpowsour.2013.09.023`.

[95] H. M. Paynter, Analysis and design of engineering systems, MIT Press, 1961.

[96] E. Sosnovsky, Nuclear Reactor Multiphysics via Bond Graph Formalism, Ph.D. thesis, Massachusetts Institute of Technology (2014).

[97] L. Xiaotian, W. Anlin, Definitions of causality in bond graph model for efficient simulation mechanism, Mechanism and Machine Theory 80 (2014) 112–124. `doi:10.1016/j.mechmachtheory.2014.05.002`.
URL `http://dx.doi.org/10.1016/j.mechmachtheory.2014.05.002`

[98] R. Tapia-Sanchez, A. Medina-Rios, N. Villa-Villasenor, Solar cell model: a bond graph approach, Simulation 91 (4) (2015) 349–359. `doi:10.1177/0037549715579538`.

[99] G. Mocellin, The Bond Graph Method Applied to Social and Life Sciences, SIMU-LATION SERIES (2001).
URL http://scholar.google.com/scholar?hl=en{&}btnG=Search{&}q=intitle:
The+Bond+Graph+Mehtod+Applied+to+Social+and+Life+Sciences{#}0

[100] J. W. Brewer, Progress in the bond graph representations of economics and population dynamics, Journal of the Franklin Institute 328 (5-6) (1991) 675–696.
doi:10.1016/0016-0032(91)90048-8.
URL http://www.sciencedirect.com/science/article/pii/0016003291900488

[101] A. Vaz, K. Singh, G. Dauphin-Tanguy, Bond graph model of extensor mechanism of finger based on hook-string mechanism, Mechanism and Machine Theory 91 (2015) 187–208. doi:10.1016/j.mechmachtheory.2015.03.011.
URL http://dx.doi.org/10.1016/j.mechmachtheory.2015.03.011

[102] F. T. Brown, Engineering system dynamics: a unified graph-centered approach, CRC press, 2006.

[103] Y. A. Çengel, M. A. Boles, Thermodynamics. An Engineering Approach, seventh ed Edition, Mcgraw-Hill, 2010.

[104] C. Spiegel, PEM Fuel Cell Modeling and Simulation Using Matlab, Academic Press, 2011.

[105] J. H. Nam, M. Kaviany, Effective diffusivity and water-saturation distribution in single- and two-layer PEMFC diffusion medium, International Journal of Heat and Mass Transfer 46 (24) (2003) 4595–4611. doi:10.1016/S0017-9310(03)00305-3.
URL http://www.sciencedirect.com/science/article/pii/S0017931003003053

[106] D. Karnopp, Bond graph models for electrochemical energy storage : electrical, chemical and thermal effects, Journal of the Franklin Institute 327 (6) (1990) 983–992.
doi:10.1016/0016-0032(90)90073-R.
URL http://www.sciencedirect.com/science/article/pii/001600329090073R

[107] Controllab Products, 20sim (2016).
URL http://www.20sim.com/

[108] S. Wiechula, Tools for Modelling and Identification with Bond Graphs and Genetic Programming, Ph.D. thesis, University of Waterloo (2006).

[109] D. Wang, M. Yu, C. B. Low, S. Arogeti, Model-based Health Monitoring of Hybrid Systems, Springer New York, New York, NY, 2013. doi:10.1007/
978-1-4614-7369-5.
URL http://books.google.com/books?id=mbVDAAAAQBAJ{&}pgis=1http://link.
springer.com/10.1007/978-1-4614-7369-5

[110] J. Antonio, C. Alvarez-Caldas, J. L. San Roma, Analysis of Dynamic Systems Using Bond Graph Method Through SIMULINK, in: A. Assi (Ed.), Engineering Education and Research Using MATLAB, InTech, 2011, Ch. 11, pp. 265–288. `doi:10.5772/19424`.

[111] Modelica Association, Modelica (2016).
URL `https://modelica.org/`

[112] ITI GmbH, Simulation X (2016).
URL `https://www.simulationx.com/simulation-software.html`

[113] Dassault Systemes, Dymola (2016).
URL `http://www.3ds.com/products-services/catia/capabilities/modelica-systems-simulation-info/dymola`

[114] Open Source Modelica Consortium, OpenModelica (2016).
URL `www.openmodelica.org`

[115] W. Borutzky, Bond graphs and object-oriented modelling–a comparison, Proceedings of the Institution of Mechanical Engineers, Part I: Journal of Systems and Control Engineering 216 (1) (2002) 21–33. `doi:10.1243/0959651021541408`.
URL `http://pii.sagepub.com/lookup/doi/10.1243/0959651021541408`

[116] F. Cellier, R. McBride, Object-Oriented Modeling of Complex Physical Systems Using the Dymola Bond-Graph Library, in: Intl. Conf. Bond Graph Modeling and Simulation, 2003, pp. 157–162.

[117] D. Zimmer, F. Cellier, The Modelica Multi-Bond Graph Library, Modelica Conference (2006) 559–568.

[118] F. Cellier, J. Greifeneder, ThermoBondLib–A New Modelica Library for Modeling Convective Flows, in: Modelica Conference, 2008, pp. 163–172.

[119] P. Fritzon, Principles of object-oriented modeling and simulation with Modelica 3.3: a cyber-physical approach, John Wiley & Sons, 2014.

[120] National Instruments, LabVIEW - National Instruments (2017).
URL `http://www.ni.com/en-us/shop/labview.html`

[121] TDI Power, TDI Dynaload Legacy Product, RBL488 Series of electronic loads (2017).
URL `http://www.tdipower.com/electronic-loads/legacy-models/rbl-488-series.html`

[122] Pragma Industries, PEM Fuel Cell Stacks (2016).
URL `http://www.pragma-industries.com/`

[123] J. A. Salva, A. Iranzo, F. Rosa, E. Tapia, Experimental validation of the polarization curve and the temperature distribution in a PEMFC stack using a one dimensional analytical model, International Journal of Hydrogen Energy 41 (45) (2016) 20615–20632. `doi:10.1016/j.ijhydene.2016.09.152`.
URL `http://dx.doi.org/10.1016/j.ijhydene.2016.09.152`

[124] Fuel Cells Etc, Gas Diffusion Layer (GDL) Comparison Chart (2017).
URL `http://fuelcellsetc.com/helpful-tools/gas-diffusion-layer-gdl-comparison-chart/`

[125] Chemours, Nafion$^{\text{TM}}$ XL Membrane (2017).
URL `https://www.chemours.com/Nafion/en{_}US/products/nafion{_}xl{_}membrane.html`

[126] H. Wang, H. Li, X.-Z. Yuan, PEM Fuel Cell Diagnostic Tools, CRC Press, 2011.

[127] MathWorks, Curve Fitting Toolbox - MATLAB (2017).
URL `https://uk.mathworks.com/products/curvefitting.html`

[128] British Standard, BS 4778-3.2:1991 Quality Vocabulary (1991).

[129] R. Isermann, Fault-Diagnosis Systems: An Introduction from Fault Detection to Fault Tolerance, Springer Berlin Heidelberg, Berlin, Heidelberg, 2006. `doi:10.1007/3-540-30368-5`.
URL `http://link.springer.com/10.1007/3-540-30368-5`

[130] P. Fiani, M. Batteux, P. Dague, N. Rapin, Fuel Cell System Improvement for Model-Based Diagnosis Analysis, Vehicle Power and Propulsion Conference IEEE VPPC (2010).

[131] R. Isermann, Fault-Diagnosis Applications: Model-Based Condition Monitoring: Actuators, Drives, Machinery, Plants, Sensors, and Fault-tolerant Systems, Springer Berlin Heidelberg, Berlin, Heidelberg, 2011. `doi:10.1007/978-3-642-12767-0`.
URL `http://link.springer.com/10.1007/978-3-642-12767-0`

[132] P. D. T. O'Connor, A. Kleyner, Practical Reliability Engineering, John Wiley & Sons, Ltd, Chichester, UK, 2011. `doi:10.1002/9781119961260`.

[133] Y. S. Chen, C. W. Yang, J. Y. Lee, Implementation and evaluation for anode purging of a fuel cell based on nitrogen concentration, Applied Energy 113 (2014) 1519–1524. `doi:10.1016/j.apenergy.2013.09.028`.
URL `http://dx.doi.org/10.1016/j.apenergy.2013.09.028`

[134] K. D. Baik, M. S. Kim, Characterization of nitrogen gas crossover through the membrane in proton-exchange membrane fuel cells, International Journal of Hydrogen Energy 36 (1) (2011) 732–739. `doi:10.1016/j.ijhydene.2010.09.046`.

[135] T. Matsuura, J. Chen, J. B. Siegel, A. G. Stefanopoulou, Degradation phenomena in PEM fuel cell with dead-ended anode, International Journal of Hydrogen Energy 38 (26) (2013) 11346–11356. `doi:10.1016/j.ijhydene.2013.06.096`.

[136] FC LAB, IEEE PHM 2014 Data Challenge (2014).
URL `http://eng.fclab.fr/ieee-phm-2014-data-challenge/`

[137] M. Fowler, J. Amphlett, Issues associated with voltage degradation in a PEMFC, Journal of New Materials for Electrochemical Systems 5 (2002) 255–262.

[138] W. G. Schneeweiss, Petri nets for reliability modeling:(in the fields of engineering safety and dependability), LiLoLe-Verlag, 1999.

[139] V. Volovoi, System-Level Maintenance Policies via Stochastic Petri nets with Aging Tokens, in: 2007 Proceedings - Annual Reliability and Maintainability Sympsoium, IEEE, 2007, pp. 89–94. `doi:10.1109/RAMS.2007.328049`.
URL `http://ieeexplore.ieee.org/lpdocs/epic03/wrapper.htm?arnumber=4126330`

[140] S. Proß, B. Bachmann, PNlib - An Advanced Petri Net Library for Hybrid Process Modeling, Proceedings 9th Modelica Conference, Munich, Germany (2012) 47–56`doi:10.3384/ecp1207647`.

[141] D. J. Smith, Reliability, Maintainability and Risk, seventh ed Edition, Elsevier, 2005.

[142] T. R. Moss, The Reliability Data Handbook, Professional Engineering Publishing, London, 2005.

[143] Management SINTEF Industrial, OREDA Offshore Reliability Data Handbook (2002).

[144] W. Denson, G. Chandler, W. Crowell, R. Wanner, Non-electronic Parts Reliability Data (1991).

[145] Department of Defense of the USA, MIL-HDBK-217F Military Handbook Reliability Prediction of Electronic Equipment (1991).

[146] M. Jouin, M. Bressel, S. Morando, R. Gouriveau, D. Hissel, M. C. Péra, N. Zerhouni, S. Jemei, M. Hilairet, B. Ould Bouamama, Estimating the end-of-life of PEM fuel cells: Guidelines and metrics, Applied Energy 177 (2016) 87–97. `doi:10.1016/j.apenergy.2016.05.076`.

[147] S. Hmam, J. C. Olivier, S. Bourguet, L. Loron, A Multirate Simulation Method for Large Timescale Systems Applied for Lifetime Simulations, 2015 IEEE Vehicle Power and Propulsion Conference, VPPC 2015 - Proceedings (2015). `doi:10.1109/VPPC.2015.7352878`.

[148] B. Thiele, M. Otter, S. E. Mattsson, Modular Multi-Rate and Multi-Method Real-Time Simulation (2014) 381–393doi:10.3384/ecp14096381.
URL http://www.ep.liu.se/ecp{_}article/index.en.aspx?issue=96;article=40

[149] N. Noguer, D. Candusso, R. Kouta, F. Harel, W. Charon, G. Coquery, A framework for the probabilistic analysis of PEMFC performance based on multi-physical modelling, stochastic method, and design of numerical experiments, International Journal of Hydrogen Energy 42 (1) (2017) 459–477. doi:10.1016/j.ijhydene.2016.11.074.

[150] N. L. Johnson, S. Kotz, N. Balakrishnan, Continuous Univariate Distributions, Vol. 1 (Wiley Series in Probability and Statistics), 1st Edition, Wiley, New York,, 1994.

[151] G. Marsaglia, Xorshift RNGs, Journal Of Statistical Software 8 (14) (2003) 1–6. doi:10.1007/978-1-4757-2446-2_10.
URL http://www.jstatsoft.org/v08/i14/paper

[152] S. Vigna, An experimental exploration of Marsaglia's xorshift generators, scrambled, ACM Transactions on Mathematical Software 30 (4) (2016). arXiv:1402.6246, doi:10.1145/2845077.
URL http://arxiv.org/abs/1402.6246

[153] Minitab Inc., Minitab (2018).
URL http://www.minitab.com

[154] R Core Team, R: A Language and Environment for Statistical Computing (2013).
URL http://www.r-project.org/

[155] Reliasoft, Weibull++ (2018).
URL https://www.reliasoft.com/Weibull/

[156] P. Kaplan, E.L; Meier, Nonparametric Estimation from Incomplete Observations, Journal of the American Statistical Association 53 (282) (1958) 457–481.

[157] W. Borutzky, Bond graph model-based fault detection using residual sinks, Proceedings of the Institution of Mechanical Engineers, Part I: Journal of Systems and Control Engineering 223 (3) (2009) 337–352. doi:10.1243/09596518JSCE666.

[158] K. Medjaher, A Bond Graph Model-Based Fault Detection and Isolation (2011) 503–512.

[159] N. T. Thomopoulos, Statistical Distributions: Applications and Parameter Estimates, Springer International Publishing, 2017. doi:10.1007/978-3-319-65112-5.
URL http://link.springer.com/10.1007/978-3-319-65112-5

[160] C. Forbes, M. Evans, N. Hastings, B. Peacock, Statistical Distributions, John Wiley & Sons, 2011.

[161] C. P. Robert, Simulation of truncated normal variables, Statistics and Computing 5 (2) (1995) 121–125. `arXiv:0907.4010, doi:10.1007/BF00143942`.